Exploring Dark Sectors in Particle Physics

Dissertation

zur Erlangung des Grades „Doktor der Naturwissenschaften“
am Fachbereich Physik, Mathematik und Informatik
der Johannes Gutenberg-Universität in Mainz

Lisa Maria Michaels

geb. in Berlin

date of submission: April 27, 2026
date of defence: July 1, 2026

Abstract

Dark matter provides one of the strongest pieces of evidence for physics beyond the Standard Model and motivates a wide range of dark sector scenarios. In this thesis, we investigate theoretical consistency conditions of gauge symmetry extensions and phenomenological signatures of two concrete dark matter models.

We first study extensions of the Standard Model by an additional $U(1)$ gauge symmetry with a new massive gauge boson Z', focusing on constraints arising from anomaly cancellation. We compute the axial–axial–vector triangle diagram inducing an effective Z–Z'–γ vertex and analyse its implications for the decay $Z \to Z'\gamma$. We consider two representative examples, $U(1)_{B-L}$ and $U(1)_B$, and show that the additional fermionic states that have to be introduced in the second case can lead to non-trivial effects such as non-decoupling. We derive constraints on the parameter space from $Z \to Z'\gamma$ and relate our results to effective field theory descriptions.

We then study the collider phenomenology of inelastic dark matter, where a small mass splitting between dark sector states suppresses direct detection signals but can lead to distinctive signatures at the Large Hadron Collider. Using simplified models with different mediator types, we recast an ATLAS monojet search and obtain exclusion limits, finding the strongest constraints for vector and axial-vector interactions. We further examine displaced vertex signatures and show that observable effects are mainly restricted to pseudoscalar mediators due to competing requirements on decay kinematics and lifetimes. We identify the key parameters controlling collider sensitivity and discuss implications for future searches.

Finally, we investigate a leptophilic dark matter model in which interactions with the Standard Model are mediated by a charged t-channel particle. In this scenario, dark matter annihilation can produce gamma-ray features via virtual internal bremsstrahlung. We show that the same interactions generate electromagnetic form factors at loop level, leading to anapole and dipole moments that can give rise to observable direct detection signals. The resulting constraints are strongest in the parameter region that enhances the gamma-ray feature, highlighting the complementarity between indirect and direct detection probes.

Overall, this work demonstrates the interplay between theoretical consistency and phenomenological signatures in dark sector models and shows how combining different experimental approaches significantly constrains physics beyond the Standard Model.

Contents

Chapter 1

Introduction

This thesis addresses two complementary and essential aspects of particle physics. The first part focuses on fundamental principles of quantum field theories and their implications for physics beyond the Standard Model. The second part presents the phenomenological imprints of two concrete models for dark matter at colliders and in direct detection experiments. These two perspectives are intrinsically connected: any viable dark matter model must satisfy the theoretical consistency requirements imposed by quantum field theory while simultaneously evading existing experimental constraints, be it in laboratory searches or astrophysical and cosmological observations.

We start by reviewing the theoretical framework that this work builds upon, namely the Standard Model of particle physics.

Our current understanding of elementary particles and their interactions is encapsulated in the Standard Model of particle physics (SM). Developed through experimental and theoretical advances spanning roughly from the 1920s to the 1970s, the SM was eventually formulated in the form we know today. Section 1.1 provides an overview of its structure and highlights its most important features. Since its first formulation, the SM has been tested with remarkable precision. The discovery of the W and Z bosons by the UA1 Collaboration and the UA2 Collaboration in the early 1980s confirmed the electroweak theory [1, 2]. The subsequent observation of the charm [3, 4] and top [5, 6] quarks further validated the model's predictive power. Most notably, in 2012, the ATLAS and the CMS Collaboration at CERN announced the discovery of the Higgs boson [7, 8], completing the particle content predicted by the SM. With this milestone, the SM became an experimentally confirmed and extraordinarily successful description of nearly all observed particle physics phenomena.

At the same time, several experimental observations indicate that the SM is incomplete, allowing to take a glimpse at a new, foreign world that lies beyond our current knowledge. These hints arise in a variety of settings, including astrophysical observations, precision measurements, and collider experiments.

A prominent example is neutrino flavour oscillation, first established through the deficit of solar neutrinos and later confirmed in atmospheric, reactor, and accelerator experiments [9–11]. Neutrino oscillations imply non-zero neutrino masses and flavour mixing. In its minimal formulation, however, the SM contains no neutrino mass terms. Oscillation experiments determine the mass-squared differences and mixing angles [12,13], while the absolute neutrino mass scale remains unknown. Measurements of Tritium-β-decay at KATRIN provide an upper limit on the mass of $m_\beta = \sqrt{\sum_i |U_{ei}|^2 m_i^2} < 0.45\,\mathrm{eV}$ [14]. In addition, a number of experimental anomalies hint at possible non-standard oscillations, which could be explained by the existence of additional neutrino states, see Refs. [15–20].

Astrophysical and cosmological observations provide compelling, independent evidence for dark matter, one of the most established examples of physics beyond the SM. The dynamics of galaxies, galaxy clusters, and the evolution of large-scale structure require the presence of much more non-baryonic, "dark", than ordinary matter. Its existence is inferred from gravitational effects, while no non-gravitational interactions with SM particles have been conclusively observed so far. Section 1.2 reviews the experimental evidence for dark matter, outlines theoretical frameworks proposed to account for it, and comments on current, ongoing searches to reveal its particle physics nature. In the second part of this thesis, we investigate the phenomenological implications of two such models.

Precision measurements also probe the internal consistency of the SM. Owing to its gauge symmetries and renormalisable structure, the SM predicts correlations among observables. This in turn allows high-precision experiments to test these correlations by comparing independent determinations of related quantities. While most measurements confirm SM predictions, several tensions have been reported. In the electroweak sector, the CDF Collaboration at the Fermilab Tevatron collider reported a measurement of the W-boson mass in tension with the SM prediction [21], although other experiments have not confirmed this deviation. Flavour physics provides additional probes, with some b-quark decay observables exhibiting mild tensions with SM expectations [22–26].[1]

Beyond experimental anomalies, several conceptual problems suggest that the SM may not be a complete theory. The Higgs mass is highly sensitive to radiative corrections from heavy states, giving rise to the hierarchy problem. The cosmological constant poses an even more severe naturalness problem: naive estimates of vacuum energy in quantum field theory exceed the observed value by many orders of magnitude. The SM also fails to account for the observed baryon asymmetry of the Universe, as its sources of CP violation are insufficient and it does not facilitate any (known) mechanism for substantial departure from equilibrium. In addition, the strong CP problem – the puzzling smallness of CP violation in quantum chromodynamics – represents another unexplained fine-tuning in the theory.

[1] Other previously reported anomalies, such as the muon $g-2$ and the proton radius puzzle, have largely converged with SM predictions following updated theoretical and experimental results [27–32].

Cosmology provides further motivation for new physics. The observed large-scale homogeneity and isotropy of the Universe, most precisely measured in the cosmic microwave background (CMB), are naturally explained by an early phase of accelerated expansion (inflation), which resolves the horizon problem and generates primordial density perturbations.

Finally, the flavour structure of the SM remains unexplained. Fermion masses and mixing angles arise from Yukawa couplings that span many orders of magnitude and exhibit hierarchical patterns without a known underlying organising principle. This flavour puzzle, together with the issues outlined above, has motivated extensions of the SM such as grand unified theories and supersymmetry.

This thesis focuses on two complementary aspects of particle physics. The first part studies fundamental principles of quantum field theory and their implications for the conceptual and experimental questions discussed above. The second part investigates the phenomenology of two specific dark matter models in colliders, precision experiments, and astrophysical observations.

We begin with a brief introduction to the SM, outlining its most important features. For a more detailed overview, the reader may be referred to textbooks, such as Refs. [33–35]. This is followed by Section 1.2, which reviews the evidence for DM, the models that could explain it, and ongoing experimental searches. Finally, Section 1.3 provides an overview of the content and structure of the main chapters of this thesis.

1.1 The Standard Model of Particle Physics

The Standard Model of particle physics (SM) is a renormalisable quantum field theory describing the strong, weak, and electromagnetic interactions. It is based on the local gauge symmetry group

$$SU(3)_c \times SU(2)_L \times U(1)_Y \,.$$

Each factor corresponds to a gauge symmetry with an associated set of gauge bosons that mediate the fundamental interactions.

The non-Abelian group $SU(3)_c$ describes the theory of strong interactions, quantum chromodynamics (QCD) [36–42]. Its eight generators give rise to eight massless gauge bosons, the gluons g. Because $SU(3)_c$ is non-Abelian, the gluons themselves carry colour charge and therefore interact with each other. For the observed number of quarks, this property leads to asymptotic freedom at high energies and confinement at low energies: the matter we encounter in everyday life is composed of hadrons – such as protons and neutrons –, which are colour-neutral bound states of quarks and gluons.

The electroweak sector is described by the product group $SU(2)_L \times U(1)_Y$ [43–45]. The subscript L indicates that $SU(2)_L$ acts only on left-handed fermions, making the

	fermions			bosons	
families	I	II	III	spin 1	spin 0
quarks	u	c	t	g	H
	d	s	b	γ	
leptons	e	μ	τ	Z	
	ν_e	ν_μ	ν_τ	$W^\pm$	

Table 1.1: Particle content of the SM (in the electroweak broken phase). On the left we have the fermions with spin 1/2, which are grouped into three families. On the right there are the bosons with integer spin, that split up further in vector (spin 1) and scalar (spin 0) particles.

weak interaction intrinsically chiral. The four corresponding gauge fields are three bosons W_μ^a associated with $SU(2)_L$ and one boson B_μ associated with $U(1)_Y$.

While at high energies, the electroweak symmetry is intact, it becomes spontaneously broken at low energies to the electromagnetic subgroup $U(1)_{em}$ via the Higgs mechanism [46, 47]. The scalar Higgs doublet acquires a non-vanishing vacuum expectation value (vev) which generates masses for the weak gauge bosons. In the broken phase, the physical gauge bosons are the massive charged bosons $W^\pm$ and the massive neutral boson Z for the weak force; the electromagnetic interaction is mediated by the massless photon γ.

1.1.1 Particle Content

The particle content of the SM, shown in Table 1.1 in the electroweak broken phase, consist of fermions with spin 1/2 and bosons with integer spin. The gauge bosons mediating the forces (g, $W^\pm$, Z, γ) are spin-1 particles. In addition, the Higgs mechanism contributes a physical scalar, the Higgs boson H, with spin 0.

The matter sector contains twelve fermionic fields (and their corresponding antiparticles), arranged into three generations. Each generation contains two quarks and two leptons:

- Quarks: (u, d), (c, s), (t, b),
- Leptons: (e, ν_e), (μ, ν_μ), (τ, ν_τ).

Quarks transform in the fundamental representation of $SU(3)_c$ and therefore carry colour charge, while leptons are colour singlets. The three generations share identical gauge quantum numbers but differ in their masses, which increase from the first to the third generation. The replication of families is an experimental fact not explained within the SM itself.

Because heavier fermions can decay into lighter ones through weak interactions, only the first generation fermions are stable. Ordinary matter is therefore mostly composed of up and down quarks, forming protons and neutrons, and electrons that are bound to the nuclei via electromagnetic interactions.

1.1.2 Chirality and Mass Generation

A central structural feature of the SM is that the weak interaction couples only to left-handed fermions and right-handed antifermions. Right-handed fermions are singlets under $SU(2)_L$. Consequently, the electroweak theory is chiral and maximally violates parity.

This chiral structure has important consequences for fermion mass terms. A Dirac mass term couples left- and right-handed components,

$$m_f \bar{f}_L f_R + \text{h.c.}\,,$$

where the fermion f acquires a mass m_f. However, such a term is not gauge invariant under $SU(2)_L \times U(1)_Y$ for the SM fermion gauge assignments, and explicit mass terms are therefore forbidden.

Instead, fermion masses arise through Yukawa interactions with the Higgs doublet Φ. The Yukawa Lagrangian for quarks and charged leptons is

$$\mathcal{L}_Y = -y_d \bar{Q}_L \Phi d_R - y_u \bar{Q}_L \tilde{\Phi} u_R - y_\ell \bar{L}_L \Phi \ell_R + \text{h.c.}\,,$$

where $Q_L = (u_L, d_L)^T$ and $L_L = (e_L, \nu_L)^T$ denote the left-handed quark and lepton doublets, while u_R, d_R, and ℓ_R the corresponding right-handed singlets. The field $\tilde{\Phi} = i\sigma_2 \Phi^*$ is the conjugate Higgs doublet. Since the SM contains three generations of quarks and leptons, the Yukawa couplings y_f are 3×3 matrices. Note that in the lepton sector, there is only one such term, since the minimal SM does not include right-handed neutrinos. After electroweak symmetry breaking, the Higgs field acquires a vev v, generating fermion masses matrices

$$m_f = \frac{y_f v}{\sqrt{2}}\,.$$

Diagonalising these matrices defines the fermion mass eigenstates. The observed hierarchy of fermion masses is therefore directly determined by the Yukawa couplings y_f, which remain free parameters of the theory.

1.1.3 Flavour Mixing and CP Violation

Because the Yukawa matrices for up- and down-type quarks cannot generally be diagonalised simultaneously, the weak interaction eigenstates differ from the mass eigenstates. Their mismatch is encoded in the Cabibbo–Kobayashi–Maskawa (CKM) matrix in the quark sector [11, 48, 49]. Within the three generations, the CKM matrix contains one irreducible complex phase, which gives rise to CP violation in weak interactions.

In the lepton sector, neutrino oscillation experiments demonstrated that neutrinos are massive and mix [9–11], as mentioned above. This mixing is described by the Pontecorvo–Maki–Nakagawa–Sakata (PMNS) matrix [12, 13]. However, in the SM neutrinos are assumed to be massless. Generating neutrino masses therefore requires an extension, for example by introducing right-handed neutrinos with Dirac masses, or through Majorana mass terms such as in seesaw mechanisms [50–52]. Since neither the absolute neutrino masses nor their underlying generation mechanism have yet been experimentally determined, neutrino masses are not included in the minimal formulation of the SM.

1.1.4 Structure of the Lagrangian and Free Parameters

The dynamics of the SM are completely specified by the most general renormalisable Lagrangian consistent with the gauge symmetries and the given particle content. The gauge principle fixes the representation structure of matter fields and the gauge interactions with possible self-interactions for non-Abelian symmetries. The fermion content of any gauge theory is strongly constrained by anomaly cancellation. Gauge anomalies would render the theory inconsistent at the quantum level; remarkably, the SM fermion content cancels all gauge anomalies and those mixed with gravity generation by generation. While additional complete generations could in principle be added without spoiling anomaly cancellation, incomplete multiplets (*e.g.* a single additional quark) would generally violate these consistency conditions.

In Chapter 2, we study an extension of the SM in which the gauge symmetry is enlarged by an additional $U(1)$ factor. This extension introduces a new gauge interaction mediated by a gauge boson Z'. A central aspect of our discussion is anomaly cancellation and we therefore introduce and explain gauge anomalies in detail in Section 2.2. The $U(1)$ symmetries we consider assign charges to subsets of the SM fermions and may require the introduction of additional fermions to ensure that all anomalies cancel. Importantly, the new fermion content must not only cancel anomalies involving the new $U(1)$, but must also preserve the cancellation of all anomalies already present in the SM.

After fixing the gauge group and particle content (*i.e.* which fields exist and in which representation they transform), the remaining freedom lies in the numerical values of the parameters. In the minimal SM with massless neutrinos, there are 19 independent parameters:

- three gauge couplings,
- two parameters defining the Higgs potential,
- six quark masses,

- three charged lepton masses,
- three CKM mixing angles,
- one CKM CP-violating phase.

These parameters are not predicted by the theory, but must be determined experimentally. One can interchange some of these variables by others, since for example fermion masses, Yukawa couplings and the Higgs vev are connected to each other, but there will always be 19 parameters that have to be fixed by experiment.

1.2 Dark Matter

The nature of dark matter (DM) remains one of the most compelling open questions in modern particle physics. Its existence is inferred from a wide range of astrophysical and cosmological observations; however, to date the evidence has been observed only through its gravitational effects. One of the earliest indications dates back to the 1930s, when Fritz Zwicky analysed the velocity dispersion of galaxies in the Coma Cluster and concluded that the visible mass was insufficient to account for the cluster's gravitational binding [53]. A major step toward establishing the existence of DM came from the work of Vera Rubin and Kent Ford in the 1970s [54, 55]. Using optical spectroscopy, they measured the rotation curves of stars and gas in spiral galaxies, extending observations far beyond the luminous disk. Their results confirmed and complemented earlier 21 cm hydrogen-line measurements by Morton Roberts [56], showing that rotation velocities remain approximately constant at large radii, rather than declining as expected from the distribution of visible matter. This flattening of the rotation curves suggests that galaxies are embedded in extended halos of non-luminous matter whose mass substantially exceeds that of the luminous components, with mass-to-light ratios reaching values of order 20 [57]. These observations provided some of the most compelling early evidence for the existence of DM and laid the foundation for subsequent studies of its distribution in galaxies.

The possibility that DM consists of non-baryonic particles emerged from studies of the role of neutrinos in cosmology. Earlier explanations for the missing mass in galaxies and clusters assumed that it consisted of faints stars, gas, or other forms of ordinary baryonic matter. Compact objects in galactic halos – such as faint stars, brown dwarfs, or stellar remnants – were later collectively referred to as MACHOs (massive astrophysical compact halo objects). Observations, in particular microlensing searches, have, however, since shown that MACHOs cannot constitute a dominant component of DM. Massive neutrinos were among the first particle candidates for DM. They stand out from other SM particles because they are stable on cosmological timescales and interact neither electromagnetically nor via the strong interaction. Historically, neutrinos were widely assumed to have non-zero masses, and comparatively large values were not yet excluded, making them attractive DM candidates. We now know that neutrinos are indeed massive, but their masses are far too small for them to account for the observed DM abundance. Constraints on neutrino masses arise, for example, from measurements of nuclear β-decay and from cosmological observations. Following the discovery of the cosmic microwave background (CMB) [58], it became possible to place limits on neutrino masses through their impact on the expansion history of the Universe [59]. Subsequent numerical simulations further showed that SM neutrinos cannot constitute the dominant component of DM. Because very light particles remain relativistic during the epoch of structure formation, they suppress the growth of small-scale structures, leading to predictions that are inconsistent with observations from galaxy surveys. While neutrinos necessarily contribute a small fraction of the DM abundance as hot DM, the dominant component must be sufficiently non-relativistic during structure formation to reproduce the observed distribution of cosmic structures. Although neutrinos cannot account for a significant fraction of the DM abundance, the cosmological constraints that exclude them – especially those related to structure formation – apply more generally to any DM candidate with similar properties.

With the exclusion of neutrinos as a viable DM candidate, the idea that the missing mass in the Universe is composed of a new, weakly interacting particle species became widely accepted. The search for such a candidate, as well as for evidence of its non-gravitational interactions, remains an active area of research. We will return to the search for DM candidates in Section 1.2.1. For a detailed historical overview of DM, see Ref. [57].

Since these early observations and considerations, several independent lines of evidence have confirmed the existence of DM. Gravitational lensing, for example, reveals that the total mass in certain galaxy clusters must be far greater than what can be accounted for by visible matter alone. It also provides direct evidence for extended DM halos surrounding individual galaxies. Weak gravitational lensing further allows the study of large-scale structures, and, when combined with redshift measurements, can probe the evolution of cosmic structures over time. Gravitational lensing has also been used to investigate colliding galaxy clusters, most famously the Bullet Cluster, where X-ray observations show a separation between the distribution of baryonic matter and the gravitational potential traced by lensing [60, 61].

Another important line of evidence for DM comes from baryon acoustic oscillations (BAO), which originate from sound waves propagating in the hot plasma of electrons, photons, and baryons prior to recombination. At recombination, electrons and protons combined to from neutral hydrogen, allowing photons to stream freely; today these photons are observed as the CMB. At this point the acoustic oscillations froze in, leaving an imprint characterised by a preferred scale known as the sound horizon. This scale can be observed both in the acoustic peaks of the CMB power spectrum and in the distribution of large-scale structures [62, 63]. The properties of these oscillations depend sensitively on the matter content of the Universe. In the absence of a non-relativistic matter component that does not interact electromagnetically, photon pressure would dominate the dynamics of the plasma, resulting in significantly different oscillation amplitudes. The observed positions, heights, and ratios of the acoustic peaks in the CMB power spectrum therefore provide strong evidence for a dominant matter component that interacts only weakly with photons, consistent with DM.

The first measurement of anisotropies in the CMB was provided by the COBE experiment [64], revealing the primordial fluctuations that later seeded the formation of cosmic structures. Subsequent observations by the WMAP satellite established precise cosmological parameters and provided strong support for the ΛCDM model[2] with a baryon density of $\Omega_b h^2 = 0.0224 \pm 0.0009$ and a total matter density of $\Omega_m h^2 = 0.135^{+0.008}_{-0.009}$ [69]. These measurements demonstrated, independently of other observations but consistent with them, that the total matter density exceeds the baryonic component by roughly a factor of five. The Planck satellite later confirmed these results with unprecedented precision [70].

Another independent cross-check is provided by Big Bang Nucleosynthesis (BBN), which describes the formation of light elements such as deuterium (D), ^{4}He, ^{3}He, and ^{7}Li in the early Universe [71]. BBN is sensitive to the baryon-to-photon ratio and yields a baryon density of $\Omega_b h^2 = 0.022 \pm 0.002$. When combined with gravitational measurements of the total matter density, this implies that the majority of matter in the Universe must be non-baryonic.

Taken together, these experimental observations provide compelling evidence for the existence of DM, pointing toward a weakly interacting, non-baryonic particle that is non-relativistic at the time of structure formation and stable on cosmological timescales. While these requirements strongly constrain its properties, they still allow for a wide range of possible particle candidates. Some of the most prominent scenarios are briefly reviewed in the following Section.

1.2.1 The WIMP Paradigm and Beyond

One of the most thoroughly studied DM candidates is the Weakly Interacting Massive Particle (WIMP), which interacts with SM particles via the weak interaction. The WIMP hypothesis is particularly appealing because it naturally explains the observed relic abundance of DM. In the early Universe, WIMPs would have been in thermal equilibrium with the SM plasma. As the Universe expanded and cooled, their interaction rate eventually dropped below the Hubble expansion rate, leading to freeze-out and a thermal relic abundance. Remarkably, a particle with weak-scale mass (~ 10 GeV $- 1$ TeV) and

[2]The ΛCDM model evolved from Einstein's theory of general relativity [65], Hubble's measurement of an expanding Universe [66], and the discovery of the accelerated expansion of the Universe [67, 68]. Its main ingredients are the cosmological constant Λ, representing dark energy, and cold DM (CDM), which dominates over ordinary baryonic matter. It is commonly referred to as the standard model of cosmology.

weak-scale cross section ($\sim 10^{-26}$ cm^3/s) naturally reproduces the observed DM density – a coincidence often referred to as the *WIMP miracle*.

WIMPs arise naturally in several extensions of the SM. In supersymmetry (SUSY), the lightest supersymmetric particle (LSP), often the neutralino, can be stable and serve as a DM candidate [72]. Models with universal extra dimensions predict stable Kaluza-Klein states due to a conserved parity [73, 74], while Little Higgs models with T-parity simultaneously address the hierarchy problem and provide a stable DM candidate [75,76]. The mechanism of WIMP DM is often generalised to so called WIMP-like particles, where DM interacts with the SM through a new mediator, such as a scalar or vector boson, but still achieves the correct abundance via freeze-out. Simplified models are often used in these studies, retaining only the DM particle and the mediator, allowing systematic phenomenological investigations without requiring a full UV (ultraviolet) complete theory.

While the WIMP paradigm is theoretically appealing and well motivated within many extensions of the SM, experimental searches have now excluded large portions of the canonical WIMP parameter space, covering wide ranges of masses and interaction strengths. This has motivated a broadening of the search for viable DM candidates beyond the traditional WIMP framework. Proposed alternatives cover an enormous range of masses and particle types, extending from ultralight fields to composite states and even primordial black holes. In the following, we highlight a few representative examples and refer the reader to the literature for more comprehensive reviews, *e.g.* Refs. [77, 78].

One prominent class of candidates arises from attempts to solve the strong CP problem in quantum chromodynamics (QCD). Introducing a new global $U(1)$ symmetry, which is spontaneously broken, gives rise to a light pseudo-Nambu-Goldstone boson: the axion [79–82]. The QCD axion has in turn inspired extensive studies of axion-like particles (ALPs), a broader class of pseudoscalar bosons, many of which can serve as viable DM candidates [83, 84]. Another possibility involves vector bosons associated with new $U(1)$ gauge symmetries. Depending on their mass, these particles are commonly referred to as dark photons or Z' bosons. Such vectors can themselves account for DM at very small masses [85, 86], although they are more often studied as mediators or portals to a richer dark sector – we will come back to the phenomenology of Z' bosons in Chapter 2.

Motivated by the existence of SM neutrino masses, new SM gauge-singlet fermions, known as sterile neutrinos, can also be DM candidates. These states mix with the active (SM) neutrinos, and their relic abundance can be generated via a freeze-in mechanism: for small mixing angles, sterile neutrinos are slowly produced through oscillations with active neutrinos, but never reach equilibrium. Unlike SM neutrinos, their masses can be in the correct range to account for DM, while remaining consistent with cosmological constraints.

Primordial black holes are a candidate for DM, where no new particle content beyond the SM is required. They are formed from large matter overdensities in the early Universe [87, 88]. Despite originating from SM matter, they do not count as baryonic matter because, once formed, they no longer participate in nuclear or electromagnetic processes relevant for, *e.g.*, Big Bang nucleosynthesis. To produce the necessary density fluctuations, however, some physics beyond the SM is required: they could form at different times through different mechanisms during inflation [89–91] or later from first-order phase transitions [92, 93]. Observations constrain their allowed mass range, but in some windows primordial black holes could constitute all or part of the DM abundance [94,95].

A multitude of other DM models exists, including asymmetric DM (mirroring the baryon asymmetry), atomic DM, millicharged particles, and decaying DM. To master the multitude of possibilities, effective field theories are often employed. If the particles associated with new physics are heavy, their imprints on experiments can be described using effective operators. These operators provide a model-independent and systematic framework that allows results from different experiments to be compared in a straightforward way. The choice of possible operators is largely guided by symmetry considerations. However, effective field theory calculations neglect the effects of lighter degrees of freedom. For this reason, simplified models have increasingly been used. These models include only a small number of new particles, such as a mediator between the dark sector and the SM and a DM candidate. Although simplified models are not UV complete and ultimately need to be embedded into a consistent underlying theory, they aim to capture the essential phenomenological features while remaining as general as possible. This is the approach that will be used for the DM models considered here.

The two scenarios we will focus on in this thesis are inelastic DM and leptophilic DM. Inelastic DM assumes the dark sector to consist of two particles: a DM particle χ and a slightly heavier partner χ^*. These particles interact with SM particles through a mediator, which we denote by ξ. By suppressing the diagonal couplings $\chi - \chi - \xi$ and $\chi^* - \chi^* - \xi$ (*e.g.* via a symmetry), signals in direct detection experiments become dependent on the mass difference of χ and χ^* and their kinetic energy [96]. Chapter 3 provides a more detailed introduction to inelastic DM and explores the collider signals it can produce. The parameter space of this model can be probed through monojet searches and displaced signatures.

Leptophilic models are characterised by mediators that couple the dark sector to the SM exclusively through leptons. One example is gauged $L_\mu - L_\tau$ symmetry, which belongs to the class of $U(1)$ extensions studied in Chapter 2. It couples to the SM muon, tau and the corresponding neutrinos and can potentially connect a dark sector to the leptonic sector of the SM [97–99]. In our analysis, however, we consider a scenario, where the dark and SM sectors are connected by a charged mediator. This mediator couples to the charged leptons of the SM: the electron, muon and tau. Such models exhibit an interesting feature: when DM annihilates via a charged t-channel mediator, a photon can be emitted from the mediator. If the mediator and the DM particle are close in mass and the DM particle is a Majorana fermion, the resulting photon spectrum can become strongly peaked and resemble a line-like gamma-ray signal [100, 101]. We study loop effects that generate effective couplings of DM to photons – namely anapole and

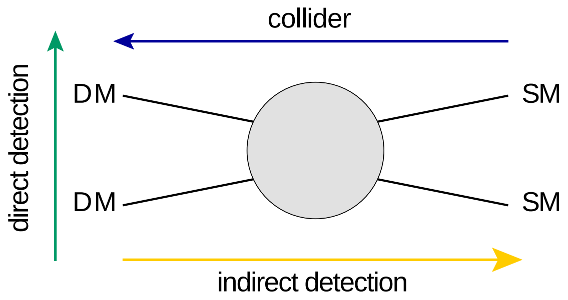

Figure 1.1: Different perspectives on DM detection: collider experiment produce DM from SM particles, direct detection observes DM scattering on SM particles, and indirect searches aim to detect annihilation or the decay of DM to SM particles.

dipole moments – which can lead to observable signals in direct detection experiments (see Chapter 4).

To study the phenomenology of DM theories, *i.e.* the experimental signatures they may produce, we now introduce the different types of experiments that search for DM.

1.2.2 Experimental Searches and Complementarity

To investigate the particle nature of DM, several complementary experimental strategies have been developed:

- **Direct detection** experiments search for nuclear recoils induced by the scattering of DM particles in ultra-low-background underground detectors. Leading experiments include XENONnT [102–104], LUX-ZEPLIN (LZ) [105, 106], and PandaX [107, 108].

- **Indirect detection** aims to detect SM particles produced in DM annihilation or decay, such as gamma rays, positrons, antiprotons, and neutrinos. Important observatories include Fermi-LAT [109, 110], HESS [111], AMS [112], and IceCube [113–115].

- **Collider searches**, for example ATLAS [116,117] and CMS [118,119] at the Large Hadron Collider (LHC), probe the production of DM particles in high-energy collisions. These searches are sensitive to DM candidates with feeble but nonzero non-gravitational interactions with SM particles. The produced DM particles escape detection, and their presence is inferred from an imbalance in transverse momentum or energy ($E_{\mathrm{T}}^{\mathrm{miss}}$), which is typically studied in monojet searches. Depending on the underlying model, additional non-standard signatures may arise, including displaced vertices or emerging jets.

As illustrated in Figure 1.1, DM production at colliders, DM scattering in direct detection experiments, and DM annihilation or decay in indirect searches are all governed by the same underlying particle physics framework. Consequently, constraints from these different probes are intrinsically connected, although their relative sensitivity depends on the structure of the theory.

In certain scenarios, DM can evade direct detection while still being probed at colliders. Inelastic DM provides a representative example, which we investigate in Chapter 3. In this case, the direct detection signal depends sensitively on the mass splitting between the two dark states: over most of the parameter space, scattering is kinematically suppressed, making direct searches ineffective, while only finely tuned regions remain accessible to some experiments. At colliders, the sensitivity depends on the search strategy. Conventional monojet searches, which rely on missing transverse momentum signatures, are largely insensitive to the size of this splitting and therefore probe complementary regions of parameter space. In contrast, dedicated searches for displaced decays are highly sensitive to it, since for larger splittings the displacement becomes too small to be resolved.

In other models, all three experimental approaches can impose relevant and overlapping constraints. The leptophilic model studied in Chapter 4, for instance, is subject to bounds from direct, indirect, and collider searches simultaneously. This framework provides a particularly clear illustration of the connection between the underlying processes: in the case of virtual internal bremsstrahlung, the region of parameter space that gives rise to a pronounced spectral feature in DM annihilation coincides with the region in which DM scattering is most efficient. This correspondence highlights the complementarity and interplay of the different search strategies.

More generally, specific model features can lead to distinctive observable signatures. In the leptophilic scenario, virtual internal bremsstrahlung produces a sharp feature in the gamma-ray spectrum relevant for indirect detection. Another example arises in inelastic DM, where the small mass splitting can lead to displaced decays at colliders. Such signatures provide powerful and complementary avenues to probe the underlying theory.

1.3 Thesis Overview

In this thesis, we begin by investigating fundamental aspects of gauge symmetries in **Chapter 2**, focusing on constraints imposed on particle physics models by consistency conditions of the underlying theory. The seminal work of Adler, Bell, and Jackiw [120, 121] demonstrated that quantum loop effects can break symmetries that are preserved at the classical level. In particular, they showed that the axial current in quantum electrodynamics is violated by the triangle diagram involving two vector currents and one axial current. This result established that symmetries of the classical Lagrangian need not survive quantisation, even in renormalisable theories. A prominent example is the decay $\pi \to \gamma\gamma$, which arises from the breaking of a global symmetry by quantum corrections.

For gauge symmetries, however, such violations would render the theory inconsistent, necessitating a careful analysis when extending the SM by additional symmetries and fermionic degrees of freedom. We consider in Chapter 2 an extension of the SM by an additional $U(1)$ factor. If fermions are charged under both the SM electroweak group and the new $U(1)$ symmetry, an effective coupling between the new gauge boson Z', the SM Z, and the photon γ is induced via the axial–axial–vector triangle diagram. Our goal is to compute and analyse the corresponding vertex function.

To this end, we evaluate the triangle diagram using the form factor decomposition introduced by Rosenberg [122], which allows for a complete determination of the vertex function. In contrast to standard textbook treatments that focus only on the divergence of the currents, this approach provides a complete description of the amplitude. We show that the general expression for the vertex function is ambiguous due to the shift symmetry of linearly divergent integrals, and must therefore be fixed by external conditions, such as the conservation of vector currents. This ambiguity arises only within effective field theory; in a UV complete theory, unphysical dependencies cancel and the result is uniquely defined.

We then apply these results to the decay $Z \to Z'\gamma$ in models with Z' associated to a new $U(1)$ gauge symmetries. Anomaly cancellation may require the introduction of additional fermions, known as anomalons. We consider two representative cases: gauged baryon minus lepton number, $U(1)_{B-L}$, where the SM fermion content extended with right-handed neutrinos is sufficient for anomaly cancellation, and gauged baryon number, $U(1)_B$, where additional fermions are required. In the latter case, the full vertex function must include contributions from anomalons. Integrating them out is non-trivial, since their masses are typically generated by the same scalar field responsible for the Z' mass. This introduces correlations between the Z' mass $m_{Z'}$, the gauge coupling g_X, and the anomalon masses, which are constrained by their maximal allowed Yukawa couplings. Moreover, their chiral structure – distinct from that of the SM fermions – can lead to the phenomenon of non-decoupling anomaly-free fermion sets.

We compute the decay width for $Z \to Z'\gamma$ in both scenarios, $U(1)_{B-L}$ and $U(1)_B$. For the case of gauged baryon number, we derive constraints on the parameter space from the decay $Z \to Z'\gamma$, followed by $Z' \to jj$. We further compare the full calculation to effective field theory approximations based on Wess-Zumino terms and quantify the impact of common simplifications on the predicted branching ratio and the resulting limits.

Then we will move on to more applied, phenomenological research on two specific simplified DM models: **Chapter 3** explores an inelastic DM model, in which the DM particle scatters into an excited state with a small mass splitting. The resulting kinematic suppression can weaken constraints from conventional direct detection experiments, while still allowing for distinctive signatures at colliders. Despite its rich phenomenology, inelastic DM has received relatively little attention in LHC searches, a gap that our work aims to address through a comprehensive study of collider signatures originating from an inelastic dark sector.

Originally, inelastic DM was proposed to reconcile the signal observed by DAMA/LIBRA [123] with the null results from CDMS [124]. The model introduces two dark sector states separated by a small mass splitting and suppresses diagonal interactions [96]. By adjusting the mass difference, signals can appear in some detector materials while remaining absent in others. Although the DAMA/LIBRA anomaly is now widely considered to be incompatible with other experimental results [125, 126], inelastic DM remains a well-motivated and widely studied alternative to standard WIMP scenarios.

We focus on collider probes of inelastic DM, going beyond previous studies that relied on effective field theory descriptions [127] by considering simplified models with explicit mediators, including vector, axial vector, scalar, and pseudoscalar interactions. For mediator masses relevant to collider searches, the effective field theory approach fails to capture the full dynamics, motivating this more complete framework. We compare the key characteristics of the simplified models, including the production cross sections, decay widths of the excited state, and kinematic observables such as missing transverse energy, jet multiplicity, and leading jet transverse momentum. Using these ingredients, we recast the ATLAS monojet analysis [128], implement the relevant selection cuts, and validate our setup with simulated background samples. We derive 95% confidence level exclusion limits for each mediator type, including regions consistent with the observed DM relic density. The limits are primarily driven by the production cross section and are strongest for the vector mediator, followed by the axial vector interactions, while scalar and pseudoscalar cases are significantly less constrained. The analysis defines multiple signal regions based on missing transverse energy thresholds; for each parameter point, we identify the region providing the strongest constraint.

Since inelastic DM features an excited state that can decay into a DM particle and visible SM states, parts of the parameter space give rise to displaced vertices at colliders. We therefore recast a dedicated ATLAS search for displaced decays [129]. The sensitivity of this analysis depends on the interplay between the mass splitting and the decay kinematics: sufficiently large splittings are required to produce visible decay products, but they also lead to shorter lifetimes and hence smaller displacements. Among the models considered, only the pseudoscalar mediator allows for a viable balance, resulting in a limited region of sensitivity in the parameter space. By relaxing some of the analysis cuts (*i.e.* selection criteria), we demonstrate that the reach can be significantly improved. We conclude by discussing additional searches that could be adapted to probe inelastic DM and the model characteristics that are relevant to these analyses.

Finally, in **Chapter 4**, we study a leptophilic DM model in which the dark sector interacts with the SM via a charged t-channel mediator. This setup gives rise to virtual internal bremsstrahlung, where DM annihilation is accompanied by photon emission from the mediator. When the mediator and DM masses are nearly degenerate, this process produces a pronounced spectral feature in the gamma-ray spectrum for the case of Majorana DM that can resemble a line-like signal. This scenario was originally motivated by tentative hints of such a feature in the Fermi-LAT data [101]. The same interaction responsible for this annihilation process also induces electromagnetic form factors at loop level: closing the external fermion lines in the annihilation diagram generates effective couplings of DM to photons. These loop-induced interactions can lead to potentially observable signals in direct detection experiments. Importantly, the corresponding constraints are strongest in the same region of parameter space that enhances the gamma-ray feature, thereby strongly limiting this interpretation. Although the original Fermi-LAT signal was later identified as a statistical fluctuation [130], the underlying connection between annihilation signatures and loop-induced interactions remains a key result of our work.

We analyse a simplified model with a fermionic DM candidate and a charged mediator coupling to the SM leptons. Even though DM is electrically neutral at tree level, loop effects induce effective electromagnetic interactions. For Majorana DM, symmetry arguments forbid electric and magnetic dipole moments, leaving the anapole moment as the leading contribution. We derive analytic expressions in the relevant kinematic regimes, depending on the relative size of the momentum transfer and the lepton mass in the loop. For Dirac DM, both anapole and magnetic dipole moments arise, with the latter typically dominating scattering processes.

These interactions induce DM–nucleus scattering and are constrained by direct detection experiments. Using data from LUX [131], we derive bounds on the annihilation cross section, including virtual internal bremsstrahlung in the Majorana case. We consider both flavour-universal and flavour-specific couplings to SM leptons. Additional constraints from collider experiments, anomalous magnetic moments, and other precision observables are generally subdominant. Overall, our results exclude significant regions of parameter space – including parts compatible with a thermal relic abundance – and demonstrate the strong complementarity between direct and indirect detection probes.

We now turn to the first part of this thesis, beginning with the study of gauge anomalies in models with $U(1)$ extensions in Chapter 2.

Chapter 2

Triple Gauge Boson Vertices with New U(1) Gauge Symmetries

2.1 Introduction

This chapter is based on Ref. [132], with calculations carried out independently by the author and the collaborator.

In this chapter, we want to look at an interesting extension to the SM, namely a new $U(1)$ gauge symmetry that is added to the SM. New $U(1)$ gauge symmetries are a common feature of beyond the SM physics, since they arise in many models, such as grand unified theories, and they can serve as portals to a dark sector. Grand unified theories aim to unite the forces of the SM into one symmetry group that subsequently breaks down to the symmetry groups of the SM and potentially additional symmetries; exemplary new $U(1)$ symmetries are gauged SM baryon minus lepton number [133, 134] or gauged baryon number and lepton number separately [135–139]. The gauge boson connected to the new $U(1)$ gauge symmetry, called Z', can connect the SM particles to a new "dark" sector including a DM candidate. It can therefore serve as a portal to DM physics. Examples can be found in Refs. [140–149].

Adding a new gauge symmetry to the SM brings along new constraints on the particle content in the form of anomaly cancellation conditions. Anomaly cancellation is an important concept in gauge theories. While an anomaly – the breakdown of a classical symmetry on quantum level – of a global symmetry can explain interesting physical phenomena (as an example one can study the pion decay $\pi^0 \to \gamma\gamma$ to two photons, see chapter 19.3 in [35]), anomalies in gauge symmetries lead to an inconsistency of the theory. This is because the gauge symmetry must be preserved as it removes non-physical degrees of freedom – the redundancies introduced by the gauge symmetry are necessary to render the theory mathematically viable. A consistent theory therefore requires that all gauge anomalies vanish [150].

The cancellation of an anomaly in a gauge symmetry can be ensured by having vector like couplings to Dirac fermions, *i.e.* the gauge coupling to left- and right-handed fermions is the same. If the couplings to left- and right-handed fermions are different, the theory is called chiral and anomaly cancellation is not obeyed automatically, but instead imposes conditions on the quantum numbers of the fermions in the theory. Note that in chiral gauge theories, bare mass terms for the fermions are also forbidden, since the mass term couples left- and right-handed Weyl fermions and it can only be gauge invariant if the fermions transform equivalently under the gauge group. The chirality of the SM electroweak gauge symmetry thus led to the introduction of the Higgs boson, which allows for the formulation of a mass term for the elementary quarks and leptons via spontaneous breaking of the electroweak symmetry.

In general, a $U(1)$ extension to the SM can involve SM fermions or it can be a symmetry in a completely secluded sector of beyond SM physics. We will focus on the first scenario, as it suggests a richer accessible phenomenology. When *e.g.* the quarks or the leptons are charged under the new symmetry, the new gauge boson Z' can generate dijet or dilepton resonances at colliders [133, 135, 139]. In most cases the introduction of new fermions is required by the conditions imposed on the charges of the fermions, an exception is given by gauging baryon minus lepton number $B - L$, which is a global symmetry of the SM, where the fermion content of the SM is already anomaly free.[1] These new fermions, often called anomalons, can also be detected at colliders, particularly the Large Electron-Positron collider (LEP) provides strong limits [151, 152].

Anomaly cancellation conditions can be analysed systematically to obtain solutions of anomaly free sets of fermions for a given $U(1)$ symmetry. For examples on possible $U(1)$ extensions to the SM and corresponding anomaly free sets of fermions, see Refs. [135, 153–156].

In our work, *i.e.* the following chapter, we want to focus on new $U(1)$ gauge symmetries that are global symmetries of the SM, in particular on gauged baryon $U(1)_B$ and gauged baryon minus lepton number $U(1)_{B-L}$. While for $U(1)_{B-L}$ the SM fermion content is anomaly free (see above), gauging baryon number requires the introduction of new fermions, since the anomaly coefficients $SU(2)_L^2 \times U(1)_B$ and $U(1)_Y^2 \times U(1)_B$ are nonzero for the SM fermion content. These new fermions that we call anomalons, give us the opportunity to compare two different cases in this model, namely the cancellation of an anomaly by fermions that are chiral under the same or two different symmetries (resulting in axial couplings to the SM Z or the new Z'_B). These two scenarios show very interesting non-decoupling behaviour; particularly, when an anomaly free set contains fermions that are chiral under different symmetries, the set does not decouple even when we take the masses to be degenerate (see Section 2.4.3).

We study primarily the vertex function $Z - Z' - \gamma$ that is reminiscent of the standard Adler-Bell-Jackiw anomaly [120, 121] (outlined in Section 2.2), but to calculate the decay width we require the full vertex structure, whereas the anomaly calculation focuses on

[1] It only requires the introduction of right-handed neutrinos.

the divergence of the current. We concretely calculate the decay $Z \to Z'\gamma$ for $U(1)_{B-L}$ and $U(1)_B$ and therefore consider the case where the Z' boson is lighter than the SM Z. We supplement this calculation with potential signatures of the anomalons in colliders and show an overview of the current constraints of the considered model parameters. We also compare the full calculation to an effective ansatz.

The chapter is constructed as follows. We first give a brief general introduction into the broad field of anomalies in gauge symmetries in Section 2.2, where we derive the famous Adler-Bell-Jackiw anomaly and explain the importance of anomaly cancellation in gauge symmetries.

In Section 2.3 we introduce the models that we will consider, namely gauged baryon minus lepton number $B-L$ and gauged baryon number B with its fermion content and Lagrangians. For the case of gauged baryon number we show the anomalon content we use and explain the two mass generation options connected to the chiral couplings to the Z or Z'_B boson respectively. We demonstrate the anomaly cancellation in detail for the two models.

Then we move on to the triple gauge boson vertex in Section 2.4, where we first calculate the general case of a vertex with two massive and one massless external gauge bosons. We explain, that the difficulty in calculating the vertex function arises from the ambiguity in the cancellation of the divergences of the two contributing triangle diagrams and show how to fix this ambiguity by applying external conditions, namely the Ward identities. Since we consider the interaction of three neutral current vector bosons at one-loop level, the fermions in the loop have a non-decoupling limit and contribute to effective Wess-Zumino terms [157]. We connect our full result to the effective ansatz with Wess-Zumino terms via the Ward identities.
Subsequently we derive the decay width of $Z \to Z'_{BL}\gamma$ and $Z \to Z'_B\gamma$ in gauged $B-L$ and B and show the branching fraction versus $m_{Z'}$ for gauge couplings between 0.1 and 1. For gauged baryon number we give both results for axial couplings of the anomalons to the SM Z and to the Z'_B and show the branching fraction also versus the vacuum expectation value (vev) of the new Higgs v_Φ. We comment on the non-decoupling behaviour of a mass-degenerate set in the case of a mixed chiral structure of an anomaly free set of fermions.

In Section 2.5 we derive the limit set by the Higgs decay to two photons $H \to \gamma\gamma$ for anomalons, whose mass is generated by the SM and the new Higgs.

Section 2.6 gives an overview over the landscape of experiments excluding parameter space for gauged baryon number in the plane g_X versus $m_{Z'_B}$, including a limit set by the L3 experiment using our result for the decay width $Z \to Z'_B\gamma$ and also a projection for a potential TeraZ factory.

We dedicate Section 2.7 to a comparison of our full calculation of the decay width to an effective ansatz using Wess-Zumino terms. In successive steps we show the impact of different approximations on the decay width up to the implementation of the Goldstone boson equivalence theorem and show how the L3 exclusion limit on $Z \to (jj)\gamma$ changes using the EFT versus the full calculation.

We conclude and summarise in Section 2.8.

2.2 Anomalies in Gauge Symmetries

Anomalies are an example of quantum corrections that break classical symmetries. In other words, a symmetry that is conserved in a classical theory can be broken when including quantum corrections. Most impressively this can be seen in theories involving chiral symmetries of massless fermions. For a massless Dirac fermion the axial vector current $j^{\mu 5}$ is conserved at classical level:

$$\partial_\mu j^{\mu 5} = \partial_\mu (\bar{\psi}\gamma^\mu \gamma^5 \psi) = 0\,, \tag{2.1}$$

where the gamma matrices are defined by their anticommutation relations:

$$\{\gamma^\mu, \gamma^\nu\} = 2\,\eta^{\mu\nu}\,\mathbb{1}_4\,, \tag{2.2}$$

$\eta^{\mu\nu}$ being the Minkowski metric and $\mathbb{1}_4$ the four dimensional identity matrix. The fifth gamma matrix is defined to be $\gamma^5 = i\gamma^0\gamma^1\gamma^2\gamma^3$.

This equation of motion, eq. (2.1), is true for a free classical theory as well as for example massless classical QED (quantum electrodynamics) and QCD (quantum chromodynamics). Let us now look at the effects that quantum corrections have on this relation. We will consider the example of massless QED, where the Lagrangian is given by

$$\mathcal{L} = -\frac{1}{4}F_{\mu\nu}F^{\mu\nu} + \bar{\psi} i \not{D} \psi\,, \tag{2.3}$$

where ψ is a massless Dirac fermion and the electromagnetic field tensor is defined as $F_{\mu\nu} = \partial_\mu A_\nu - \partial_\nu A_\mu$ with the photon field A_μ.

To introduce into the upcoming computations in this chapter that will revolve around the calculation of triangle diagrams, we will sketch the quantum effects here through the calculation of the triangle diagrams[2] of the divergence of an axial vector current into two vector currents, *i.e.* two photons in the case of QED, where we follow the notation in chapter 19.2 of [35], illustrated in Figure 2.1. We will see that unlike eq. (2.1) lets us expect, this divergence will not vanish and the axial vector current is no longer conserved.

We have to calculate the divergence of the following matrix element:

$$\int d^4x e^{-iq\cdot x}\langle p,k|j^{\mu 5}(x)|0\rangle = (2\pi)^4\delta^{(4)}(p+k-q)\epsilon^*_\nu(p)\epsilon^*_\lambda(k)\mathcal{M}^{\mu\nu\lambda}(p,k)\,, \tag{2.4}$$

[2] For an operator level or functional integral calculation see *e.g.* chapter 19.2 of [35].

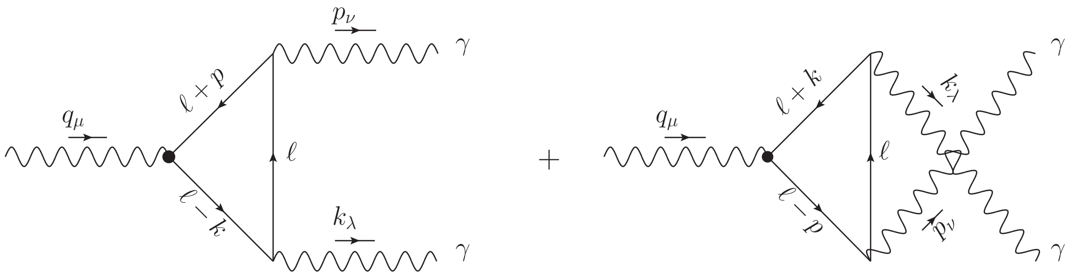

Figure 2.1: The triangle diagrams at one-loop order contributing to the divergence of the axial vector current in the case of QED, *i.e.* into two photons.

where we consider only the leading order diagrams for $\mathcal{M}^{\mu\nu\lambda}$, as depicted in Figure 2.1. We can calculate this to be

$$i\mathcal{M}^{\mu\nu\lambda} = (-1)\int \frac{d^4\ell}{(2\pi)^4}\,\mathrm{Tr}\left[i\gamma^\mu\gamma^5\frac{i(\not{\ell}-\not{k})}{(\ell-k)^2}(-ie\gamma^\lambda)\frac{i\not{\ell}}{\ell^2}(-ie\gamma^\nu)\frac{i(\not{\ell}+\not{p})}{(\ell+p)^2}\right] + [(p,\nu)\leftrightarrow(k,\lambda)]\,, \tag{2.5}$$

where the second diagram is obtained by interchanging the momenta $p \leftrightarrow k$ and the indices $\nu \leftrightarrow \lambda$ in the expression of the first diagram. When now wanting to take the divergence, we note that in momentum space

$$\int d^4x e^{-iq\cdot x}\langle p,k|\partial_\mu j^{\mu 5}(x)|0\rangle = \int d^4x e^{-iq\cdot x}\langle p,k|q_\mu j^{\mu 5}(x)|0\rangle\,, \tag{2.6}$$

meaning we have to dot the matrix element with q_μ. This gives us a $\not{q}$ in eq. (2.5), where before γ^μ appeared. Naïvely, γ^5 anticommutes with the other gamma matrices and we can replace

$$\not{q}\gamma^5 = (\not{\ell}+\not{p}-\not{\ell}+\not{k})\gamma^5 = (\not{\ell}+\not{p})\gamma^5 + \gamma^5(\not{\ell}-\not{k})\,, \tag{2.7}$$

which we can use to separate the first diagram of the matrix element into two contributions:

$$\begin{aligned} iq_\mu\mathcal{M}^{\mu\nu\lambda}_{(\text{1st diag.})} &= e^2\int\frac{d^4\ell}{(2\pi)^4}\,\mathrm{Tr}\left[\frac{-\gamma^5\gamma^\lambda\not{\ell}\gamma^\nu(\not{\ell}+\not{p})}{\ell^2(\ell+p)^2}+\frac{\gamma^5(\not{\ell}-\not{k})\gamma^\lambda\not{\ell}\gamma^\nu}{(\ell-k)^2\ell^2}\right] && (2.8)\\ &= e^2\int\frac{d^4\ell}{(2\pi)^4}\,\mathrm{Tr}\left[\frac{-\gamma^5\gamma^\lambda\not{\ell}\gamma^\nu(\not{\ell}+\not{p})}{\ell^2(\ell+p)^2}+\frac{\gamma^5\not{\ell}\gamma^\lambda(\not{\ell}+\not{k})\gamma^\nu}{(\ell+k)^2\ell^2}\right], && (2.9)\end{aligned}$$

where in the second line we shifted $\ell \to \ell + k$ in the second part of the sum. Now it becomes obvious that when we include the second diagram where $(p,\nu) \leftrightarrow (k,\lambda)$ are interchanged, both sums cancel each other out, and we would confirm the conservation of the axial vector current.

But actually, assuming γ^5 to anticommute with the other gamma matrices γ^μ is only valid in four dimensions, as γ^5 is defined in four dimensions only. To reconcile this issue in dimensional regularisation[3] – which we want to use in this calculation – Ref. [159] proposes to treat γ^5 to anticommute with the gamma matrices γ^μ for $\mu = 0, 1, 2, 3$ but to commute otherwise.

This can be depicted by separating the loop momentum ℓ into its components living in the dimensions $0, 1, 2, 3$, which we call parallel $\ell_{||}$, and into the other (perpendicular) components, represented by $\ell_\perp$. The other momenta are external and therefore always four-dimensional. By replacing $\ell = \ell_{||} + \ell_\perp$ we can rewrite our eq. (2.7) into

$$\not{q}\gamma^5 = (\not{\ell} + \not{p})\gamma^5 + \gamma^5(\not{\ell} - \not{k}) - 2\gamma^5 \not{\ell}_\perp \, , \tag{2.10}$$

where we thereby take into account that the perpendicular part $\ell_\perp$ commutes with the other gamma matrices. The first two contributions cancel, as we deduced above, when we add up both diagrams. The third contribution proportional the perpendicular part of $\ell_\perp$, however, does not cancel. From the first diagram, the remaining contribution reads

$$iq_\mu \mathcal{M}^{\mu\nu\lambda}_{(\text{1st diag.}),\ell_\perp} = e^2 \int \frac{d^4\ell}{(2\pi)^4} \operatorname{Tr}\left[-2\gamma^5 \not{\ell}_\perp \frac{(\not{\ell} - \not{k})}{(\ell - k)^2} \gamma^\lambda \frac{\not{\ell}}{\ell^2} \gamma^\nu \frac{(\not{\ell} + \not{p})}{(\ell + p)^2} \right] . \tag{2.11}$$

Now we need to use the tools of dimensional regularisation to evaluate this expression. By using Feynman parameters, we can combine the denominators, shifting the loop momentum by $\ell \to \ell + xk - yp$. We need four gamma matrices to contract with γ^5 in the trace and an even number of loop momenta to give a nonzero result, leaving us with the factor $\not{\ell}_\perp$ and one $\not{\ell}$, where then also only the perpendicular part contributes. The integral has then the form

$$\int \frac{d^4\ell}{(2\pi)^4} \frac{(\not{\ell}_\perp)^2}{(\ell^2 - \Delta)^3} \, , \tag{2.12}$$

where Δ is defined by the Feynman parameter shift and is a function of the external momenta k and p and the Feynman parameters x and y. The perpendicular part of the loop momentum relates to the full loop momentum by

$$(\not{\ell}_\perp)^2 \to \frac{(d-4)}{d} \ell^2 \tag{2.13}$$

and we are left with an expression that can be evaluated by the usual dimensional regularisation tools (for details see *e.g.* chapter 19.2 of [35]). We get for the first diagram

$$iq_\mu \mathcal{M}^{\mu\nu\lambda}_{(\text{1st diag.}),\ell_\perp} = \frac{-ie^2}{32\pi^2} \operatorname{Tr}\left[2\gamma^5(-\not{k})\gamma^\lambda \not{p}\gamma^\nu\right] = \frac{e^2}{4\pi^2} \varepsilon^{\alpha\lambda\beta\nu} k_\alpha p_\beta \, . \tag{2.14}$$

[3]In dimensional regularisation, the number of spacetime dimensions is taken to be a non-integer value $d = 4 - \varepsilon$ to calculate the integrals that diverge for $d = 4$, and finally after regulating the expressions, the limit of $\varepsilon \to 0$ reveals the finite contributions [158, 159].

Since this is symmetric under the exchange of $(p, \nu) \leftrightarrow (k, \lambda)$ the second diagram gives the same result and we get a total contribution of

$$\langle p, k|\partial_\mu j^{\mu 5}(x)|0\rangle = \frac{e^2}{2\pi^2} \langle p, k| \varepsilon^{\alpha\lambda\beta\nu} k_\alpha p_\beta |0\rangle \epsilon^*_\nu(p)\epsilon^*_\lambda(k) . \tag{2.15}$$

Using the QED Feynman rules we can rewrite this expression and get

$$\langle p, k|\partial_\mu j^{\mu 5}(x)|0\rangle = -\frac{e^2}{16\pi^2} \langle p, k|\varepsilon^{\alpha\lambda\beta\nu} F_{\alpha\lambda}F_{\beta\nu}(0)|0\rangle , \tag{2.16}$$

whereby we reproduced the well known Adler-Bell-Jackiw anomaly [120,121], that demonstrated the non-conservation of the axial vector current and which has been proven by Ref. [160] to be true to all orders in perturbation theory. For a calculation on the operator level resulting in

$$\partial_\mu j^{\mu 5} = -\frac{e^2}{16\pi^2}\varepsilon^{\alpha\beta\mu\nu}F_{\alpha\beta}F_{\mu\nu} \tag{2.17}$$

we have to use the path integral formulation [161] (see Ref. [33] section 30.3 or Ref. [35] section 19.2 for a detailed calculation).

One could expect this non-vanishing of the axial vector current to be due to the use of dimensional regularisation, where we have seen that the definition of γ^5 has to be adjusted outside of four-dimensional spacetime. But if the matrix element is obtained by using *e.g.* Pauli-Villars regularisation[4] (a detailed calculation can be found in Ref. [163]), we actually obtain the same result. Generally, a regularisation scheme can break a gauge symmetry and be therefore unsuitable for a certain calculation. But if we cannot find any regularisation scheme conserving all relevant gauge symmetries of the problem, then the diagram is anomalous.

The non-conservation of the axial vector current has important implications if the current is not linked to a global symmetry but instead to a gauge symmetry. We will see this in the following section.

2.2.1 Anomaly Cancellation

After realising that quantum corrections can break symmetries of classical theories we need to look at the emerging implications for different types of symmetries. For a global chiral symmetry we deduce that if the divergence of the axial vector current is no longer vanishing, the axial charge is no longer conserved. This merely implies that the number of right- and/or left-handed fermions is not an observable, which by itself is not a problem.

[4] In Pauli-Villars regularisation, for each fermion in the loop one adds another fermion with opposite statistics and a large mass M. The regulator mass is finally taken to infinity $M \to \infty$. [162]

However, if we look at a theory where a gauge boson couples to an axial vector current, *i.e.* a chiral gauge symmetry like the weak interactions in the SM, the anomalous terms lead to a violation of the Ward identities of the currents.

In a chiral gauge theory left- and right-handed fields belong to a different representation of the gauge group. In the SM weak interactions only the left-handed fields are charged under $SU(2)$, while the right-handed are singlets. The interaction Lagrangian looks like

$$\mathcal{L}_{\text{int}} = \bar{\psi} i \gamma^{\mu} \left(\partial_{\mu} - i g A^{A}_{\mu} t^{A} \left(\frac{1-\gamma^5}{2} \right) \right) \psi \,, \tag{2.18}$$

where the fermion fields are represented by ψ, A^A_μ is the (non-abelian) gauge field, g is the coupling constant and t^A are the basic generators of the symmetry group that are connected by structure constants f^{ABC}

$$[t^A, t^B] = i f^{ABC} t^C \,. \tag{2.19}$$

For more details on non-abelian gauge theories, see for example part III in Ref. [35]. The axial vector anomaly that we calculated above now places tight restrictions on the representation that the fermions are in. If we assume that the external fields in Figure 2.1 are the gauge bosons of the $SU(2)$ gauge symmetry of the SM weak interactions, the current we are determining is

$$j^{\mu A} = \bar{\psi} \gamma^{\mu} \left(\frac{1-\gamma^5}{2} \right) t^A \psi \tag{2.20}$$

that includes the left projection operator $P_L = (1-\gamma^5)/2$ because only the left-handed fields are charged under $SU(2)$. We proceed as in the calculation above and get

$$\langle \, p^B_\nu \, k^C_\lambda \, | \partial_\mu j^{\mu A} | 0 \rangle = \frac{g}{8\pi^2} \varepsilon^{\alpha\nu\beta\lambda} \, p_\alpha \, k_\beta \, \mathcal{A}^{ABC} \tag{2.21}$$

for the term containing a γ^5. Compared to the result from above we get an additional factor of $1/2\,\mathcal{A}^{ABC}$ which comes from the fact that we consider a non-abelian theory here,

$$\mathcal{A}^{ABC} = \sum_f \text{Tr} \, [t^A, \{t^B, t^C\}] \tag{2.22}$$

is the trace over the group matrices that are in the representation of the fermion fields and we have to sum over the fermions.

Therefore we conclude that this current is not conserved if the trace over the group matrices does not vanish. Calculating $\partial_\nu j^{\nu B}$ or $\partial_\lambda j^{\lambda C}$ actually gives an equivalent result, since the trace $\mathcal{A}^{ABC}$ is totally symmetric in its indices. Following the computational ansatz in Ref. [164] that introduces arbitrary constant four-vector shifts a and b to the loop momenta of the two respective triangle diagrams, we can deduce more properties of the anomaly structure. Although the divergence of the axial vector current results to be finite, we encounter diverging integrals in its calculation and therefore the outcome indeed depends on the choice of the parameters a and b. With this choice we can actually move around the position of the anomaly, it can be in one of the three currents or in all three, but we can never remove it completely.

If the trace over the group matrices $\mathcal{A}^{ABC}$ does not vanish, the structure of the gauge theory that we constructed is violated. It leads to the divergence of the gauge boson mass and the broken Ward identity implies that non-physical states do no longer vanish and the scattering matrix is not necessary unitary [35,165]. Therefore, we need the trace to vanish, $\mathcal{A}^{ABC} = 0$, and the theory to be anomaly free.

To check the consistency of a gauge theory regarding its anomaly structure, we therefore need to calculate all group matrix traces resulting from the possible combinations of external gauge boson in the triangle diagrams. This shows us, for example, that combining the $SU(2)$ gauge symmetry with the electromagnetic $U(1)$ and analysing thus the trace

$$\mathrm{Tr}\left[Q\{t^B, t^C\}\right] \tag{2.23}$$

where $t^{B,C}$ are the generators of $SU(2)$ and Q the electric charge of the fermions in the loop, requires the existence of both quarks and leptons in the theory. This trace is proportional to the trace, and thus the sum, of the electric charges of the fermions in the loop, and it only cancels out if we combine quarks and leptons. We can also see that the sum of these charges cancels for each generation individually. It is therefore possible, from the point of anomaly cancellation, to introduce a fourth generation of quarks and leptons to the SM, but impossible to have a new doublet of only one of them.

Equivalently, when gauging another global symmetry of the SM, like *e.g.* baryon minus lepton number $B-L$ or baryon and lepton number B, L separately, we can check whether the SM fermion content is anomaly free under this symmetry, or whether it is necessary to introduce additional fermion content to render the theory consistent. By the rules of anomaly cancellation we can then find various sets of fermions that cancel the arising anomalies, whose charges are thereby defined. We will see that the fermions in a theory can be chiral under the same or two different gauge symmetries and these two cases will have very distinct properties.

Later in this chapter we will calculate triangle diagrams featuring gauge bosons of the additional $U(1)$ symmetries gauged baryon number B and gauged baryon minus lepton number $B-L$. The following Section 2.3 therefore introduces these symmetries.

2.3 Models of Additional U(1) Gauge Symmetries

Since the global symmetry of the SM (assuming Dirac neutrino masses) is $U(1)_B \times U(1)_L$, we can gauge a subgroup of this product symmetry while leaving the Yukawa structure intact. Cancelling all anomalies while assuming a minimal set of at most two new fermions (anomalons) per generation leads to a general parametrisation of possible new $U(1)$ symmetries: they can be subsumed as $U(1)_L$ and $U(1)_{B-xL}$, where x is a real multiplicative factor [135]. $x = 1$ gives us $U(1)_{B-L}$, gauged baryon minus lepton number. Other choices $x \neq 1$ require the introduction of anomaly cancelling fermions, since the contribution of SM fields to the $SU(2)_L^2 \times U(1)_{B-xL}$ and $U(1)_Y^2 \times U(1)_{B-xL}$ anomalies is nonzero. These anomalons must then have electroweak charges and we have to be careful not to spoil all other gauge anomalies.

As exemplary theories to study the behaviour of triple gauge boson vertices we want to look at two kinds of theories: Models where all fermions are chiral under the same symmetry, *i.e.* their axial couplings are to the same gauge boson, and models where there are two types of fermions, one being axially charged under one of the spontaneously broken symmetries, while others have axial couplings to the second massive gauge boson. These two types of theories show very different non-decoupling behaviours for the fermions in the theory. As we will see, in theories where the fermions are chiral under two different symmetries, an anomaly free set of fermions does not necessarily decouple, while this is always given when all fermions share the same chirality structure.

We will introduce the gauged baryon minus lepton number symmetry $B - L$ in Section 2.3.1, which is anomaly free for the SM fermion content when including three right-handed neutrinos. Here, all fermions are chiral under the SM hypercharge symmetry, and vector like under the new symmetry $U(1)_{B-L}$. Therefore, an additional Higgs needs to be introduced solely to give mass to the new gauge boson Z'_{BL}, or a Stückelberg mechanism could serve as a source of its mass. The mass of the fermions is unconnected to this scale, as they are generated by the spontaneous breaking of the SM electroweak symmetry, *i.e.* the SM Higgs vev. The vertex function for the decay $Z \to Z'_{BL}\gamma$ will then be studied in Section 2.4.2.

As a second example we will study gauged baryon number B. The model is introduced in Section 2.3.2 and the vertex function of $Z \to Z'_B\gamma$ is discussed in Section 2.4.3. This symmetry is anomalous under the SM fermion content, since compared to $B - L$ it lacks the cancellation of the quark B with the lepton L contribution. Therefore it needs to either be considered as an effective theory, introducing Wess-Zumino terms [157] to the Lagrangian, or we need to include new fermion fields that have to carry electroweak charges and mimic the SM leptons in the cancellation of anomaly contributions. The masses of these so called anomalons could theoretically be generated by the SM Higgs vev, but this option is (mostly) experimentally excluded by the measurement of the SM Higgs decay width to two photons, see Section 2.5. Thus, we introduce a new Higgs boson Φ that acquires a vev and gives mass not only to the new gauge boson Z'_B, but also to the new fermions (at least dominantly). This leads to a close connection of the mass of the boson and the anomalons, since they are generated by the same scale. When we take the new Higgs vev v_Φ to generate the mass of the new fermions, their mass is bound from above by the maximum possible value for the Yukawa coupling y_{max}, the mass of the gauge boson $m_{Z'_B}$ and the value of the gauge coupling g_X.

name	$SU(3)_c$	$SU(2)_L$	$U(1)_Y$	$U(1)_B$	$U(1)_L$
$Q_L = (u,d)_L$	3	2	1/6	1/3	0
$L_L = (\nu,e)_L$	1	2	-1/2	0	1
u_R^c	$\bar{3}$	1	-2/3	-1/3	0
d_R^c	$\bar{3}$	1	1/3	-1/3	0
e_R^c	1	1	1	0	-1
ν_R^c	1	1	0	0	-1

Table 2.1: Table of SM fermion quantum numbers for the SM gauge symmetries and gauged baryon B and lepton number L including three right-handed neutrinos ν_R.

We will discuss a possible UV completion of this model in detail in Section 2.3.2 and show the effect of the common scale of anomalons and the gauge boson on the decay width $Z \to Z'_B\gamma$ in Section 2.4.3. The connection between the UV complete theory to the corresponding effective description through Wess-Zumino terms will be discussed in Section 2.7.

2.3.1 Gauged Baryon minus Lepton Number

Baryon minus lepton number $B-L$ is a global symmetry of the SM and when we introduce right-handed neutrinos to cancel the $\sum U(1)_L$ and $U(1)_L^3$ anomalies, it becomes anomaly free. Gauging $B-L$ is motivated for example by grand unifying theories [133, 134] and has been studied since it can prevent proton decay [133]. The quarks are charged as 1/3, while leptons carry charges of 1, this renders each SM generation anomaly free independently. Therefore we will see in Section 2.4.2 that a mass degenerate generation of SM fermions will not contribute to the $Z \to Z'_{BL}\gamma$ decay width and generally an anomaly free set of fermions will contribute with the charge-weighted mass difference of the fermions in the set. This behaviour is similar to that of the GIM mechanism [166][5].

The $B-L$ interaction Lagrangian is given by

$$\mathcal{L}_{\mathrm{BL}} = g_{BL}\left(\frac{1}{3}\bar{q}\gamma^\mu Z'_{BL,\mu}q - \bar{\ell}\gamma^\mu Z'_{BL,\mu}\ell - \bar{\nu}\gamma^\mu Z'_{BL,\mu}\nu\right) \ . \tag{2.24}$$

We listed the quantum number of the SM fermions including right-handed neutrinos in Table 2.1. The triangle diagrams that arise with the addition of this gauge symmetry to the symmetries of the SM and the respective anomaly traces that we need to evaluate are the following:

$$\mathcal{A}(SU(3)^2 \otimes U(1)_{B-L}) \quad = \quad \sum_f \mathrm{Tr}\,[T^a T^b Q^c_{BL}] \ , \tag{2.25}$$

[5] The GIM mechanism led to the discovery of the charm quark by noting a divergence in the calculation of the kaon mixing $K^0 \to \bar{K}^0$ mediated by the up quark. If the charm quark mass were equal to the up quark mass, both contributions to the mixing would exactly cancel.

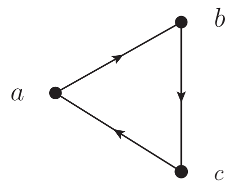

Figure 2.2: Pictograph of the triangle anomaly.

$$\begin{aligned}
\mathcal{A}(SU(2)^2 \otimes U(1)_{B-L}) &= \sum_f \mathrm{Tr}\left[t^a t^b Q^c_{BL}\right] , &(2.26)\\
\mathcal{A}(U(1)_Y^2 \otimes U(1)_{B-L}) &= \sum_f \mathrm{Tr}\left[Q^a_Y Q^b_Y Q^c_{BL}\right] , &(2.27)\\
\mathcal{A}(U(1)_Y \otimes U(1)_{B-L}^2) &= \sum_f \mathrm{Tr}\left[Q^a_Y Q^b_{BL} Q^c_{BL}\right] , &(2.28)\\
\mathcal{A}(U(1)^3_{BL}) &= \sum_f \mathrm{Tr}\left[Q^a_{BL} Q^b_{BL} Q^c_{BL}\right] , &(2.29)\\
\mathcal{A}(U(1)_{B-L}) &= \sum_f \mathrm{Tr}\left[Q^a_{BL}\right] , &(2.30)
\end{aligned}$$

where we depicted the vertices by the indices a, b and c as shown in Figure 2.2. We always have to sum over the fermions in the loop. The generators with capital letters T^a, T^b are used for the $SU(3)$ gauge group, while the small letters t^a, t^b represent the generators of the $SU(2)$ gauge group. Q_Y and Q_{BL} are the hypercharge and $B-L$ charges of the fermions, respectively. The last trace involving only one vertex with the $B-L$ gauge boson Z'_{BL} arises from the coupling of an abelian gauge boson to gravity.

We will show the calculation for a selection of these traces. As the first example we calculate the anomaly trace of the triangle diagram involving two gluons and a $B-L$ gauge boson Z'_{BL} as external particles:

$$\mathcal{A}(SU(3)^2 \otimes U(1)_{B-L}) = 3\left(\frac{1}{2}\cdot 2\cdot\left(\frac{1}{3}\right) + \frac{1}{2}\cdot\left(-\frac{1}{3}\right) + \frac{1}{2}\cdot\left(-\frac{1}{3}\right)\right) = 0 , \qquad (2.31)$$

where the factor three in front of the brackets comes from the three generations. Note that for the right-handed quarks we have to use the charge conjugate, leading to a $B-L$ charge of $-1/3$. The factor $1/2$ comes from the trace of the generators of $SU(3)$, while we get the factor 2 for the left-handed quarks since it is a doublet. We thereby confirm that the $SU(3)^2 \otimes U(1)_{B-L}$ anomaly cancels.

The anomaly trace of $U(1)_Y^2 \otimes U(1)_{B-L}$, for example, shows the cancellation between the quark and lepton sector:

$$\mathcal{A}(U(1)_Y^2 \otimes U(1)_{B-L}) = 3\cdot 3\left(2\cdot\left(\frac{1}{6}\right)^2\left(\frac{1}{3}\right) + \left(-\frac{2}{3}\right)^2\left(-\frac{1}{3}\right) + \left(\frac{1}{3}\right)^2\left(-\frac{1}{3}\right)\right)$$

$$+3\left(2\cdot\left(-\frac{1}{2}\right)^2(1)+(1)^2(-1)\right)=-\frac{3}{2}+\frac{3}{2}=0\,. \quad (2.32)$$

The first line are the quarks that again come in three colours and three generations, while the second line are the leptons that do not carry colour charge. Considering only quarks or leptons in the theory, or equally gauging B and/or L separately, would lead to a non-zero anomaly in this case. The same applies for the anomaly trace of $SU(2)^2 \otimes U(1)_{B-L}$.

Let us also look at the anomalies that involve just the $B-L$ gauge boson, where the right-handed neutrinos appear. Since they are singlets under the SM gauge groups they do not contribute to any triangle diagrams involving SM gauge bosons.

$$\begin{aligned}\mathcal{A}(U(1)^3_{BL}) &= 3\cdot 3\left(2\cdot\left(\frac{1}{3}\right)^3+\left(-\frac{1}{3}\right)^3+\left(-\frac{1}{3}\right)^3\right) \\ &+ 3\left(2\cdot(1)^3+(-1)^3+(-1)^3\right) = 0\,.\end{aligned} \quad (2.33)$$

The first line are again the quarks and the second the leptons. We see that quarks and leptons cancel the anomaly separately, which is then also true for the separate gauge symmetries B and L. The calculation for $U(1)_{B-L}$ is completely analogous. We therefore see that the anomaly in the lepton sector only cancels because we introduced the right-handed neutrinos.

2.3.2 Gauged Baryon Number

A mixed chiral structure can be obtained by gauging an anomalous global symmetry of the SM. We chose to work with the model of gauged baryon number $U(1)_B$. Here, the SM quarks are charged as 1/3 under the new symmetry, but we lack the cancellation of the leptons that occurred when gauging $B-L$. Therefore the anomaly coefficients of the mixed anomalies $SU(2)^2_L \otimes U(1)_B$ and $U(1)^2_Y \otimes U(1)_B$ are nonzero [137]:

$$\begin{aligned}\mathcal{A}(SU(2)^2_L \otimes U(1)_B) &= \mathrm{Tr}\,[t^a t^b Q^c_B] = \quad (2.34)\\ &= 3\cdot 3\cdot(1/2\cdot 1/3+0\cdot(-1/3)+0\cdot(-1/3)) = 3/2\,,\\ \mathcal{A}(U(1)^2_Y \otimes U(1)_B) &= \mathrm{Tr}\,[Q^a_Y Q^b_Y Q^c_B] = \quad (2.35)\\ &= 3\cdot 3\cdot(2\cdot(1/6)^2\cdot 1/3+(-2/3)^2\cdot(-1/3)+(1/3)^2\cdot(-1/3)) = -3/2\,,\end{aligned}$$

where t^a, t^b are again the generators of $SU(2)$ and Q_Y and Q_B the hypercharge and baryon number charge, respectively. We sum over the contributions from all SM quarks. The factor $3\cdot 3$ before the brackets are the three generations and three colours, while in the bracket we multiply the $SU(2)_L$ times the baryon number charge and the $U(1)^2_Y$ times the baryon number charge, respectively. The other gauge anomalies vanish.

To render this theory anomaly free we have to introduce new fermions that cancel the two above anomalies but of course also keep the other gauge anomalies zero. Note that these new fermions do not need to carry colour charge, since the anomaly coefficient of $SU(3)_c^2 \otimes U(1)_B$ is already vanishing; instead they can mimic the SM leptons (copying the cancellation from the $B-L$ case). In any case they need to carry electroweak quantum numbers to contribute to the two above anomalies.

We want to keep the fermion content minimal and following Refs. [167–169] we introduce a set of colour neutral anomalons named L_L, L_R, E_L, E_R, N_L, and N_R. When we choose their mass to be generated by the SM Higgs, their behaviour mimics the SM leptons (in their entirety, because we do not have three copies). We introduce a $U(1)_B$ breaking Higgs Φ, giving mass to the Z'_B and optionally the anomalons. The relevant quantum numbers of the newly introduced fields are shown in Table 2.2. The fields appear in vector like pairs under the SM electroweak symmetries, ensuring that the pure electroweak gauge anomalies are still cancelled. The fields L_L, L_R, E_L, and E_R carry electroweak quantum numbers and are chosen such that they cancel the $SU(2)_L^2 \times U(1)_B$ and $U(1)_Y^2 \times U(1)_B$ mixed anomalies, but since they give rise to $U(1)_B$ and $U(1)_B^3$ anomalies, the SM singlets N_L and N_R are introduced to cancel the latter[6]. Since the sum of baryon number and hypercharge quantum numbers also satisfies the trace condition $\sum_f \mathrm{Tr}\,(q_B Y) = 0$, this scenario avoids a large mixing of the Z'_B and the hypercharge gauge boson [169]. The interaction Lagrangian of the SM quarks with the Z'_B vector is given by

$$\mathcal{L} \supset g_X \frac{1}{3} Z'_{B\mu} \left(\overline{q}\gamma^\mu q\right) \ , \tag{2.36}$$

denoting the $U(1)_B$ gauge coupling by g_X. Note that the SM quarks have vector like couplings to the Z'_B boson.

Field	L_L	L_R	E_L	E_R	N_L	N_R	Φ
$SU(2)_L$	2	2	1	1	1	1	1
$U(1)_Y$	-1/2	-1/2	-1	-1	0	0	0
$U(1)_B$	-1	2	2	-1	2	-1	3

Table 2.2: Electroweak and baryon number charges of a set of colourless anomalons and the $U(1)_B$ breaking Higgs field Φ, from Refs. [167–169].

The masses of the anomalons can be generated by both the SM Higgs and the $U(1)_B$ breaking Higgs field Φ. The cases, where the new fermions couple to only the SM Higgs or only to the new Higgs Φ can be interpreted as the limiting cases of the mixed scenario, where they couple to both Higgs fields. The Weyl fermions listed in Table 2.2 can thus pair into different mass eigenstates, depending on the values of the Yukawa couplings. Note that the case where the masses of the anomalons are exclusively generated by the $U(1)_B$ breaking Higgs is insinuated by the naming of the states.

[6]Note that the $U(1)_B$ charges of N_L and N_R can also be interchanged.

The Lagrangian for the anomalon content in Table 2.2 is given by a kinetic contribution, the Yukawa interactions and the couplings of the scalar Φ, including a mixing to the SM Higgs field:

$$\mathcal{L} = \mathcal{L}_{\text{kin}} + \mathcal{L}_{\text{Yuk}} + \mathcal{L}_{\text{scalar}} \,, \tag{2.37}$$

$$\mathcal{L}_{\text{kin}} = \bar{L}_L i\not{D} L_L + \bar{L}_R i\not{D} L_R + \bar{E}_L i\not{D} E_L + \bar{E}_R i\not{D} E_R + \bar{N}_L i\not{D} N_L + \bar{N}_R i\not{D} N_R \,, \tag{2.38}$$

$$\begin{aligned}\mathcal{L}_{\text{Yuk}} = &- y_L \bar{L}_L \Phi^* L_R - y_E \bar{E}_L \Phi E_R - y_N \bar{N}_L \Phi N_R \\ &- y_1 \bar{L}_L H E_R - y_2 \bar{L}_R H E_L - y_3 \bar{L}_L \tilde{H} N_R - y_4 \bar{L}_R \tilde{H} N_L + \text{ h.c.} \,,\end{aligned} \tag{2.39}$$

$$\mathcal{L}_{\text{scalar}} = |D_\mu \Phi|^2 - \mu_\Phi^2 |\Phi|^2 - \lambda_\Phi |\Phi|^4 - \lambda_{H\Phi} |H|^2 |\Phi|^2 \,. \tag{2.40}$$

For the rest of this work, we will assume $U(1)_B$ to be spontaneously broken, *i.e.* μ_Φ^2 to be smaller than zero, and the scale of the breaking to be given by $\langle \Phi \rangle = v_\Phi/\sqrt{2}$. Furthermore we take the scalar – Higgs portal coupling $\lambda_{H\Phi}$ to be negligible as well as the kinetic mixing of the hypercharge and baryon number field strengths.

Ignoring kinetic mixing effects of the gauge bosons, we can write down the parts of the currents of the three gauge bosons that are generated by the anomalons. We use the convention where $Q = T_3 + Y$, and write the doublets as $L_L = (\nu_L, e_L)^T$ and $L_R = (\nu_R, e_R)^T$. The interaction of the anomalons can then be formulated in terms of the γ-, Z- and Z'_B-mediated currents:

$$\mathcal{L}_{\text{int}} = e_{\text{em}} A_\mu J^\mu_{\text{em}} + \frac{g}{c_W} Z_\mu J^\mu_Z + g_X Z'_{B\mu} J^\mu_{Z'_B} \,, \quad \text{with} \tag{2.41}$$

$$J^\mu_{\text{em}} = \bar{e}_L(-1)\gamma^\mu e_L + \bar{e}_R(-1)\gamma^\mu e_R + \bar{E}_L(-1)\gamma^\mu E_L + \bar{E}_R(-1)\gamma^\mu E_R \,, \tag{2.42}$$

$$\begin{aligned}J^\mu_Z = &\bar{e}_L \left(\frac{-1}{2} + s_W^2\right) \gamma^\mu e_L + \bar{e}_R \left(\frac{-1}{2} + s_W^2\right) \gamma^\mu e_R \\ &+ \bar{E}_L \left(s_W^2\right) \gamma^\mu E_L + \bar{E}_R \left(s_W^2\right) \gamma^\mu E_R + \bar{\nu}_L \frac{1}{2} \gamma^\mu \nu_L + \bar{\nu}_R \frac{1}{2} \gamma^\mu \nu_R \,,\end{aligned} \tag{2.43}$$

$$\begin{aligned}J^\mu_{Z'_B} = &\bar{e}_L(-1)\gamma^\mu e_L + \bar{e}_R(2)\gamma^\mu e_R + \bar{E}_L(2)\gamma^\mu E_L + \bar{E}_R(-1)\gamma^\mu E_R \\ &+ \bar{\nu}_L(-1)\gamma^\mu \nu_L + \bar{\nu}_R(2)\gamma^\mu \nu_R + \bar{N}_L(2)\gamma^\mu N_L + \bar{N}_R(-1)\gamma^\mu N_R \,,\end{aligned} \tag{2.44}$$

where we abbreviate c_W and s_W as the cosine and sine of the Weinberg mixing angle.

The mass generation of the anomalons can have two sources, the SM Higgs vev v_H and the vev v_Φ of the $U(1)_B$ breaking Higgs Φ. In eq. (2.39) the first case implies that the masses are set by the couplings y_1 to y_4, while in the second case the couplings y_L, y_E, and y_N are non-zero. If the SM Higgs vev generates the masses, the mass eigenstates of the anomalons mimic the SM leptons and the anomaly cancellation works analogously to the $B - L$ case. If the masses are generated by the new vev v_Φ, these masses are vector like under the SM symmetries and the mass eigenstates form as insinuated by the naming of the anomalon fields.

Note, that if the SM Higgs boson is the dominant source of the anomalon masses, the charged anomalon fields can have a large (non-decoupling) impact on the SM Higgs diphoton decay rate $H \to \gamma\gamma$, which is restricted to be SM-like by the measurements at the LHC [170]. Since the anomalons include two charged matter fields, their contributions could, however, cancel each other in certain regions of the parameter space. Also if the primary source of the mass is given by the vev of new Higgs Φ, this could dilute the effects on $H \to \gamma\gamma$. We will analyse these effects in Section 2.5 on direct searches for anomalons.

Anomalon Masses Generated by the New Higgs

The above being said we will mainly examine the scenario where the anomalon masses are generated by the $U(1)_B$ breaking Higgs (which is also the case that is suggested by the naming of the states). Therefore, the anomalons have vector like couplings to the SM Z boson, axial vector couplings occur only to the Z'_B boson. We obtain three mass eigenstates, the electroweak doublet L, the singlet E and the complete SM singlet N. We split the doublet as before into the states $L = (\nu, e)$, copying the SM lepton notation.[7] The mass Lagrangian of the anomalons then becomes

$$\mathcal{L}_{\text{mass}} = -\, m_L \left(1 + \frac{\phi}{v_\Phi}\right)(\bar{\nu}\nu + \bar{e}e) - m_E \left(1 + \frac{\phi}{v_\Phi}\right)\bar{E}E - m_N \left(1 + \frac{\phi}{v_\Phi}\right)\bar{N}N \;, \quad (2.45)$$

where the masses are given by

$$m_L = y_L v_\Phi/\sqrt{2}\,, \quad (2.46)$$

$$m_E = y_E v_\Phi/\sqrt{2}\,, \quad (2.47)$$

$$m_N = y_N v_\Phi/\sqrt{2}\,. \quad (2.48)$$

While the complete SM gauge singlet N will not play a role in our calculations, both the state e in the electroweak doublet L and the singlet E are electrically charged and contribute to the decay width $Z \to Z'_B\gamma$. In Sections 2.4.3 and 2.5 we will mostly consider these two states to be degenerate for simplicity, $M = m_L = m_E$, but we will comment on the effects of unequal masses. Combining now the Weyl fermions from before into mass eigenstates as generated by the vev v_Φ, the currents from eqs. (2.42) to (2.44) become

$$J^\mu_{\text{em}} = \bar{e}(-1)\gamma^\mu e + \bar{E}(-1)\gamma^\mu E \;, \quad (2.49)$$

$$J^\mu_Z = \bar{e}\left(\frac{-1}{2} + s_W^2\right)\gamma^\mu e + \bar{E}s_W^2\gamma^\mu E + \bar{\nu}(\frac{1}{2})\gamma^\mu\nu \;, \quad (2.50)$$

$$\begin{aligned} J^\mu_{Z'_B} = \bar{e}\left(\frac{1}{2}\gamma^\mu + \frac{3}{2}\gamma^\mu\gamma^5\right)e + \bar{E}\left(\frac{1}{2}\gamma^\mu - \frac{3}{2}\gamma^\mu\gamma^5\right)E\, + \\ + \bar{\nu}\left(\frac{1}{2}\gamma^\mu + \frac{3}{2}\gamma^\mu\gamma^5\right)\nu + \bar{N}\left(\frac{1}{2}\gamma^\mu - \frac{3}{2}\gamma^\mu\gamma^5\right)N \;. \end{aligned} \quad (2.51)$$

[7] They should not be confused with the SM neutrino and electron!

Note that the Yukawa couplings y_1 to y_4 to the SM Higgs and the axial vector coupling to the SM Z boson are intimately tied together. If these Yukawa couplings vanish, so does the axial coupling and the anomalons then are chiral under $U(1)_B$ and vector like under the SM. This connection prevents perturbative unitarity violation in the process $f\bar{f} \to VV$, where an axial vector coupling between the fermion f and the gauge boson V leads to a divergence if the s-channel diagram mediated by the corresponding Higgs boson is omitted [171].

Anomalon Masses Generated by the SM Higgs

Although the case of the anomalon masses being entirely generated by the SM Higgs boson is phenomenologically not viable (see above), we will use it illustrate the crucial role of the axial vector coupling. The behaviour of the A–V–V vertex function will differ significantly between the two scenarios, where either the axial vector coupling is to the same gauge boson for all fermions in the loop or on the other hand if there are two types of fermions each with an axial vector coupling to one of the two massive gauge boson, whose masses are then consequently generated by the two respective Higgs bosons. These two cases will be illustrated in Section 2.4.3.

If the masses of the anomalons are entirely generated by the SM Higgs, *i.e.* the Yukawa couplings y_L, y_E and y_N are vanishing, the anomalons combine to different mass eigenstates and the Lagrangian becomes

$$\begin{aligned}\mathcal{L}_{\text{mass}} =& - m_1 \left(1 + \frac{h}{v_H}\right) \bar{e}_L E_R - m_2 \left(1 + \frac{h}{v_H}\right) \bar{e}_R E_L \\ & - m_3 \left(1 + \frac{h}{v_H}\right) \bar{\nu}_L N_R - m_4 \left(1 + \frac{h}{v_H}\right) \bar{\nu}_R N_L + \text{ h.c. } ,\end{aligned} \tag{2.52}$$

where now the indices L and R can not be interpreted as the left- and right-handed projections of the fields, but are instead parts of different Dirac fermions. The masses are given by

$$m_i = y_i \, v_H/\sqrt{2} \,, \tag{2.53}$$

for $i = 1, \ldots, 4$. From the currents in eqs. (2.42) to (2.44) we can see that the states are vector-like under the $U(1)_B$ symmetry, but have axial vector couplings to the SM Z boson. We name the two charged states $(e_L, E_R)^T = E_1$ and $(E_L, e_R)^T = E_2$ and the neutral states $(\nu_L, N_R)^T = N_1$ and $(N_L, \nu_R)^T = N_2$. The currents for the SM Higgs induced mass eigenstates are then

$$J^\mu_{\text{em}} = \bar{E}_1(-1)\gamma^\mu E_1 + \bar{E}_2(-1)\gamma^\mu E_2 \ , \tag{2.54}$$

$$\begin{aligned}J^\mu_Z =& \bar{E}_1 \left(\frac{1}{4}\gamma^\mu \left((-1 + 4s_W^2) + \gamma^5\right)\right) E_1 + \bar{E}_2 \left(\frac{1}{4}\gamma^\mu \left((-1 + 4s_W^2) - \gamma^5\right)\right) E_2 \\ & + \bar{N}_1 \left(\frac{1}{4}\left(1 - \gamma^5\right)\gamma^\mu\right) N_1 + \bar{N}_2 \left(\frac{1}{4}\left(1 + \gamma^5\right)\gamma^\mu\right) N_2 \ ,\end{aligned} \tag{2.55}$$

$$J^{\mu}_{Z'_B} = \bar{E}_1(-1)\gamma^{\mu}E_1 + \bar{E}_2(2)\gamma^{\mu}E_2 + \bar{N}_1(-1)\gamma^{\mu}N_1 + \bar{N}_2(2)\gamma^{\mu}N_2 \; . \tag{2.56}$$

We see that both state E_1 and E_2 have an electric charge of -1 and the Z boson current in eq. (2.55) shows that the couplings are identical to the SM leptons. The charges in the current to the Z'_B boson differ from the couplings of the SM leptons to the Z'_{BL} boson. Nevertheless, if we take a degenerate set of SM leptons, their charges relevant to the Z–Z'_{BL}–γ vertex are multiplied and add up to $3 \cdot (1/4) \cdot (-1) \cdot (-1) = 3/4$, where the multipliers are the number of generations, the axial charge to the Z boson, the $B - L$ charge and the electric charge, respectively. For the case of degenerate anomalons E_1 and E_2 we get $(1/4) \cdot (-1) \cdot (-1) + (-1/4) \cdot 2 \cdot (-1) = 3/4$, where the charges are again to the Z boson, the Z'_B boson and the photon. If the anomalons (with masses from the SM Higgs) and the SM lepton were thus to be all the same, the Z–Z'_{BL}–γ and Z–Z'_B–γ vertex function would be identical.

In Section 2.4.3 we will analyse the differences of the vertex function between the two limiting cases of mass generation in the $U(1)_B$ model. One important restriction should be noted at this point: when the masses of the anomalons are generated by the SM Higgs, the corresponding vev is given by $v_H = 246\,\text{GeV}$ and thus we have a fixed upper limit on the anomalon masses by the restriction of perturbativity of the Yukawa coupling. On the other hand we obtain in this case a decoupling of the anomalon masses and the Z'_B mass, which are generated by different Higgses.

2.4 The Triple Gauge Boson Vertex Structure

2.4.1 The Generic A–A–V Vertex Structure

The axial anomaly is often illustrated by a calculation of the three vector boson triangle diagram [35, 164]. The divergence, which is zero for a pure vector current, is shown not to vanish in the axial vector case. In this section we want to calculate the full vertex function for a triangle diagram mediated by fermions, with one conserved current, *i.e.* a pure vector current, and two axial vector currents.

We will later take the vector current to be the photon and one of the axial currents to be the SM Z boson, the other will be a Z' boson associated to a new gauge symmetry. In this section, however, the calculation is generic and the naming of the bosons and couplings is solely intuitive for the concrete cases in the next sections. It should be noted that in this calculation featuring one generic fermion in the loop, the anomaly can certainly not be cancelled and the result will depend on the anomaly description.

The two diagrams contributing to the vertex function are shown in Figure 2.3 and we can write the corresponding matrix elements as

$$i\mathcal{M}_1 = \frac{-Qe_{\text{em}}gg_X}{(2\pi)^4}\varepsilon_{\mu}(p_1+p_2)\varepsilon^*_{\nu}(p_1)\varepsilon^*_{\rho}(p_2) \times \int d^4k \; \text{Tr}\Big[(g^Z_v\gamma^{\mu} + g^Z_a\gamma^{\mu}\gamma^5)\cdot$$

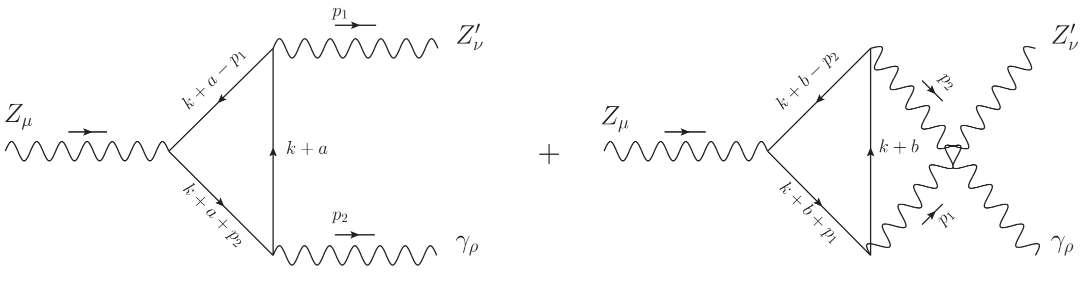

Figure 2.3: The triangle diagrams corresponding to the $Z - Z' - \gamma$ vertex function.

$$\frac{\not k + \not a - \not p_1 + m}{(k+a-p_1)^2 - m^2}(g_v^{Z'}\gamma^\nu + g_a^{Z'}\gamma^\nu\gamma^5)\frac{\not k + \not a + m}{(k+a)^2 - m^2}\gamma^\rho \frac{\not k + \not a + \not p_2 + m}{(k+a+p_2)^2 - m^2}\Bigg], \tag{2.57}$$

$$iM_2 = \frac{-Qe_{\rm em}gg_X}{(2\pi)^4}\varepsilon_\mu(p_1+p_2)\varepsilon^*_\nu(p_1)\varepsilon^*_\rho(p_2) \times \int d^4k\ \mathrm{Tr}\Bigg[(g_v^Z\gamma^\mu + g_a^Z\gamma^\mu\gamma^5)\cdot$$
$$\frac{\not k + \not b - \not p_2 + m}{(k+b-p_2)^2 - m^2}\gamma^\rho \frac{\not k + \not b + m}{(k+b)^2 - m^2}(g_v^{Z'}\gamma^\nu + g_a^{Z'}\gamma^\nu\gamma^5)\frac{\not k + \not b + \not p_1 + m}{(k+b+p_1)^2 - m^2}\Bigg], \tag{2.58}$$

where m is the mass of the fermion in the loop and k the loop momentum, Q is the fermion charge in the vector current. $g_{v,a}$ are the vector and axial couplings to the massive gauge bosons, $p_{1,2}$ are the outgoing momenta of the latter. $e_{\rm em}$, g, and g_X are the three gauge couplings. The constant four-vectors a and b are introduced [164], since although the (linear) divergences in the two diagrams cancel each other, a residual dependence on a shift in the loop momentum remains in the vertex function, as we will see. In the case of an effective theory, the physicality of the result therefore has to be ensured by fixing the values for a and b by external physical condition, such as for example the conservation of a vector current.

Note that if a fermion would indeed have axial couplings under two symmetries, its mass would be generated by both corresponding Higgs vevs, and therefore in the mass basis we have flavour changing neutral currents. The calculation of the matrix elements would then involve mixing angles between the states and two different fermion mass eigenstates in the loop. In the concrete loop calculation we will therefore assume each fermion to have an axial coupling to only one of the gauge bosons.

As mentioned above, both matrix elements contain linearly divergent integrals that mutually cancel, but the result depends on arbitrary shifts in the loop momenta k that we denoted by a and b. Regularising each diagram with, for example, Pauli-Villars or dimensional regularisation [159] does not solve this ambiguity but rather shifts it to the choice of the position of γ^5. The result therefore has to be fixed by external physical conditions. Decomposing the vertex function into form factors that are allowed by parity and the Lorentz structure gives us this most general expression [122, 172]

$$\begin{aligned}\Gamma^{\mu\nu\rho}(p_1,p_2;w,z) = {} & F_1(p_1,p_2)\epsilon^{\nu\rho|p_1||p_2|}p_1^\mu + F_2(p_1,p_2)\epsilon^{\nu\rho|p_1||p_2|}p_2^\mu \\ & + F_3(p_1,p_2)\epsilon^{\mu\rho|p_1||p_2|}p_1^\nu + F_4(p_1,p_2)\epsilon^{\mu\rho|p_1||p_2|}p_2^\nu \\ & + F_5(p_1,p_2)\epsilon^{\mu\nu|p_1||p_2|}p_1^\rho + F_6(p_1,p_2)\epsilon^{\mu\nu|p_1||p_2|}p_2^\rho \\ & + G_1(p_1,p_2;w)\epsilon^{\mu\nu\rho\sigma}p_{1\sigma} + G_2(p_1,p_2;z)\epsilon^{\mu\nu\rho\sigma}p_{2\sigma}\ ,\end{aligned} \tag{2.59}$$

where we introduce the notation $\epsilon^{\nu\rho|p_1||p_2|} = \epsilon^{\nu\rho\alpha\beta}p_{1\alpha}p_{2\beta}$, etc. We set $a = -b$, cancelling thus a non-chiral anomaly. We express the remaining arbitrary four-vector a^μ in terms of the external momenta $a^\mu = z\,p_1^\mu + w\,p_2^\mu$, where w and z are constant scalars.

Already from naive power counting we can see that the form factors F_1 to F_6 are finite and can be calculated by the usual diagrammatic methods. This is reflected by the fact that they are independent of w and z. Two of these form factors can even be eliminated exploiting the limited number of independent vectors in four-dimensional space. Following [172] we choose to eliminate F_1 and F_2 by applying the identities

$$-p_1^\mu\epsilon^{\nu\rho|p_1||p_2|} = -p_1^\nu\,\epsilon^{\mu\rho|p_1||p_2|} + p_1^\rho\,\epsilon^{\mu\nu|p_1||p_2|} + \epsilon^{\mu\nu\rho\alpha}\left((p_1\cdot p_2)\,p_{1\alpha} - p_1^2\,p_{2\alpha}\right)\ , \tag{2.60}$$

$$-p_2^\mu\epsilon^{\nu\rho|p_1||p_2|} = -p_2^\nu\,\epsilon^{\mu\rho|p_1||p_2|} + p_2^\rho\,\epsilon^{\mu\nu|p_1||p_2|} - \epsilon^{\mu\nu\rho\alpha}\left((p_1\cdot p_2)\,p_{2\alpha} - p_2^2\,p_{1\alpha}\right)\ , \tag{2.61}$$

absorbing F_1 and F_2 into redefinitions of F_3' to F_6' and G_1', G_2' where the prime marks the redefined quantities.

The form factors $G_1^{(\prime)}$ and $G_2^{(\prime)}$, however, arise from the cancellation of linearly divergent integrals and depend on the scalars w and z. In an effective theory we therefore have to find external physical conditions to fix w and z, thus uniquely determining the vertex function[8]. The Ward identity structure can be a possibility for such a physical condition. For the general vertex structure, equation (2.59), the Ward identities are given by

$$(p_{1\mu} + p_{2\mu})\Gamma^{\mu\nu\rho} = (G_2' - G_1')\,\epsilon^{\nu\rho|p_1||p_2|}\,, \tag{2.62}$$

$$-\,p_{1\nu}\Gamma^{\mu\nu\rho} = (-F_3'\,p_1^2 - F_4'\,p_1\cdot p_2 + G_2')\epsilon^{\mu\rho|p_1||p_2|}\,, \tag{2.63}$$

$$-\,p_{2\rho}\Gamma^{\mu\nu\rho} = (-F_5'\,p_1\cdot p_2 - F_6'\,p_2^2 + G_1')\epsilon^{\mu\nu|p_1||p_2|}\,. \tag{2.64}$$

We are going to pursue an ansatz that has been employed in [172], using calculations from [120,122,173]. The divergent pieces in the vertex function get isolated and evaluated using a momentum shift integral identity [173], where the momentum shift constants w and z translate into the definitions of $G_1^{(\prime)}$ and $G_2^{(\prime)}$.

For the particular case of our A–A–V vertex function, we calculate the finite form factors F_1 to F_6 in Mathematica [174] using Package-X [175, 176], and adopt the definitions of G_1' and G_2' from [172]. The generalised Ward identities for this case are

$$(p_{1\mu} + p_{2\mu})\,\Gamma^{\mu\nu\rho} = \frac{Qe_{\mathrm{em}}gg_X}{4\pi^2 c_W}\epsilon^{\nu\rho|p_1||p_2|}((w-z)(g_v^{Z'}\,g_a^Z + g_v^Z\,g_a^{Z'}) + 4m^2 g_v^{Z'}\,g_a^Z\,C_0(m))\,, \tag{2.65}$$

[8] We will see that for a UV complete theory the dependence on w and z will cancel out.

$$-p_{1\nu}\Gamma^{\mu\nu\rho} = \frac{Qe_{\rm em}gg_X}{4\pi^2 c_W}\epsilon^{\mu\rho|p_1||p_2|}((w-1)(g_v^{Z'}g_a^Z + g_v^Z g_a^{Z'}) - 4m^2 g_v^Z g_a^{Z'} C_0(m))\,, \tag{2.66}$$

$$-p_{2\rho}\Gamma^{\mu\nu\rho} = \frac{Qe_{\rm em}gg_X}{4\pi^2 c_W}\epsilon^{\mu\nu|p_1||p_2|}(z+1)(g_v^{Z'}g_a^Z + g_v^Z g_a^{Z'})\,. \tag{2.67}$$

where

$$C_0(m) \equiv C_0(0, m_{Z'}^2, m_Z^2, m, m, m) \tag{2.68}$$

is the Passarino-Veltman scalar loop function for the triangle loop, using Package-X conventions [175–177]. m is here the mass of the fermion in the loop, $m_{Z'}$ and m_Z are the gauge boson masses.

We see that a constant, fermion mass independent, anomaly piece is present in all three Ward identities, it gets multiplied by the constant scalars w and z. The divergences in the vertices with the massive vectors, here Z_μ and Z'_ν, also contain a fermion mass dependent piece proportional to $m^2 C_0(m)$ that appears only if the fermion has an axial coupling to the respective vector boson. Since we will consider only flavour conserving couplings, each fermion mass eigenstate is taken to have an axial coupling to only one of the two massive vector bosons. The gauge boson of the unbroken symmetry, later taken to be the photon γ_ρ, couples vector like to all fermions and thus does not contain any fermion mass dependent piece in its divergence. The constant anomaly piece can, however, be present, depending on the choice of w and z in an effective theory.

If we naively use the choice of w and z to ensure that for each fermion the two vector Ward identities vanish and only the axial vector Ward identity has a non vanishing contribution (which would be a naive application of the method used in Ref. [122]), our ansatz becomes inconsistent. Instead we have to make one unique choice of w and z for all fermions in the loop. This problem, however, appears only in theories with two broken gauge symmetries, where the anomaly cancellation involves fermions that have axial couplings to different massive gauge bosons. In a theory like gauged $B-L$, where all relevant fermions have axial couplings to the SM Z boson only, we can consistently set the Ward identities on the Z' and γ vertices to zero. For the gauged baryon number symmetry $U(1)_B$ we will in contrast consider the case, where the anomaly in the SM fermion sector is cancelled by new fermions, called anomalons, that are chiral under $U(1)_B$, since the case of SM chiral new fermions is strongly limited by the observation of the SM consistent rate of the Higgs diphoton decay [170] (see Section on the model of gauged baryon number 2.3.2 and Section 2.5). This leads to the case of two types of fermions, the SM fermions that have axial couplings to the SM Z boson, and the anomalons that have axial couplings to the Z'_B. If we consider the complete theory and add up the contributions of all fermions to the vertex function, the dependence on the constants w and z drops out and we can unambiguously calculate the decay width $\Gamma(Z \to Z'_B\gamma)$.

We can extend this to a general statement. In a UV complete theory, the dependency of the vertex function on w and z will drop out and the constant anomaly part in the

Ward identities vanishes, they will even vanish completely for massless or degenerate fermions. It is therefore an equivalent condition for an anomaly free theory that the total Ward identities vanish independently of the value of w and z (as long as they are identical for all fermions). This shows that in an anomaly free model, the vertex function is insensitive to a shift in the loop momentum and thus to the above described ambiguity.

Now we want to clarify the relation of an anomaly cancelling UV completion to an effective description via Wess-Zumino terms [157], *i.e.* explain how the choice of w and z relates to these terms in the Lagrangian. An effective description corresponds to the heavy fermion limit, the relevant expression in the Ward identities becomes

$$\lim_{m\to\infty} m^2 C_0(m) = -\frac{1}{2}\,, \tag{2.69}$$

and eqs. (2.65) and (2.66) thus exhibit non-decoupling.

Explicitly, we can write down the Wess-Zumino terms that can cancel an anomaly in the SM electroweak sector:

$$\mathcal{L}_{\mathrm{WZ}} = C_B g_X g'^2 \epsilon^{\mu\nu\rho\sigma} Z'_\mu B_\nu \partial_\rho B_\sigma - C_B g_X g^2 \epsilon^{\mu\nu\rho\sigma} Z'_\mu \left(W^a_\nu \partial_\rho W^a_\sigma + \frac{1}{3} g \epsilon^{abc} W^a_\nu W^b_\rho W^c_\sigma \right)\,, \tag{2.70}$$

where B is the SM hypercharge field, W^a are the weak gauge fields and Z' is the gauge field of a new $U(1)$ gauge symmetry. We already set the Wilson coefficients C of the hypercharge and the weak gauge bosons to be equal but opposite sign to avoid breaking the electromagnetic gauge symmetry [143,178,179] and induce an anomaly in the $Z' - \gamma - \gamma$ vertex. From these Wess-Zumino terms we isolate the corresponding term of the $Z - Z' - \gamma$ interaction:

$$\mathcal{L} \supset -C_B \frac{e_{\mathrm{em}} g g_X}{c_W} \epsilon^{\mu\nu\rho\sigma} Z'_\mu \left(Z_\nu \partial_\rho A_\sigma + A_\nu \partial_\rho Z_\sigma \right). \tag{2.71}$$

To compare with our calculation of the $Z - Z' - \gamma$ vertex induced by a fermion in the loop, we calculate the Ward identities in each vertex:

$$(p_{1\mu} + p_{2\mu})\Gamma^{\mu\nu\rho} = C_B \frac{e_{\mathrm{em}} g g_X}{c_W} \epsilon^{\nu\rho|p_1||p_2|}\,, \tag{2.72}$$

$$-\, p_{1\nu}\Gamma^{\mu\nu\rho} = 2C_B \frac{e_{\mathrm{em}} g g_X}{c_W} \epsilon^{\mu\rho|p_1||p_2|}\,, \tag{2.73}$$

$$-\, p_{2\rho}\Gamma^{\mu\nu\rho} = C_B \frac{e_{\mathrm{em}} g g_X}{c_W} \epsilon^{\mu\nu|p_1||p_2|}\,. \tag{2.74}$$

We see that the Wess-Zumino terms generate a contribution to all three divergences, that are all proportional to the Wilson coefficient C_B. An individual Ward identity cannot be set to zero. If this Wess-Zumino description is thus chosen to cancel the SM fermion contribution to the vertex, it dictates the use of a symmetric regularisation scheme, where the anomaly contributes in all three currents. This is called the consistent anomaly.

Matching to our vertex calculation, eqs. (2.65) to (2.67), we can calculate the equivalent choices of w and z. For a SM like fermion, where $g_v^Z = g_a^{Z'} = 0$ [9] and $g_v^{Z'}, g_a^Z \neq 0$, we have to set $2z = w - 3$. For an anomalon like fermion, *i.e.* $g_v^{Z'} = g_a^Z = 0$ and $g_v^Z, g_a^{Z'} \neq 0$, we get $2z = w - 1$. We see, however, that there is still a degree of freedom left, since the restrictions are only relating w and z. A more thorough discussion of the relation of the full calculation to the effective ansatz will follow in Section 2.7.

As mentioned before, in a UV complete theory, which includes all contributing fermions, the calculation of the vertex function does not depend on the arbitrary momentum shift variables w and z. In the following sections we will calculate the vertex function for two different complete theories, the SM augmented by one of the two gauge symmetries, gauged baryon minus lepton number $U(1)_{B-L}$ (Section 2.4.2) and gauged baryon number $U(1)_B$ (Section 2.4.3), with the fermion content from Section 2.3.2.

2.4.2 The Vertex Function in Gauged Baryon minus Lepton Number

As explained in Section 2.3.1, the addition of right-handed neutrinos renders the fermion content of the SM anomaly free in gauged $B - L$. The relevant interaction Lagrangian of the Z'_{BL} is given by

$$\mathcal{L}_{\mathrm{BL}} = g_{BL}\left(\frac{1}{3}\overline{q}\gamma^\mu Z'_\mu q - \overline{\ell}\gamma^\mu Z'_\mu \ell - \overline{\nu}\gamma^\mu Z'_\mu \nu\right) , \tag{2.75}$$

where g_{BL} is the $B - L$ gauge coupling, q represents the up- and down-type quarks, ℓ the charged leptons and ν the neutrinos.

Summing over the contributions from all fermions f with masses m_f, electric charge Q_f^e, $B - L$ charge Q_f^{BL} and number of colours $N_c(f)$ we get the following expression for the vertex function for the decay width of $Z \to Z'_{BL}\,\gamma$

$$\Gamma(Z \to Z'_{BL}\gamma) = \frac{\alpha_{em}\alpha\alpha_{\mathrm{BL}}}{96\pi^2 c_W^2}\frac{m_{Z'}^2}{m_Z}\left(1 - \frac{m_{Z'}^4}{m_Z^4}\right) \times \tag{2.76}$$

$$\left|\sum_f \left[T_3(f)N_c(f)Q_f^e Q_f^{BL}\left(2m_f^2 C_0(m_f) + \frac{m_Z^2}{m_Z^2 - m_{Z'}^2}\left(B_0(m_Z^2, m_f) - B_0(m_{Z'}^2, m_f)\right)\right)\right]\right|^2 ,$$

where the weak isospin is given by $T_3(f) = +1$ for up-type quarks and -1 for down-type quarks and charged leptons. We also introduce the following notation

$$B_0(m_V^2, m_f) \equiv B_0(m_V^2, m_f, m_f) , \tag{2.77}$$

being the Passarino-Veltman bubble scalar loop function [177].

[9] Note that the vector like coupling to the Z boson does not actually have to vanish, but it does not contribute if $g_a^{Z'} = 0$, because of the number of γ^5 in the trace.

We can see from the structure of eq. (2.76) that for a generation of SM fermions with equal masses the induced partial decay width vanishes, since the prefactor, summing the charges over all fermions $\sum_f T_3(f) N_c(f) Q^e_f Q^{BL}_f$, adds up to zero – the anomaly cancels for each generation individually. Therefore, the largest contribution will come from the hierarchy within one generation, making it the third SM generation with the top and bottom quark and the tau lepton. This hierarchy within the third SM generation dominates the decay width, shown in Figure 2.4, while the other generations become relevant only for small $m_{Z'}$ masses (their contribution is below 10 % for $m_{Z'} \gtrsim 20\,\text{GeV}$). The hierarchies within the second and first generation generate the small bumps on top of the smooth curve that lie below $m_{Z'} \lesssim 10\,\text{GeV}$. These bumps are induced by the threshold behaviour of the lighter fermions, where the fermions in the loop become on-shell. They enhance the decay with by up to a factor of two compared to the contribution from the mass of the top quark.

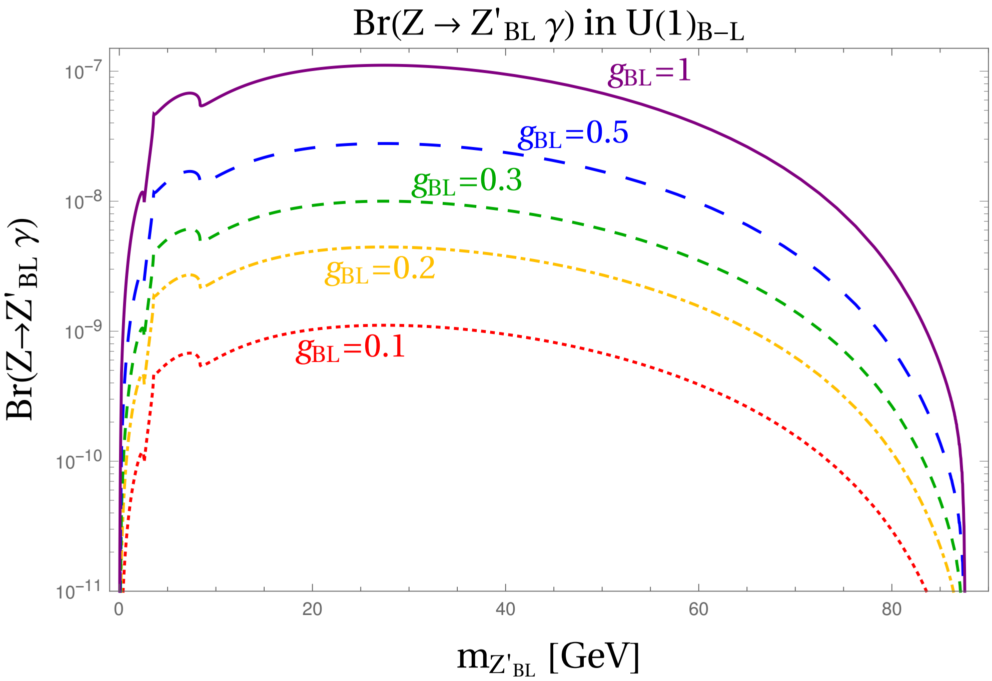

Figure 2.4: Branching fraction for $Z \to Z'_{BL}\gamma$ for various choices of g_{BL}. The mass of the top quark dominates the decay width, while the masses of the lighter SM fermions create small bumps at $m_{Z'} \lesssim 10\,\text{GeV}$.

An important feature of this model is the shared chiral symmetry of the fermions: the axial couplings are solely to the SM Z boson, while the couplings to the Z'_{BL} boson are vector like. This also leads to the ensured anomaly cancellation and a vanishing contribution to the width of a mass-degenerate generation of fermions. Furthermore, the expected behaviour of the width for vanishing $m_{Z'_{BL}}$, the Landau-Yang limit [180, 181] of a massive spin-1 particle decaying to two massless vector bosons, is obviously obeyed, it can be seen in eq. (2.76) and in Figure 2.4. In the next section we will, however, examine a model where the chiral structure is generated by two different symmetries and this will lead to an interesting behaviour.

2.4.3 The Vertex Function in Gauged Baryon Number

For the model of gauged baryon number we can theoretically pursue two different scenarios that have very distinct properties concerning their decoupling in the Z–Z'_B–γ vertex function. In the case where the $U(1)_B$ breaking Higgs generates the anomalon masses, the Z'_B and the anomalons share the same underlying scale and in the limit of small $m_{Z'_B}$ they cannot be integrated out and instead become part of the spectrum. If the masses of the anomalons were generated by the SM Higgs vev, they could decouple independently of the Z'_B mass throughout the entire $m_{Z'_B}$ mass range, since the gauge coupling setting the SM Z boson mass is small enough to allow for fermions in the theory that can be integrated out in the $Z \to Z'_B\gamma$ decay. In the $B-L$ case we saw already that the top quark is heavy enough to be effectively decoupled. For SM Higgs induced anomalon masses the calculation is analogous to the $B-L$ case above, as we explained in Section 2.3.2, but since the SM leptons and the anomalons do not necessarily share the same mass, the result will differ.

For both cases, the interaction Lagrangian for the SM quarks with the Z'_B boson is given by

$$\mathcal{L} \supset g_X \left(\frac{1}{3}\bar{q}\gamma^\mu Z'_{B,\mu} q\right) , \tag{2.78}$$

while the SM Z, the Z'_B and the electromagnetic currents for the anomalons are given in Section 2.3.2 for the different options of mass generation.

We will briefly discuss the case of SM Higgs induced masses first and show some plots for different anomalon mass values. Thereafter we will analyse the case of anomalon masses induced by the $U(1)_B$ breaking Higgs, where we will elaborate on the differences to the above case.

The B–L-like Case

As stated above, the calculation of the $Z \to Z'_B\gamma$ decay width in the case that the anomalon masses are generated by the SM Higgs is analogous to the $B-L$ case and the expressions for the widths are identical when replacing the $B-L$ coupling constant and the $B-L$ charges:

$$\Gamma(Z \to Z'_B\gamma) = \frac{\alpha_{\rm em}\alpha\alpha_X}{96\pi^2 c_W^2}\frac{m_{Z'}^2}{m_Z}\left(1-\frac{m_{Z'}^4}{m_Z^4}\right)\times \tag{2.79}$$

$$\left|\sum_f T_3(f)N_c(f)Q^e_f Q^B_f \left[2m_f^2 C_0(m_f) + \frac{m_Z^2}{m_Z^2 - m_{Z'}^2}\left(B_0(m_Z^2, m_f) - B_0(m_{Z'}^2, m_f)\right)\right]\right|^2 .$$

The weak isospin is given by $T_3(f) = +1$ for up-type quarks and the anomalon E_2 and $T_3(f) = -1$ for down-type quarks and E_1. For a degenerate set of fermions the prefactor $\sum_f T_3(f)N_c(f)Q^e_f Q^B_f$ again adds up to zero, but the intragenerational cancellation is absent, since the role of the three generations of SM leptons is played by the two states E_1 and E_2.

In Figure 2.5 we show the branching fraction for various choices of anomalon masses. The first case, where $m_{E_1} = m_{E_2} = 200\,\text{GeV}$, the top quark and both anomalons are effectively integrated out and the width is dominated by these three states, such that even the bumps of the other SM quarks are barely visible. In the second line both anomalon masses are at 40 GeV and 20 GeV, respectively, and are thus light enough to go on-shell at $m_{Z'_B} = 2\,m_E$. These points are visible as cusps and they lead to an increase in the branching fraction to up to 10^{-5} and the impact of the lighter quarks are again not noticeable. In the last line we chose two different masses for the anomalons, $m_{E_1} = 15\,\text{GeV}$ and $m_{E_2} = 40\,\text{GeV}$, and they cause two bumps in the spectrum, as expected. The last plot shows the analogue to the $B - L$ case, where we chose tiny anomalon masses of order $\mathcal{O}(0.1\,\text{MeV})$. The branching fraction becomes smaller, since it is mostly induced only by the integrated out top quark, and the cusps of the lighter quarks can be seen where they become on-shell, as before. The missing tau lepton, which is heavy enough to appear in the $B - L$ case, makes the bump structure look slightly different.

Note that we do not include any experimental limits in these plots, since we study this scenario solely for illustrative purposes. For larger anomalon masses, *i.e.* Yukawa couplings, this scenario is excluded by the value of the $H \to \gamma\gamma$ measured at the LHC [170], for masses below about 90 GeV new weakly coupled charged fermions are excluded by measurements at LEP [151, 152]. This excludes basically the whole parameter space of this scenario.

Anomalon Masses Generated by the New Higgs

Now we want to discuss the case where the masses of the anomalons are generated by the $U(1)_B$ breaking Higgs and thus there are two types of fermions in the theory: the SM quarks that have axial vector couplings to the SM Z boson and the anomalons that are vector like under the SM symmetries, but couple axially to the Z'_B boson.

When we assume that the anomalons are degenerate with masses M, we can calculate the $Z \to Z'_B\gamma$ decay width to be

$$\Gamma(Z \to Z'_B\gamma) = \frac{\alpha_{\text{em}}\alpha\alpha_X}{96\pi^2 c_W^2}\frac{m'^2_Z}{m_Z}\left(1 - \frac{m^4_{Z'}}{m^4_Z}\right).$$

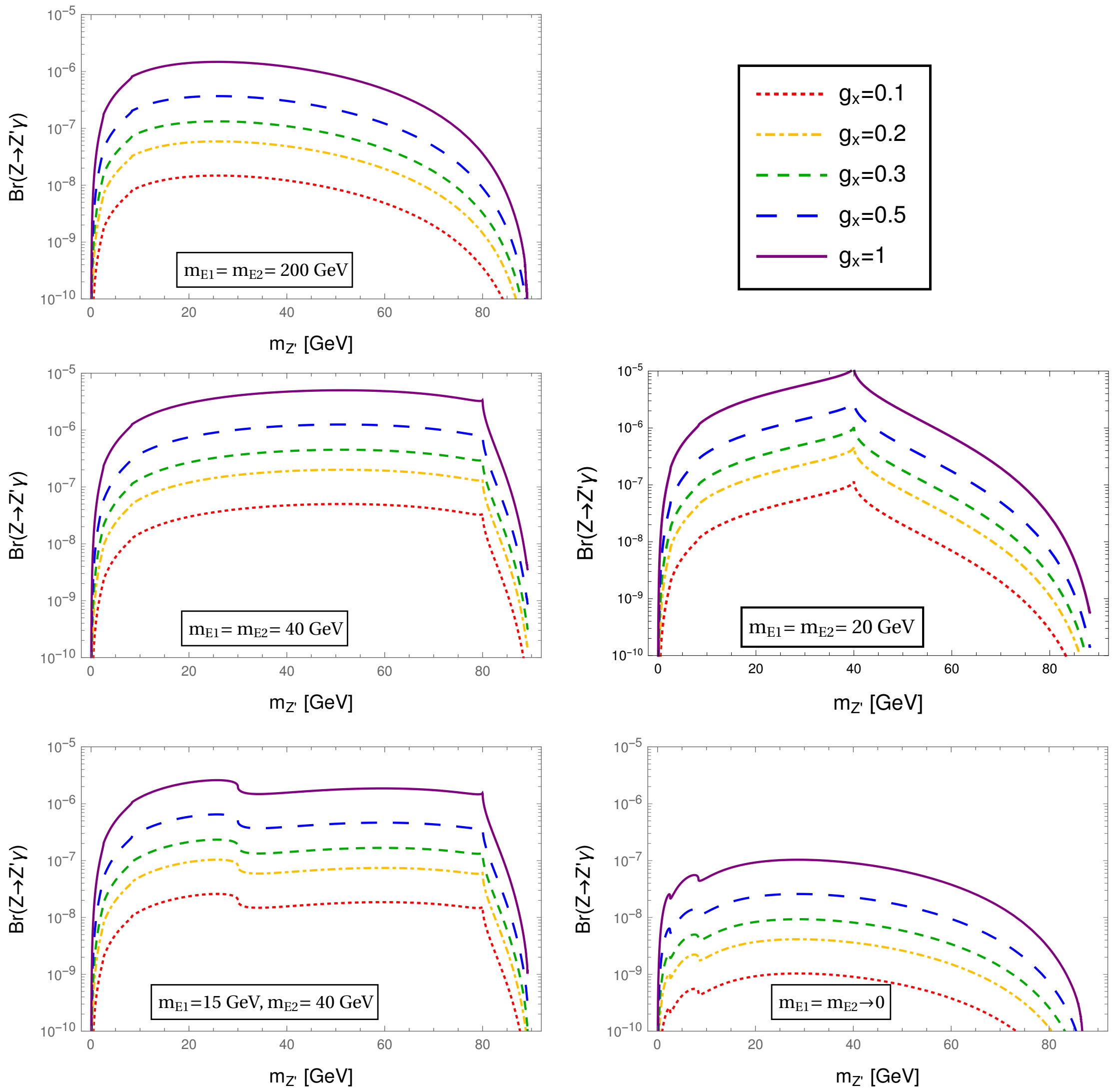

Figure 2.5: Branching fraction for the decay $Z \to Z'\gamma$ in $U(1)_B$, where the masses of the anomalons E_1 and E_2 are generated by the SM Higgs, each plotted for five different values of the gauge coupling g_X. The plots differ by the choice of the anomalon masses, while the quark masses remain fixed to their SM values. In the first plot the anomalon masses are above the scale of the process, we chose $m_{E_1} = m_{E_2} = 200\,\text{GeV}$. For smaller values of anomalon masses they can become on-shell at $m_{Z'_B} = 2\,m_E$, resulting in a bump in the spectrum. When the anomalons are not degenerate, here $m_{E_1} = 15\,\text{GeV}$ and $m_{E_2} = 40\,\text{GeV}$, two cusps are visible where they become on-shell. For the limit of very small anomalon masses the width becomes analogous to the $B - L$ case, where it is dominated by the mass of the top quark and we can see the bumps of the charm and bottom quarks.

$$\left| - \sum_{f\in\,\mathrm{SM}} T_3(f) Q_f^e \left[\frac{m_Z^2}{m_Z^2 - m_{Z'}^2} \left(B_0(m_Z^2, m_f) - B_0(m_{Z'}^2, m_f) \right) + 2m_f^2 C_0(m_f) \right] \right.$$
$$\left. +3 \left(\frac{m_Z^2}{m_Z^2 - m_{Z'}^2} \left(B_0(m_Z^2, M) - B_0(m_{Z'}^2, M) \right) + 2M^2 \frac{m_Z^2}{m_{Z'}^2} C_0(M) \right) \right|^2 , \qquad (2.80)$$

where we sum over all SM quarks and the weak isospin $T_3(f)$ is again $T_3(f) = +1$ for up-type quarks and -1 for down-type quarks. As required, the w and z dependence drops out and the width can be calculated unambiguously, because we consider an anomaly free theory. Note that since the top quark and the anomalons dominate this width, the masses of the other five quarks have a minimal impact and we can set all of them to $\mathcal{O}(1)$ MeV, which agrees with the exact result to better than 1% precision.

The experimental limits on new weakly coupled states are quite severe – for masses below 90 GeV they are excluded entirely by measurements at LEP [151, 152] – we will therefore set both anomalon masses to their maximal value. Since the vev of the $U(1)_B$ breaking Higgs is fixed when choosing a set of parameters $m_{Z'_B}$ and g_X (because $m_{Z'_B} = 3g_X v_\Phi$), the masses of the anomalons are limited by the largest possible Yukawa coupling. We generally take their mass to be $M = M_{max} = (4\pi/3)v_\Phi/\sqrt{2}$, which fixes the Yukawa couplings to be $y_E = y_L = 4\pi/3$, and show the resulting branching fraction $Z \to Z'_B\gamma$ in Figure 2.6 for g_X between 0.1 and 1 versus the mass $m_{Z'_B}$ and the vev v_Φ, respectively.

Since the mass of the anomalons (fixed by their Yukawa coupling) decreases, the smaller the mass $m_{Z'_B}$ becomes, we mark the point where they equal 90 GeV with a dot. The branching fraction left of these dots is excluded because the anomalons become too light and would have been detected at LEP by L3 and ALEPH [151,152]. For $g_X = 1$ this limit excludes the entire parameter space. The largest possible value for the branching fraction in this scenario is then at most $\mathcal{O}(\text{few}) \times 10^{-5}$. Furthermore we include the direct limit on the branching fraction $Z \to Z'\gamma$, where Z' decays hadronically, which has been measured by L3 at LEP [182, 183]. It is shown in grey for the plot versus $m_{Z'_B}$ and in purple ($g_X = 1$) and red ($g_X = 0.1$) for the plot versus the vev v_Φ, where the limit varies with g_X. This limit is viable when the Z'_B boson dominantly decays to a dijet resonance, which is true when it is heavier than the pion $m_{Z'_B} \gtrsim m_\pi$ [139, 184], provided that the anomalons are heavier than the Z'_B boson.

Note again the cusp behaviour of the curves, where the anomalons become on-shell. In this case the position of these maxima are given by the relation of anomalon masses with the SM Z boson mass $2M = m_Z$, since the relation between the mass of the Z'_B boson $m_{Z'_B}$ and the anomalon masses M is here fixed. The maxima are, however, positioned in the excluded region because $m_Z/2 < 90$ GeV.

The strict correlation between (maximal) anomalon masses M and the mass of the Z'_B boson could be alleviated if the masses of the anomalons were generated by a combination of contributions from the SM Higgs and the $U(1)_B$ breaking Higgs. For a certain range of Yukawa couplings this scenario evades the limits by the $H \to \gamma\gamma$ signal strength, as we

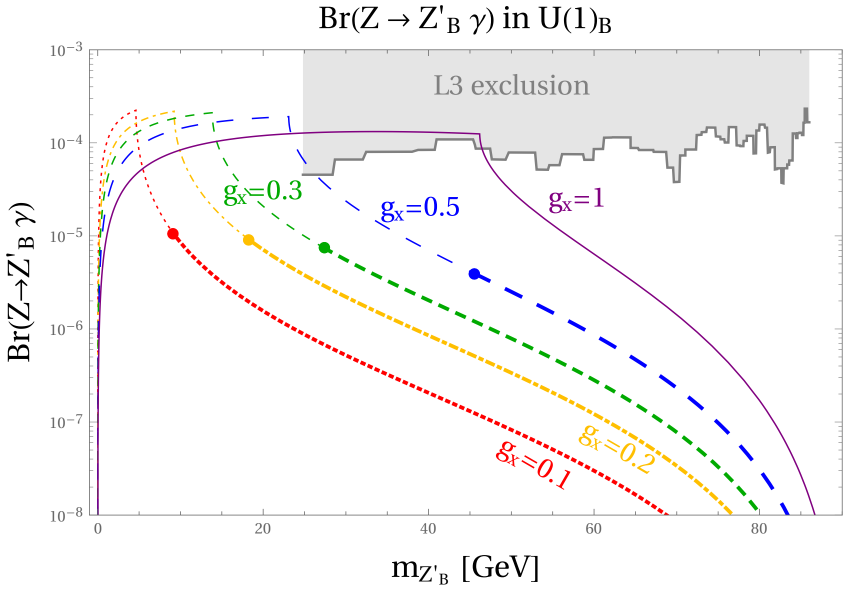

(a) Branching fraction $Z \to Z'_B\gamma$ versus $m_{Z'}$.

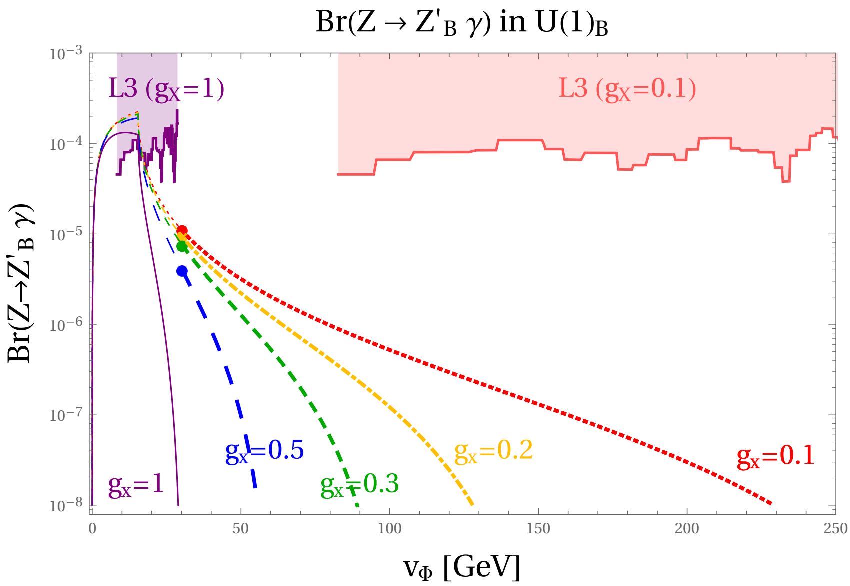

(b) Branching fraction $Z \to Z'_B\gamma$ versus v_Φ.

Figure 2.6: Branching fraction for the decay $Z \to Z'_B\gamma$ for various g_X. Both anomalon masses M are set to a maximum value of $(4\pi/3)v_\Phi/\sqrt{2}$. The coloured dots mark the points where these masses are equal to the LEP limit of 90 GeV [151, 152], implying that the parameter space left of the dots is excluded. (For $g_X = 1$ the dot lies outside the plot range and all the parameter space is excluded.) The grey (purple and red) shaded region constitutes the branching fraction which is excluded by the L3 search for the decay $Z \to (jj)_{\text{res}} + \gamma$ [182]. It is g_X dependent for the plot versus the vev v_Φ.

will see in Section 2.5. If the dominant part of the mass is generated by the new Higgs, there can be considerable contributions from the SM Higgs as well, such that branching fractions up to $\mathrm{Br}(Z \to Z'_B\gamma) \sim 10^{-5}$ could be induced.

Finally, we remark that the branching fractions in Figure 2.6 show a turnover, ensuring that the Landau-Yang behaviour [180, 181] of the decay of a massive vector to two massless vectors is obeyed in the limit of $m_{Z'_B} \to 0$. The peaks move to smaller Z'_B masses for smaller gauge couplings g_X, where the masses of the anomalons are larger. We will see in Section 2.7 that for an effective calculation, assuming the anomalons to be decoupled over the entire range of $m_{Z'_B}$, there will be no turnover and the branching fraction diverges in the limit of small $m_{Z'_B}$.

If the LEP constraint on the masses of new charged weakly-coupled fermions were relaxed to smaller values[10] the branching fraction of $Z \to Z'_B\gamma$ could even become as high as $\mathcal{O}(\text{few}) \times 10^{-4}$, where LEP experiments [182, 183] searching for the exotic decay of $Z \to Z'\gamma$ (Z' decaying hadronically) already exclude some of the parameter space. At the LHC there is so far no search for a $jj + \gamma$ resonance from the SM Z boson and hadronic decays of a light Z' are more challenging to reconstruct. The resonance is, however, an interesting feature that could make the reconstruction of a relatively light, hadronically decaying Z' possible. Similarly one could use the $Z \to Z'\gamma$ decay to search for a leptonically decaying Z' boson at the LHC, where limits on the branching fraction of order 10^{-5} from the OPAL collaboration [186] could be improved.

Non Decoupling Furthermore we want to comment on the non-decoupling feature of the decay width in eq. (2.80). We saw for the case of $U(1)_{B-L}$ and for the SM Higgs induced mass case for $U(1)_B$ that a degenerate and anomaly free set of fermions do not contribute to the decay width of $Z \to Z'\gamma$. In contrast, in the case where the anomalon masses are generated by the $U(1)_B$ breaking Higgs Φ, the contribution to the width of an anomaly free set of degenerate fermions does not cancel. It is possible, whenever the axial vector couplings of the fermions are in two distinct vertices, as pointed out in Ref. [172]. The decay width in eq. (2.80) simplifies, when we set all quark and anomalon masses to the same value m, to the following expression (the superscript deg indicates that all fermions are degenerate):

$$\Gamma(Z \to Z'_B\gamma)^{\mathrm{deg}} = \frac{3\,\alpha_{\mathrm{em}}\alpha\alpha_X}{8\,\pi^2 c_W^2}\frac{(m_Z^2 - m_{Z'}^2)^2}{m_Z m_{Z'}^2}\left(1 - \frac{m_{Z'}^4}{m_Z^4}\right)\left|m^2 C_0(m)\right|^2 \ . \tag{2.81}$$

Taking the $\lim_{m\to\infty}$ limit of the Passarino-Veltman scalar loop function, see eq. (2.69), the width becomes for a set of very heavy fermions

$$\lim_{m\to\infty}\Gamma(Z \to Z'_B\gamma)^{\mathrm{deg}} = \frac{3\,\alpha_{\mathrm{em}}\alpha\alpha_X}{32\,\pi^2 c_W^2}\frac{(m_Z^2 - m_{Z'}^2)^2}{m_Z m_{Z'}^2}\left(1 - \frac{m_{Z'}^4}{m_Z^4}\right) . \tag{2.82}$$

[10] Ref. [185] considers possible models.

In this particular scenario the heavy fermions would include those, whose masses are generated by the SM Higgs, and it is thus certainly not viable. It shows, however, that it is not in general true, that an anomaly free set of degenerate fermions decouples – in a theory with two sources of chiral symmetry breaking. Instead, the decoupling is intimately tied to the axial coupling structure, and thus the mass generation, of the involved fermions. Depending on the axial vector and vector charges of the fermions, the contribution of an anomaly free set of fermions can add up to zero, but as in our case, it can also give a finite contribution. Details on the sum rules of the charges can be found in Ref. [172].

Varying the Anomalon Masses Finally, we want to look at the effect of varying the anomalon masses and then comparing this case to the SM Higgs induced masses before.

In Figure 2.7 we plot the branching fraction for the case of anomalon masses generated by the new Higgs. Note that these scenarios are almost completely excluded by the LEP searches for weakly charged new particles [151,152], again we study them for illustration. As before, the masses of the anomalons are varying with respect to $m_{Z'_B}$ since $m_{Z'_B} = 3g_X v_\Phi$ defines the value of the vev of the new Higgs and the highest possible mass is then given by the maximum Yukawa coupling $M_{max} = (4\pi/3)v_\Phi/\sqrt{2}$. The smaller $m_{Z'_B}$ becomes, the more decreases the vev v_Φ and the smaller become the anomalon masses. Therefore, we can never integrate the anomalons out over the whole spectrum of $m_{Z'_B}$ – as we could in the SM Higgs generated anomalon mass case – and we see their cusp at different points, depending on the Yukawa coupling and the value of g_X. The branching fraction is in this case here larger than in the SM Higgs induced case (note the different scales on the ordinate). It is highest for the case of maximal Yukawa couplings that we plotted in Figure 2.6, with a maximal branching fraction of $\mathcal{O}(\text{few}) \cdot 10^{-4}$, which is more than one order of magnitude larger.

Comparing the first plot with masses $m_E = m_L = 0.8\, M_{max}$ to the second (with $0.5\, M_{max}$) we can see that the smaller we choose the anomalon masses, the further right move the bumps. This is because the anomalons go on-shell at $M = m_Z/2$, which requires v_Φ to be larger for smaller anomalon Yukawas. In the third plot with $m_E = m_L = 0.1\, M_{max}$ the bump is visible only for the small gauge coupling of $g_X = 0.1$ and therefore the smallest (plotted) gauge coupling induces the largest branching fraction. The smaller the gauge coupling g_X, the bigger the vev v_Φ at a given mass $m_{Z'_B}$; this makes the anomalon mass larger for smaller g_X. Therefore, $M = m_Z/2$ is satisfied at smaller $m_{Z'_B}$ and thus further left in the plot. While for $m_E = m_L = 0.1\, M_{max}$ the on-shell condition is beyond the plot range for $g_X \geq 0.2$, it is still visible for $g_X = 0.1$. Note that the cusps at $g_X = 1$ are from the SM charm and bottom quark, which are also visible in the last plot. The fourth plot shows again the behaviour for two differing anomalon masses.

In the last plot we set the masses of the anomalons to be tiny and recover the $B - L$ case, as before. For negligible anomalon masses it thus does not make a difference which

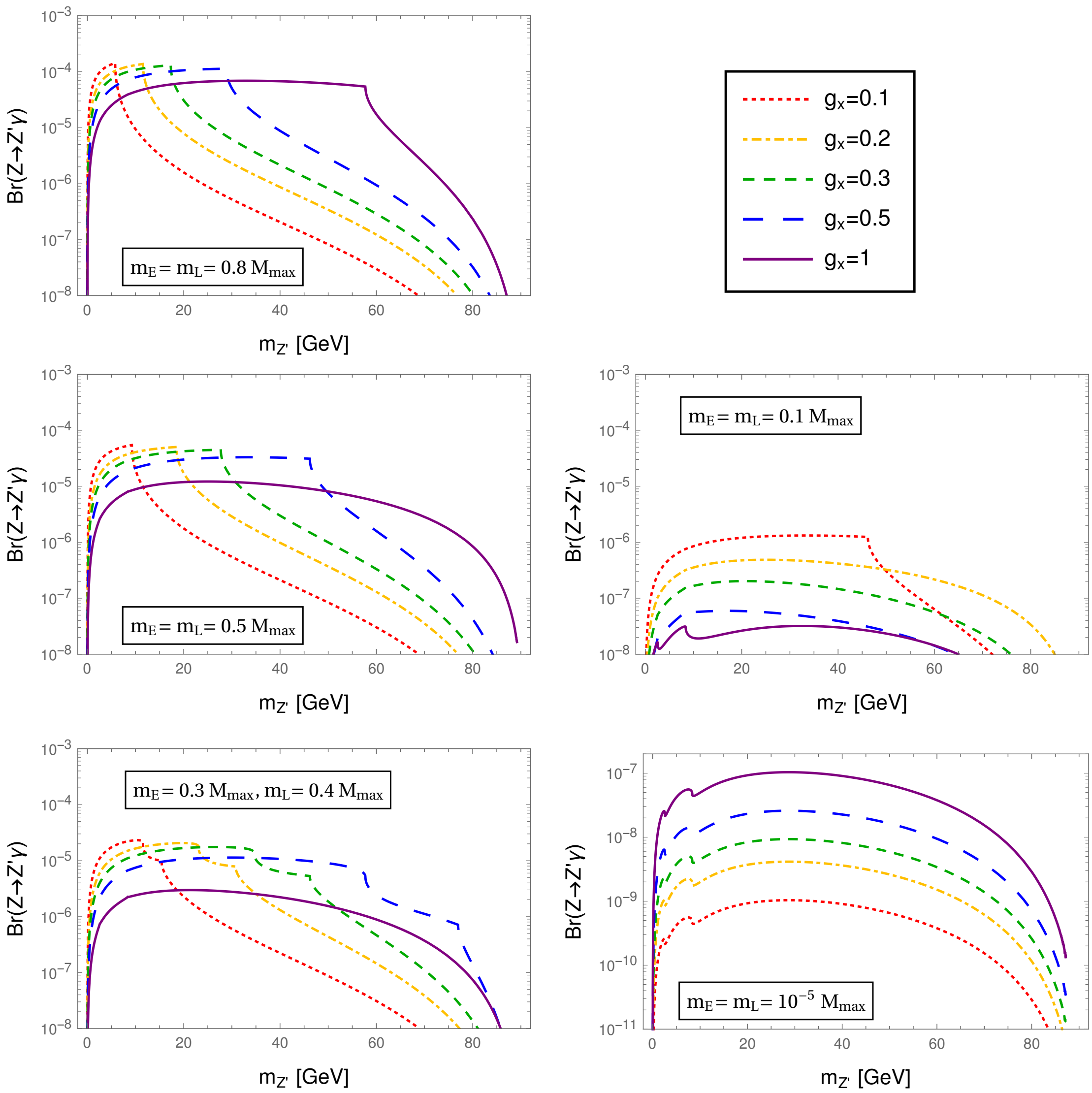

Figure 2.7: Branching fraction for the decay $Z \to Z'_B\gamma$ in $U(1)_B$, where the masses of the anomalons E and L are generated by the $U(1)_B$ breaking Higgs, each plotted for five different values of the gauge coupling g_X. The plots differ by the choice of the anomalon masses, defined relative to the maximum possible value $M_{max} = 4\pi/3 \cdot v_\Phi/\sqrt{2}$, while the quark masses remain fixed to their SM values. The first plot sets $m_E = m_L = 0.8\, M_{max}$. In the second line the masses are chosen smaller, $m_E = m_L = 0.5\, M_{max}$, and $m_E = m_L = 0.1\, M_{max}$. In the last line we set them different from each other, $m_E = 0.3\, M_{max}$, $m_L = 0.4\, M_{max}$, where we can see two bumps when they go on-shell. In the last plot we set the masses to be tiny $m_E = m_L = 10^{-5}\, M_{max}$ (note the different scales on the ordinate) and recover the $B-L$ and the SM Higgs induced B case.

Higgs generates the masses, which is what we expect. For small anomalon masses the largest gauge coupling g_X also induces the largest branching fraction, which can be reversed for some plots because of the big influence of the cusp behavior of the width, where the anomalons become on-shell.

2.5 Collider Searches for Anomalons

In this section we want to comment on the collider phenomenology of the anomalons. Depending on their mass generation they can mimic a fourth generation of leptons (when their mass is generated by the SM Higgs) or the electroweakino sector from supersymmetry (when their mass is generated by the $U(1)_B$ breaking Higgs). When the charged anomalons are then slightly heavier than the neutral states, they show a compressed mass spectrum.

In the first case, or even when the SM Higgs vev v_H contributes partly to the mass generation of the anomalons, they alter the SM Higgs boson decay into two photons. This decay $H \to \gamma\gamma$ has then to be calculated as the coherent sum of all relevant contributions, namely from the top and bottom quark, the W boson, and the two charged anomalons.

To cover the general case of both Higgs bosons contributing to the mass generation, but to keep the parameter space small enough, we assume all Yukawa couplings to be real and set $y_E = y_L \equiv y_\Phi$ and $y_1 = y_2 \equiv y_H$. The mass Lagrangian for the charged anomalons thus reads

$$\mathcal{L}_{\text{mass}} \supset -\frac{y_\Phi}{\sqrt{2}} v_\Phi \bar{e}_L e_R - \frac{y_\Phi}{\sqrt{2}} v_\Phi \bar{E}_L E_R - \frac{y_H}{\sqrt{2}} v_H \bar{E}_L e_R - \frac{y_H}{\sqrt{2}} v_H \bar{e}_L E_R + \text{ h.c.}\,. \tag{2.83}$$

The masse are then given by

$$M_1 = \frac{1}{\sqrt{2}} \left(y_\Phi v_\Phi + y_H v_H \right) \,, \tag{2.84}$$

$$M_2 = \frac{1}{\sqrt{2}} \left| y_\Phi v_\Phi - y_H v_H \right| \,. \tag{2.85}$$

The Yukawa couplings of the two charged anomalons to the SM Higgs are therefore $\pm y_H$, but their masses depend also on the parameter y_Φ and the vev v_Φ.

Complementing the expression from Ref. [187] by the contributions of the two anomalons, the decay width for $H \to \gamma\gamma$ becomes

$$\Gamma(H \to \gamma\gamma) = \frac{G_F \alpha_{\text{em}}^2 M_H^3}{128\sqrt{2}\pi^3} \times \tag{2.86}$$
$$\left| \frac{4}{3} A_f(\tau_t) + \frac{1}{3} A_f(\tau_b) + A_V(\tau_W) + \frac{y_H v_H}{M_1\sqrt{2}} A_f(\tau_{M1}) - \frac{y_H v_H}{M_2\sqrt{2}} A_f(\tau_{M2}) \right|^2 \,,$$

G_F being the Fermi constant, $M_H = 125\,\text{GeV}$ the SM Higgs mass and α_{em} has to be taken at the energy scale of $q^2 = 0$, because of the real photons in the final state. The first and second contributions are given by the top and bottom quark (contributions from the other quarks are negligible), the third by the W boson loop, followed by the new contributions of the two charged anomalons. The loop functions for the fermions A_f and the W boson A_V are defined as

$$A_f(\tau_f) = \frac{2}{\tau_f^2}(\tau_f + (\tau_f - 1)f(\tau_f)) , \tag{2.87}$$

$$A_V(\tau_W) = -\frac{1}{\tau_W^2}(2\tau_W^2 + 3\tau_W + 3(2\tau_W - 1)f(\tau_W)) , \tag{2.88}$$

where the function $f(\tau)$ is

$$f(\tau) = \begin{cases} (\arcsin\sqrt{\tau})^2, & \tau \leq 1 \\ -\frac{1}{4}\left(\log\frac{1+\sqrt{1-\tau^{-1}}}{1-\sqrt{1-\tau^{-1}}} - i\pi\right)^2, & \tau > 1 \end{cases} \tag{2.89}$$

depending on the mass ratios τ to the SM Higgs mass: $\tau_{f,W} = \frac{M_H^2}{4m_{f,W}^2}$.

In Figure 2.8 we show how the decay rate of $H \to \gamma\gamma$ changes with the introduction of the two charged anomalons, as a function of the two Yukawa couplings $\pm y_H$ to the SM Higgs boson, and y_Φ to the $U(1)_B$ breaking Higgs Φ. The vev of the Higgs Φ is fixed to a value of $v_\Phi = 300\,\text{GeV}$. We normalise the decay rate including the anomalons to the SM value from the top and bottom quark and the W boson loops only. The gray band covers the region where the anomalon masses are below the LEP limit of 90 GeV [151, 152] and is thus excluded. The hatched regions are the two sigma exclusion limits on the $H \to \gamma\gamma$ rate at ATLAS [188]. They measure a signal strength of

$$\mu(gg \to H \to \gamma\gamma) = 0.99^{+0.15}_{-0.14} , \tag{2.90}$$

including the 1 σ uncertainties. The anomalons affect the $H \to \gamma\gamma$ rate only mildly and there is a lot of open parameter space when y_Φ dominates over y_H. The searches for the charged anomalons at LEP cover again big parts of the parameter space at smaller y_Φ, making direct searches the most promising avenue to test this parameter space. At very small y_Φ but high y_H there is also some parameter space allowed by the $H \to \gamma\gamma$ limits, but we expect electroweak precision measurements to exclude this open region.

If loop corrections make the electrically neutral anomalon states ν and N slightly lighter than the charged states e and E, our model would be analogous to the supersymmetric electroweakino and slepton searches. The signatures from these decays include soft leptons [189–191] and are therefore very hard to detect at LHC experiments. Because of the $SU(2)$ charges of the anomalons, electroweak Drell-Yan production rates are possible, but in the decay of the charged anomalon small mass splittings would give very soft leptons or pions with missing energy. This means that there could even be no limit from LHC experiments [191] and LEP experiments would give the only limits. Even these LEP limits can be relaxed in certain more complicated scenarios, lowering the limit on new charged particles from about 90 GeV to about 75 GeV [185].

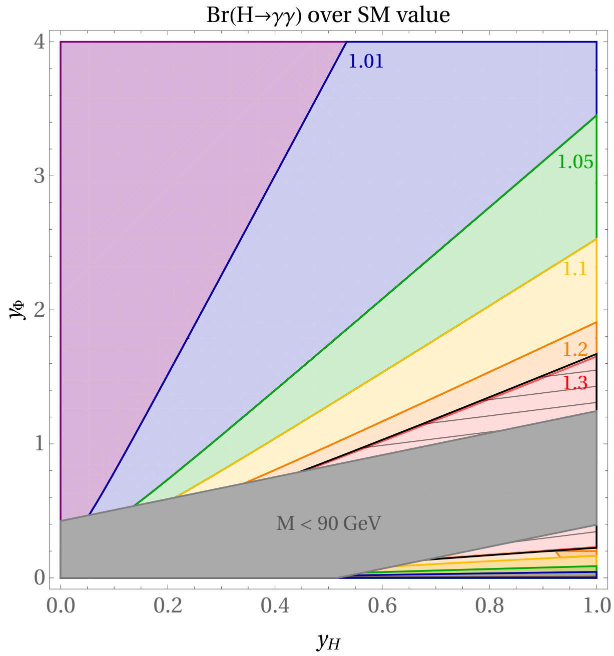

Figure 2.8: Normalised $H \to \gamma\gamma$ branching fraction including both charged anomalons, $\pm y_H$ being their coupling to the SM Higgs boson and y_Φ to the $U(1)_B$ breaking Higgs. We chose a value for the new vev of $v_\Phi = 300\,\mathrm{GeV}$. The region where one of the charged anomalon masses is below the LEP bound of 90 GeV [151, 152] is marked by the grey band. The hatched regions are the two sigma exclusion limits as measured by ATLAS [188].

2.6 Coupling-Mass Constraint for Gauged Baryon Number

Now we want to give an overview for the $U(1)_B$ model on Z'_B boson searches for masses $m_{Z'_B}$ below the SM Z boson mass, we summarise the searches in Figure 2.9.

The constraint marked "L3" (solid green) in Figure 2.9 is derived from eq. (2.80) using the limit on the $Z \to Z'\gamma$, $Z' \to jj$ decay rate by the L3 experiment [182]. The anomalon masses are determined by their Yukawa coupling that we set to $4\pi/3$ and for the top quark mass we use the SM value, while the other quark masses are set to be of order MeV. Note that when we solve the branching fraction at a certain mass point $m_{Z'_B}$ for the value of the gauge coupling g_X, we get two values for g_X. The limit is given by the smaller value, but in the case of a discovery, this ambiguity would have to be resolved by an independent measurement.

We project this $Z \to (jj)\gamma$ resonance search for a potential TeraZ factory at the FCC-ee (light, dotted green), where we extrapolate the limit from the L3 experiment accounting for the increase in statistics: the expected number of Z bosons is 3×10^{12} in four years of runtime of the FCC-ee [192], while LEP produced 1.7×10^7 Z bosons [193].

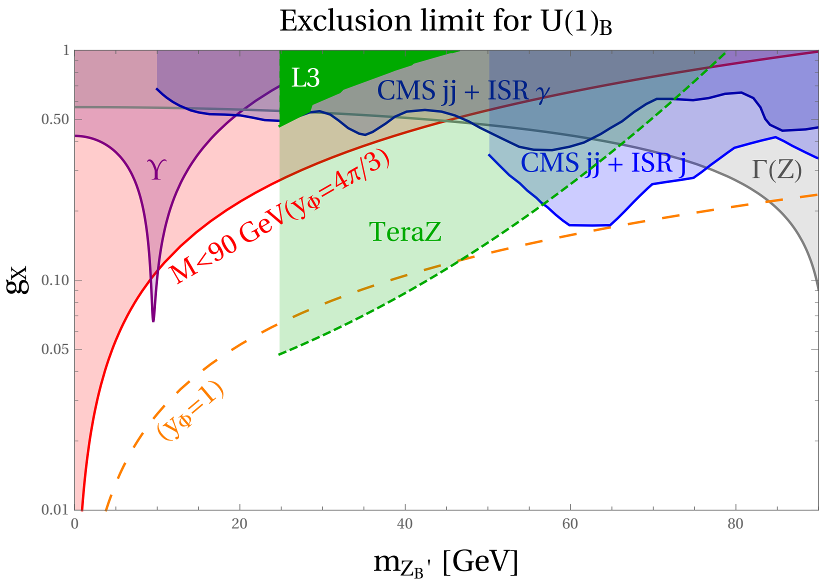

Figure 2.9: $U(1)_B$ exclusion limits in the g_X, $m_{Z'_B}$ plane. The L3 limit from measurements of the $Z \to (jj)\gamma$ decay rate [182] calculated from eq. (2.80) is shown in solid green, a projection for a TeraZ factory in lighter green. We plot the direct bound on the charged anomalon masses ($M < 90\,\text{GeV}$) from LEP searches [151, 152] for a Yukawa coupling of $y_\Phi = 4\pi/3$ (in red), which is the value we use for the calculations. We include the same limit for a Yukawa coupling of $y_\Phi = 1$ (yellow, dashed) for comparison. The limits from the decay of the Υ (in purple) and from the width of the SM Z boson (in gray) are taken from Ref. [169]. The low-mass dijet resonance search from CMS (darker blue) is based on a dijet resonance and an ISR photon [194], while the "CMS jj + ISR j" search (lighter blue) is based on jet substructure and an ISR jet [195].

The sensitivity is assumed to increase only from statistics, possible improvements in mass reach and an analysis of backgrounds and systematic uncertainties are omitted.

The LEP constraints on new charged particles to be heavier than at least 90 GeV [151, 152] is shown in Figure 2.9 for two values of anomalon Yukawa couplings. $y_\Phi = 4\pi/3$ (red) is the value we use for the calculations of the L3 and TeraZ limit, $y_\Phi = 1$ is shown as a reference (yellow, dashed). Note that we assume here that the anomalon masses are entirely generated by the $U(1)_B$ breaking Higgs, a possible contribution from the SM Higgs could alleviate these bounds. As we have shown in Figure 2.8 the SM Higgs Yukawa coupling y_H can be non-zero and thus increase the anomalon masses, for a coupling $y_\Phi = 4\pi/3$ it can even be up to $y_H = 1$. This would weaken the direct anomalon mass bounds, but leave the other bounds unchanged.

We show in Figure 2.9 also the constraint from the Υ search by the ARGUS collaboration [196] (in purple). They measured the ratio of hadronic decays of the Υ compared to the muonic decay, $R_\Upsilon = \Gamma(\Upsilon \to \text{ hadrons})/\Gamma(\Upsilon \to \mu^+\mu^-) < 2.1$. The corresponding limit is taken from Refs. [169, 197]. Quarks induce a mixing of the Z'_B boson with the SM Z boson through loops, which is constrained by measurements of the Z boson width [169, 197–200]. We take this contraint from Ref. [169], it is marked "$\Gamma(Z)$" (in grey). For very small masses $m_{Z'_B} \lesssim 1\,\text{GeV}$ see Ref. [201] for a broader overview on kinetic mixing constraints.

Furthermore we include dijet resonance searches by the CMS experiment at the LHC. The search using an ISR photon as a trigger [194] ("CMS jj + ISR γ", darker blue) covers a large region up to small Z'_B masses, while the search triggered by an ISR jet [195] that uses a jet substructure analysis ("CMS jj + ISR j", lighter blue), is stronger but sets in at higher Z'_B masses.

We want to remark that within all of these constraints, the $Z \to Z'_B\gamma$ decay is an irreducible probe of the model of gauged baryon number for $m_{Z'_B} < m_Z$. Unlike the direct anomalon searches it is independent of the decay channels of the anomalons, which are very model dependent. Because the SM fermion content is anomalous under the $U(1)_B$ gauge symmetry, the (heavy) anomalons have to cancel this anomaly and the $Z \to Z'_B\gamma$ decay rate will be sensitive to their anomaly coefficient. In an effective theory, the gauge coupling g_X and the mass of the Z'_B are then the only continuous parameters, since the anomaly coefficient of any global $U(1)$ symmetry of the SM is necessarily discrete. This gives a strong motivation for future searches of the $Z \to Z'_B\gamma$ exotic decay.

2.7 Comparison to Effective Result

When gauging an anomalous symmetry, as in the case of gauged baryon number, the theory can be fixed either through the introduction of anomaly cancelling fermions or by Wess-Zumino terms. We saw in Section 2.4.1 how a Wess-Zumino Lagrangian contributes to the divergences in the different vertices. Here, we want to use the Wess-Zumino description, specifically eq. (2.71), to calculate an effective result for the $Z \to Z'_B\gamma$ decay width and compare its validity to our full calculation. Additionally, we want to compare to the calculation performed in Refs. [141, 143], where Wess-Zumino terms are used to obtain the longitudinal Goldstone boson equivalent part of the decay width. We will reproduce the decay width from Refs. [141, 143] using Goldstone boson equivalence, starting from a Wess-Zumino Lagrangian (eq. (2.70)) and also modify our full result, eq. (2.80), to analyse the different approximations of the effective calculation and their validity.

The Wess-Zumino terms cancelling an anomaly in the electroweak sector are

$$\mathcal{L}_{\text{WZ}} = C_B g_X g'^2 \epsilon^{\mu\nu\rho\sigma} Z'_\mu B_\nu \partial_\rho B_\sigma - C_B g_X g^2 \epsilon^{\mu\nu\rho\sigma} Z'_\mu (W^a_\nu \partial_\rho W^a_\sigma + \frac{1}{3} g \epsilon^{abc} W^a_\nu W^b_\rho W^c_\sigma)\,, \tag{2.91}$$

where we already set the Wilson coefficients C_B such that the electromagnetic gauge symmetry is safe. B is, as before, the SM hypercharge field, W^a are the weak gauge fields and Z' is the gauge field of the new $U(1)$ gauge symmetry. This ansatz cannot be valid over the entire range of $m_{Z'}$ masses if the mass generation of the anomalons is coupled to the $U(1)_B$ breaking scale, as we saw in the last section. But in a certain parameter region, where the $U(1)_B$ gauge coupling g_X is small and the anomalon masses can therefore be large even for small gauge boson masses, the effective calculation should be valid. But we have to be careful, since for $m_{Z'} \to 0$, the anomalons will go on-shell, since their masses are fixed via their Yukawa coupling and the vev v_Φ, leading to the cusp and recovering of the Landau-Yang limit – exactly in the regime of applicability of the Goldstone boson equivalence.

To analyse the longitudinal enhancement of the decay width, as obtained in Refs. [141, 143], we use the Goldstone boson equivalence theorem to isolate the longitudinal polarisation of the Z' boson. We calculated the contribution of these Wess-Zumino terms to the Z–Z'–γ vertex already in eq. (2.71), replacing the Z' boson with the corresponding Goldstone pseudoscalar $Z'_\mu \to \partial_\mu \varphi/(g_X f_{Z'})$, where φ couples derivatively and is linearly realised, and integrating by parts gives the longitudinally equivalent Lagrangian:

$$\mathcal{L} \supset C_B \frac{\varphi}{f_{Z'}} \cdot g g' Z_{\mu\nu} \tilde{F}^{\mu\nu} \,. \tag{2.92}$$

We define the pseudoscalar decay constant as $f_{Z'} = m_{Z'}/g_X$ and $\tilde{F}^{\mu\nu} = (1/2)\,\epsilon^{\mu\nu\rho\sigma} F_{\rho\sigma}$ is the dual electromagnetic field tensor. To cancel the anomaly of the SM fermions introduced by gauging the baryon number symmetry we choose the Wilson coefficient to be $C_B = \mathcal{A}_{Z'BB}/(16\pi^2)$, where $\mathcal{A}_{Z'BB} = 3/2$ is the baryon number anomaly coefficient [137]. Note that comparing to Refs. [141, 143] the Lagrangian is a factor of two smaller, since we did not include the SM fermion contribution into this effective ansatz. We will see the impact thereof later. It reflects two different interpretations of the Goldstone boson equivalence approach: when the Z' boson is replaced in the resolved vertex function, the Z' Goldstone couples to the anomalons only; when the Z' boson is replaced on operator level, the Goldstone also couples to the SM fermions (and we obtain an effective factor of two).

The Goldstone boson equivalence theorem is valid in the limit of small $m_{Z'}$ and g_X, while their ratio $f_{Z'}$ has to remain constant. It neglects the transverse mode of the Z' boson and is therefore expected to break down for growing $m_{Z'}$.

From the Lagrangian in eq. (2.92), we can then calculate the decay width of $Z \to \varphi\gamma$:

$$\begin{aligned}\Gamma_{GBE} &= \frac{1}{24\pi} C_B^2 \frac{e_{\text{em}}^2 g^2}{c_W^2} \frac{m_Z^3}{f_{Z'}^2} \left(1 - \frac{m_\varphi^2}{m_Z^2}\right)^3 \\ &\approx \frac{1}{24\pi} C_B^2 \frac{e_{\text{em}}^2 g^2}{c_W^2} \frac{m_Z^3}{f_{Z'}^2}\end{aligned}$$

$$= \frac{3e_{\mathrm{em}}^2 g^2 g_X^2}{8192\pi^5 c_W^2} \frac{m_Z^3}{m_{Z'}^2} \,, \tag{2.93}$$

in the second line we approximated the Goldstone mass $m_{Z'}$ to be small compared to the Z boson mass and in the last line we set the Wilson coefficient C_B such that it cancels the SM $U(1)_B$ anomaly.

2.7.1 Reproducing the Effective Ansatz from the Full Calculation

In order to analyse the simplifications that are needed to obtain the effective Goldstone boson equivalent width in eq. (2.93) we will explain the impact of the different approximations on the full expression in eq. (2.80). The points that we will focus on are

- integrating out the anomalons in the calculation of the width and comparing this effective result to the Wess-Zumino terms,
- the contribution of the SM fermions,
- the reconstruction of the width calculated with Goldstone boson equivalence from the full calculation.

To decouple the anomalons, let us look at the generalised Ward identities that we calculated in Section 2.4.1, eq. (2.65) to (2.67). Considering the anomalons with vector like couplings to the SM Z boson and axial vector couplings to the Z_B' boson from Table 2.2, taking their masses to infinity $\lim\limits_{m\to\infty} m^2 C_0(m) = -1/2$ and summing up their contributions to the Ward identities we obtain

$$(p_{1\mu} + p_{2\mu})\,\Gamma^{\mu\nu\rho} = \frac{3e_{\mathrm{em}} g g_X}{16\pi^2 c_W} \epsilon^{\nu\rho|p_1||p_2|}(w - z)\,, \tag{2.94}$$

$$-p_{1\nu}\Gamma^{\mu\nu\rho} = \frac{3e_{\mathrm{em}} g g_X}{16\pi^2 c_W} \epsilon^{\mu\rho|p_1||p_2|}(w + 1)\,, \tag{2.95}$$

$$-p_{2\rho}\Gamma^{\mu\nu\rho} = \frac{3e_{\mathrm{em}} g g_X}{16\pi^2 c_W} \epsilon^{\mu\nu|p_1||p_2|}(z + 1)\,. \tag{2.96}$$

For the case of SM Higgs generated masses the prefactors remain identical, only the structure of the momentum shift variables changes to $(w - z - 2)$, $(w - 1)$ and $(z + 1)$, respectively.

In eq. (2.72) to (2.72) we calculated the Ward identity structure introduced by the Wess-Zumino terms (2.70). Matching this structure requires for the case of anomalons with axial vector couplings to the Z_B' boson that the momentum shift variables obey $2z = w-1$ and the Wilson coefficient becomes $C_B = 3(z+1)/(16\pi^2)$. This shows that the momentum shift dependence in the SM fermion loop calculation for the decay $Z \to Z'\gamma$ is affecting the Wess-Zumino terms introduced to represent the anomaly cancelling physics in the UV.

For the case of axial vector couplings to the SM Z boson and vector like couplings to the Z'_B (SM Higgs induced masses) we get the condition $2z = w - 3$ to match the Wess-Zumino terms, while the Wilson coefficient is the same $C_B = 3(z+1)/(16\pi^2)$.

Let us now look at the contribution of the SM fermions to the Ward identities

$$(p_{1\mu} + p_{2\mu})\,\Gamma^{\mu\nu\rho} = -\frac{3e_{\text{em}}gg_X}{16\pi^2 c_W}\epsilon^{\nu\rho|p_1||p_2|}(w-z)\,, \tag{2.97}$$

$$-p_{1\nu}\Gamma^{\mu\nu\rho} = -\frac{3e_{\text{em}}gg_X}{16\pi^2 c_W}\epsilon^{\mu\rho|p_1||p_2|}(w-1)\,, \tag{2.98}$$

$$-p_{2\rho}\Gamma^{\mu\nu\rho} = -\frac{3e_{\text{em}}gg_X}{16\pi^2 c_W}\epsilon^{\mu\nu|p_1||p_2|}(z+1)\,, \tag{2.99}$$

where we consider all SM fermions to be massless. Note that in both cases, for SM Higgs and Φ induced anomalon masses, the sum of SM fermion and anomalon contributions to the photon vertex cancel out, independent of the shift parameters. In the case of Φ induced anomalon masses this is also true for the SM Z boson vertex, while the divergence in the Z'_B vertex is non-zero. For the case of SM Higgs induced masses we get a non-zero contribution in the SM Z boson vertex, while it vanishes for the Z'_B boson.

Now we want to reconstruct the width we calculated using the Goldstone boson equivalence theorem starting from the matrix elements in eqs. (2.57) and (2.58). We set the SM fermion masses to zero and the anomalon masses to infinity. To compare to the width from Goldstone boson equivalence we need to consider the longitudinal polarisation of the Z'_B boson only. Therefore we take from the usual polarisation sum $\sum \epsilon_\nu(p_1)\epsilon^*_\beta(p_1) = -g_{\nu\beta} + \frac{p_{1\nu}p_{1\beta}}{m^2_{Z'}}$ only the longitudinal part, *i.e.* $\frac{p_{1\nu}p_{1\beta}}{m^2_{Z'}}$. Then the momentum coupling of the Z'_B corresponds exactly to the derivatively coupled Goldstone boson from eq. (2.92). We obtain the following longitudinal decay width (expanded in powers of $m^2_{Z'}/m^2_Z$)

$$\Gamma(Z \to Z'_{B,\,\text{long}}\gamma) = \frac{3e^2_{\text{em}}g^2g^2_X m^3_Z}{2048\pi^5 c^2_W m^2_{Z'}}\left(1 + \mathcal{O}\left(\frac{m^2_{Z'}}{m^2_Z}\right)\right)^3 . \tag{2.100}$$

The result is a factor 4 larger than the width from Goldstone boson equivalence in eq. (2.93). This difference stems from the inclusion of the constant anomaly contribution from the SM fermions. Neglecting it, and setting the parameters w and z as explained above to match the Wess-Zumino description, we reproduce the width from Goldstone boson equivalence from our full calculation.

We have therefore established that taking the width obtained from Goldstone boson equivalence alone (when replacing the Z' in the resolved triangle vertex) does not reproduce a correct result for the decay width $\Gamma(Z \to Z'_B\gamma)$, since the constant piece from the SM fermions cannot be neglected. It confirms the inclusion of a factor two in the effective Lagrangian (2.92) from Refs. [141, 143].

To understand the impact of the different simplifications from the full calculation to the result from Goldstone boson equivalence, we plot the width for two values of the gauge

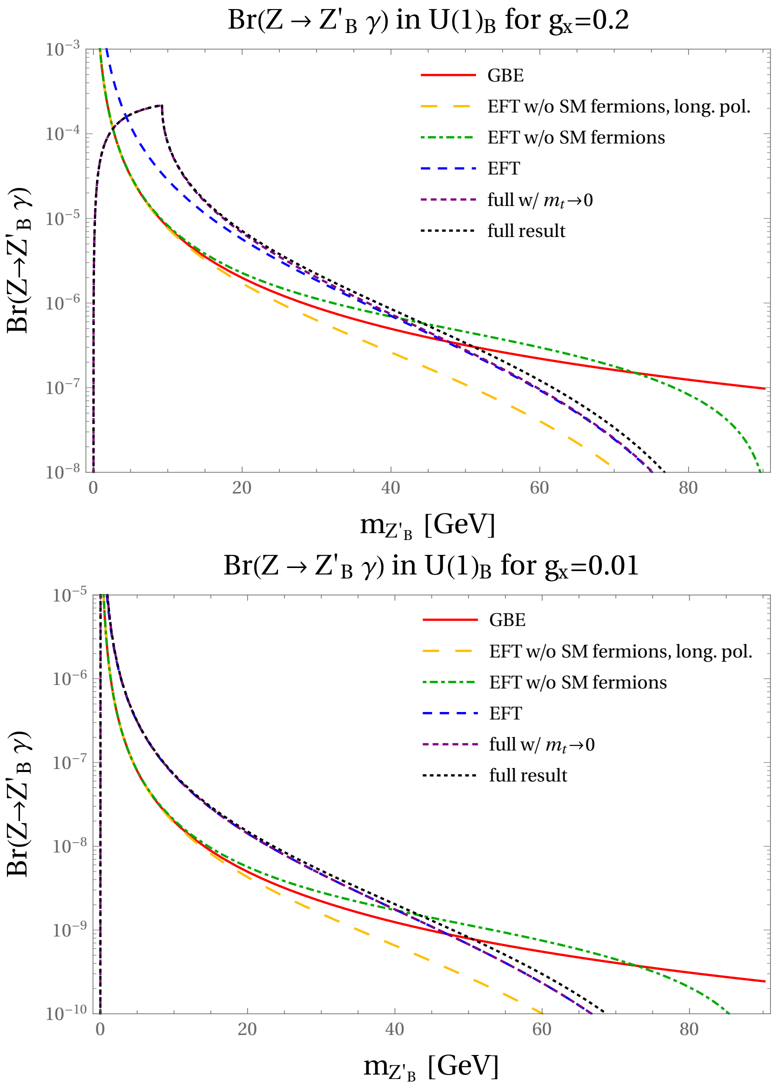

Figure 2.10: Branching fraction for the decay $Z \to Z'_B\gamma$ for two values of g_X. The "full result" (black, dotted) uses the full calculation in eq. (2.80) and sets the anomalon masses by the maximal value for the Yukawa couplings of $4\pi/3$, the SM value for the top quark mass m_t and sets the other quark masses to $\mathcal{O}(\text{MeV})$. In "full w/ $m_t \to 0$" the anomalon masses are still taken to be set by the maximal Yukawa coupling, but all quark masses are set to MeV. "EFT" (blue, medium dashed) includes the SM quarks (with masses $m_q \to 0$) and anomalons (with masses $M \to \infty$), while "EFT w/o SM fermions" (green, dot-dashed) takes the anomalons only with $M \to \infty$ and neglects the SM fermions altogether, setting w and z as described in the text. Neglecting then the transverse polarisation gives "EFT w/o SM fermions, long. pol." (yellow, large dashing). The red curve finally is the result from Goldsone boson equivalence, eq. (2.93), calculated from Wess-Zumino terms and neglecting SM fermions, the transverse polarisation of the Z'_B and approximates $m_Z \gg m_{Z'_B}$.

coupling g_X in Figure 2.10, successively implementing the necessary approximations. We choose a rather larger value, $g_X = 0.2$, and a smaller one, $g_X = 0.01$, to check the validity of the effective ansatz.

Beginning the discussion from the "full result" (black, dotted curve), we take the width from (2.80) with anomalon masses generated by the $U(1)_B$ breaking Higgs with $M_{\max} = 4\pi/3 \cdot v_\Phi/\sqrt{2}$, the SM value for the top quark mass, the other quark masses are approximated to be of order MeV. Approximating also the top quark mass to be of order MeV ("full result w/ $m_t \to 0$", purple, small dashing) has little impact on the branching fraction, it only decreases slightly for large Z'_B masses when we neglect the large value of the top quark mass. Both of these curves have a peak where the anomalons become on-shell and then turn over, recovering the Landau-Yang limit for $m_{Z'_B} \to 0$.

We reproduce an effective field theory ansatz ("EFT", blue, medium dashing) by integrating out the anomalons ($M \to \infty$) and assuming all SM quarks to be massless ($m_q \to 0$), which is a good approximation for small gauge couplings g_X, as expected. Deviations come from the top quark mass at higher $m_{Z'_B}$, as before, and the curve does not show a turnover for $m_{Z'_B} \to 0$, but diverges instead, making it invalid for very small Z'_B masses. With decreasing gauge coupling g_X, however, the range of validity of the effective ansatz increases.

In the next step we neglect all contributions from the SM fermions entirely, not only setting them to be massless, but also disregarding their constant anomaly piece. Therefore we calculate the width for the anomalons only, fixing the shift parameters w and z, as explained above, for the case of axial vector couplings to the Z'_B. The parameters are then $w = 2z + 1$ and $z = -3/2$, which reproduces the correct Wess-Zumino terms. The anomalons are also integrated out, $M \to \infty$, giving the curve "EFT w/o SM fermions" (green, dot-dashed). It shows that the anomaly contribution from the SM fermions cannot be neglected, the curve deviates from the full calculation and the EFT for small as well as large gauge couplings and over the whole range of Z'_B masses.

Taking the longitudinal polarisation only of the Z'_B ("EFT w/o SM fermions, long. pol.", yellow, large dashing), where we still neglect the SM fermions completely and the anomalons are integrated out, deviates for large Z'_B masses. The branching fraction becomes considerably smaller for masses $m_{Z'_B} \gtrsim 20\,\text{GeV}$ compared to the EFT result without SM fermions but including the full polarisation for Z'_B. This result is expected, as also the Goldstone boson equivalence is valid at an energy scale $\gg m_{Z'_B}$. Finally, the branching fraction from the Goldstone boson equivalence calculation ("GBE", red, solid) additionally expands in small $m_{Z'_B}$ compared to the Z boson mass, recuperating the overly steep fall of the branching fraction for longitudinal Z'_B only.

In summary, the most important finding is that we cannot neglect the constant anomaly piece from the SM fermions in the calculation. The EFT approach that includes the SM fermions is valid for a wide range of Z'_B masses, the smaller the gauge coupling g_X, the larger becomes the interval. The impact of the large mass of the top quark is actually rather small and only visible for larger Z'_B masses. Disregarding the constant anomaly contribution from the SM fermions, however, invalidates the calculation independent of the values of the gauge coupling g_X and the Z'_B gauge boson mass.

We therefore conclude that an effective calculation, using Wess-Zumino terms such as eq. (2.70) to represent the anomaly cancelling physics, is valid only if the SM fermions are also included in the calculations, leading to an additional factor 1/2 in eq. (2.92) [141,143]. For the SM fermion contribution the shift parameters w and z have to be chosen such that they match the Wilson coefficient C_B of the Wess-Zumino terms and the Wess-Zumino and SM fermion contributions have to be added up coherently.

Let us also comment on the case, where all fermions in the theory are chiral under the same symmetry, like in the case of gauged $B-L$ or like the hypothetical situation where the anomalon masses are generated by the SM Higgs, with an axial vector coupling in the Z vertex. If we want to integrate out a fermion in these theories and represent in by Wess-Zumino terms instead – like *e.g.* the top in gauged $B-L$ –, we analogously have to define the Wilson coefficient of the Wess-Zumino terms in coherence with the shift parameters w and z of the now anomalous remaining fermion content. Since in this scenario the symmetry breaking scale of the Z' boson is independent of the scalar that generates the fermion masses, the validity of the EFT is independent of the parameters of the $U(1)'$ symmetry, *i.e.* the gauge coupling and the mass of the Z' gauge boson.

Having analysed the validity of an effective treatment of the anomalon contribution and furthermore the Goldstone boson equivalence calculation, we want to comment on the determination of a limit on the $U(1)_B$ coupling constant g_X from the L3 measurement [182] of the $Z \to (jj)\gamma$ branching fraction from the full calculation versus an effective ansatz. In Figure 2.11 we show the full calculation in solid green, which assumes the anomalon masses to be determined by a Yukawa coupling of $M = 4\pi/3\, v_\Phi/\sqrt{2}$, the top quark mass is set to its SM value, while the masses of the lighter quarks are taken to be of order MeV. The effective ansatz, shown in shaded blue and labelled “EFT”, uses the expression from eq. (2.100) and includes anomalons with $M \to \infty$ and SM quarks with $m_q \to 0$. The omission of the transverse polarisation of the Z'_B boson limits the validity of the effective calculation to light Z'_B bosons, which seems a questionable assumption regarding the mass range covered by the L3 experiment ($24\,\mathrm{GeV} < m_{Z'_B} < 86\,\mathrm{GeV}$). Furthermore for large gauge couplings g_X the anomalons become part of the active spectrum even for larger Z'_B masses, nevertheless we see in Figure 2.11 that the “EFT” limit differs only little from the full limit. The effective limit is a little too strong in most of the parameter space, for lighter $m_{Z'_B}$ by about 10-20% and for larger $m_{Z'_B}$ this overestimation generally gets worse. We therefore suggest the use of the full calculation of the $Z \to Z'_B\gamma$ decay width, eq. (2.80), for phenomenological studies.

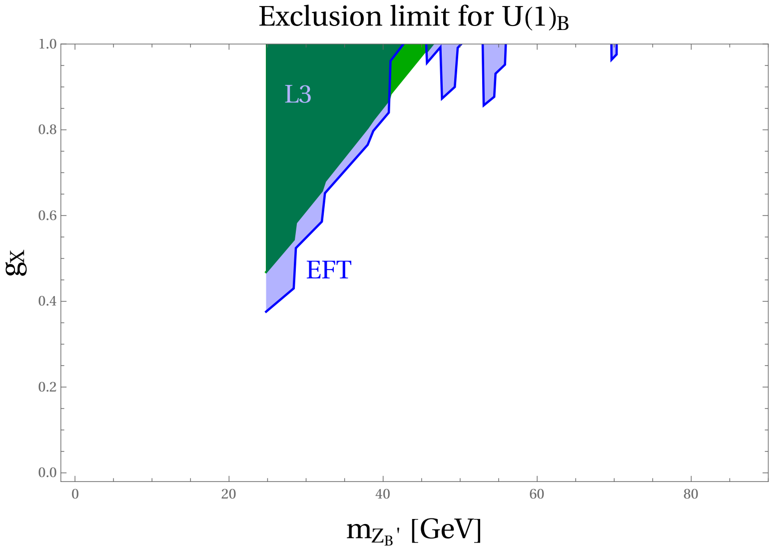

Figure 2.11: $U(1)_B$ exclusion limit in the g_X, $m_{Z'_B}$ plane from the measurement of the $Z \to (jj)\gamma$ branching fraction by the L3 expermiment [182]. The limit from our full calculation is shown in solid green, with anomalon masses set by $M = 4\pi/3\, v_\Phi/\sqrt{2}$, the SM value of the top quark and lighter quark masses of order MeV. Lighter blue covers the limit from an effective calculation including anomalons with masses $M \to \infty$ and massless SM fermions ($m_q \to 0$), using the longitudinal Goldstone approximation, eq. (2.100).

2.8 Conclusions

In the present chapter we have studied the $Z - Z' - \gamma$ vertex function, calculating the $Z \to Z'\gamma$ decay width for two $U(1)$ gauge symmetries, gauged baryon number B and gauged baryon minus lepton number $B-L$. While textbooks, *e.g.* Refs. [35,164], focus on the divergences of the different currents to show that in the axial vector case the current is not conserved, we calculated the full vertex function and evaluated the decay width for two concrete cases. We defined the unphysical parameters in the vertex function by evaluating the (anomalous) Ward-Takahashi identities of the three external currents. To illustrate the differing behaviour of heavy fermions, and thereby of the generated anomaly in the light fermion content, we chose to elaborate on the two mentioned $U(1)$ gauge symmetries, namely gauged $B - L$, for which the SM fermion content is anomaly free and thus all fermions have chiral couplings to the SM Z boson, and gauged B, where the SM fermion content is anomalous and the introduction of new fermions becomes necessary. The masses of these new fermions can theoretically be generated by the SM Higgs or by the new Higgs that breaks the $U(1)_B$ symmetry. In the first case, which is however excluded by experiment, all fermions are chiral under the same symmetry and the new fermions resemble the SM leptons – we can confirm this when comparing this scenario with the $B - L$ case from above: when we take the new fermions to be light, like the SM leptons, we see in Figure 2.5 that the branching fraction resembles the one of $Z \to Z'_{B-L}\,\gamma$, Figure 2.4.

In both these cases, where all fermion masses are generated by the vev of the same Higgs boson, taking the fermions to be degenerate causes the branching fraction of $Z \to Z'\,\gamma$ to vanish, as we would expect. Any anomaly free set of degenerate fermions does not contribute to these decay widths, independent of their mass scale.

This statement, however, becomes invalid when the fermions within an anomaly free set do not share the same chiral structure. As an example we studied the case of gauged baryon number, where the anomalon masses are generated by the $U(1)_B$ breaking Higgs in Section 2.4.3. Taking the SM fermion masses and the anomalon masses to all share the same value M, the decay width does not vanish, but gives a finite result, eq. (2.81). The fact that for theories with more complex chiral structure, degenerate anomaly free sets of fermions do not necessarily give a vanishing contribution to the decay width, was first noted in Ref. [172].

Apart from the non-decoupling behaviour of fermions in gauged baryon number, we also calculated the decay width respecting the necessary connection between fermion masses, gauge coupling constant and gauge boson mass. Assuming the fermion masses to be generated by the $U(1)_B$ breaking Higgs places an upper limit on these masses when fixing the gauge coupling and the gauge boson mass. We set the Yukawa coupling of the anomalons to a fixed value of $4\pi/3$ and plotted the branching fraction for the $Z \to Z'_B\gamma$ decay versus the parameters gauge boson mass $m_{Z'_B}$ as well as Higgs vev v_ϕ for different values of the gauge coupling g_X in Figure 2.6.

In Section 2.6 we then integrated the resulting limit on the branching fraction using the measurement from the L3 collaboration [182] into existing limits in the $g_X - m_{Z'_B}$ plane, see Figure 2.9. The plot includes the LEP searches for electroweakly charged anomalons, CMS searches for low-mass Z' decaying to a dijet resonance, limits from the Upsilon decay and measurements of Z-pole observables that limit the $Z - Z'_B$ mixing. All these probes are sensitive to different details of the theory of gauged baryon number – the fermion content, the decay channel of the gauge boson or the fermions, the couplings to the new Higgs boson, etc. – but nevertheless turn out to be generally competitive. By the difference in their sensitivity to the model parameters and by their different backgrounds and systematic uncertainties these probes are complementary in testing the model of gauged baryon number.

As we commented before, assuming the anomalons to be heavy enough to treat them as effective degrees of freedom can be problematic, depending on the model parameters, especially if the anomalon masses are generated by the $U(1)'$ breaking Higgs. We therefore showed the connection of an effective ansatz using Wess-Zumino terms and our full calculation in Section 2.7 for the model of gauged baryon number. We discussed the importance of the coherent inclusion of light fermions and the effective contribution, where we saw that the shift parameters of the light fermions restrict the Wilson coefficient of the Wess-Zumino terms and vice versa. In Figure 2.10 we saw that for rather large gauge couplings the effective calculation is valid for large Z'_B masses only, since at small $m_{Z'_B}$ the anomalons become on-shell and lead to a peak and then a turnover in the decay width. The smaller the gauge coupling, the wider the range of validity of the EFT calculation. Using Goldstone boson equivalence in the Z'_B vertex implies neglecting the transverse polarisation of the Z'_B boson and therefore this approximation is only valid for small $m_{Z'_B}$, which for large gauge couplings should be in conflict with the assumption of heavy anomalons. Nevertheless, we see in Figure 2.11 that the effective calculation is in the right ballpark of the full result for small $m_{Z'_B}$, when calculating a limit using the measurements of the $Z \to (jj)\gamma$ branching fraction from the L3 experiment. The EFT ansatz, however, tends to overestimate the limit, which becomes worse for larger $m_{Z'_B}$.

In this chapter we have seen that introducing new $U(1)$ symmetries to the SM requires the fermion content to cancel all triangle anomalies, which can make the introduction of new fermions necessary. The mass generation of these anomalons can be connected to the symmetry breaking of the new $U(1)$ symmetry or the SM or both and these scenarios have rich phenomenological and theoretical consequences that can differ greatly, because of the diverse chiral structure that occurs. We have compared these different behaviours by examining two models, gauged baryon minus lepton number $U(1)_{B-L}$ and gauged baryon number $U(1)_B$, analysing the structure of the Z–Z'–γ vertex. For the case of $U(1)_B$, where the introduction of anomalons is necessary, we studied the non-decoupling behaviour of these fermions in the $Z \to Z'_B\gamma$ decay. We calculated a limit in the gauge coupling versus gauge boson mass plane and compared to the result from an effective ansatz. We saw that this limit is competitive with other probes and that model assumptions can make these probes complementary tests of $U(1)_B$.

Chapter 3

Inelastic Dark Matter at the LHC

3.1 Introduction

This chapter presents work that has not been published elsewhere. The calculations and simulations were carried out by the author with the support of my supervisor and a collaborator. The dark matter relic density calculations in MicrOmegas were performed by my supervisor.

To reveal the nature of dark matter (DM), many experiments have been built, taking many different approaches and ruling out parameter space of a great variety of models. For example, the “vanilla” DM candidates, namely the Weakly Interacting Massive Particles (WIMPs), are being searched for by direct detection experiments, indirect searches and the Large Hadron Collider (LHC). In direct searches for DM–nucleus scattering, the sensitivity has improved by almost three orders of magnitude over the past decade [202–206], ruling out tiny spin-independent cross sections. Indirect searches look for the annihilation products of DM in high energy cosmic rays, where new observatories, such as AMS-02 [207] and Fermi-LAT [208–210] are pushing the frontier. On top of that, the LHC is looking for DM signatures, mostly via missing transverse energy ($E_{\mathrm{T}}^{\mathrm{miss}}$), but also by searching for specific imprints of (simplified) models. The LHC experiments have by now collected almost $400\,\mathrm{fb}^{-1}$ of integrated luminosity each, along with tremendous advances in analysis techniques. Due to the continued null results, it is certainly a good idea to cast a wider net by investigating DM candidates with properties different from vanilla WIMPs. One pioneering and successful attempt in this direction is inelastic DM (iDM) [96].

The possibility of DM scattering inelastically off of nucleons [96], where elastic scattering is suppressed or forbidden, was first suggested when the DAMA/LIBRA [123,211,212] collaboration detected a DM signal with an annual modulation, while other experiments (at the time CDMS [124, 213], later *e.g.* CRESST [214] and XENON [103, 215]) were excluding the same parameter space for a standard WIMP model [96, 202]. The dark sector is augmented to contain two states, the DM candidate χ and an excited state χ^*, which is slightly heavier. Interactions with the SM particles are subsequently forced to be off-diagonal: the scattering $\chi N \to \chi N$ is suppressed and the process for DM detection becomes $\chi N \to \chi^* N$. The mass splitting $(m_{\chi^*} - m_\chi)/m_\chi$ is chosen to be $\ll 1$, leaving the kinematics of DM annihilation and production at colliders mostly unaffected. Non-relativistic DM–nucleus scattering in direct detection experiments, however, is significantly altered. If the mass difference of the two states $\Delta = m_{\chi^*} - m_\chi$ is chosen such that it resembles the kinetic energy of the DM particles in the halo, DM particles that are too slow cannot scatter off the nuclei in the targets. The minimal velocity necessary to excite the state χ into χ^* and deposit a minimum energy in the experiment depends on the mass of the nuclei of the target material and favours heavier nuclei [216]. This way, the signal detected by the DAMA/LIBRA collaboration, which used an sodium iodine (NaI) target (the atomic number of iodine is 127), could be reconciled with the null results from CDMS [213] with a germanium (Ge) target (germanium has an atomic number of 73).

There are various possibilities to embed the concept of inelastic DM into a UV complete, greater theory. Supersymmetry provides a candidate with the sneutrino, where the two states are its odd and even CP eigenstates [96, 217]. The DM particle could *e.g.* be composite, bound by a new force that resembles the SM strong force and leads to meson-like states. A new $U(1)$ gauge boson couples the dark sector to the SM via kinetic mixing with the hypercharge boson and induces an inelastic hyperfine splitting, whose transition corresponds to the inelastic coupling that could be seen in direct detection experiments [218]. If DM had a magnetic dipole moment, which can happen in asymmetric mirror DM [219] or fermionic technibaryons [220], the interaction via the dipole operator naturally occurs inelastically [221]. Extra dimensions can produce an inelastic DM candidate, in a warped fermion or scalar model [217]. As we can see, there is a broad variety of UV completions, that can lead to inelastic scattering of the DM particles in direct detection experiments.

In subsequent work, following the idea triggered from the DAMA/LIBRA anomaly, direct detection of inelastic DM has been studied in detail both theoretically and experimentally, leading to the eventual exclusion of the parameter region favoured by DAMA/LIBRA [125, 126, 222–238]. Nevertheless, vast parameter regions are still viable, so that inelastic DM is by now one of the most-studied DM candidates. For instance, the authors of Refs. [217, 218, 221, 239] discuss inelastic DM from the model-building and phenomenology point of view, and Refs. [240–247] focus on the phenomenology associated with inelastic DM capture and annihilation in the Sun, in white dwarfs, and in neutron stars. Finally, collider signals of inelastic DM have been investigated in Refs. [127, 248, 249].

It is the last set of references that we build on in the present work. In particular, our goal is to derive limits on the parameter space of inelastic DM by searches from run II of the LHC. Specifically, we will consider χ–χ^* production in proton–proton collisions, possibly accompanied by extra jets from initial state radiation:

$$p + p \to \bar{\chi} + \chi^*,\, \chi + \bar{\chi^*} \quad (+\, j)\,. \tag{3.1}$$

The excited DM state χ^* will eventually decay back to χ plus SM particles. We focus in particular on the decay mode

$$\chi^* \to \chi + \bar{q} + q\,. \tag{3.2}$$

We will consider two characteristic signatures, namely the generic monojet signature [127,128,250] and events with displaced vertices and missing transverse momentum [129]. In Section 3.7, we will also discuss other searches that can potentially be sensitive, but without actually recasting them. We focus here on searches by the ATLAS collaboration, but of course similar signatures have also been searched for in CMS [251, 252].

The outline of this chapter is the following: In the next Section 3.2 we will introduce the simplified models that we will work with and describe some of their basic properties, such as the decay width of the state χ^* and the collider signatures it can generate. Details on the signal simulation and the analysis procedure are given in Section 3.3. In the following Section 3.4 we will compare the simplified models to an effective operator approach, examining cross sections and kinematic properties. Furthermore, we will compare the relevant kinematic variables of the different mediators. The monojet analysis is presented in Section 3.5, with cuts and uncertainties explained in detail. We will then move to look at a search for displaced vertices in Section 3.6, where we are motivated to investigate the option of relaxing the cuts of the analysis. Section 3.7 discusses other LHC searches that could be sensitive to inelastic DM signatures. We conclude and summarise in Section 3.8.

3.2 Simplified Models for Inelastic Dark Matter

In an inelastic DM model the dark sector has to contain at least two states. We will consider here a simplified model with two states χ and χ^* and a mediator ξ that connects the dark sector with the SM. The mass of χ^* is slightly larger than the mass of χ, the difference is denoted by $\Delta = m_{\chi^*} - m_\chi$ and the mass of the mediator is assumed to be much larger than this splitting, $m_\xi \gg \Delta$. The interaction vertex of the DM states with the mediator has to feature both states $\bar{\chi}$–χ^*–ξ (or χ–$\bar{\chi}^*$–ξ), suppressing thus the interaction of the DM relic χ in direct detection experiments. Diagonal couplings, *i.e.* χ–$\bar{\chi}$–ξ and χ^*–$\bar{\chi}^*$–ξ, are assumed to be negligible or absent. We will generally consider different types of mediators ξ, vector (V), axial vector (AV), scalar (S) and pseudoscalar (PS). The interactions of the different mediator types with the SM quarks and the DM states are given by these respective Lagrangians:

$$\mathcal{L}_{\rm int}^{\rm V} = g_q\, \xi^\mu \sum_q \bar{q}\gamma_\mu q + \Big(g_\chi\, \xi^\mu\, \bar{\chi}^* \gamma_\mu \chi + \text{h.c.}\Big)\,, \tag{3.3}$$

$$\mathcal{L}_{\text{int}}^{\text{AV}} = g_q\, \xi^\mu \sum_q \bar{q}\gamma_\mu\gamma_5 q + \Big(g_\chi\, \xi^\mu\, \bar{\chi}^* \gamma_\mu\gamma_5 \chi + \text{h.c.} \Big)\,, \tag{3.4}$$

$$\mathcal{L}_{\text{int}}^{\text{S}} = g_q\, \xi \sum_q \bar{q} q + \Big(g_\chi\, \xi\, \bar{\chi}^* \chi + \text{h.c.} \Big)\,, \tag{3.5}$$

$$\mathcal{L}_{\text{int}}^{\text{PS}} = i\, g_q\, \xi \sum_q \bar{q}\gamma_5 q + \Big(i\, g_\chi\, \xi\, \bar{\chi}^* \gamma_5 \chi + \text{h.c.} \Big)\,, \tag{3.6}$$

where the sum runs over all quark flavours q.

The mass of the dark state χ^* is taken to be larger than the one of χ and therefore it will decay to χ via its coupling to the mediator ξ. But since we take the mediator to be much heavier than the splitting of the DM states, this process will be off-shell and we will have an effective three body decay, where the mediator decays to a quark – antiquark pair: $\chi^* \to \chi\bar{q}q$. The decay width for a three body decay is given by [253]

$$\Gamma = 3 \sum_q \iint \frac{1}{(2\pi)^3} \frac{1}{32 m_{\chi^*}} \overline{|\mathcal{M}|^2}\, dm_{12}^2 dm_{23}^2\,, \tag{3.7}$$

where the quantities m_{ij} are defined by the relations

$$p_{ij} = p_i + p_j\,, \tag{3.8}$$

$$m_{ij} = p_{ij}^2 = (p_i + p_j)^2\,. \tag{3.9}$$

$\overline{|\mathcal{M}|^2}$ is the spin averaged matrix element of the decay process. The factor three in front stems from the three colours of the quarks. For the subsequent calculation we define χ to be particle 1 and the quarks to be particles 2 and 3. We can then calculate the spin averaged matrix elements for the process $\chi^* \to \chi\bar{q}q$ with a generic SM quark q for the four different mediator types:

$$\begin{aligned} \overline{|\mathcal{M}_{\text{AV}}|^2} &= \frac{4 g_\chi^2 g_q^2}{(m_{23}^2 - m_\xi^2)^2} (-2m_{12}^4 + m_{12}^2(-m_{23}^2 + m_{\chi^*}^2 + m_\chi^2) - m_{23}^4 + \\ &\qquad + m_{23}^2 (m_{\chi^*} + m_\chi)^2 - 2 m_{\chi^*}^2 m_\chi^2)\,, \end{aligned} \tag{3.10}$$

$$\begin{aligned} \overline{|\mathcal{M}_{\text{V}}|^2} &= \frac{4 g_\chi^2 g_q^2}{(m_{23}^2 - m_\xi^2)^2} (-2m_{12}^4 + 2m_{12}^2(-m_{23}^2 + m_{\chi^*}^2 + m_\chi^2) - m_{23}^4 + \\ &\qquad + m_{23}^2 (m_{\chi^*} - m_\chi)^2 - 2 m_{\chi^*}^2 m_\chi^2)\,, \end{aligned} \tag{3.11}$$

$$\overline{|\mathcal{M}_{\text{S}}|^2} = \frac{2 g_\chi^2 g_q^2}{(m_{23}^2 - m_\xi^2)^2} m_{23}^2 ((m_{\chi^*} + m_\chi)^2 - m_{23}^2)\,, \tag{3.12}$$

$$\overline{|\mathcal{M}_{\text{PS}}|^2} = \frac{2 g_\chi^2 g_q^2}{(m_{23}^2 - m_\xi^2)^2} m_{23}^2 ((m_{\chi^*} - m_\chi)^2 - m_{23}^2)\,, \tag{3.13}$$

where we neglected the masses of the final state quarks, $m_q \to 0$.

With setting the quark masses to zero, we also obtain simplified values for the decay widths for $\chi^* \to \chi\bar{q}q$:

$$\begin{aligned}
\Gamma_{\mathrm{AV}} = \; & \tfrac{n_q g_\chi^2 g_q^2}{128\pi^3 m_\xi^4 m_{\chi^*}^3} \Big(m_{\chi^*}^8 + 2m_{\chi^*}^7 m_\chi - 8m_{\chi^*}^6 m_\chi^2 + 18m_{\chi^*}^5 m_\chi^3 - 18m_{\chi^*}^3 m_\chi^5 + 8m_{\chi^*}^2 m_\chi^6 \\
& +24\, m_{\chi^*}^3 m_\chi^3 \cdot (m_{\chi^*}^2 - m_{\chi^*} m_\chi + m_\chi^2) \log \tfrac{m_\chi}{m_{\chi^*}} - 2m_{\chi^*} m_\chi^7 - m_\chi^8 \Big) \,, \qquad (3.14) \\
\Gamma_{\mathrm{V}} = \; & \tfrac{n_q g_\chi^2 g_q^2}{128\pi^3 m_\xi^4 m_{\chi^*}^3} \Big(m_{\chi^*}^8 - 2m_{\chi^*}^7 m_\chi - 8m_{\chi^*}^6 m_\chi^2 - 18m_{\chi^*}^5 m_\chi^3 + 18m_{\chi^*}^3 m_\chi^5 + 8m_{\chi^*}^2 m_\chi^6 \\
& +24\, m_{\chi^*}^3 m_\chi^3 \cdot (m_{\chi^*}^2 + m_{\chi^*} m_\chi + m_\chi^2) \log \tfrac{m_{\chi^*}}{m_\chi} + 2m_{\chi^*} m_\chi^7 - m_\chi^8 \Big) \,, \qquad (3.15) \\
\Gamma_{\mathrm{S}} = \; & \tfrac{n_q g_\chi^2 g_q^2}{512\pi^3 m_\xi^4 m_{\chi^*}^3} \Big(m_{\chi^*}^8 + 4m_{\chi^*}^7 m_\chi - 8m_{\chi^*}^6 m_\chi^2 + 36m_{\chi^*}^5 m_\chi^3 - 36m_{\chi^*}^3 m_\chi^5 + 8m_{\chi^*}^2 m_\chi^6 \\
& +24\, m_{\chi^*}^3 m_\chi^3 \cdot (2m_{\chi^*}^2 - m_{\chi^*} m_\chi + 2m_\chi^2) \log \tfrac{m_\chi}{m_{\chi^*}} - 4m_{\chi^*} m_\chi^7 - m_\chi^8 \Big) \,, \qquad (3.16) \\
\Gamma_{\mathrm{PS}} = \; & \tfrac{n_q g_\chi^2 g_q^2}{512\pi^3 m_\xi^4 m_{\chi^*}^3} \Big(m_{\chi^*}^8 - 4m_{\chi^*}^7 m_\chi - 8m_{\chi^*}^6 m_\chi^2 - 36m_{\chi^*}^5 m_\chi^3 + 36m_{\chi^*}^3 m_\chi^5 + 8m_{\chi^*}^2 m_\chi^6 \\
& +24\, m_{\chi^*}^3 m_\chi^3 \cdot (2m_{\chi^*}^2 + m_{\chi^*} m_\chi + 2m_\chi^2) \log \tfrac{m_{\chi^*}}{m_\chi} + 4m_{\chi^*} m_\chi^7 - m_\chi^8 \Big) \,. \qquad (3.17)
\end{aligned}$$

We added here a factor n_q denoting the number of kinematically accessible quarks. Their masses are, however, still taken to be zero, and they all couple with the same coupling strength g_q. Compared to a full numerical calculation taking into account the actual value of the quark masses, this approximation leads to a deviation of about 30% for a DM mass splitting of $\Delta = 10\,\mathrm{GeV}$ and about 5% for $\Delta = 30\,\mathrm{GeV}$. In our numerical simulations, in which we will obtain the decay rates from MadGraph [254, 255], we will set the up, down, strange, and charm masses to zero while retaining the bottom quark mass. This reduces the error to 6% for $\Delta = 10\,\mathrm{GeV}$ and 0.6% for $\Delta = 30\,\mathrm{GeV}$ for vector, axial vector and scalar mediator. For the pseudoscalar mediator the deviation is only 3% for $\Delta = 10\,\mathrm{GeV}$ and 0.3% for $\Delta = 30\,\mathrm{GeV}$. Neglecting the masses of the four lightest SM quarks therefore proves to be a valid approximation.

Since in an inelastic DM model the splitting $\Delta = m_{\chi^*} - m_\chi$ is usually much smaller than the DM mass itself and the mass of the mediator, the above expressions can be simplified further by expanding in Δ and we obtain at leading order

$$\Gamma_{\mathrm{V}} = \frac{n_q g_\chi^2 g_q^2 \Delta^5}{20\pi^3 m_\xi^4} \,, \qquad (3.18)$$

$$\Gamma_{\mathrm{AV}} = \frac{3 n_q g_\chi^2 g_q^2 \Delta^5}{20\pi^3 m_\xi^4} \,, \qquad (3.19)$$

$$\Gamma_{\mathrm{S}} = \frac{n_q g_\chi^2 g_q^2 \Delta^5}{20\pi^3 m_\xi^4} \,, \qquad (3.20)$$

$$\Gamma_{\mathrm{PS}} = \frac{3 n_q g_\chi^2 g_q^2 \Delta^7}{560\pi^3 m_\xi^4 m_\chi^2}\,, \tag{3.21}$$

where again n_q denotes the number of kinematically accessible quarks. We see here, that the decay widths are identical for a vector and scalar mediator, while the axial vector case is larger by a factor three. The pseudoscalar case, however, has a completely different dynamic because of an additional factor of Δ^2/m_χ^2, which makes the decay width decrease with increasing DM mass.

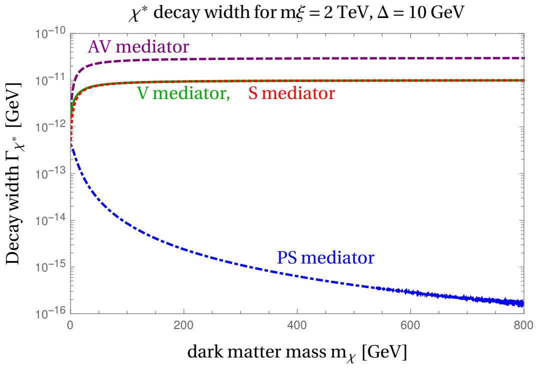

(a) Decay width $\Gamma(\chi^* \to \chi\bar{q}q)$ for a splitting of the DM states of $\Delta = 10\,\mathrm{GeV}$, setting the mediator mass to $m_\xi = 2\,\mathrm{TeV}$.

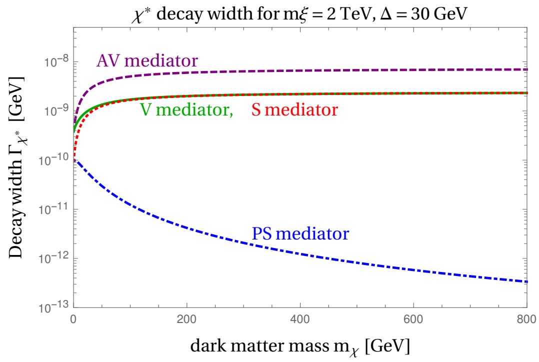

(b) Decay width $\Gamma(\chi^* \to \chi\bar{q}q)$ for a splitting of the DM states of $\Delta = 30\,\mathrm{GeV}$, setting the mediator mass to $m_\xi = 2\,\mathrm{TeV}$.

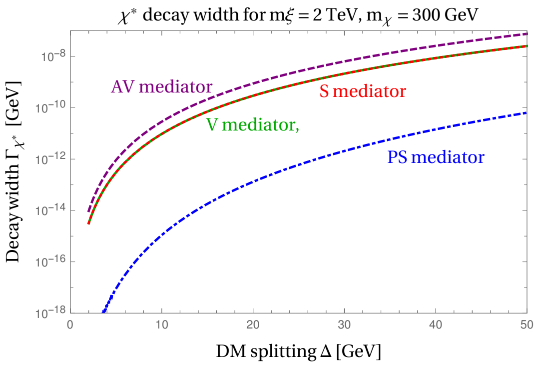

(c) Decay width $\Gamma(\chi^* \to \chi\bar{q}q)$ for a DM mass of $m_\chi = 300\,\mathrm{GeV}$ and a mediator mass $m_\xi = 2\,\mathrm{TeV}$.

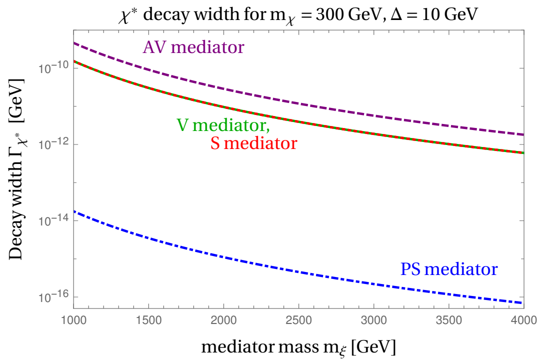

(d) Decay width $\Gamma(\chi^* \to \chi\bar{q}q)$ for a splitting of the DM states of $\Delta = 10\,\mathrm{GeV}$ and a DM mass $m_\chi = 300\,\mathrm{GeV}$.

Figure 3.1: Decay width of the heavier DM state χ^* to a massless quark pair $q\bar{q}$ and the DM state χ, $\Gamma(\chi^* \to \chi\bar{q}q)$, plotted versus the DM mass m_χ (first line), versus the splitting of the DM states Δ and the mediator mass m_ξ. The curves show the widths for the different mediator types: axial vector (AV, dashed, purple), vector (V, green, solid), pseudoscalar (PS, blue, dot-dashed) and scalar (S, red, dotted) mediator.

In Figure 3.1 we show a plot of the decay width $\Gamma(\chi^* \to \chi\bar{q}q)$ for a generic massless quark q. Considering multiple quarks in the final state increases the width accordingly

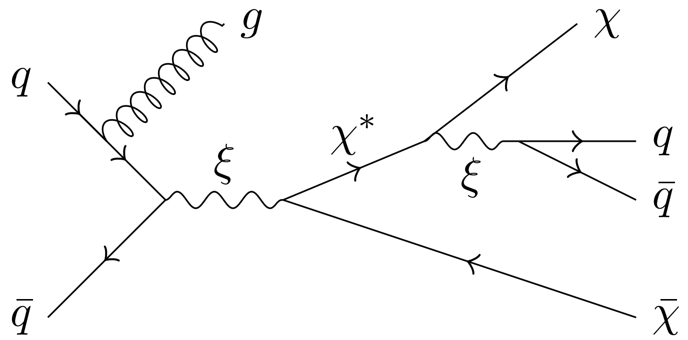

Figure 3.2: DM production and decay via $pp \to \bar{\chi}(\chi^* \to \chi\bar{q}q)$, accompanied by emission of an ISR jet. The diagram corresponds to the simplified model, where ξ is a vector, axial vector, scalar, or pseudoscalar mediator (see eqs. (3.3) to (3.6)).

by a constant factor.[1] The first two panels show the dependence of the decay widths on the DM mass for a fixed mediator mass and mass splitting. We can see the similar behaviour of the scalar, vector and axial vector case nicely, while the pseudoscalar case differs considerably in its dependence on the DM mass, due to the factor Δ^2/m_χ^2 as we saw in eqs. (3.18) to (3.21). This factor, as well as the smaller numerical factors, reduce the pseudoscalar decay width considerably, when considering its dependence on the mass splitting and the mediator mass. This makes the pseudoscalar case particularly interesting, as the small decay width leads to large decay distances that could actually be detected in the experiments, as we will see in Section 3.6.

A generic LHC event mediated by the interactions induced by our simplified models is shown in Figure 3.2: a quark–antiquark pair annihilates into a $\bar{\chi}$–χ^* (or equivalently χ–$\bar{\chi}^*$) pair, and the χ^* decays subsequently to χjj. In addition, there is typically some amount of initial state radiation (ISR), illustrated in Figure 3.2 by a gluon radiated off one the incoming quarks.

A monojet search, which requires a large amount of $E_\mathrm{T}^\mathrm{miss}$ and a very energetic jet, will typically trigger on such an ISR jet. The $E_\mathrm{T}^\mathrm{miss}$ is provided by the two final state χ particles recoiling against the ISR jet. The small mass splitting Δ between the two DM states implies that the jet(s) from χ^* decay are too soft to fire a monojet trigger. Our recasting on an ATLAS monojet analysis is described in detail in Section 3.5.

While a small splitting Δ makes the jet(s) from χ^* decay relatively soft, it may also result in a non-negligible lifetime of χ^*. In this case, the decay products emerge from a vertex displaced from the primary interaction point. Therefore, also analyses searching for displaced vertices are sensitive to the signals in Figure 3.2. In Section 3.6, we will

[1] This is true unless we get close to the regime where a quark just becomes kinematically accessible, *i.e.* $\Delta = 2m_q$.

consider an ATLAS analysis sensitive to tracks starting at high-mass displaced vertices in events with large $E_{\mathrm{T}}^{\mathrm{miss}}$.

3.3 Signal Simulation and Analysis

To predict the expected inelastic DM signals at the LHC, we have implemented the different models from eqs. (3.3) to (3.6) in Feynrules 2.3 [256], and have then used MadGraph v2.6.2 [254, 255] to generate events. In addition to the dark particles, we allow for the production of up to two additional jets at the matrix elements level. Parton showering and hadronisation was done in Pythia 8 [257], while Delphes 3.4.1 [258] was used as a fast detector simulation. We have verified our implementation by reproducing results from an effective calculation from Ref. [127], see the next Section 3.4 for details. In Figure 3.3 we illustrate how the DM production cross section varies as a function of the DM mass and the coupling structure of the mediator.

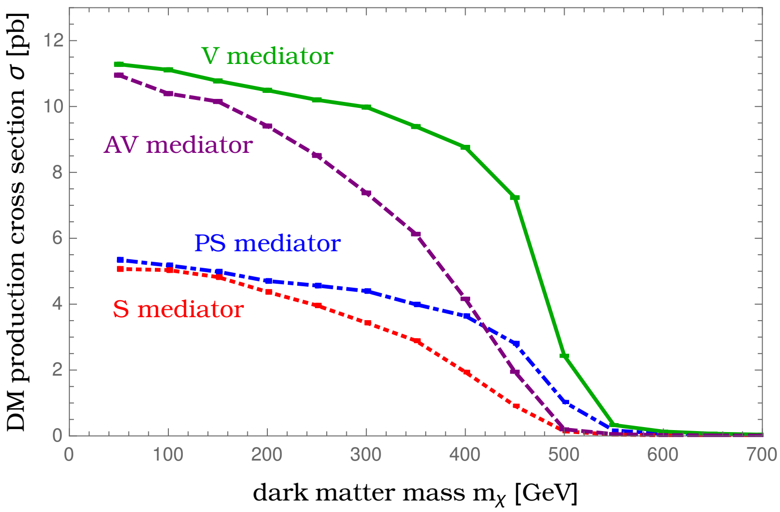

Figure 3.3: The cross section for DM production via $pp \to \chi^* \bar{\chi}, \bar{\chi^*}\chi$, where we included up to two initial state radiation (ISR) jets. The mass of the mediator is fixed to $m_\xi = 1\,\mathrm{TeV}$ and the splitting of the dark states is $\Delta = 10\,\mathrm{GeV}$. The coupling constant of the mediator to the SM quarks is set to $g_q = 0.25$, which is the value we use for our analyses.

As Delphes does not simulate displaced decays, we have supplemented it with our own implementation of vertex displacement. For each event, we randomly draw the χ^* lifetime $t(x)$ from a distribution of the form

$$P(t) = \frac{\Gamma}{\gamma} \cdot \exp\left[-\frac{\Gamma \cdot t}{\gamma}\right], \tag{3.22}$$

where γ is the Lorentz boost factor of χ^*, and Γ is the χ^* decay width. We extract the latter from the MadGraph simulation, but we verified that it agrees with eqs. (3.16) to (3.14). To optimize Monte Carlo efficiency, we restrict the generated values of t to the range to which ATLAS is sensitive; for the displaced vertex search from Ref. [129], this implies restricting the transverse decay length L_{xy} to be between $L_{xy,\min} = 0.4$ cm and $L_{xy,\max} = 30$ cm. Here, the transverse decay length is given by $L_{xy} = v\,t \sin[2\arctan(e^{-|\eta|})]$, where v is the velocity of χ^*, t is its lifetime randomly drawn from the distribution above, and η is its pseudorapidity. Similarly, the longitudinal decay length is given by $L_z = v\,t\cos[2\arctan(e^{-|\eta|})]$. The fact that events falling outside this range would be lost to the analysis is taken into account by assigning each event an appropriate weight factor, given by the integral of eq. (3.22) over the range of t values that correspond to transverse decay lengths between $L_{xy,\min}$ and $L_{xy,\max}$.

For setting limits, we use the HistFitter routine [259]. To draw smooth exclusion contours between irregularly spaced sampling points in the m_χ–m_ξ plane, we interpolate the CLs significance (number of standard deviations) at which the sampling points are disfavoured using Delaunay triangulation [260]. Limits are given at 95% CL.

3.4 Kinematics and Comparison to EFT

3.4.1 Comparison to EFT

To verify the implementation of our model we reproduce the results from an effective field theory calculation from Ref. [127] and compare our simulation with the simplified models to the effective operator based approach. Since Ref. [127] uses an ansatz where the dark sector couples exclusively to SM up-quarks, we will also assume this here in the beginning.

The interactions of the dark sector particles χ and χ^* we described in eqs. (3.3) to (3.6) can be connected to an effective field theory calculation, where the interactions are instead described by the following operators [127], assuming a coupling only to up-quarks u:

$$\mathcal{O}_1 = \frac{[\bar{u}\gamma_\mu\gamma_5 u][\bar{\chi}^*\gamma^\mu\gamma_5\chi]}{\Lambda_1^2}\,, \tag{3.23}$$

$$\mathcal{O}_2 = \frac{[\bar{u}\gamma_5 u][\bar{\chi}^*\gamma_5\chi]}{\Lambda_2^2}\,, \tag{3.24}$$

$$\mathcal{O}_3 = \frac{[\bar{u}u][\bar{\chi}^*\chi]}{\Lambda_3^2}\,, \tag{3.25}$$

$$\mathcal{O}_4 = \frac{[\bar{u}\gamma_\mu u][\bar{\chi}^*\gamma^\mu\chi]}{\Lambda_4^2}\,. \tag{3.26}$$

The scale Λ_i determines the strength of the interaction and the Lagrangian has to include the complex conjugate of the respective operator as well. The first operator $\mathcal{O}_1$ corresponds to an interaction via an axial vector mediator, $\mathcal{O}_2$ to pseudoscalar interactions, $\mathcal{O}_3$ to scalar, and $\mathcal{O}_4$ to vector interactions. For a coupling to all SM quarks we simply add the corresponding expressions for each quark.

To validate our model we reproduce the DM production cross sections for the effective operator $\mathcal{O}_1$ from Ref. [127]. We simulate $pp \to \chi^* \bar{\chi}$, $\bar{\chi}^* \chi$ in MadGraph v2.6.2 [261] including up to two additional ISR jets at a centre-of-mass energy of 7 TeV and for a scale $\Lambda = 1$ TeV, parton showering and hadronisation are done in Pythia 8 [262], and we use Delphes 3.4.1 [263] for the detector simulation. Subsequently we cut for at least one jet in the event and missing transverse energy $E_\mathrm{T}^\mathrm{miss} > 150\,\mathrm{GeV}$. Furthermore we reproduce in Figure 3.4 the Lorentz boost factor of the DM particle χ^* and the hadronic transverse momentum from its decay for a mass splitting of the DM particles $\Delta = m_{\chi^*} - m_\chi = 2\,\mathrm{GeV}$. Our results agree nicely with those of Ref. [127], compare to Figures 3 and 4 therein.

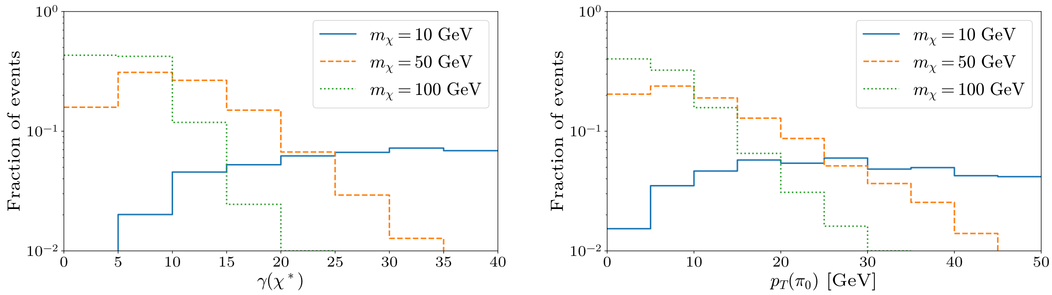

(a) Lorentz boost of the particle χ^*, γ_{χ^*}.

(b) Hadronic p_T resulting from the decay of χ^*, $\chi^* \to \chi \bar{u} u$.

Figure 3.4: Plots of the Lorentz boost factor of the DM particle χ^* and the hadronic transverse momentum for the effective operator $\mathcal{O}_1$ (see eq. (3.23)) for three different DM masses $m_\chi = 10\,\mathrm{GeV}$ (blue, solid), $m_\chi = 50\,\mathrm{GeV}$ (orange, dashed), and $m_\chi = 100\,\mathrm{GeV}$ (green, dotted), each for a mass splitting of the DM particles of $\Delta = 2\,\mathrm{GeV}$. The plots agree with the results from Ref. [127].

In the next step we now want to validate the implementation of the simplified models given by eqs. (3.3) to (3.6) by comparing cross sections and different kinematic variables to the results of the effective ansatz. First, we compare cross sections and the decay width of the χ^* for the effective operators and corresponding mediators with mass $m_\xi = 100\,\mathrm{TeV}$ (we set the couplings of the mediator to be $g_u = g_\chi = 1$) at $\sqrt{s} = 7\,\mathrm{TeV}$ centre-of-mass energy. For the EFT we set, as before, $\Lambda = 1$ TeV. After correcting for an additional factor of 10^{-8} when comparing the cross section and the decay width of χ^*, which both scale with $1/(m_\xi^4)$, we observe they agree for effective operators and mediators, as expected. Then we simulate a dataset at $\sqrt{s} = 13\,\mathrm{TeV}$ centre-of-mass energy and with a mass splitting of the DM states of $\Delta = 10\,\mathrm{GeV}$, where we included the coupling to all SM quarks for the mediators and the effective operators. For the mediator coupling to quarks we set $g_q = 0.25$. This is the setting we will also use later for our analyses.

In Figure 3.5 we compare different kinematic variables for the effective ansatz and the simplified models with a coupling to all SM quarks. We can see that the missing transverse energy $E_{\mathrm{T}}^{\mathrm{miss}}$ (left row) produced in the process $pp \to \chi^* \bar{\chi}, \bar{\chi^*}\chi$, where χ^* subsequently decays to χ and a pair of quarks, agrees nicely between the EFT and the simplified model with a very high mediator mass of $m_\xi = 100\,\mathrm{TeV}$. The same is true for the number of jets N[jets] (middle row) and the transverse momentum of the hardest jet $p_T(j_1)$ (right row). The model with a low mediator mass of $m_\xi = 1\,\mathrm{TeV}$, however, differs slightly from the other two scenarios. This is due to on-shell effects of the mediator, whose mass is small enough to be produced on-shell, causing a boost that gets passed on to the dark sector particles (and thus the $E_{\mathrm{T}}^{\mathrm{miss}}$) and leading jet-$p_{\mathrm{T}}$, and causes more jets to be counted. The jets that are affected by the on-shell boost stem from the quarks from the χ^* decay and they are more likely to be detected with higher energy, while for the effective ansatz and the high mediator mass more of them are not energetic enough to fulfil the trigger requirements. Therefore, the number of events with no jet goes down for the low mass mediator and we get more events with one or more jets.

This verifies our implementation of the simplified models, eqs. (3.3) to (3.6), showing that both cross sections and kinematic distributions can be matched from the simplified models to the effective ansatz, which furthermore agrees with the results from Ref. [127]. It also motivates the use of simplified models, where we include the mediator into the simulations, since at low mediator masses – those which will be relevant for our analyses – we see on-shell effects of the mediators, that change the relevant kinematic parameters. These effects would not be covered by an effective operator calculation.

3.4.2 Kinematics of the Different Mediators

Finally, we want to compare the different mediators by examining their kinematic properties. Samples are simulated at a centre-of-mass energy of 13 TeV and for a mass splitting of $\Delta = 10\,\mathrm{GeV}$, including up to two ISR jets, with $g_q = 0.25$. The cross sections of the different mediator types differ as expected, we give an example for a DM mass of 50 GeV and a mediator mass $m_\xi = 1\,\mathrm{TeV}$ in Table 3.1. The width of the dark sector particle χ^* (almost) agrees for scalar (S) and vector (V) mediator as we saw in eqs. (3.20) and (3.18) and in Figure 3.1, which also showed that the width of χ^* is substantially smaller for interactions via a pseudoscalar mediator. In the approximated expressions for the decay width, eqs. (3.21), the pseudoscalar decay width shows an additional factor of Δ^2/m_χ^2, which leads to this effect. The decay widths of the mediator ξ are similar for vector and axial vector and for scalar and pseudoscalar.

We show the kinematic distributions for the different mediator types in Figure 3.6. We can see that the differences are small, which makes us expect that the differences in the sensitivities of the monojet analysis towards the different mediators, see Section 3.5,

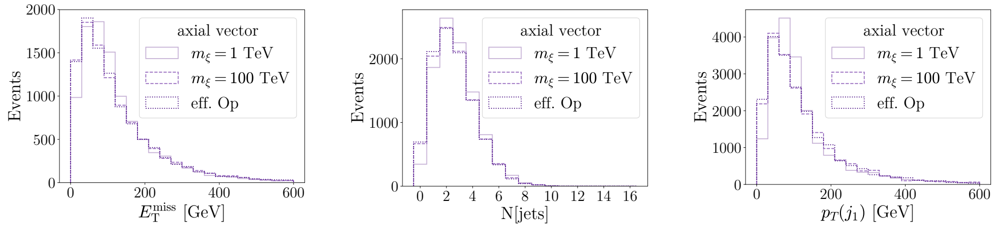

(a) Operator $\mathcal{O}_1$ vs axial vector mediator (with $m_\xi = 1\,\text{TeV}$ and $100\,\text{TeV}$)

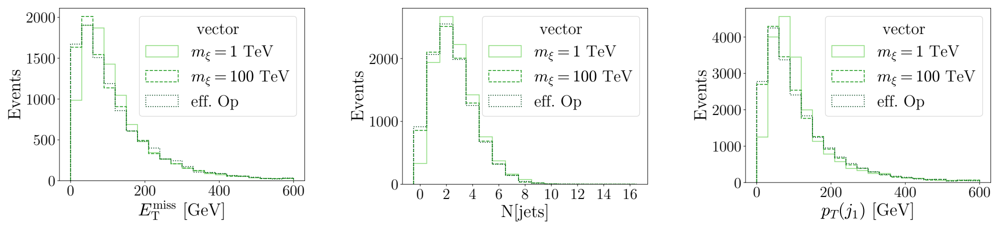

(b) Operator $\mathcal{O}_4$ vs vector mediator (with $m_\xi = 1\,\text{TeV}$ and $100\,\text{TeV}$)

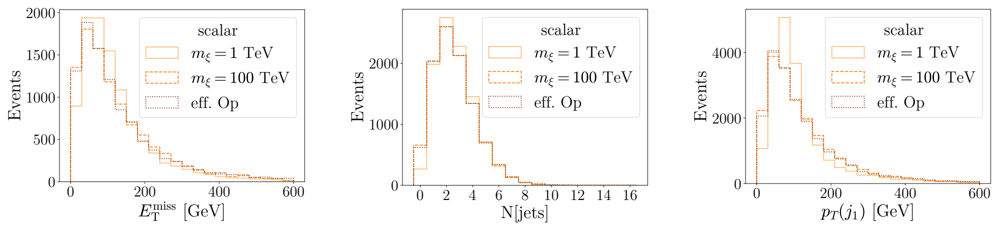

(c) Operator $\mathcal{O}_3$ vs scalar mediator (with $m_\xi = 1\,\text{TeV}$ and $100\,\text{TeV}$)

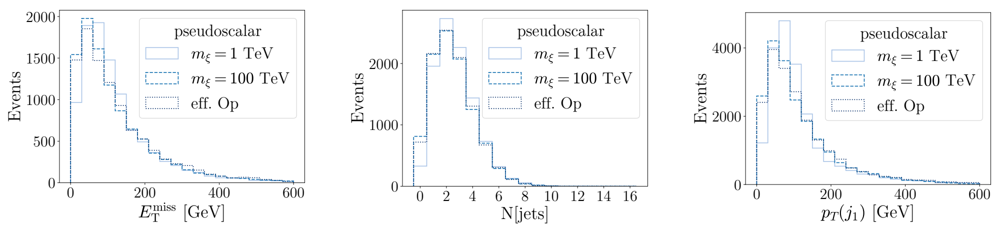

(d) Operator $\mathcal{O}_2$ vs pseudoscalar mediator (with $m_\xi = 1\,\text{TeV}$ and $100\,\text{TeV}$)

Figure 3.5: Comparison of the effective ansatz to their respective simplified models that include the mediator with a coupling to all SM quarks. The left row compares the missing energy E_T^{miss} in the process $pp \to \bar{\chi}^*\chi, \chi^*\bar{\chi}$, the middle row the number of jets $N(j)$ and the right row the transverse momentum p_T of the hardest jet. We compare the effective operators (dotted) each to a simplified model with mediator mass $m_\xi = 100\,\text{TeV}$ (dashed) and $m_\xi = 1\,\text{TeV}$ (solid). The DM mass is set to $m_\chi = 50\,\text{GeV}$ and the splitting to $\Delta = 10\,\text{GeV}$ and we use $g_q = 0.25$.

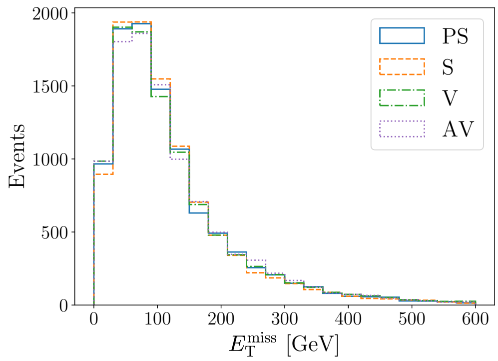

(a) Missing transverse energy $E_{\mathrm{T}}^{\mathrm{miss}}$

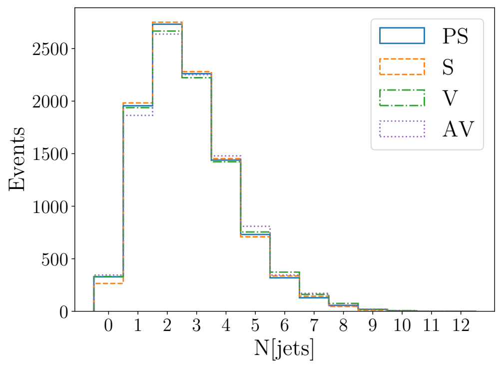

(b) Number of jets N(j)

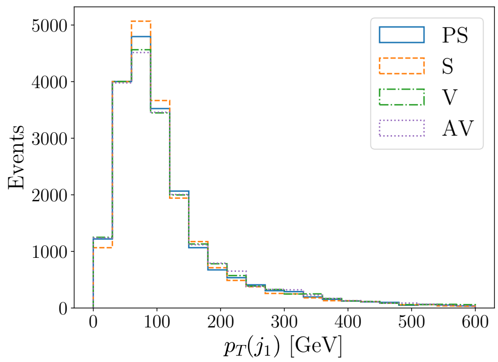

(c) Transverse momentum of the hardest jet

Figure 3.6: Comparison of the kinematic properties of the different mediator types for mediator masses of $m_\xi = 1\,\mathrm{TeV}$, DM mass $m_\chi = 50\,\mathrm{GeV}$ and a splitting of $\Delta = 10\,\mathrm{GeV}$ at a centre-of-mass energy of $\sqrt{s} = 13\,\mathrm{TeV}$ and with couplings $g_q = 0.25$, $g_\chi = 1$. Interactions by a pseudoscalar mediator (PS) are shown in blue, solid, by scalar mediator (S) in orange, dashed, by vector mediator (V) in green, dash-dotted, and by axial vector mediator (AV) in purple, dotted.

type	xsec [pb]	Γ_{χ^*} [GeV]	Γ_ξ [GeV]
AV	10.952 ± 0.020	$9.08 \cdot 10^{-11}$	81.08
V	11.281 ± 0.021	$3.09 \cdot 10^{-11}$	82.86
S	5.068 ± 0.030	$2.99 \cdot 10^{-11}$	121.61
PS	5.345 ± 0.031	$1.07 \cdot 10^{-13}$	123.39

Table 3.1: Comparison of the production cross section $pp \to \bar{\chi^*}\chi$, $\chi^*\bar{\chi}$ (with up to two ISR jets) at 13 TeV centre-of-mass energy and the decay widths of χ^* and the mediator ξ for different mediator types, for a DM mass $m_\chi = 50\,\text{GeV}$, a mediator mass of $m_\xi = 1\,\text{TeV}$ and a splitting of $\Delta = 10\,\text{GeV}$. The mediator coupling to quarks is set to $g_q = 0.25$.

are mostly due to the differences in the production cross sections. The most important cuts in the monojet analysis are on the missing transverse energy $E_{\mathrm{T}}^{\mathrm{miss}}$ and the transverse momentum of the most energetic jet $p_{\mathrm{T}}(j_1)$, which Figure 3.6 shows to have coincident distributions for all mediators. For the displaced vertex analysis, Section 3.6, the decay width of the DM state χ^*, which determines the displacement of the vertex in the detector together with the boost of χ^*, will have the most important influence on the cuts in the analysis. Furthermore, we have a cut on the mass of the displaced vertex, which is defined by its charged decay products. It depends primarily on the splitting of the dark states and thus the energy that is passed on to the quarks in the χ^* decay. The decay width differs substantially for the mediators, which will add upon the differences in the cross sections. In fact, only the model with the pseudoscalar mediator will generate decay distances that are large enough to be detected, while the search is insensitive to the scalar, vector, and axial vector case, see Section 3.6.

3.5 Monojet Analysis

In the following, we recast the ATLAS monojet search from Ref. [128] to derive limits on inelastic DM. The search is based on $139\,\text{fb}^{-1}$ of integrated luminosity, taken at a centre-of-mass energy of $\sqrt{s} = 13\,\text{TeV}$. Selected events are required to contain at least one energetic jet (anti-k_T, $R = 0.4$) with transverse momentum $p_T \geq 150\,\text{GeV}$ and pseudorapidity $|\eta| < 2.4$. The total number of jets with $p_T > 30\,\text{GeV}$ and $|\eta| < 2.8$ must be no more than four. Ref. [128] defines 25 different (but partially overlapping) signal regions with varying restrictions on the missing transverse energy $E_{\mathrm{T}}^{\mathrm{miss}}$. In particular, the $E_{\mathrm{T}}^{\mathrm{miss}}$ threshold is varied between 200 GeV and 1200 GeV in steps of 50 GeV up to 400 GeV and steps of 100 GeV above. For each threshold value, both an inclusive signal region (containing all events with $E_{\mathrm{T}}^{\mathrm{miss}}$ above the threshold) is defined, as well as an exclusive signal region that only contains events with $E_{\mathrm{T}}^{\mathrm{miss}}$ between a given threshold and the next higher one. The hardest exclusive signal region ($E_{\mathrm{T}}^{\mathrm{miss}} > 1200\,\text{GeV}$) does not have an upper cut-off on the missing energy and is therefore identical to the hardest inclusive region. The azimuthal angle between each jet and the missing transverse momentum is required to be larger than $\Delta\phi(\text{jet}, p_T^{\text{miss}}) > 0.4$ for events with $E_{\text{T}}^{\text{miss}} > 250\,\text{GeV}$ and $\Delta\phi(\text{jet}, p_T^{\text{miss}}) > 0.6$ for events with $E_{\text{T}}^{\text{miss}}$ between 200 GeV and 250 GeV. Finally, in Ref. [128], events containing electrons with $p_T > 7\,\text{GeV}$, $|\eta| < 2.47$, muons with $p_T > 7\,\text{GeV}$, $|\eta| < 2.5$, taus with $p_T > 10\,\text{GeV}$, $|\eta| < 2.5$, or photons with $p_T > 10\,\text{GeV}$, $|\eta| < 2.37$ are rejected. We do not explicitly implement these cuts because our signal samples do not contain isolated hard leptons or photons at the matrix element level, and generating them from hadron decay is very unlikely.

We have verified our analysis by simulating the $W+\text{jets}$ background, where the W-boson decays to a muon and an (anti)neutrino, as well as the $Z+\text{jets}$ background, where the Z-boson decays to a neutrino and an antineutrino. These samples where generated with MadGraph at leading order, including up to four jets at the matrix element level. As a cross-check, we have also considered samples generated with MadGraph at next-to-leading order, including up to two jets in the matrix element. For our actual analysis, we have not used these background samples, but instead rely on the ones published by ATLAS in Ref. [128], see in particular Table 8 therein. Besides $W+\text{jets}$ and $Z+\text{jets}$, additional backgrounds arise from diboson, $t\bar{t}$, and single-top production.

There are several sources of systematic uncertainties: *(i)* Uncertainties related to the modelling of initial- and final-state radiation. These errors translate into a 3–6% uncertainty in the signal acceptance, common to all s-channel models considered here. *(ii)* PDF uncertainties. The choice of different PDF sets results in a variation of up to 20%, depending on the model considered. *(iii)* Renormalisation and factorisation scales. Varying these scales introduces changes of up to 50% in the cross section after cuts, depending on the model considered. *(iv)* Experimental uncertainties in the jet and $E_{\text{T}}^{\text{miss}}$ scales. Depending on the parameters of the model, these uncertainties vary between 1% and 7%, with the relative uncertainties in energetic events being generally larger than those in softer events. They are similar for the vector, axial vector, scalar, and pseudoscalar models. *(v)* Luminosity. The uncertainty in the total integrated luminosity is 1.7%. We subsume uncertainties *(i)*–*(iii)* into a flat 30% signal uncertainty, and *(iv)* is described in our analysis by a 10% uncertainty that is correlated between signal and background. Uncertainty *(v)* is included separately. While this approach is certainly less accurate than the one employed by the ATLAS collaboration, it is sufficient for our purposes, given that we are studying simplified models, and deviations between those and the true model of DM can be expected to be much larger. For instance, the dominant signal error, arising from the variation of renormalisation and factorisation scales, is effectively a measure for the impact of higher-order corrections. However, it can play that role only as long as no additional particles exist in the model. If there are additional states that contribute to DM production (at tree level or in loop diagrams), these may lead to extra deviations from the predictions of the simplified model.

Our main results for the ATLAS monojet analysis [128] are shown in Figure 3.7. The four panels in this figure correspond to vector, axial vector, scalar, and pseudoscalar mediators, respectively. In each panel we show the 95% confidence level (CL) limit on the

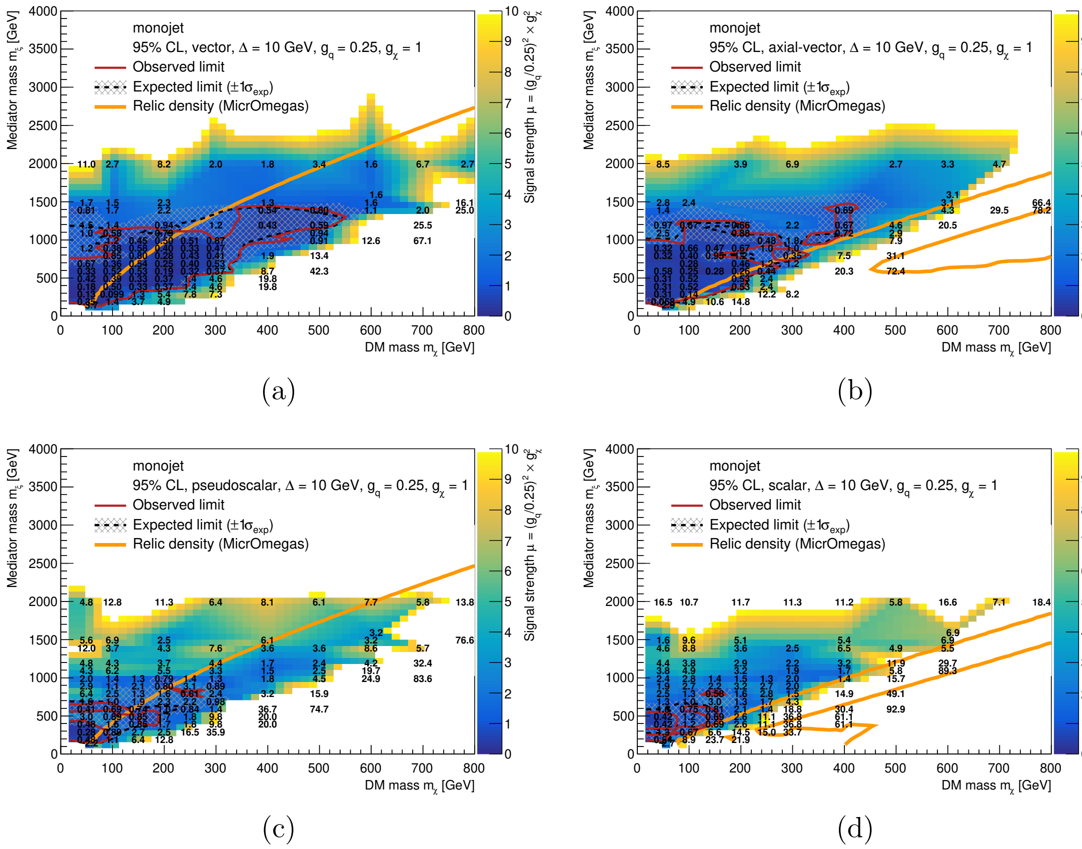

Figure 3.7: 95% CL limits set by our recasting of the ATLAS monojet analysis [128] on the DM production cross section via $pp \to \chi^* \bar{\chi}\,(j)$, plus the corresponding CP-conjugate processes. For the chosen values of the coupling constants, $g_q = 0.25$ and $g_\chi = 1$, the red contours show the regions in the m_χ–m_ξ (DM mass vs. mediator mass) plane that are excluded. Dashed black contours show the corresponding expected limits, and the hatched regions indicate the 1σ uncertainty on that expectation. Away from the exclusion contours, the colour code demonstrates the excluded signal strength. In other words, it shows by how much stronger or weaker the signal at a given point would need to be compared to the benchmark scenario for the exclusion contour to move to that point. The excluded values of the coupling constants at given m_χ, m_ξ, can be directly inferred from this. We show in orange the parameter values at which the correct DM relic density is predicted in the corresponding simplified model using MicrOmegas [264]. The four panels correspond to (a) vector, (b) axial vector, (c) pseudoscalar, and (d) scalar mediators, respectively.

DM–SM couplings as a function of the DM mass m_χ and the mediator mass m_ξ. We do so by indicating, at each point, the limit on the "signal strength" μ, *i.e.* the DM production cross section relative to a benchmark parameter point. The latter is defined by $g_q = 0.25$, $g_\chi = 1$, so that $\mu = (g_q/0.25)^2 \cdot g_\chi^2$. Colour-shading represents the same information graphically and interpolates between the sampling points in (m_χ, m_ξ). The red contour delimits the parameter region that is excluded at the 95% CL, while the black dashed contour and hatched band indicate the expected limit and its 1σ uncertainty, respectively. Note that the uneven distribution of the limits is not physical, but instead caused by the sensitivity to fluctuations of our limit setting algorithm. Our signal strength limits indicate how close the analysis gets to an exclusion limit at a given parameter point, $\mu = 1$ defines the limit. In all panels, we have assumed a mass splitting of the dark states of $\Delta = 10\,\mathrm{GeV}$, but we note that the monojet search is not sensitive to Δ unless the splitting becomes so large that the kinematics of χ and χ^* differ substantially.

As expected from the cross sections displayed in Figure 3.3, limits are strongest for the vector-mediated model, followed by the axial vector model. Mediator masses up to almost 1.5 TeV can be excluded in some cases thanks to resonant enhancement of DM production. The DM mass, on the other hand, can only be probed up to $\sim 600\,\mathrm{GeV}$. The reach in m_χ is more limited first because two DM particles need to be produced in each event, and second because at high mass, only a small fraction of the partonic centre-of-mass energy will typically be left for the required ISR jet.

In Figure 3.8 we show the best signal regions that are selected by the limit setting analysis. The four panels correspond to the limit plots of the different mediators in Figure 3.7. Each coloured symbol in the plot marks a simulation point and indicates the signal region providing the best limit for that set of parameters. We obtain the best limits mostly for the high $E_\mathrm{T}^\mathrm{miss}$ exclusive regions E8 to E12 with very few exceptions. This implies we get an effective $E_\mathrm{T}^\mathrm{miss}$ cut of over 800 GeV (E8 selects the $E_\mathrm{T}^\mathrm{miss}$ interval of 800 to 900 GeV) up to 1.2 TeV (E12 selects $E_\mathrm{T}^\mathrm{miss} > 1200\,\mathrm{GeV}$). We expect the higher $E_\mathrm{T}^\mathrm{miss}$ regions to give better limits, since the background rates decrease faster with increasing $E_\mathrm{T}^\mathrm{miss}$ than the signal rates.

In Figure 3.9 we show an exemplary data set to illustrate the distribution of signal and background in the different $E_\mathrm{T}^\mathrm{miss}$ signal regions. We chose a DM mass of $m_\chi = 50\,\mathrm{GeV}$, a mediator mass of $m_\xi = 600\,\mathrm{GeV}$ and a splitting $\Delta = 10\,\mathrm{GeV}$ and the couplings are again $g_q = 0.25$ and $g_\chi = 1$. The plot shows the overwhelming background in the lower $E_\mathrm{T}^\mathrm{miss}$ bins that makes it difficult to set a limit. At higher $E_\mathrm{T}^\mathrm{miss}$, the number of signal and SM background events become comparable, but also the uncertainties are more dominant. Comparing to Figure 3.8, our plot illustrates that low signal regions are not providing the best limits due to the dominant background.

We note that our limits are weaker than the limits on the standard WIMP scenario in the ATLAS monojet analysis itself [128] (Figure 5 therein), where they give limits on the axial vector and pseudoscalar mediated case. For the pseudoscalar mediator, this is primarily because, in Ref. [128], the mediator coupling to quarks is set to $g_q = 1$ instead

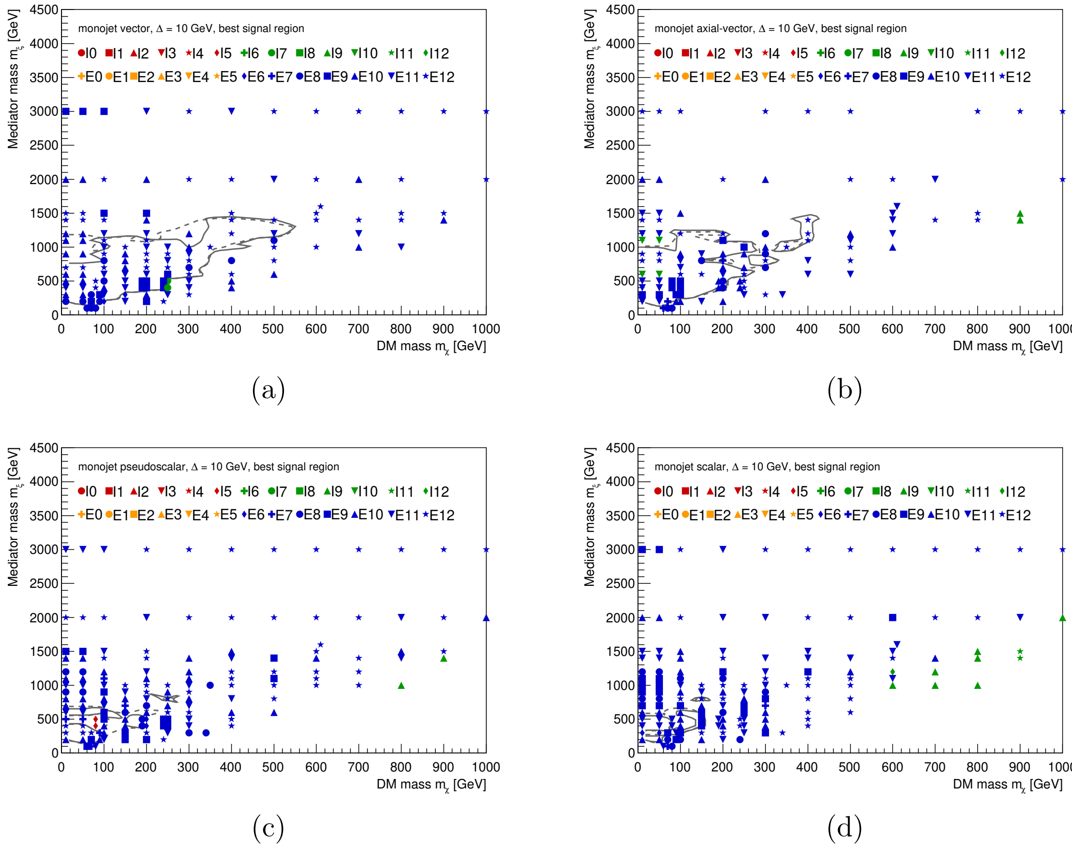

Figure 3.8: Best signal regions that are selected by the limit setting analysis for the ATLAS monojet analysis [128]. The plots for the different mediators correspond to the respective plots in Figure 3.7. The couplings are as before set to $g_q = 0.25$ and $g_\chi = 1$. The four panels correspond to (a) vector, (b) axial vector, (c) pseudoscalar, and (d) scalar mediated interactions, respectively.

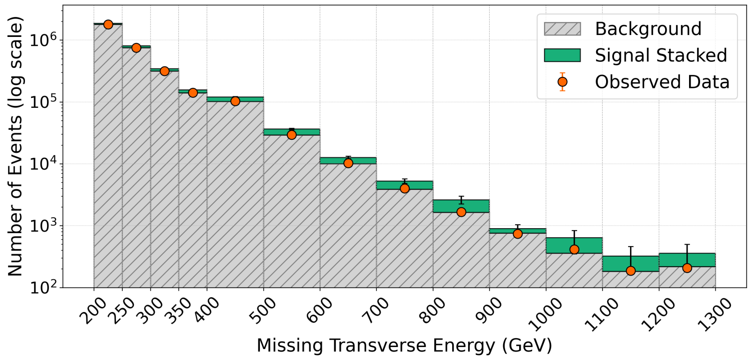

Figure 3.9: Exemplary plot showing number of events in each exclusive signal region for the SM background (grey, hatched), stacked signal events (green) and observed data (orange, circles). The chosen model parameters are a DM mass of $m_\chi = 50\,\text{GeV}$, mediator mass $m_\xi = 600\,\text{GeV}$ and splitting $\Delta = 10\,\text{GeV}$. The couplings are as before set to $g_q = 0.25$ and $g_\chi = 1$.

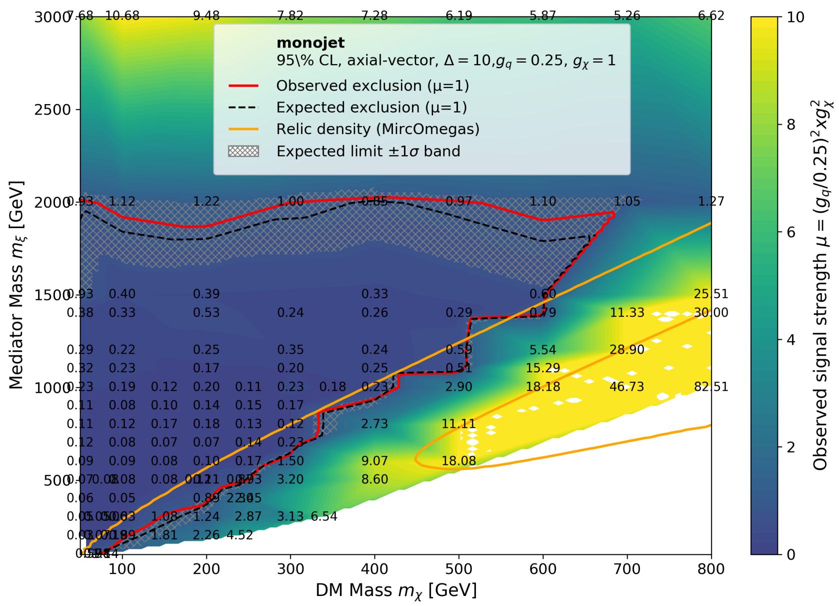

Figure 3.10: Exclusion limit on the DM production cross section via $pp \to \chi^* \bar{\chi}$, plus the corresponding CP-conjugate processes for the axial vector case, assuming systematic errors of only 1%. As before we have set the coupling constants to $g_q = 0.25$ and $g_\chi = 1$. The red contour shows the observed exclusion limit, while the expected limit including the hatched error band is shown in black, dashed. The colouring encodes the observed exclusion limit on the signal strength μ. The plot corresponds to the axial vector case in Figure 3.7 (b), simply reducing the systematic errors.

of our choice of $g_q = 0.25$. For the axial vector mediated case the coupling constants coincide, $g_q = 0.25$ and $g_\chi = 1$. Most importantly, our inelastic DM scenario admits two DM production processes ($\bar{q}q \to \chi\bar{\chi}^*$ and $\bar{q}q \to \chi^*\bar{\chi}$), as opposed to only one $\bar{q}q \to \chi\bar{\chi}$ in ATLAS' simplified model. However, the limits in Ref. [128] are better because of their more elaborate analysis. While our analysis is very susceptible to the large systematic errors that we assume, the combination of the individual signal regions would help reduce the effect of these errors. We show in Figure 3.10 an adjusted plot, assuming a systematic error of only 1% for the axial vector mediated case. This limit is comparable or even slightly stronger (reaching to higher DM masses) than the ATLAS limit on the WIMP scenario. Therefore, combining the different signal regions and thereby reducing the effect of systematic errors, would greatly improve our monojet limits in Figure 3.7.

Each plot includes a contour (shown in orange) that indicates the values of m_χ and m_ξ for which the correct relic density is predicted at the nominal values of the ξ couplings indicated in the plots ($g_q = 0.25$, $g_\chi = 1$). The computation of the relic density has been carried out in MicrOMEGAs v5.2.7 [264–266]. In the region above the orange curves (large m_ξ), the model over predicts the relic density as ξ-mediated annihilation is inefficient, so freeze-out happens too early. Parameter points in this region might still be viable if there are extra annihilation or co-annihilation channels that are active in the early Universe, but not included in the simplified Lagrangians from eqs. (3.3) to (3.6). In the region below the orange curves, the predicted relic density is too low, possibly necessitating the existence of additional DM species. Note that, for the axial vector model, a secondary "wedge" of allowed parameter values appears at $m_\chi \gtrsim 500\,\mathrm{GeV}$. For the scalar model, a similar feature can be seen, extending to even lower DM masses. At the lower boundary of these wedges, the correct relic density is achieved through $\chi\bar{\chi} \to \xi\xi$ rather than $\chi\bar{\chi}^* \to q\bar{q}$ annihilation. Inside the wedge, $\chi\bar{\chi} \to \xi\xi$ becomes inefficient, leading to a relic density that is too large. As m_ξ is increased further, the ξ-mediated s-channel process $\chi\bar{\chi}^* \to q\bar{q}$ eventually becomes resonantly enhanced, leading to an intermittent drop in the predicted Ωh^2 at $m_\xi \simeq 2m_\chi$. The differences in the shape of the wedge between the scalar and axial vector models has to do with the different suppression factors of $\chi\bar{\chi}^* \to q\bar{q}$ in these two scenarios. For the scalar, annihilation to quarks is a p-wave process and is therefore velocity-suppressed. For the axial vector case, s-wave annihilation is possible, but comes with a chiral suppression factor m_q^2/m_χ^2 [267]. Note that the aforementioned resonance feature at $m_\xi \simeq 2m_\chi$ exists also for the vector and pseudoscalar scenarios. But for those, the relic density remains smaller than the observed value everywhere below the resonance because $\chi\bar{\chi}^* \to q\bar{q}$ annihilation through vector or pseudoscalar couplings is an unsuppressed s-wave process. This is also the reason why the correct relic density is achieved at higher m_ξ for these models than for the scalar and axial vector ones.

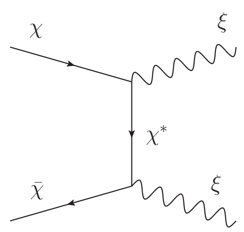

Figure 3.11: $\chi\bar{\chi} \to \xi\xi$

Essential probes on models featuring a mediator ξ coupled to a quark pair $\bar{q}q$ are dijet searches via $pp \to \xi \to jj$. ATLAS and CMS show limits that exclude large parts of our parameter space, see Refs. [268, 269]. However, this is a common problem of simplified models, which could be fixed by a larger DM coupling g_χ or a smaller value of the coupling to quarks g_q, see Section 3.7 for more details.

3.6 Displaced Vertex Search

Decays of long-lived dark sector particles – like our excited DM state χ^* – can lead to displaced vertex signatures in combination with large missing transverse momentum. If a sufficient fraction of the long-lived particle's energy goes to visible decay products, the mass $m_{\rm DV}$ associated with the displaced vertex (defined as the invariant mass of all visible particles emerging from the vertex) can be very large. Final states with displaced vertices are being searched for by the ATLAS and CMS collaborations, see for instance Ref. [270] for an ATLAS analysis of $20.3\,\mathrm{fb}^{-1}$ of data taken at $\sqrt{s} = 8\,\mathrm{TeV}$, Ref. [129] for an ATLAS analysis using $32.8\,\mathrm{fb}^{-1}$ of 13 TeV data, and Ref. [252] for an analysis using $132\,\mathrm{fb}^{-1}$ of 13 TeV CMS data. Unfortunately, the observed event counts in all the above references are consistent with background expectations.

In the following, we recast the analysis from Ref. [129] into limits on inelastic DM. We use the same simulation chain as for the monojet analysis, described in Section 3.3 (MadGraph v2.6.2 [254, 255], Pythia 8 [271], Delphes 3.4.1 [258]). The analysis requires at least one displaced vertex (DV), fulfilling the following criteria:

1. The transverse distance between the displaced vertex and the primary interaction point, L_{xy}, has to satisfy $4\,\mathrm{mm} < L_{xy} < 300\,\mathrm{mm}$. The displacement along the beam axis, L_z, must be $< 300\,\mathrm{mm}$.
2. There have to be at least five charged and (within the tracking volume) stable particles originating from the displaced vertex. They must have $p_T > 1\,\mathrm{GeV}$ and an approximate transverse impact parameter with respect to the primary vertex of $d_0 = L_{xy} \sin\Delta\phi > 2\,\mathrm{mm}$. Here, $\Delta\phi$ is the azimuthal angle between the particle momentum at creation and the vector from the interaction point to the displaced vertex. The cut on d_0 ensures that tracks originating from the primary vertex rather than the displaced one are rejected more efficiently. Unfortunately, it also tends to reject the forward-boosted decays of very energetic χ^* particles, which would otherwise be easiest to detect.
3. The invariant mass of the displaced vertex, $m_{\rm DV}$, reconstructed from the visible decay products fulfilling the above criteria, has to be larger than 10 GeV.

Besides a displaced vertex with the above properties, events must have $E_{\rm T}^{\rm miss} > 200\,\mathrm{GeV}$,[2] and in 75% of the data it was moreover required that either one displaced jet with

[2] In Ref. [129] the cited cut at reconstruction level is $E_{\rm T}^{\rm miss} > 250\,\mathrm{GeV}$, but the efficiencies from the auxiliary material are based on this truth level cut and take the efficiencies of passing the reconstruction level cut into account.

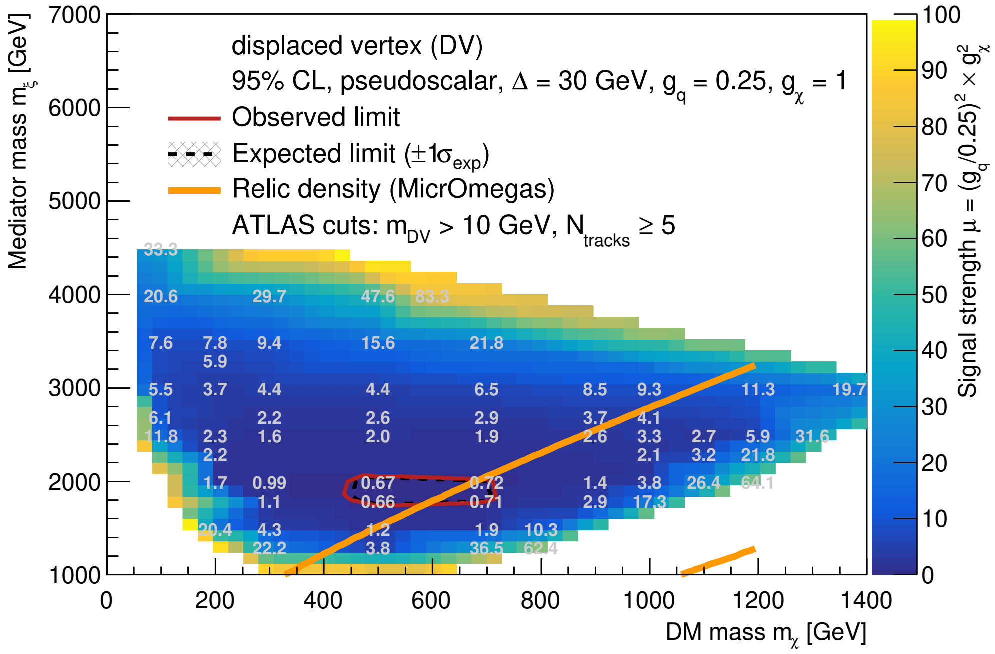

Figure 3.12: Limits set by the ATLAS displaced vertex search from Ref. [129] on the production of inelastic DM with a pseudoscalar mediator and a splitting between the dark states of $\Delta = 30\,\text{GeV}$. The couplings are set to $g_q = 0.25$ and $g_\chi = 1$. Limits are given in terms of the signal strength $\mu = (g_q/0.25)^2 \cdot g_\chi^2$ (numbers in the plot and interpolating colour gradient), while the benchmark couplings $g_q = 0.25$, $g_\chi = 1$ are excluded at 95% CL within the red contour. The black contour and the hatched band show the expected limit and its 1σ uncertainty, respectively. The masses at which the correct relic density is predicted with $g_q = 0.25$, $g_\chi = 1$ is shown in orange.

$p_T > 70\,\text{GeV}$, or two such jets with $p_T > 25\,\text{GeV}$ are present. A jet is called displaced if the scalar p_T sum of all charged particles associated with the jet and originating from the primary vertex does not exceed $5\,\text{GeV}$. A particle is associated with the primary vertex if its impact parameter is $d_0 < 2\,\text{mm}$. Monte Carlo events fulfilling these additional displaced jet criteria are fully counted in our analysis, while events not passing are weighted by a factor of 0.25.

Events surviving the above cuts are first weighted with the E_T^{miss}-dependent event-level efficiency factors shown in Figure 20 of the auxiliary material published with Ref. [129]. In a second step, events are binned by their transverse χ^* decay distance L_{xy}, their invariant mass of the displaced vertex m_{DV}, and the number of identified tracks associated with the displaced vertex. We then apply the vertex identification efficiencies from Figures 21 and 22 of Ref. [129]'s auxiliary material.

The following systematic uncertainties are relevant: *(i)* Variation of simulated pile-up. The signal efficiencies determined in Ref. [129] vary by up to 10% as a function of the amount of pile-up included in the Monte Carlo samples. *(ii)* Track and displaced vertex reconstruction efficiency. This uncertainty amounts to 5–10% as well. *(iii)* Treatment of ISR. Depending on how radiation effects are modelled, the signal acceptance varies by up to 25%. *(iV)* The uncertainty in the total integrated luminosity is 3.2%. We combine uncertainties *(i)* and *(ii)* into a flat 15% systematic error. The 25% error *(iii)*, as well as the luminosity uncertainty *(iV)* are included separately. Note that using the uncertainties quoted in Ref. [129] as a basis for our treatment of systematics is justified even though the signal model considered there (R-hadrons) is different from our inelastic DM scenarios. One may wonder whether in particular uncertainty *(iii)* – treatment of ISR – depends on this. However, ISR should be largely independent of the hard process, therefore we expect only little model dependence in the systematic error estimates.

Note that there is no SM background in high-mass displaced vertex searches; any backgrounds are instrumental in origin, and tiny. For instance, the prediction for the instrumental backgrounds in Ref. [129] is $0.02^{+0.02}_{-0.01}$ events.

In Figure 3.12 we show the resulting limit of our recast of the ATLAS analysis from Ref. [129]. Because of the cut on the invariant mass of the displaced vertex, $m_{\mathrm{DV}} > 10\,\mathrm{GeV}$, the search requires the mass splitting of the dark states Δ to be well above that value. We show the limit for a splitting of $\Delta = 30\,\mathrm{GeV}$. This large value of the mass splitting of the dark states leads to a decrease in the χ^* lifetime, which causes us to loose sensitivity for the vector, axial vector and scalar mediators. For a pseudoscalar mediator ξ, the χ^* decay width is suppressed by an additional factor Δ^2/m_χ^2 (see eq. (3.21)), hence its lifetime is sufficiently long to lead to an appreciable number of displaced vertex events. Therefore, we show only limits on the pseudoscalar model in Figure 3.12. The numbers in the plot and the colour gradient once again give the 95% CL limit on the signal strength, the red contour is the observed exclusion limit on the benchmark model with $g_q = 0.25$, $g_\chi = 1$, the black contour is the expected limit, and the hatched band is the 1σ error on the latter. In orange, we show again the $(m_\chi,\, m_\xi)$ combinations for which the correct relic density is obtained at $g_q = 0.25$, $g_\chi = 1$ (computed in MicrOMEGAs).

In contrast to the monojet analysis, the sensitivity of the displaced vertex analysis depends strongly on the χ and ξ masses, as can be seen in the rapid increase of the excluded signal strength away from the red contour in Figure 3.12. At low m_ξ, the decay length of the intermediate χ^* becomes too short, so its decay vertices will not be sufficiently displaced from the primary vertex, see Figure 3.13 as an example. At large m_ξ, the DM production cross section drops rapidly. The analysis can exclude DM masses between about 450 GeV and 700 GeV for a mediator mass of roughly two TeV. The displaced vertex search is complementary to the monojet search as it is sensitive to the pseudoscalar mediated model, for which the monojet limits stayed below mediator masses of one TeV and DM masses of 300 GeV. Keep in mind, though, that the splitting of the dark states is taken to be 30 GeV in the displaced vertex search, compared to

10 GeV for the monojet search. Taking a smaller splitting would significantly lower the reach in DM and mediator mass.

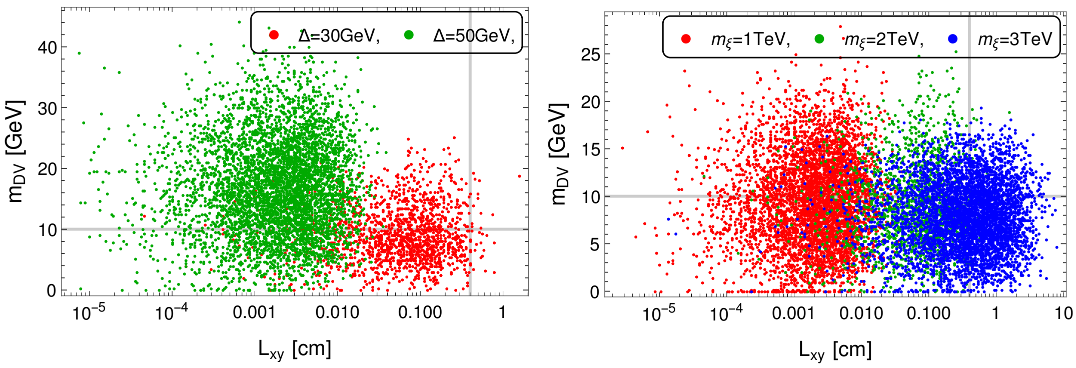

(a) $m_\chi = 100\,\text{GeV}$, $m_\xi = 2\,\text{TeV}$

(b) $m_\chi = 100\,\text{GeV}$, $\Delta = 30\,\text{GeV}$

Figure 3.13: Distribution of parameter points in the plane of the mass of the displaced vertex m_{DV} and the transverse decay distance L_{xy} for a pseudoscalar mediator and a DM mass of $m_\chi = 100\,\text{GeV}$. The left panel varies the splitting $\Delta = 30\,\text{GeV}$ (red dots), $\Delta = 50\,\text{GeV}$ (green dots) and keeps the mediator mass at $m_\xi = 2\,\text{TeV}$. The right panel varies the mediator masses between $m_\xi = 1\,\text{TeV}$ (red dots), $m_\xi = 2\,\text{TeV}$ (green dots) and $m_\xi = 3\,\text{TeV}$ (blue dots) for fixed $\Delta = 30\,\text{GeV}$. The grey grid lines mark the cuts on m_{DV} and L_{xy}.

To illustrate the impact of the model parameters on the key observables of this analysis, we show the distributions of events in the plane of transverse decay distance L_{xy} and invariant mass of the displaced vertex m_{DV} in Figure 3.13. A larger mass splitting of the dark states shifts the mass of the displaced vertex m_{DV} to higher values, as expected, but also significantly decreases the transverse decay distance L_{xy}, making it difficult to balance the requirements on $m_{\text{DV}} > 10\,\text{GeV}$ and $0.4\,\text{cm} < L_{xy} < 30\,\text{cm}$, see Figure 3.13 (a). We include grey grid lines to depict the cuts, the upper right corner is passing the requirements. All events for $\Delta = 50\,\text{GeV}$ are excluded, and only very few for $\Delta = 30\,\text{GeV}$ are passing both cuts. In Figure 3.13 (b) we can see that a higher mediator mass m_ξ shifts the decay distance L_{xy} to higher values, but again it diminishes the mass of the displaced vertex m_{DV} at the same time. The correlation is, however, weaker than for the splitting. Mediator masses of $m_\xi = 1\,\text{TeV}$ are entirely excluded, for $m_\xi = 2\,\text{TeV}$ a few events pass the cuts. With varying the DM mass, there is no clear correlation visible for the DM mass range we considered, neither with respect to L_{xy}, nor to m_{DV}; hence we did not include a corresponding plot.

Because of the large impact of the cut on the displaced vertex mass m_{DV}, we have also investigated how relaxing the m_{DV} cut and the cut on the number of tracks associated with the displaced vertex, N_{tracks}, could change the sensitivity to simplified inelastic DM models.

In Ref. [272], the authors propose to relax the cuts from the ATLAS analysis in

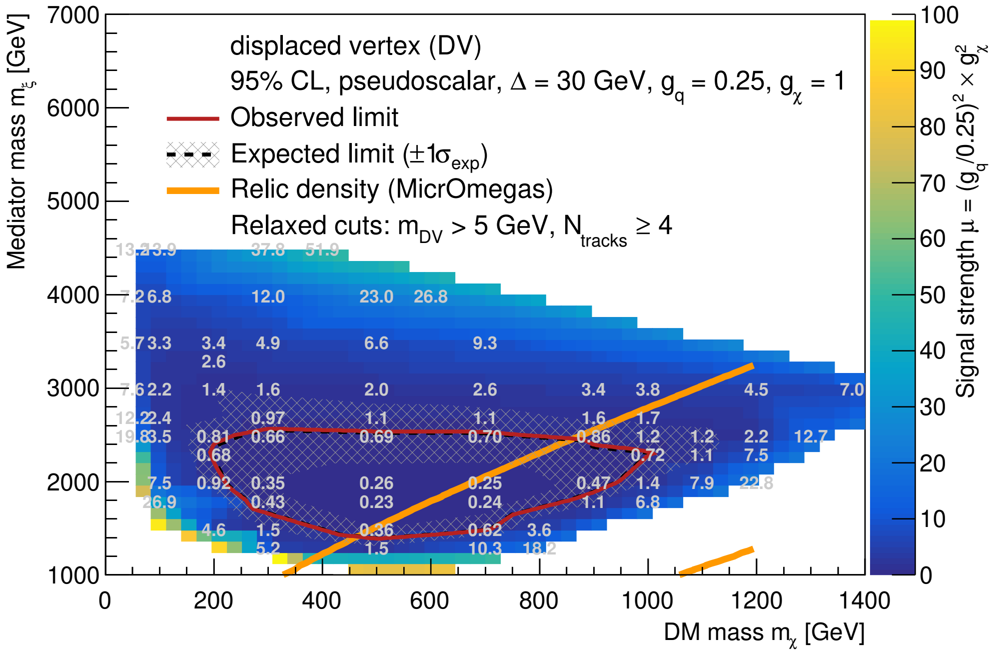

(a)

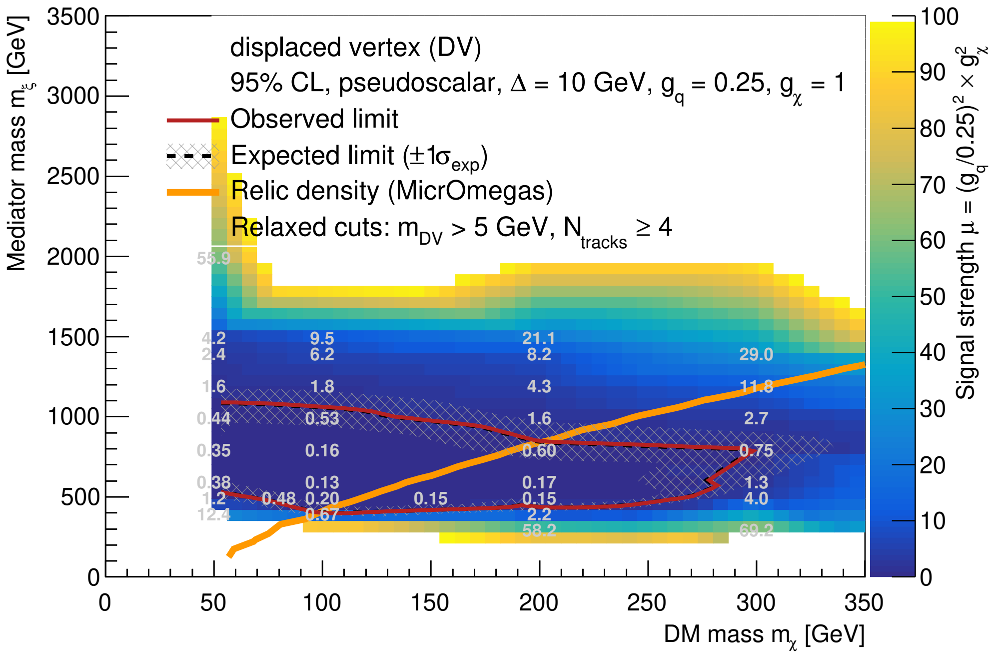

(b)

Figure 3.14: Projected limit on the production of inelastic DM, similar to Figure 3.12, but with relaxed cuts on N_{tracks} and m_{DV}. Panel (a) corresponds to a mass splitting $\Delta = 30\,\text{GeV}$ (same as in Figure 3.12), while panel (b) is for $\Delta = 10\,\text{GeV}$.

Ref. [129], inspired by a study in Ref. [273]. The cut on N_{tracks} is reduced by one to be $N_{\text{tracks}} \geq 4$, and the vertex mass is required to be only $m_{\text{DV}} > 5\,\text{GeV}$. We assume the efficiencies given in Ref. [129]'s auxiliary material to be constant for m_{DV} below 10 GeV and N_{tracks} below 5.

One might worry that this relaxation of cuts could raise the background rates. However, Figure 7 in Ref. [129] shows that no events are observed in the data even within the extended signal region with $m_{\text{DV}} > 5\,\text{GeV}$ and $N_{\text{tracks}} \geq 4$. Moreover, Table 1 in that same reference indicates that a low-$E_{\text{T}}^{\text{miss}}$ control region with $N_{\text{tracks}} = 4$ contains only about a factor of two more events than a similar control region with $N_{\text{tracks}} \geq 5$, which suggests that also the number of background events expected to spill over into the signal regions will not increase significantly with the weakened cuts. This motivates us to posit that backgrounds will remain negligible even with relaxed cuts.

Repeating the statistical analysis with relaxed cuts on N_{tracks} and m_{DV}, we obtain for a mass splitting of $\Delta = 30\,\text{GeV}$ the projected limit shown in Figure 3.14 (a). The reach at low mediator mass m_ξ remains more or less unchanged since it is dominated by the cut on L_{xy}: below $m_\xi \approx 1.5\,\text{TeV}$ the decay length of χ^* becomes too short to be above the required 4 mm (particularly visible in Figure 3.13 (b)). We can see, however, compared to Figure 3.12, that the projected limit extends to a larger region of DM masses: while in the original analysis we can exclude parameter space between DM masses of about 450 to 700 GeV, relaxing the cuts would allow to exclude a region from 200 GeV to one TeV. Also the reach in mediator mass m_ξ shifts to higher values (we saw in Figure 3.13 (b) that for higher m_ξ, the mass of the vertex decreases), allowing for a significantly larger chunk of the parameter space to be excluded.

As we mentioned above, the strict cut on the displaced vertex mass m_{DV} forced us to consider quite a large mass splitting Δ of the dark states. Relaxing this cut now opens up the possibility to study smaller values of Δ. We therefore reanalysed the case we studied in the monojet analysis, where we considered a mass splitting of $\Delta = 10\,\text{GeV}$. This mass splitting is still too large to induce decay lengths above 4 mm for the vector, axial vector and scalar mediators, but we obtain a projected limit in the pseudoscalar-mediated case, see Figure 3.14 (b). For our benchmark couplings, we could now exclude the parameter space between $m_\xi \sim 400\,\text{GeV}$ and $m_\xi \sim 1.1\,\text{TeV}$ at DM masses m_χ up to around 300 GeV.[3]

3.7 Other Searches

Besides the monojet and displaced vertex searches discussed above, inelastic DM can appear in a number of other LHC analyses. These include, for instance, studies targeting so-called displaced lepton jets or dark photon jets. These searches are sufficiently

[3] Note that the cut below DM masses of 50 GeV that is striking out in this plot is simply because our simulated parameter points start there. We did not consider smaller DM masses, since then the mass splitting becomes too large compared to the total DM mass.

generic to pick up also displaced hadronic jets. However, they typically require pairs of displaced dark photon jets, motivated by new models in which long-lived particles are pair-produced [274–276]. A similar limitation applies to many dedicated analyses of displaced hadronic jets, with several examples provided by CMS [277–281] and ATLAS [282–284].

We took a more detailed look into the analysis in Ref. [276], where the crucial type of jet for our purposes is the displaced hadronic dark photon jet (hDPJ). It is defined as a jet with an electromagnetic energy fraction (meaning the ratio of jet energy deposited in the electromagnetic calorimeter, E_{ECAL}, over the total energy of the jet, E_{total}) less than 0.4.[4] In addition, no muons are allowed inside the jet cone. Two of these dark photon jets (DPJs) are required in the analysis.

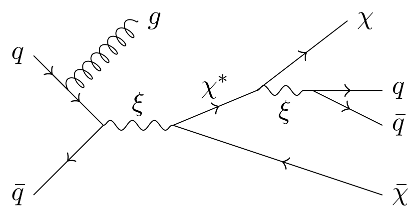

Figure 3.15: DM production $pp \to \bar{\chi}(\chi^* \to \chi\bar{q}q)$ including ISR (quoting Figure 3.2)

According to the Feynman diagram from Figure 3.15 (quoting Figure 3.2), the two displaced jets would need to arise from the two final state quarks in the $\chi^* \to \chi + (\xi \to q\bar{q})$ decay. However, in most events, the quarks will be either too collimated or too soft to pass the analysis cuts. Moreover, the requirement of low $E_{\mathrm{ECAL}}/E_{\mathrm{total}}$ implies that the search is most sensitive to jets originating beyond the inner edge of the electromagnetic calorimeter. This corresponds to a minimum displacement of 147.1 cm. In our inelastic DM scenario, these decay lengths can be achieved by either very small mass splittings of the dark states or rather large mediator masses. A small mass splitting would leave very little energy to the hadronic decay products of the χ^*, making a detection very unlikely. Large mediator masses, on the other hand, lead to a large boost of the decay products and the quarks from the χ^* decay would be collimated into one single jet. For the pseudoscalar case, the decay length also grows with increasing DM mass (see Figure 3.1), but at the same time the cross section decreases too fast.

Overall, the requirement of two displaced jets together with a large displacement make it impossible for the search to place limits on the simplified inelastic DM models considered here. To illustrate the problem we plotted the number of jets N(j) and the transverse momentum of the leading jet $p_T(j_1)$ in a sample without initial state radiation (ISR), final state radiation (FSR) and multi-parton interactions (MPI). This leaves only the (displaced) jets from the χ^* decay. We show the results for $\Delta = 10\,\mathrm{GeV}$, $m_\chi = 50\,\mathrm{GeV}$ and different mediator masses in Figure 3.16 on the left. On the right we show the same plots for a splitting of $\Delta = 2\,\mathrm{GeV}$. There are almost no events containing two jets, as we would need for the analyses quoted above. The comparison of the plots showing the leading jet p_T illustrates clearly that with decreasing mass splitting Δ, the

[4]Since the ECAL is the calorimeter closest to the beamline, a low fraction of energy deposited in the ECAL indicates that the particle decayed within or beyond its position. For a detailed description of the ATLAS detector and its calorimeters, see Ref. [285].

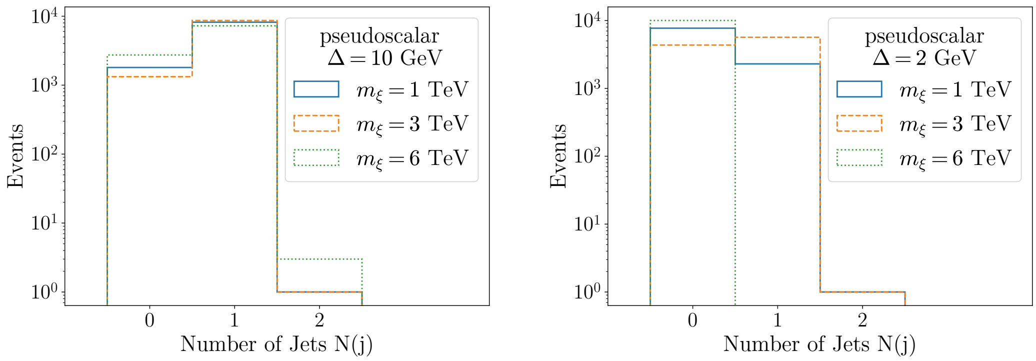

(a) Jet multiplicity N(j) for $\Delta = 10\,\text{GeV}$ **(b)** Jet multiplicity N(j) for $\Delta = 2\,\text{GeV}$

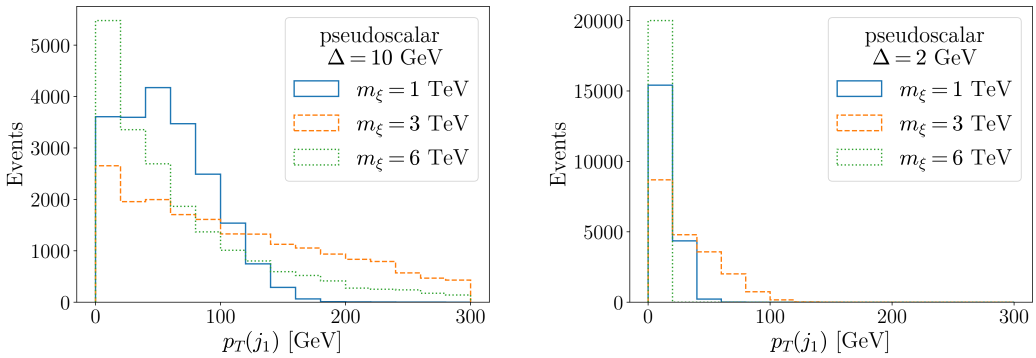

(c) Leading jet $p_T(j_1)$ for $\Delta = 10\,\text{GeV}$. **(d)** Leading jet $p_T(j_1)$ for $\Delta = 2\,\text{GeV}$.

Figure 3.16: Jet multiplicity N(j) and transverse momentum of the leading jet $p_T(j1)$ for a pseudoscalar mediator, given without initial and final state radiation (ISR, FSR) and multi parton interactions (MPI) to display only the potentially displaced jets from the decay of χ^*. We set the DM mass to $m_\chi = 50\,\text{GeV}$ and as before we use $g_q = 0.25$, $g_\chi = 1$. The mediator mass is varied from $m_\xi = 1\,\text{TeV}$ (blue, solid) to $m_\xi = 3\,\text{TeV}$ (orange, dashed) to $m_\xi = 6\,\text{TeV}$ (green, dotted) and we also plot two different splittings of the dark states, $\Delta = 10\,\text{GeV}$ (left row) and $\Delta = 2\,\text{GeV}$ (right row). The overwhelming majority of events contain none or only one jet (note the logarithmic scale). With decreasing mass splitting, the transverse momentum of the leading jet decreases rapidly. Note that for the transverse momentum of the leading jet, events with no (detectable) jets are included in the plot with $p_T(j_1) = 0$.

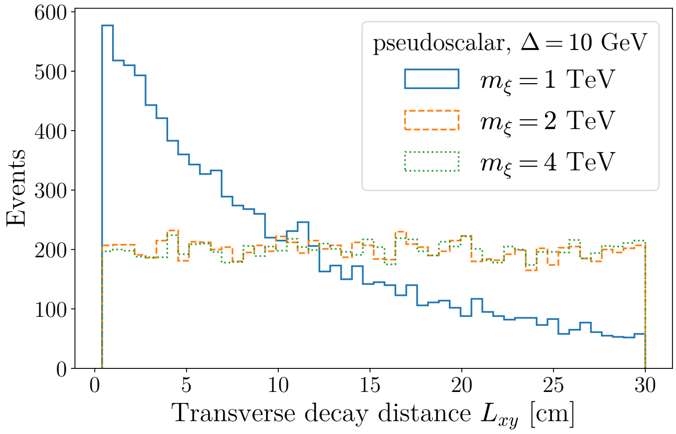

Figure 3.17: The transverse decay distance L_{xy} for mediator masses of $m_\xi = 1\,\text{TeV}$ (blue, solid), $m_\xi = 2\,\text{TeV}$ (orange, dashed), and $m_\xi = 4\,\text{TeV}$ (green, dotted). The DM mass is $m_\chi = 50\,\text{GeV}$ and we use the couplings $g_q = 0.25$, $g_\chi = 1$. Note that the data include here a Monte Carlo level cut on $E_T^{\text{miss}} > 120\,\text{GeV}$.

energy left to the two quarks in the χ^* decay decreases rapidly. (Note that events with no (detectable) jet are included in the plot with $p_T(j_1) = 0$.) In Figure 3.17 we show the dependence of the transverse decay distance on different mediator masses, $m_\xi = 1\,\text{TeV}$, $m_\xi = 2\,\text{TeV}$, and $m_\xi = 4\,\text{TeV}$. For higher mediator masses, the boost of the mediator leads to larger decay distances, as long as it can become on-shell. The production cross section is, however, decreasing at the same time – it scales with $1/(m_\xi^4)$. A lower mass splitting Δ also significantly increases the decay distance, but leaves a lot less energy to the decay products, see Figure 3.16, second line. Most jets for a splitting of $\Delta = 2\,\text{GeV}$ will therefore be undetected. The example of $m_\xi = 6\,\text{TeV}$ and $\Delta = 2\,\text{GeV}$ even produces no jet at all from the χ^* decay.

The jet multiplicity is also plotted in Figures 3.6 and 3.5. Note that since these plots include initial and final state radiation and multi-parton interactions, the number of jets is a lot larger. These additional jets are, however, not displaced and do not contribute to the analyses considered here.

These considerations motivate to look for analyses that do not require a pair of displaced jets. There are some searches allowing for only one displaced hadronic jet, but they require leptons in the final state [286–288]. Another search is even targeting inelastic DM, but assumes the mediator to couple to muons [289], whereas our model assumes a coupling to quarks. For a broad overview on dark sector searches at CMS, see Ref. [290]. We found two searches requiring only one displaced hadronic jet, where the decay has to take place in the muon spectrometer [116] (distance to primary vertex between 3 and 14 m) or the muon endcap detectors [291] ($c\tau$ between about 1 to 10 m), requiring very large decay lengths. These searches might be sensitive at small mass splittings and larger mediator masses, such that the proper decay length becomes longer and is additionally boosted by the energy of the mediator. Another search by CMS [292] allows for one displaced jet and smaller decay lengths, but the mass splitting has to be rather large for the analysis to be efficient[5]. We leave the study of these interesting searches for future work.

A crucial probe of inelastic DM models are dijet searches looking for the mediator of the simplified models. In fact, the resonant process $pp \to \xi \to jj$ offers significant discovery potential up to very large m_ξ. The most recent ATLAS dijet search is the one in Ref. [293], while the corresponding CMS result is Ref. [294]. The exclusion plots in these papers cover resonance masses $> 1.5\,\text{TeV}$ (ATLAS) and $> 1.8\,\text{TeV}$ (CMS), respectively, which are outside the m_ξ range that is of prime interest to us. Other analyses such as Refs. [268, 269] cover also lower masses. Ref. [268] shows exclusion regions in the same parameter plane as in our Figures 3.7, 3.12 and 3.14 and emphasizes that, at the benchmark couplings $g_q = 0.25$, $g_\chi = 1$ large swaths of parameter space are excluded. This is a well-known feature of simplified models [295, 296]. Dijet limits will be weaker at larger g_χ, where the ξ branching ratio into quarks is reduced, or at smaller g_q, where in addition the ξ production cross section is lowered.

It is finally important to keep in mind that simplified models are expected to be incomplete, and their completion often enables extra detection channels [296].

3.8 Conclusions

In summary, we have explored the sensitivity of the LHC to inelastic DM, that is models in which DM χ has a slightly heavier partner χ^*, with couplings such that the "off-diagonal" process $pp \to \bar{\chi}\chi^*, \chi\bar{\chi}^*$ dominates DM production at the LHC. We analysed the decay width of the heavier dark state χ^* for different mediator types connecting the dark sector to the SM, where we took into account vector, axial vector, scalar and pseudoscalar mediators. The decay width for vector, axial vector and scalar mediators turn out to show very similar behaviour with respect to their dependence on DM mass, mediator mass and mass splitting of the two dark states. The pseudoscalar case, however, is markedly different from the other mediators and since the decay width is significantly smaller, it generates large enough decay distances to be detectable in displacement searches (see Section 3.6). When comparing kinematic properties of the process $pp \to \chi^*\bar{\chi}, \bar{\chi}^*\chi$ induced by effective operators and the different mediator types, we see that variables like missing transverse energy, number of jets and p_T of the hardest jet turn out to be very similar for EFT and heavy mediators (Section 3.4), but on-shell effects show up for smaller mediator masses and change the spectra observably. The different mediator types show likewise

[5] The models studied in the analysis itself are gauge-mediated SUSY breaking and split-SUSY and the smallest mass difference between gluino and neutralino that the search is still sensitive to is about 20 GeV.

very similar kinematic properties compared to each other. We have recast ATLAS results on the generic monojet signature (see Figure 3.7 for our main results), where we obtain the strongest limits for the vector-mediated model, followed by the axial vector, pseudoscalar and scalar case, as we expected from the cross sections. The distributions of the cross sections dominate the relation of the limits between the different mediators, since the kinematic properties of $pp \to \chi^* \bar{\chi}$ are essentially the same. Exclusion limits reach up to almost 1.5 TeV for the mediator mass and 550 GeV for the DM mass.

In a more targeted search for displaced vertices, we used the finite lifetime of the dark state χ^* to set limits on the pseudoscalar model (see Figure 3.12). Displaced vertices can arise when the small mass splitting between χ and χ^* allows χ^* to travel a macroscopic distance before decaying to $\chi +$ hadrons. We encountered the dilemma that large enough decay distances require the mass splitting of χ^* and χ to be small, while a small splitting leaves very little energy to the detectable decay products that are needed to identify the displaced vertex. A cut on the transverse impact parameter used to reject tracks from the primary vertex unfortunately rejects forward-boosted decays of χ^*, which could have provided more energy to the decay products. We chose a mass splitting of the dark states of $\Delta = 30\,\mathrm{GeV}$, well above the value for the monojet analysis, since the cut on the invariant mass of displaced vertex $m_{\mathrm{DV}} > 10\,\mathrm{GeV}$ requires the splitting to be quite large. We are able to exclude a small fraction of parameter space for DM masses between 450 and 750 GeV at a mediator mass of about 2 TeV (see Figure 3.12). We were motivated to discuss how a slight relaxation of cuts may improve the sensitivity, since background rates appear to be negligible even for an extended signal region. Lowering the cut on the displaced vertex mass to $m_{\mathrm{DV}} > 5\,\mathrm{GeV}$ and the number of associated tracks $N_{\mathrm{tracks}} \geq 4$ significantly improved the reach of the search and made it possible to reconsider the case of a mass splitting of 10 GeV (see Figure 3.14). For $\Delta = 30\,\mathrm{GeV}$ we were able to exclude DM masses between 200 GeV and 1 TeV for mediator masses between about 1.5 and 2.5 TeV. Reconsidering the smaller splitting of $\Delta = 10\,\mathrm{GeV}$, we can exclude DM masses up to 300 GeV for mediator masses between 500 GeV and about one TeV.

Our results highlight once again the significant potential of the LHC to explore DM models, but they also emphasise that we are still far from having covered all possible scenarios. Even for a rather simple model like inelastic DM, significant discovery potential remains untapped, but could be brought to bear with more adapted analysis strategies. We saw in the previous section in particular, that a targeted analysis looking for a single so called dark photon jet, would open up these searches for our inelastic DM model. The inelastic DM model requires a compromise between the decay length of the excited state χ^*, which grows as the mass splitting decreases, and the energy available to its detectable decay products, which grows with increasing mass splitting.

Chapter 4

Leptophilic Dark Matter

4.1 Introduction

This chapter is based on Ref. [297]. The calculation of the internal bremsstrahlung cross section was performed by the author, who also contributed to the calculation of the anapole and dipole moments of dark matter and to the manuscript. The remaining calculations, in particular those related to experimental limits, were carried out by the collaborators.

In this chapter we want to set our focus on a type of dark matter (DM) models generating a very interesting signature that could facilitate DM detection. Models, where DM annihilates via a charged t-channel mediator, allow for the emission of a photon from the mediator. When mediator and DM particle are close in mass and DM is a Majorana particle[1], the resulting photon energy is strongly peaked and we obtain a line-like gamma ray signal (if the width is below the energy resolution of the detector). Peaks in the cosmic gamma ray spectrum are among the cleanest signatures for indirect DM detection. This is because first, astrophysical sources are not known to mimic such a signal[2], and second, gamma ray observatories are improving tremendously in their resolution, statistics and control of systematic uncertainties. A gamma ray line can be generated in DM annihilation to two photons, or to one photon and a Z- or Higgs boson. These processes are, however, loop suppressed, since DM needs to be electrically neutral. Then, other annihilation or decay channels usually dominate. In the case where the photon is emitted by the mediator in DM annihilation – called virtual internal bremsstrahlung (VIB) – this suppression is absent, making them a particularly interesting class of models, when gamma ray lines were to appear in indirect detection experiments.

[1]In the case that DM is a Dirac particle we do not observe a peaked photon spectrum, compare Figures 4.2 and 4.3 in the following section.

[2]There is the idea that a pulsar wind nebula with a particular composition could generate a peaked gamma ray signal [298], but if the same peak would be observed at different regions in the galaxy, one could rule out this explanation.

Within the variation of models including such a charged mediator, we want to focus here on so called leptophilic models, where the mediator of the DM – SM interactions couples only to the SM leptons, not the quarks. These models were studied for example in the light of the excess of cosmic ray positrons observed by PAMELA [299,300], by the Fermi-LAT collaboration [301], and by AMS-02 [302]. Coupling DM solely to leptons evades then the problem of an excess that should otherwise also appear in the antiproton flux [303, 304], examples include the models in Refs. [305–314]. Furthermore, leptophilic DM models could account for anomalies in gamma ray signals, such as in the Galactic Centre spectrum [315–317] or in emissions from the Fermi Bubbles [318–321]. Radio signals from structures in filaments in the inner galaxy also show anomalies that can be explained when DM couples only to the SM leptons [322]. We see that there are plenty of indications from experiments that motivate to study leptophilic DM models. Furthermore, one can add that DM couplings to quarks are being strongly constrained by very different kinds of experiments, including direct detection experiments [323–325], observations of gamma ray emissions from dwarf galaxies [326, 327], and additionally collider searches at the LHC [250, 328–335]. Direct detection constraints on leptophilic DM are less stringent and can be found *e.g.* in Refs. [336–338].

Our work will focus on constraining these leptophilic DM models including a charged mediator via loop processes. Then we will translate these bounds into limits on the cross section for internal bremsstrahlung $\chi\chi \to \ell^+\ell^-\gamma$. We use a simplified model, adding a charged scalar mediator η and a fermionic DM candidate χ to the SM with a coupling of the form $\bar{\chi}\,\ell\,\eta$ + h.c., ℓ being a charged SM lepton field (e, μ, τ). This simplified model could be embedded into models of supersymmetry, identifying χ with the lightest neutralino and η with a slepton (see *e.g.* Ref. [101]). Another possible realisation would be a radiative neutrino mass model, see Ref. [339] for the direct detection phenomenology.

We start by observing that even in leptophilic DM models, loop processes endow DM with non-zero electromagnetic moments, inducing interactions in direct detection experiments. For the case of a Majorana DM candidate we obtain an anapole moment [340,341], while for Dirac DM, both anapole and magnetic dipole moments are generated. DM with anapole interactions in an effective field theory setting has been studied in Refs. [342–345], while Refs. [339, 343, 346–350] calculated magnetic dipole interactions for DM.

In turn, loop processes involving the DM particle and the mediator can modify the electromagnetic properties of the SM leptons, in particular their magnetic dipole moments and the hyperfine splitting of $\ell^+\ell^-$ bound systems. For a general model including also flavour violating couplings, we obtain contributions to flavour violating decays, like *e.g.* $\mu \to e\gamma$. For the case of DM coupling to electrons, it can be directly produced at the e^+e^- collider LEP (or a future facility), making a mono-photon plus missing energy search possible.

We will introduce the simplified model framework in section 4.2, where we also calculate the cross section for the internal bremsstrahlung process $\chi\chi \to \ell^+\ell^-\gamma$. We plot the differential cross section to show how close mediator and DM mass have to be to generate a peaked photon spectrum in indirect detection experiments. In the following Section 4.3 we will calculate the electromagnetic form factors of the DM particle χ that are generated at loop-level, for the Majorana case the anapole form factor (Subsection 4.3.1) and for the Dirac case the magnetic dipole moment (Subsection 4.3.2). The next Section 4.4 uses these form factors and the measurements of direct detection experiments to set limits on the virtual internal bremsstrahlung annihilation cross section. Section 4.5 uses data from an e^+e^- collider (LEP), where monophoton searches with missing energy set constraints on models where DM couples to electrons. These constraints are supplemented by limits from the modifications our model introduces to the lepton magnetic dipole moments – the anomalous magnetic moments are calculated in Section 4.6. We also look at the effects on lepton-antilepton bound states in Section 4.7, where we get contributions to the hyperfine splitting. For models including lepton flavour violating couplings, we get limits by searches for lepton flavour violating decays $\ell_\alpha \to \ell_\beta \gamma$ in Section 4.8. We conclude and summarise our findings in Section 4.9.

4.2 Leptophilic Dark Matter and Internal Bremsstrahlung

In this work we want to study a simplified scenario, adding an additional fermion χ to the SM as a DM candidate, which interacts with the SM particles via a charged scalar mediator η. χ can be a Dirac or Majorana fermion. We will use a four component notation for the spinors.[3] The new physics Lagrangian is given by

$$\mathcal{L} \supset \frac{1}{2}\overline{\chi} i\partial\!\!\!/ \chi - \frac{1}{2} m_\chi \overline{\chi}\chi + (D_\mu \eta)^\dagger (D^\mu \eta) - m_\eta^2 \eta^\dagger \eta + \mathcal{L}_{\chi\eta} \,, \tag{4.1}$$

where D_μ is the covariant derivative that defines the kinematics and the interactions of the mediator η. The last term describes the interaction of the DM particle χ with the SM fermions, which will be through the mediator η. The mediator η is chosen to be a singlet[4] under $SU(3)_c$ and $SU(2)_L$ and has a hypercharge $Y = 1$. We are not considering the scalar potential of our mediator η, since it does not contribute to the phenomenology we will study in this work.

Deciding on leptophilic interactions of DM means the DM particle χ will couple to the SM leptons only:

$$\mathcal{L}_{\chi\eta} = -y \bar{\chi} P_R \ell \eta + \text{h.c.} \,, \tag{4.2}$$

where ℓ is a charged SM leptons and P_R is the right-handed projection operator $P_R = (1+\gamma^5)/2$. y is the Yukawa coupling constant defining the magnitude of these interactions. This model has been studied before, *e.g.* in Ref. [100]. We will consider only couplings to

[3] For a detailed discussion of the two component notation see Ref. [351], Ref. [352] also gives a nice pedagogical introduction to Majorana fermions, mostly in the two component notation.

[4] Note that η can only be an $SU(2)_L$ singlet if it couples to right-handed SM leptons only, as defined in the following interaction Lagrangian, eq. (4.2).

right-handed SM leptons, since couplings to left-handed leptons are tightly constrained by collider searches and electroweak precision tests [353]. When including a coupling to left-handed leptons, we also need η to carry $SU(2)_L$ charge. This Lagrangian describes the coupling of η to one specific lepton ℓ. It can be motivated by introducing a new symmetry and assigning η the suitable quantum number. The part of the Lagrangian describing the relevant interactions for our calculations is then given by

$$\mathcal{L}_{\text{int}} = -y\bar{\chi}P_R\ell\eta - ie\eta A^\mu\partial_\mu\eta^* + \text{h.c.}\,, \tag{4.3}$$

where the interaction of η with the photon field A^μ is defined by its hypercharge. We omit here the vertex $e^2\eta^*\eta A^\mu A_\mu$, since it is of higher order and will be phenomenologically negligible. We will use this model to calculate the direct detection limits shown in Figures 4.9a (Majorana case) and 4.9d (Dirac case).

We will then also use a flavour universal coupling of three different mass degenerate mediators η to all three SM leptons:

$$\mathcal{L} \supset \sum_{\alpha=e,\mu,\tau} (-y\bar{\chi}P_R\ell^\alpha\eta^\alpha - ie\eta^\alpha A^\mu\partial_\mu\eta^{\alpha*}) + \text{h.c.}\,. \tag{4.4}$$

Limits on this simplified model are shown in Figures 4.9b and 4.9c (including direct detection limits by LUX, collider limits from LEP and limits from the lepton magnetic dipole moments). For the e^+e^- collider limits in Figures 4.9b and 4.9d, as well as the magnetic dipole moments of the SM leptons (Figure 4.9b), calculated in Section 4.6, and the hyperfine splitting of lepton-antilepton bound systems in Section 4.7 we can use either the model from eq. (4.3) or the flavour universal model, eq. (4.4).

Finally, we will use a very general model, where the couplings are taken to be to both left- and right-handed fermions and the couplings are allowed to be flavour off-diagonal. The Lagrangian then reads:

$$\mathcal{L} \supset \sum_{\alpha,j}\left(-y_R^{\alpha j}\bar{\chi}P_R\ell^\alpha\eta^j - y_L^{\alpha j}\bar{\chi}P_L\ell^\alpha\eta^j\right) - ie\sum_j \eta^j A^\mu\partial_\mu\eta^{j*} + \text{h.c.}\,, \tag{4.5}$$

where $y_{L,R}^{\alpha j}$ are then Yukawa matrices and η^j are the mass eigenstates of the mediator, whose number can be arbitrary, $j = 1, 2, ...$ These off diagonal couplings lead to flavour violating decays of the SM leptons $\ell_\alpha \to \ell_\beta\gamma$, see Section 4.8. The index α denotes the three lepton flavours, as before, $\alpha = e, \mu, \tau$. Note that the mediators η^j would need to carry $SU(2)_L$ charges in this case.

For details on the model for a Majorana fermion χ in eq. (4.3) and possible realisations within the framework of supersymmetry, see Ref. [101] and references therein. The DM candidate would then be the lightest neutralino, while the mediator η would be the lightest slepton. The other sleptons and squarks are assumed to be much heavier. For the case of a flavour universal coupling with three mediators (eq. (4.4)), the mediators η^α are given by the three sleptons. A radiative neutrino mass model could also serve as a UV completion of these interactions [339].

The simplified model with the Lagrangian from eq. (4.3) that we study here, can give rise to a peaked gamma ray signal via a process called virtual internal bremsstrahlung (VIB). It has been used in Ref. [101] to explain a line-like feature in the data set from Fermi-LAT[5]. When two Majorana DM particles χ annihilate via a charged t-channel mediator η, the mediator can emit a photon. If the masses of η and the DM particle χ are almost degenerate, we obtain a peak in the gamma ray spectrum, see Figure 4.2. An additional advantage of the final state photon is the following: When decomposing the scattering process $\chi\chi \to \ell^+\ell^-$ into incoming partial waves with definite incoming angular momentum we obtain an s-wave and a p-wave contribution. For Majorana fermions, the s-wave contribution, which is usually dominant, is helicity suppressed, *i.e.* suppressed by the ratio of lepton over DM mass m_ℓ^2/m_χ^2. When looking at the Lagrangian eq. (4.3) we can see that the Yukawa interaction produces two leptons in the final state with the same chirality for the process of DM annihilation. If DM is a Majorana particle, however, Pauli blocking makes the initial state DM particles have opposite spin. This is where the mass insertion on one of the final state leptons becomes necessary to conserve angular momentum. The helicity suppression of the Majorana s-wave DM annihilation can now be alleviated by having an additional photon, which is a spin one particle, in the final state, $\chi\chi \to \ell^+\ell^-\gamma$, see Refs. [358,359]. Note that this alleviation of a helicity suppression of the two body DM annihilation compared to the three body process including internal bremsstrahlung can also be seen in models with a vector mediator [350] and for fermionic mediators coupling to scalar DM [350, 360, 361].

For Dirac DM, however, the s-wave contribution dominates because of the small relative velocity of DM particles in the Milky Way, which enters as v_{rel}^2 into the p-wave part.

The corresponding Feynman diagrams for Majorana DM annihilation including a photon in the final state following eq. (4.3) are shown in Figure 4.1. In appendix A.1 we specify the matrix elements that belong to these diagrams. The spin averaged matrix element for a Majorana DM particle χ is given by

$$\overline{|\mathcal{M}^2|} = \frac{4e^2y^4E_1E_3\sin^2(\theta/2)(E_1^2 + E_1E_3\cos(\theta) - E_1E_3 + E_3^2)}{m_\chi^2(2E_1 + (\mu-1)m_\chi)^2(2E_3 + (\mu-1)m_\chi)^2}\,, \tag{4.6}$$

where e and y are the electromagnetic and the Yukawa coupling constant respectively, E_1 and E_3 are the energies of the two leptons and θ is the angle between them. m_χ is the DM mass and $\mu = m_\eta^2/m_\chi^2$ the ratio of mediator over DM mass. Note that we took the initial state DM particles to be non-relativistic and the final state leptons to be massless. The resulting differential three body cross section is then [101]

$$v_{\mathrm{rel}}\frac{d\sigma(\chi\chi \to \ell^+\ell^-\gamma)}{dx_\gamma} \simeq \frac{y^4\alpha_{\mathrm{em}}N_\ell}{32\pi^2m_\chi^2}\left(1-x_\gamma\right)\left[\frac{2x_\gamma}{(\mu+1)(\mu+1-2x_\gamma)} - \frac{x_\gamma}{(\mu+1-x_\gamma)^2}\right.$$

[5] There was a feature in the Fermi-LAT data at around 135 GeV. In Ref. [101] they performed a fit on the data resulting in a preferred DM mass of $m_\chi = 149 \pm 4\,(\mathrm{stat})\,^{+8}_{-15}(\mathrm{syst})$ GeV and an annihilation cross section of $\langle\sigma v_{\mathrm{rel}}\rangle_{\chi\chi\to\ell^+\ell^-\gamma} = (6.2 \pm 1.5\,^{+0.9}_{-1.4}) \cdot 10^{-27}\ \mathrm{cm^3s^{-1}}$, where v_{rel} is the relative velocity of the annihilating DM particles that is being averaged over, see also Refs. [130, 301]. The feature later turned out to be a statistical fluctuation [130, 354–357].

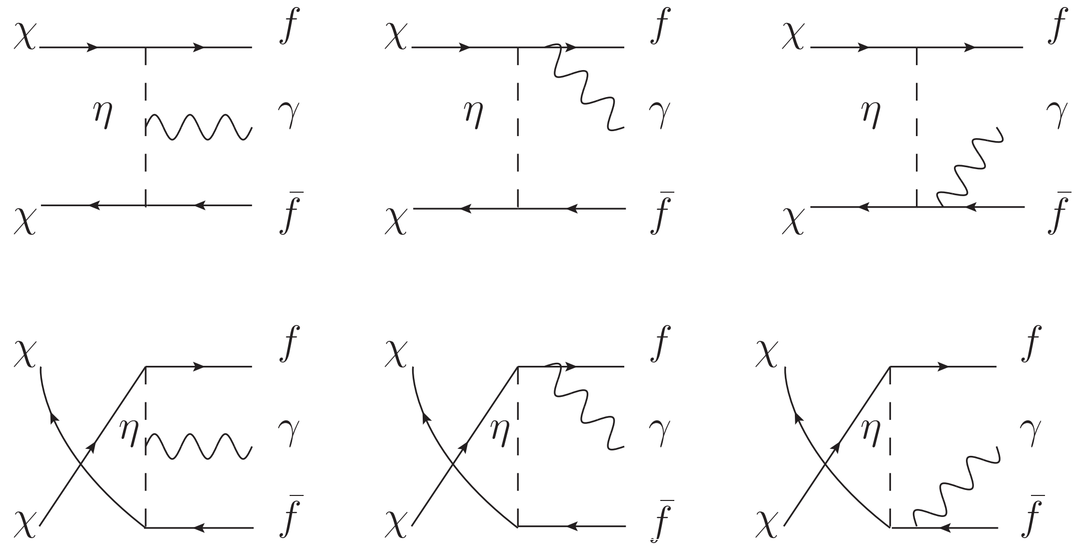

Figure 4.1: Feynman diagrams contributing to the process of internal bremsstrahlung in a leptophilic DM model for a Majorana fermion χ, whose interactions are described by eq. (4.3). For the case of a Dirac DM particle, the crossed diagrams in the second line are absent.

$$- \frac{(\mu+1)(\mu+1-2x_\gamma)}{2(\mu+1-x_\gamma)^3} \log\left(\frac{\mu+1}{\mu+1-2x_\gamma}\right)\Bigg] , \tag{4.7}$$

where $\alpha_{\rm em}$ is the electromagnetic fine structure constant and N_ℓ the number of lepton flavours that the mediator couples to. x_γ is the normalised photon energy $x_\gamma = E_\gamma/m_\chi$. The resulting photon spectrum of this process is of course continuous, but for the case of a Majorana DM particle χ the spectrum develops a peak, if the mediator m_η and DM mass m_χ are close, see Figure 4.2. The emission of a photon from the mediator, *i.e.* from virtual internal bremsstrahlung (which are the two diagrams on the left in Figure 4.1), is then strongly peaked at energies E_γ close to m_χ. One of the final state leptons becomes here very soft and the corresponding propagator of the mediator η close to being on-shell. This means that for $m_\eta \approx m_\chi$ and $E_\gamma \approx m_\chi$ the process of internal bremsstrahlung can be interpreted as the annihilation of DM into a lepton and a photon, where a soft lepton is emitted as something similar to initial state radiation.[6] If the width of this peak is below the resolution of the detector, it will appear as a line-like feature on top of the continuous cosmic gamma ray spectrum. In contrast to gamma ray lines that are emitted in DM annihilation to $\gamma\gamma$, γZ or γH, this process of internal bremsstrahlung is not loop suppressed and its cross section can be sizeable.

Coming back to the photon spectrum in Figure 4.2. It becomes clear that we need

[6]Even though the peaked spectrum is in this case caused by the dominant contribution of the diagrams where the photon is radiated from the mediator, the diagrams with final state radiation are crucial to ensure gauge invariance.

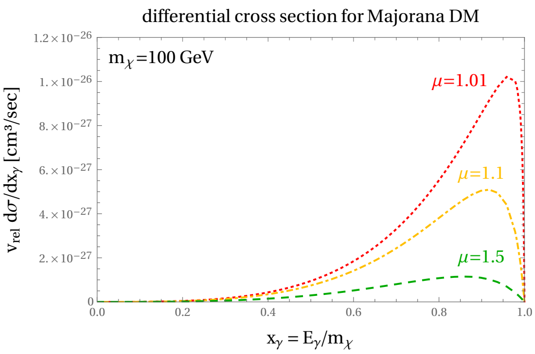

(a) Differential cross section $v_{\rm rel}\, d\sigma/dx_\gamma$ for a Majorana DM particle χ with m_χ = 100 GeV.

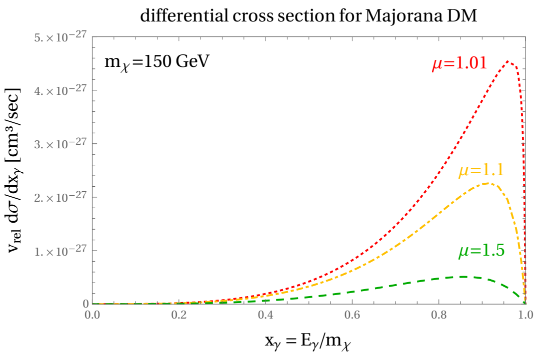

(b) Differential cross section $v_{\rm rel}\, d\sigma/dx_\gamma$ for a Majorana DM particle χ with m_χ = 150 GeV.

Figure 4.2: Differential cross section $v_{\rm rel}\, d\sigma/dx_\gamma(\chi\chi \to \ell^+\ell^-\gamma)$ for a Majorana DM particle χ for two different masses of the DM particle. The coupling is taken to be to one specific lepton flavour, *i.e.* $N_\ell = 1$, and the Yukawa coupling is set to one, $y = 1$. The curves show different levels of degeneracy of the masses of the DM particle χ and the mediator η, $\mu = m_\eta^2/m_\chi^2$, $\mu = 1.5$ (green, dashed), $\mu = 1.1$ (yellow, dash dotted), and $\mu = 1.01$ (red, dotted).

quite a small degeneracy parameter $\mu \lesssim 1.1$ in order to obtain a peaked gamma ray spectrum. When integrating over the photon energy x_γ in eq. (4.7) we get the full cross section for the process $\chi\chi \to \ell^+\ell^-\gamma$ [101]

$$\begin{aligned} v_{\rm rel}\sigma(\chi\chi \to \ell^+\ell^-\gamma) \simeq & \frac{y^4\alpha_{\rm em}N_\ell}{64\pi^2 m_\chi^2}\left[\frac{1}{2\mu}(4\mu^2 - 3\mu - 1)\log\left(\frac{\mu-1}{\mu+1}\right) + \frac{4\mu+3}{\mu+1}\right. \\ & \left. -(\mu+1)\left\{\log^2\left(\frac{\mu+1}{2\mu}\right) + 2\mathrm{Li}_2\left(\frac{\mu+1}{2\mu}\right) - \frac{\pi^2}{6}\right\}\right], \end{aligned} \tag{4.8}$$

with Li_2 being the dilogarithm function

$$\mathrm{Li}_2(x) = \sum_{n=1}^{\infty} \frac{x^n}{n^2}\,. \tag{4.9}$$

For the case of a Dirac DM particle χ we find that we cannot take the limit of small lepton mass and set $m_\ell \to 0$, since the cross section $v_{\rm rel}\,\sigma(\chi\chi \to \ell^+\ell^-\gamma)$ develops infrared divergences for a soft photon that is collinear with a final state lepton. Therefore we evaluated the cross section for finite m_ℓ, where we do not obtain an analytic expression and thus calculate numerically[7]. We plotted the cross section for two different degeneracy parameters μ in Figure 4.3 for a coupling to electron, muon and tau-lepton separately.

[7]We verified that the logarithms that appear in $v_{\rm rel}\,\sigma(\chi\chi \to \ell^+\ell^-\gamma)$ are small enough to allow for an approximate perturbative treatment.

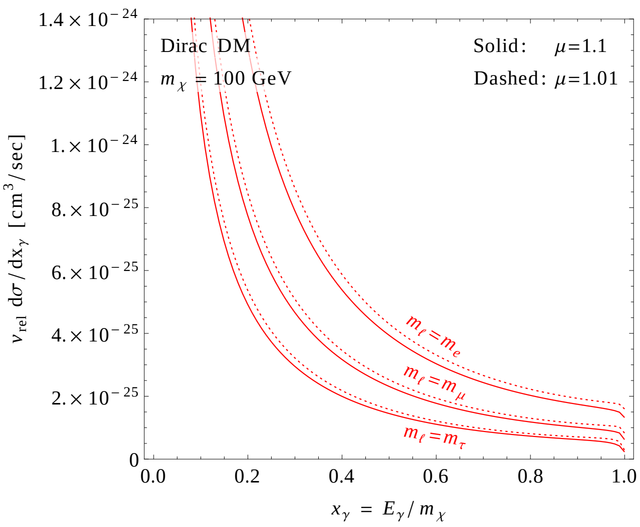

Figure 4.3: Differential cross section $v_{\rm rel}\, d\sigma/dx_\gamma(\chi\bar{\chi} \to \ell^+\ell^-\gamma)$ for Dirac DM. The cross section is evaluated numerically for a coupling to the different SM leptons. The degeneracy parameter $\mu = m_\eta^2/m_\chi^2$ is taken to be $\mu = 1.1$ (solid) and $\mu = 1.01$ (dashed). The Yukawa coupling is again set to $y = 1$ and the DM mass to $m_\chi = 100\,\mathrm{GeV}$.

We see that the dominant effect is final state radiation - causing the IR divergence of soft photons - and the virtual internal bremsstrahlung does not produce any sharp feature. The cross section varies only little with the ratio of mediator and DM mass μ. In the case of Dirac DM the process of internal bremsstrahlung thus does not produce a gamma ray line. For the indirect detection limits in Section 4.4, we will therefore use the two-body annihilation cross section.

In this work, we want to evaluate the effective couplings that are generated by the interactions defined by the Lagrangian (4.3) for the case of a Majorana and a Dirac DM fermion χ. Via loop processes the mediator induces a coupling of the DM particle to the photon by an electromagnetic form factor, see Section 4.3. The interactions furthermore alter the magnetic dipole moments of the respective lepton(s), see Section 4.6, and in systems of two oppositely charged leptons, like positronium e^+e^- or true muonium $\mu^+\mu^-$, they shift the hyperfine splitting of the system, see Section 4.7.

In the later Section 4.4 we will show the limits that can be placed on the parameter space of this model with the calculations of the effective interactions.

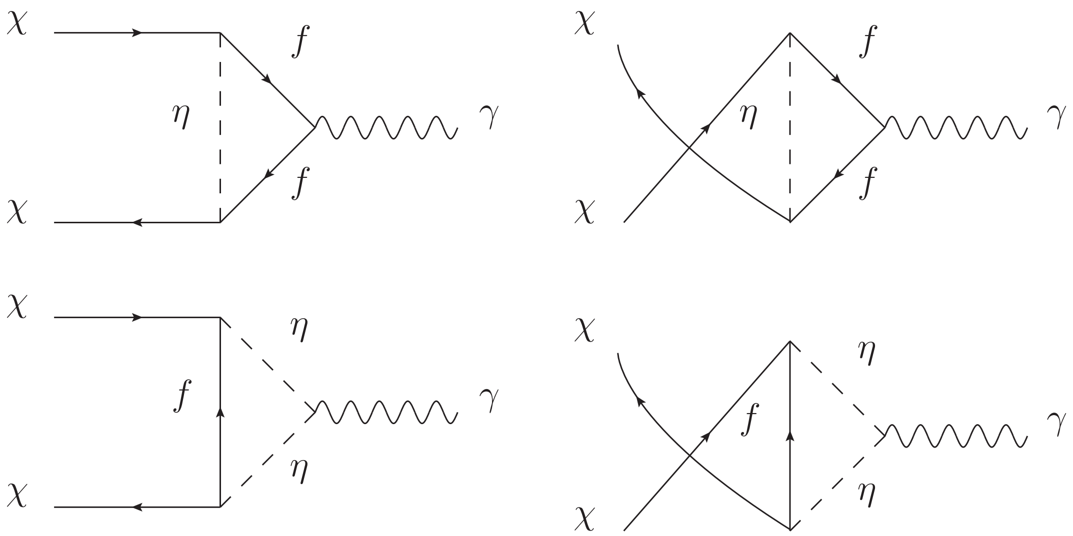

Figure 4.4: Feynman diagrams at one-loop order that couple the Majorana DM particle χ to the photon γ. For a Dirac DM particle, only the left two diagrams are present.

4.3 Electromagnetic Form Factors for DM

Assuming our DM candidate χ to couple to the SM leptons via the charged mediator η, as given by the Lagrangian eq. (4.3), necessarily induces DM to couple to photons at one-loop level. We can see this by connecting the fermion lines for the process of internal bremsstrahlung shown in Figure 4.1. Depending on the nature of χ the leading order Feynman diagrams are then either the four depicted diagrams in Figure 4.4 if we assume χ to be a Majorana fermion, or only the two on the left hand side for a Dirac fermion. These diagrams induce an effective coupling of the DM fermion χ to the photon, which can be most generally described by the Lagrangian terms [362]

$$\mathcal{L}_{\text{eff}} \supset \frac{d_M}{2}\bar{\chi}\sigma^{\mu\nu}\chi F_{\mu\nu} + \frac{d_E}{2}\bar{\chi}\sigma^{\mu\nu}\gamma^5\chi F_{\mu\nu} + \mathcal{A}\,\bar{\chi}\gamma^\mu\gamma^5\chi\,\partial^\nu F_{\mu\nu}\,, \tag{4.10}$$

where we obtain effective operators at dimension five and six. d_M is here the magnetic dipole moment, d_E the electric dipole moment, and $\mathcal{A}$ the anapole moment of the fermion χ. $F_{\mu\nu}$ is the electromagnetic field strength and $\sigma^{\mu\nu} = i/2[\gamma^\mu, \gamma^\nu]$. For a Majorana fermion χ, the magnetic and electric dipole moments vanish from its definition to be invariant under charge conjugation:

$$\hat{C}\chi\hat{C} \equiv -i\gamma^2\chi^* = \chi\,. \tag{4.11}$$

Inserting this identity into eq. (4.10) we can see that d_M and d_E must vanish, and the anapole moment $\mathcal{A}$ is thus the only contribution in this case [340, 341].

Note that for the case of internal bremsstrahlung in models with scalar DM and a fermionic mediator or Majorana DM with a vector mediator, the same connection occurs between DM annihilation and loop-induced electromagnetic form factors [363, 364]. In all these models, internal bremsstrahlung dominates over the standard two-body annihilation of DM. A similar connection of DM annihilation inducing a gamma ray line and direct detection signals for models with loop-induced DM annihilation to photons can be found in Ref. [365].

4.3.1 Anapole Moment for Majorana DM

For Majorana DM, the four diagrams in Figure 4.4 give us the anapole form factor $\mathcal{A}$ in eq. (4.10). When neglecting the four-momentum transfer q, we obtain

$$\mathcal{A} = -\frac{ey^2}{96\pi^2 m_\chi^2}\left[\frac{3}{2}\log\frac{\mu}{\epsilon} - \frac{1+3\mu-3\epsilon}{\sqrt{(\mu-1-\epsilon)^2-4\epsilon}}\operatorname{arctanh}\left(\frac{\sqrt{(\mu-1-\epsilon)^2-4\epsilon}}{\mu-1+\epsilon}\right)\right], \quad (|q^2| \ll m_\ell^2)\,, \tag{4.12}$$

with the mass ratios $\mu = m_\eta^2/m_\chi^2$ and $\epsilon = m_\ell^2/m_\chi^2$. Since the arctanh function diverges as its argument approaches one, we can see easily that also the anapole moment $\mathcal{A}$ diverges logarithmically when $1 \gg \mu - 1 \gg \epsilon \to 0$:

$$\mathcal{A} \approx \frac{ey^2}{48\pi^2 m_\chi^2} \times \frac{\log(\epsilon)}{(\mu-1)} \quad \text{for} \quad (1 \gg \mu-1 \gg \epsilon \to 0 \text{ and } |q^2| \ll m_\ell^2) \tag{4.13}$$

We can understand this behaviour by noting that if $m_\eta \approx m_\chi$ and $q^2 \approx 0$ the three propagators in the loops in Figure 4.4 can be almost on-shell simultaneously. If $\mu - 1 \ll \epsilon \ll 1$, however, the leading order term in $\mathcal{A}$ becomes proportional to $1/\sqrt{\epsilon}$. In this limit, the argument of the arctanh function in eq. (4.12) becomes imaginary. We have plotted the anapole moment in Figure 4.5 as a function of the mass degeneracy parameter μ, assuming a Yukawa coupling of $y = 1$ and a DM mass of $m_\chi = 100\,\text{GeV}$. We normalise $\mathcal{A}$ to the nuclear magneton $\mu_N = e\hbar/2m_p$. If we take the mediator to couple to the electron, however, we cannot assume the momentum transfer to vanish, since in typical DM–nucleus interaction we get $|q^2| \gg m_e^2$. Therefore we instead set $m_\ell = m_e = 0$, define the variable $\xi = \sqrt{|q^2|}/m_\chi$ and keep the leading order term in ξ. This gives us

$$\mathcal{A} = -\frac{ey^2}{32\pi^2 m_\chi^2}\left[\frac{-10+12\log\xi-(3+9\mu)\log(\mu-1)-(3-9\mu)\log\mu}{9(\mu-1)}\right], \quad (|q^2| \gg m_\ell^2)\,. \tag{4.14}$$

This result gives us the solid line in Figure 4.5, where we used $\sqrt{|q^2|} = 50$ MeV as a typical nuclear recoil momentum.[8] We checked that, even for very small ϵ or ξ the

[8] This value is calculated from the nuclear recoil energy, which is assumed to be at the order of a few keV, and the nuclear mass of xenon, which is about 120 GeV.

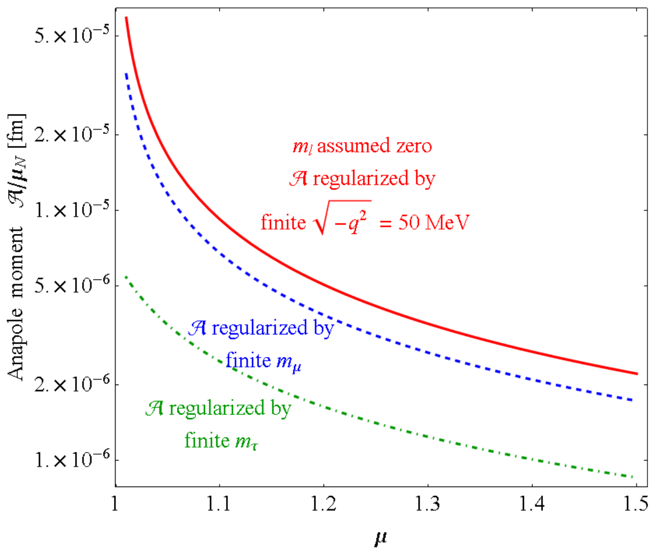

Figure 4.5: The anapole moment for Majorana DM as a function of the mass ratio $\mu = m_\eta^2/m_\chi^2$. The coupling is taken to be to the electron, muon and tau-lepton, respectively. We have set $y = 1$ and $m_\chi = 100\,\text{GeV}$. When coupling to the electron, $\mathcal{A}$ is regularised by a finite q^2 rather than m_e, as in typical DM-nucleus scatterings we have $|q^2| \gg m_e^2$.

calculation is still valid at fixed order in perturbation theory. When taking $\mu - 1 \gg \epsilon$ ($\mu - 1 \gg \xi$), which we will assume in the following, the diverging logarithms appearing in eqs. (4.12) and (4.14) are at most of $\mathcal{O}(10)$.

4.3.2 Dipole Moment for Dirac DM

When we take χ to be a Dirac fermion, then we obtain only the two Feynman diagrams on the left in Figure 4.4. The resulting anapole moment is half as large as for the Majorana case in eq. (4.12) and the magnetic dipole moment d_M is given by

$$d_M = \frac{y^2 e}{32\pi^2 m_\chi}\left[-1 + \frac{1}{2}(\epsilon-\mu)\log\left(\frac{\epsilon}{\mu}\right) - \frac{(\mu-1)(\mu-2\epsilon)-\epsilon(3-\epsilon)}{\sqrt{(\mu-1)^2-2\epsilon(\mu+1)+\epsilon^2}}\times \right. \\ \left. \times \operatorname{arctanh}\left(\frac{\sqrt{(\mu-1)^2-2\epsilon(\mu+1)+\epsilon^2}}{\mu-1+\epsilon}\right)\right], \tag{4.15}$$

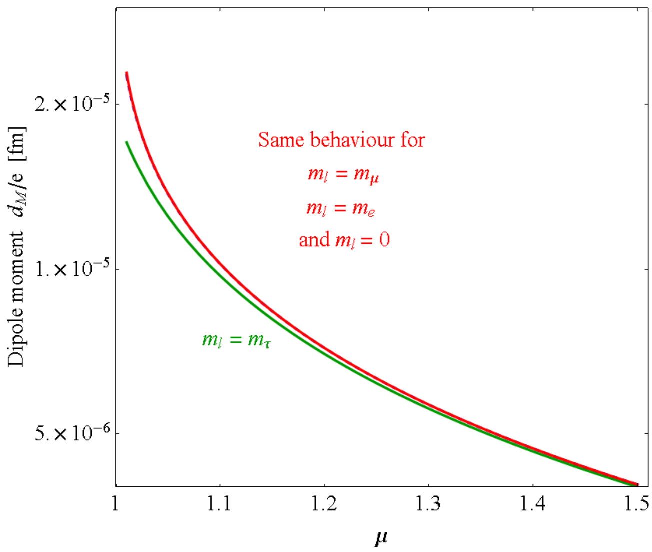

Figure 4.6: The magnetic dipole moment for Dirac DM as a function of the mass ratio $\mu = m_\eta^2/m_\chi^2$. The coupling is taken to be to the electron, muon and tau-lepton, respectively. We have set $y = 1$ and $m_\chi = 100\,\text{GeV}$.

where again we assumed $q^2 \to 0$. The dipole moment will numerically dominate over the anapole moment for Dirac DM in the scattering processes calculated later, therefore we will consider only limits from d_M for Dirac DM. For very small lepton masses compared to the DM mass, *i.e.* $\epsilon \to 0$, eq. (4.15) simplifies to

$$d_M = \frac{y^2 e}{32\pi^2 m_\chi}\left(\mu \log\left(\frac{\mu}{\mu - 1}\right) - 1\right) . \tag{4.16}$$

The dipole moment is thus not divergent for $\epsilon \to 0$, in contrast to the anapole moment. For $\mu - 1 \ll \epsilon \ll 1$ we can expand in ϵ and the leading order term for d_M becomes proportional to $1/\sqrt{\epsilon}$. We show d_M as a function of the mass degeneracy μ in Figure 4.6, again for $y = 1$ and $m_\chi = 100\,\text{GeV}$. We normalise d_M to the electric charge e. We see that for the mediator coupling to the electron and muon, the lepton masses are negligible and the curves for $m_\ell = m_\mu$, $m_\ell = m_e$ and $m_\ell = 0$ coincide. For the tau-lepton, $m_\ell = m_\tau$, there is a slight difference for $\mu \to 1$ from the larger mass of the tau-lepton.

4.4 Direct Detection Constraints

The anapole moment $\mathcal{A}$ that we calculated for a Majorana DM particle, as well as the magnetic dipole moment d_M for Dirac DM induce interactions of DM with the SM that can be tested in direct detection experiments. For an effective field theory calculation of such limits see [342, 343, 345, 347, 348, 366–371]. We want to calculate here the direct detection limits on the simplified models, eq. (4.3) and eq. (4.4), using the data from LUX [131] and XENON100 [372] and therefrom place constraints on the expected indirect detection signals. The data of these experiments has to be fitted at the event level, since the differential DM–nucleus scattering cross section $d\sigma/dE_r$, E_r being the nuclear recoil energy, differs from the usual spin-dependent and spin-independent scenarios. This was done using a framework from Refs. [224, 336, 373], where data from the LUX experiment was added and anapole and dipole DM interactions were implemented.

The anapole moment $\mathcal{A}$ induces a DM–nucleus interaction of the form [342, 345]

$$\frac{d\sigma_{\chi N}^{\text{anapole}}}{dE_r} = 4\alpha_{\text{em}}\mathcal{A}^2 Z^2 [F_Z(E_r)]^2 \left[2m_N - \left(1 + \frac{m_N}{m_\chi}\right)^2 \frac{E_r}{v^2}\right] + 4\mathcal{A}^2 d_A^2 [F_s(E_r)]^2 \left(\frac{J+1}{3J}\right) \frac{2E_r m_N^2}{\pi v^2}\,, \tag{4.17}$$

whereas the magnetic dipole moment d_M gives [221, 367, 369, 374]

$$\frac{d\sigma_{\chi N}^{\text{dipole}}}{dE_r} = \frac{\alpha_{\text{em}} Z^2 [F(E_r)]^2 d_M^2}{E_r} \left[1 - \frac{E_r}{2m_N v^2}\left(1 + 2\frac{m_N}{m_\chi}\right)\right] + d_M^2 d_A^2 [F_s(E_r)]^2 \left(\frac{J+1}{3J}\right) \frac{m_N}{\pi v^2}\,. \tag{4.18}$$

m_N is here the nuclear mass, v the velocity of the incoming DM particle, $F_Z(E_r)$ is the nuclear charge form factor and $F_s(E_r)$ the spin form factor. The nuclear charge form factor will be parametrised as [72]

$$F_Z(E_r) = 3e^{-\kappa^2 s^2/2} \frac{[\sin(\kappa r) - \kappa r\cos(\kappa r)]}{(\kappa r)^3} \tag{4.19}$$

with $\kappa = \sqrt{2m_N E_r}$, $s = 1$ fm, $r = \sqrt{R^2 - 5s^2}$, $R = 1.2A^{1/3}$ fm (A being the nuclear mass number). For the spin form factor we use [369]

$$F_s(E_r) = \sin\left(\frac{\kappa A^{1/3}}{qA^{1/3}}\right) \tag{4.20}$$

for $\kappa A^{1/3} < 2.55$ and $\kappa A^{1/3} > 4.5$, and $F_s(E_r) = 0.217$ otherwise.

In eqs. (4.17) and (4.18) the first line describes the scattering of the DM particle on the nuclear charge Z and the second line that on the nuclear dipole moment d_A. These

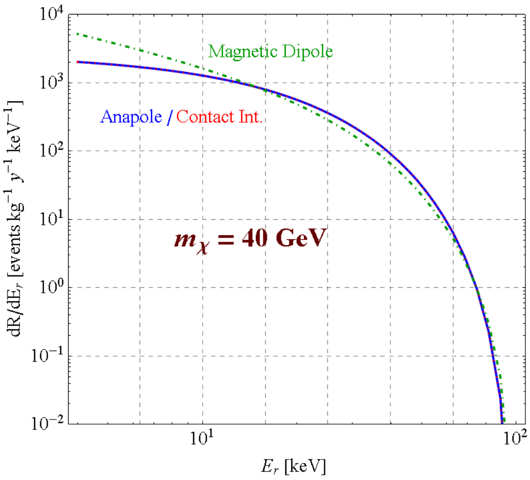

(a) Theoretical event rates without nuclear form factor and detector effects.

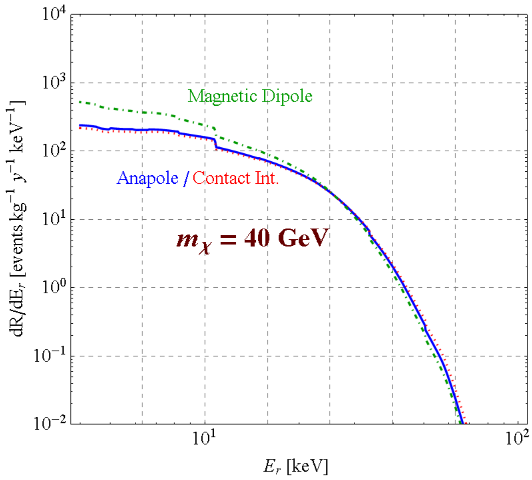

(b) Event rates estimated for the XENON100 detector including the effects of detection efficiency, light yield and energy resolution from Refs. [372, 375].

Figure 4.7: Differential DM – nucleus scattering rates, where the nucleus belongs to a xenon target. It compares anapole interactions (blue) with magnetic dipole interactions (green dot-dashed) and conventional spin-independent contact interactions (red, dotted). The DM mass is set to $m_\chi = 40\,\text{GeV}$. The coupling constants used are $\mathcal{A} = 3.8 \times 10^{-3}\mu_N{\cdot}\text{fm}$ for the anapole moment, $d_M = 1.9 \times 10^{-4}e{\cdot}\text{fm}$ for the dipole moment, and $\sigma_{\chi p} = 5.0 \times 10^{-41}$ cm^2 for the contact interaction. DM velocity profile and nuclear form factor are assumed to follow standards, see text.

contributions have to be considered separately, since for the DM–dipole scattering the extension of the nucleus has to be taken into account. The nuclear dipole interaction is, however, subdominant for many target materials, also for xenon (which is the relevant material in LUX and XENON100). For the anapole interaction, eq. (4.17), we can calculate the total cross section, while the dipole interaction, eq. (4.18), diverges in the infrared and the total cross section is therefore ill-defined. This divergence is equivalent to standard calculations involving a t-channel massless mediator, like *e.g.* electron – muon scattering, $e^-\mu^- \to e^-\mu^-$, where for small scattering angles the differential cross section becomes singular and thus the total cross section is also ill-defined. This is called a forward scattering divergence and is cured by the finite resolution of a physical detector that can only measure the scattering angle up to a minimum resolution θ_{min}. Compare *e.g.* Ref. [35], chapter 5.4.

In a direct detection experiment, the differential DM–nucleus scattering rate per unit of target mass can be written as

$$\frac{dR}{dE_r} = \frac{\rho_0}{m_\chi m_N} \int\limits_{v_{\min}}^{\infty} d^3v \frac{d\sigma}{dE_r} v\, f_\oplus(\vec{v})\,, \tag{4.21}$$

with the local DM density $\rho_0 \simeq 0.3$ GeV/cm^3 and the minimal DM velocity $v_{\min} = \sqrt{m_N E_r/2}/M_{\chi N}$ that is needed to induce a recoil energy E_r. $M_{\chi N} = m_\chi m_N/(m_\chi + m_N)$ is the reduced mass of the DM–nucleus system and $f_\oplus(\vec{v})$ parametrises the DM velocity distribution in the rest frame of the detector. We assume the DM velocity in the Milky Way rest frame f_{MW} to follow the usual Maxwell-Boltzmann distribution with a smooth cut-off

$$f_{\mathrm{MW}} \propto \exp\left(\frac{-\vec{v}^2}{v_0^2}\right) - \exp\left(\frac{-v_{\mathrm{esc}}^2}{v_0^2}\right) \tag{4.22}$$

and take for the velocity dispersion a value of $v_0 = 220$ km/s and for the escape velocity $v_{\mathrm{esc}} = 550$ km/s. $f_\oplus(\vec{v})$ is then obtained by a Galilean transformation. The dependence of the limits on the chosen velocity profile should be similar as for DM scattering via contact interactions, see [376–379].

Figure 4.7 shows the differential scattering rate dR/dE_r for anapole (blue, solid) and dipole interactions (green, dash dotted) and compares them to the usual spin-independent contact interactions (red, dotted). The plot on the right includes the nuclear form factors and detector effects, which the one on the left does not. To compare the different interactions, the rates were normalised to one event above 10 keV per kilogram per day before including detector and form factor effects. While the spectra of anapole and contact interactions are indistinguishable, dipole interactions are enhanced at low energies because of the $1/E_r$ dependence of the first term in eq. (4.18) and should be distinguishable with enough statistics. The nuclear form factor suppresses the rate at high energies. At low energies Poisson statistics cause a detectable number of photoelectrons to occur occasionally and therefore the rate remains sizeable.

Since there has been no sign of signal events so far, the data can be used to set limits on the anapole moment $\mathcal{A}$ and the dipole moment d_M of DM, which are shown in Figure 4.8. The analysis uses 85.3 days of LUX data [131] and 225 days for XENON100 data [372] and implements Yellin's maximum gap method [380]. The limit setting was done with a code developed in [224,336,373] and it was tested by reproducing the standard limits on spin-independent DM–nucleus scattering for both experiments. The shape of the exclusion limits is similar to the usual limit on contact interactions, for magnetic dipole interactions the $1/E_r$ enhancement we saw in Figure 4.7 leads to a comparatively better sensitivity at low DM masses.

These limits on the anapole moment $\mathcal{A}$ and the dipole moment d_M in Figure 4.8 can be translated into limits on the DM annihilation cross section, where the LUX data gives the stronger constraints. For the anapole moment the limit is set on $\langle \sigma v_{\mathrm{rel}} \rangle_{\chi\chi \to \ell^+\ell^-\gamma}$ given

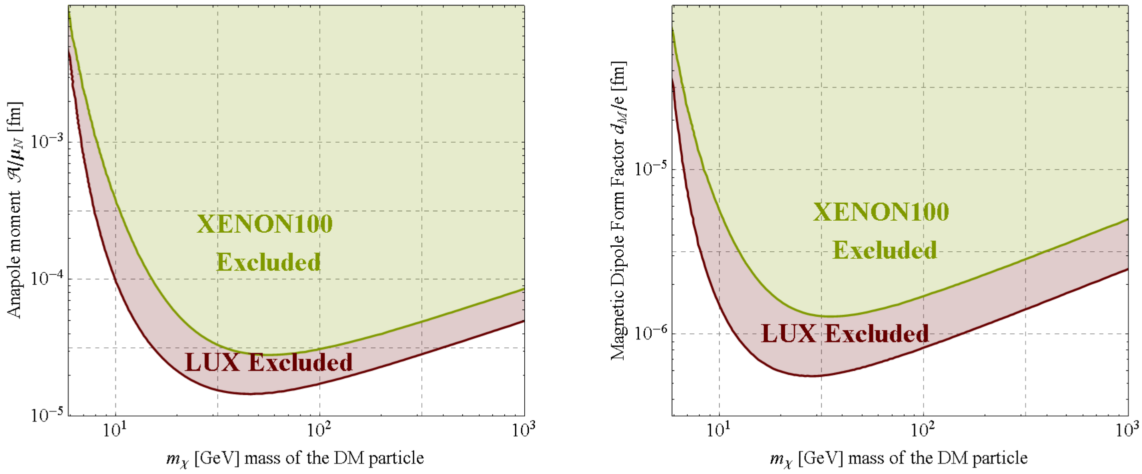

(a) Limit on the anapole moment of DM. **(b)** Limit on the dipole moment of DM.

Figure 4.8: Limits at 90 % CL on the anapole and dipole moments of DM from observations of the XENON100 and LUX experiments. Note the different scales on the ordinate.

by eq. (4.8) using the expression for $\mathcal{A}$ from eq. (4.12). Because of the infrared divergence in the process $\chi\bar{\chi} \to \ell^+\ell^-\gamma$ for Dirac DM and the lacking enhancement compared to the Majorana case, the limit is set on the two-body annihilation cross section, which is given by

$$v_{\mathrm{rel}}\sigma_{\chi\bar{\chi}\to\ell^+\ell^-} = \frac{y^4 N_\ell}{32\pi m_\chi^2}\frac{1}{(1+\mu)^2}\,, \tag{4.23}$$

where $\mu = m_\eta^2/m_\chi^2$, N_ℓ is the number of lepton flavours the mediator couples to and y is the Yukawa coupling from eq. (4.3) or eq. (4.4), as before. The expression for d_M is given by eq. (4.15).

The resulting limits on the DM annihilation cross section are shown in Figure 4.9, where Figures 4.9a to 4.9c are for a Majorana DM particle and Figure 4.9d is for Dirac DM. Figures 4.9a and 4.9d assume the mediator to couple to one respective lepton flavour e, μ, or τ, while Figures 4.9b and 4.9c assume a flavour-universal coupling to all SM leptons. In each plot, the grey area covers the region where the Yukawa coupling exceeds $y^2 > 4\pi$ and perturbativity breaks down. Close to this region perturbative calculations become increasingly inaccurate.

All plots include an estimate on the upper bound for a thermal relic DM particle.

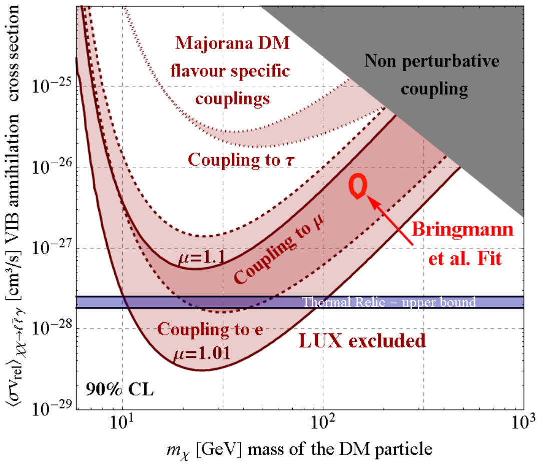

(a) Direct detection limits from anapole interactions of Majorana DM (red shaded regions). The coupling is taken to electrons only (thick solid), muons only (thick dotted), and tau only (thin dotted). Upper and lower boundaries correspond to mass ratios of $\mu = 1.1$ and $\mu = 1.01$, respectively.

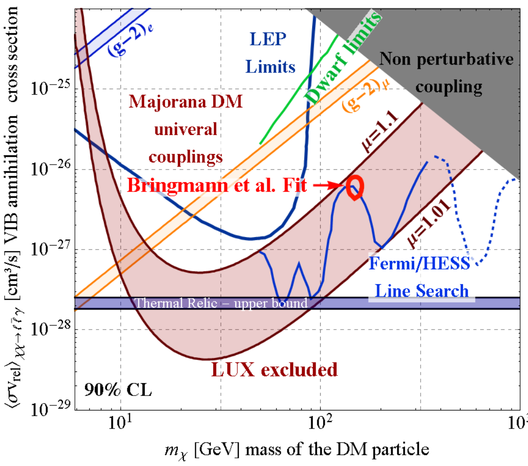

(b) Limits on Majorana DM with flavour-universal couplings comparing LUX and LEP mono-photon searches (see sec. 4.5), measurements of $g-2$ (see Section 4.6), the Fermi-LAT search for continuum gamma rays from dwarf galaxies [101], and searches for gamma ray lines from the galactic centre in Fermi-LAT (solid) and H.E.S.S. (dotted) [325].

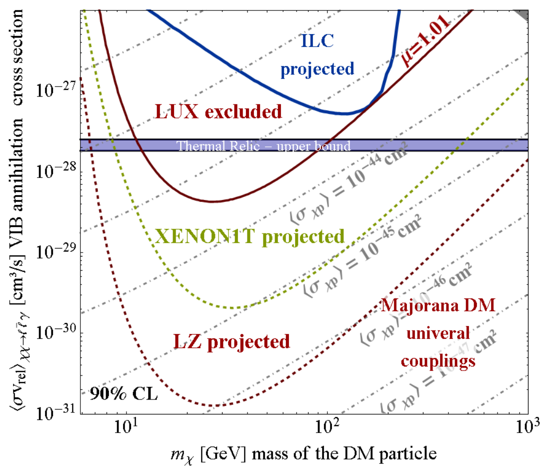

(c) Projection of sensitivities of XENON1T and LZ and the ILC for Majorana DM with flavour-universal couplings and $\mu = 1.01$. The plot includes dashed lines of constant velocity-averaged direct detection cross sections $\langle \sigma_{\chi p} \rangle$, compare eq. (4.25).

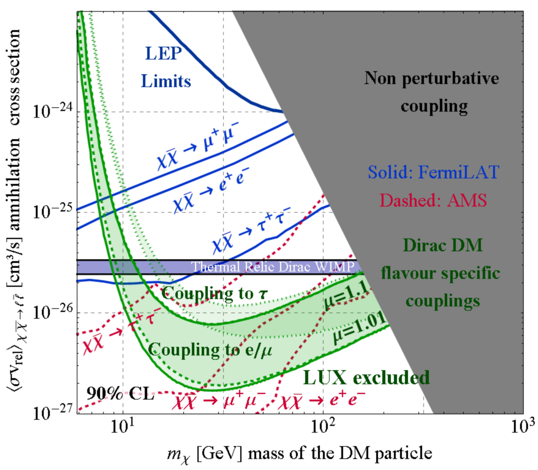

(d) Direct detection constraint on magnetic dipole interactions for Dirac DM coupling to e, μ or τ, including LEP mono-photon limits, Fermi-LAT limits from dwarf galaxies [327], and AMS limits [313]. Remember that the annihilation of Dirac DM does not induce sharp features in the gamma ray spectrum.

Figure 4.9: LUX limits on the DM annihilation cross section at 90 % CL for the simplified model, eq. (4.3). All plots include the upper limit on the DM cross section required for a thermal relic, where coannihilations are neglected and the relic density is calculated as in eq. (4.24). The red circle marks the best fit region by Ref. [101]. In grey shaded regions the Yukawa coupling exceeds $y^2 > 4\pi$.

For Majorana DM this is given by the following expression for the relic density [101]

$$\Omega_\chi h^2 \simeq 0.11 \frac{1}{N_\ell} \left(\frac{0.35}{y}\right)^4 \left(\frac{m_\chi}{100\ \text{GeV}}\right)^2 \frac{(1+\mu)^4}{1+\mu^2}\,, \tag{4.24}$$

which is valid for $\mu \gtrsim 1.2$. For smaller mass ratios μ, the relic density becomes diminished by an $\mathcal{O}(1)$ factor by coannihilations [101], the quantitative effect is shown in [361], Figure VII. The simplified model, eq. (4.3), thereby naturally predicts a thermal relic DM candidate within the relevant parameter space, $0.1 \lesssim y \lesssim 1$, $m_\chi \gtrsim 100\,\text{GeV}$. The lower limit $0.089 < \Omega_\chi$ is taken from WMAP [381] to be conservative, while the upper limit $\Omega_\chi h^2 < 0.1227$ is given by Planck [382]. This should qualitatively take into account the unresolved tension in different measurements of the Hubble constant $H_0 = h \cdot 100$ km s^{-1} Mpc^{-1}. Figure 4.9a shows that direct detection experiments are close to constraining the relevant parameter space for a thermal relic Majorana DM particle for couplings to electrons and muons. Note though, that the effects from coannihilations will move the line of thermal relic DM down to smaller cross sections.

In Figure 4.9a we can see the dependence of the anapole moment on the parameter $\epsilon = m_\ell^2/m_\chi^2$, where $\mathcal{A}$ increases for smaller m_ℓ and thus the limits are strongest for the coupling to electrons and weakest for τ-leptons. The effect of degenerate mediator and DM masses is also evident, for $\mu = m_\eta^2/m_\chi^2$ closer to one, the anapole moment is larger and the limits on the DM annihilation cross section become stronger.

Figures 4.9a and 4.9b include a region marked "Bringmann et al. Fit", which refers to an anomaly in the gamma ray spectrum at $\sim 135\,\text{GeV}$ that was found in the Fermi-LAT data [101, 130, 301]. Even though this line-like feature could not be confirmed [130, 354–357], it demonstrates that models of internal bremsstrahlung can provide relevant explanations for peaks in the gamma ray spectrum. The limits derived here on the DM annihilation cross section place constraints on the explanation of this feature from [101]. It is still compatible for $\mu = 1.1$, but excluded for $\mu = 1.01$ at the 5σ confidence level for a mediator coupled to electrons and at 3σ for coupling to muons.

In Figure 4.9b we can see the comparison of constraints from different experiments for a Majorana DM particle with flavour-universal couplings to the SM leptons. For a degeneracy parameter μ close to one, direct detection constraints become much more constraining than gamma ray observations of dwarf galaxies [101], which are labelled "dwarf limits" (in green). Comparing to gamma ray line searches from Fermi-LAT and H.E.S.S. [325], direct detection limits become comparable. Note that the gamma ray line limits are shown for $m_\chi \gtrsim 50\,\text{GeV}$, as in [101, 325], but Fermi-LAT and H.E.S.S. are actually sensitive also to lower DM masses. The anomalous magnetic moments $(g-2)$ of the electron and muon (see Section 4.6) become the strongest constraints at about $m_\chi \lesssim 10\,\text{GeV}$.

Figure 4.9c shows a projection of an estimated sensitivity for XENON1T [383] and LUX-ZEPLIN (LZ) [384], which can improve the limits on the annihilation cross section by about two orders of magnitude. With these upgrades a thermal relic Majorana DM particle will be covered in a vast fraction of the parameter space. The estimate uses a total exposure of 2 200 kg years for XENON1T and 10 000 kg years for LZ, which should correspond to about two years of data taking for both experiments. The plot also includes constant lines of the direct detection cross section averaged over the DM velocity distribution $\langle\sigma_{\chi p}\rangle$ (gray dash-dotted lines), which are given by

$$\langle\sigma_{\chi p}\rangle \equiv \langle\sigma_{\chi N}^{\text{anapole}}\rangle = \int_{v_{min}}^{\infty} f_{\oplus}(\vec{v})\,\sigma_{\chi N}^{\text{anapole}}\,d^3v\,. \tag{4.25}$$

These limits on the DM–nucleon scattering cross section are an order of magnitude weaker for anapole interactions than for the usual contact interactions, because of the velocity dependence in $\sigma_{\chi N}^{\text{anapole}}$ and since anapole interactions are sensitive to the nuclear charge of the target rather than its nuclear mass. Contributions from nuclear dipole moments are subdominant for xenon targets, as mentioned above.

Finally, Figure 4.9d shows limits on flavour specific couplings for Dirac DM. We can see that for the direct detection limits from LUX the shape of the limits is similar to the Majorana case, but the dependence on the lepton mass is less distinct. The plot furthermore shows limits from Fermi-LAT from gamma rays from dwarf galaxies [327] (in blue, solid) and from AMS [313] (red, dotted) for each lepton flavour, labelled $\chi\bar{\chi} \to \ell^+\ell^-$. For a degeneracy parameter μ close to one, direct detection limits are stronger than those from AMS and Fermi-LAT for DM masses $m_\chi \gtrsim 10\,\text{GeV}$ and a thermal relic can be excluded for $10\,\text{GeV} \lesssim m_\chi \lesssim \mathcal{O}(1)\cdot 100\,\text{GeV}$.

4.5 Limits from Collider Searches

We want to calculate here the limits from collider searches. Since we are considering a leptophilic DM model, DM can only be produced at loop level in hadron colliders [250, 328, 329, 385–388] and LEP mono-photon searches [389] still give the strongest limits. If a future linear collider will be built, these mono-photon limits would improve [390].

The analysis from [389] can be applied to the simplified model from eq. (4.3) or eq. (4.4). Events are simulated for $e^+e^- \to \chi\chi\gamma$ in CalcHEP 3.4 [265], where initial state radiation and beamstrahlung (using default parameters) are included in the beam energy. MadAnalysis 1.1.2 [391] was modified to include efficiencies and resolutions of the DELPHI detector at LEP [392, 393], details are given in Ref. [389]. The simulation was verified by reproducing the $\gamma\bar{\nu}\nu$ background from [393]. The simulated signal is added to the backgrounds calculated in Ref. [393] and the resulting event numbers are compared to the data in Figure 1 in Ref. [393], corresponding to an integrated luminosity of 650 pb^{-1}. As in Ref. [389], a χ^2 analysis is used to set limits on the Yukawa coupling y as a function of mediator and DM mass, m_η and m_χ. By converting these limits into constraints on the cross section $\langle\sigma v\rangle_{\chi\chi\to\ell^+\ell^-\gamma}$ the "LEP Limits" in Figures 4.9b and 4.9d

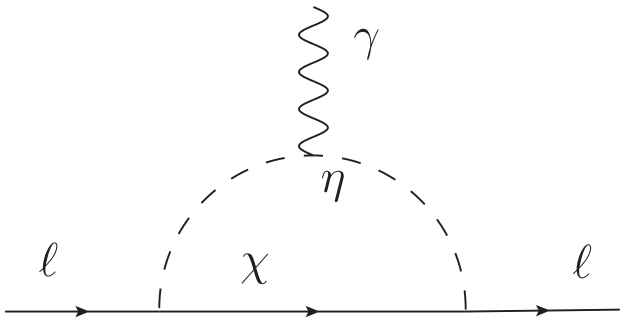

Figure 4.10: Feynman diagram at one-loop order describing the contribution of the DM particle χ and the mediator η to the magnetic dipole moment of the lepton ℓ.

are obtained, taking $m_\chi \approx m_\eta$, since we set $\mu \leq 1.1$. The analysis neglects systematic uncertainties, since they are subdominant to the statistical uncertainties in DELPHI.

The estimates of the sensitivity of a possible future linear collider, labelled "ILC" in Figure 4.9c, are calculated at a centre-of-mass energy of $\sqrt{s} = 500\,\text{GeV}$ and for a luminosity of 50 fb^{-1}. The signal and the dominant background $\gamma\bar{\nu}\nu$ were simulated in CalcHEP 3.4 [265]. The other important sources of background are the $\gamma\gamma\bar{\nu}\nu$ final state, where one photon escapes undetected, and γe^+e^-, where both electron and positron remain undetected. For these backgrounds the procedure of Ref. [390] is used: the $\gamma\bar{\nu}\nu$ background is increased by 10% to include also $\gamma\gamma\bar{\nu}\nu$ events and for the γe^+e^- background the $\gamma\bar{\nu}\nu$ spectrum is reweighed by a factor $0.825\,[1 - E/(0.9\text{ GeV})]^2$. Negative reweighing factors were excluded. The ILC detector response is modelled according to Refs. [390, 394, 395]. The energy resolution is assumed to be $\Delta E/E = 0.011 \oplus 0.166/\sqrt{E/\text{GeV}}$, where $\oplus$ indicates that the two contributions correspond to separate Gaussian distributions that are statistically independent. The photon energy ranges from 10 GeV to 220 GeV and is binned into 5 GeV fragments to eliminate events with on-shell Z boson production. Furthermore the rapidity is restricted to $|y| < 2.3$. The detection efficiency is energy dependent: $0.941 - 0.00129E_\gamma/\text{GeV}$. A χ^2 analysis is used to determine the limits while systematic uncertainties are neglected.

4.6 Lepton Magnetic Dipole Moments

By twisting the diagrams leading to the effective coupling of DM to photons (Figure 4.4), we obtain a loop of DM and mediator leading to a new contribution to the anomalous magnetic moment $(g-2)_\ell$ of the respective lepton ℓ, see Figure 4.10. This contribution can be used to constrain DM models with annihilation via a charged mediator for the Dirac and Majorana case, see Refs. [101, 362]. If we take the Yukawa couplings to be complex, the diagram also creates a contribution to the electric dipole moment of the lepton, which we will, however, not consider here. For small lepton masses $m_\ell \ll m_\eta$, m_χ we obtain a contribution to the anomalous magnetic moment of [101]

$$\Delta a_\ell \equiv \Delta\Big(\frac{g-2}{2}\Big)_\ell = -\frac{y^2 m_\ell^2}{96\pi^2 m_\chi^2}\frac{\mu^3 - 6\mu^2 + 3\mu + 6\mu\log(\mu) + 2}{(\mu-1)^4}\,, \tag{4.26}$$

where again $\mu = m_\eta^2/m_\chi^2$. We can compare the results to the deviation between SM prediction and experimental measurements for the electron and muon. Because of the short lifetime of the tau-lepton, its magnetic moment has not been measured precisely enough to make a meaningful comparison of SM prediction and experimental value.

For the case of a coupling to electrons, we have a very small difference between SM prediction and experiment of [396]

$$a_e^{\rm exp} - a_e^{\rm SM} = (-1.06 \pm 0.82) \times 10^{-12}\,. \tag{4.27}$$

We include the resulting limit on $\langle\sigma v_{\rm rel}\rangle_{\chi\chi\to\ell^+\ell^-\gamma}$ in Figure 4.9b, where the width of the blue band is given by a variation of the mass ratio μ: the upper edge is the limit for $\mu = 1.01$, the lower edge for $\mu = 1.1$.

For the anomalous magnetic moment of the muon, the deviation between SM prediction and experimental value is actually significant [397]:

$$a_\mu^{\rm exp} - a_\mu^{\rm SM} = [2.87 \pm 0.63\,({\rm exp.}) \pm 0.49\,({\rm theor.})] \times 10^{-9}\,. \tag{4.28}$$

Unfortunately, the discrepancy has the opposite sign to the correction given by our simplified model in eq. (4.26). For the resulting constraint on the model, the experimental and theoretical uncertainties are added in quadrature. To bridge the remaining discrepancy we linearly add an ad-hoc uncertainty of 2.87×10^{-9} (the central value of the difference), thus inflating the error by hand. The limits, shown as an orange band, as before for $\mu = 1.1$ to $\mu = 1.01$, are also included in Figure 4.9b.

For small DM masses, $m_\chi < 10$ GeV, these constraints on the anomalous magnetic moments of the leptons are competitive with direct and indirect DM searches, see Figure 4.9b.

4.7 Hyperfine Splitting in Lepton-Antilepton Systems

Positronium (e^+e^-) and true muonium ($\mu^+\mu^-$) are lepton-antilepton bound states that can be accurately analysed with spectroscopy while they are theoretically much simpler than for example atoms – in particular, any nuclear effects are completely absent. They are therefore very well suited for QED precision tests. The interaction from our simplified model for the Dirac and Majorana case leads to an interaction depicted in the box diagrams in Figure 4.11. They can be parametrised by an effective contact interaction:

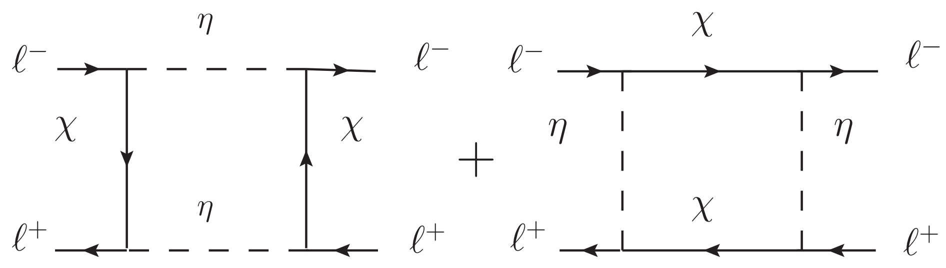

Figure 4.11: Feynman diagrams altering the hyperfine splitting of systems like positronium (e^+e^-) or true muonium ($\mu^+\mu^-$).

$$\mathcal{L}_{\ell^+\ell^-} \equiv \frac{1}{2} C_{\ell^+\ell^-} (\bar{\ell}\gamma^\mu P_R \ell)(\bar{\ell}\gamma_\mu P_R \ell) \tag{4.29}$$

with the coefficient

$$C_{\ell^+\ell^-} = -\frac{y^4}{64\pi^2 m_\chi^2} \frac{\mu^2 - 2\mu \log(\mu) - 1}{(\mu - 1)^3} \,. \tag{4.30}$$

This contact interaction alters the electrostatic potential between the two leptons ℓ^+ and ℓ^- and therefore modifies the hyperfine splitting E_{hfs}, which is the energy difference between the ortho-state $^3\text{S}_1$ (parallel spins) and the para-state $^1\text{S}_0$ (antiparallel spins). We calculate the modification ΔE_{hfs} via the Hamilton operator: First, we insert explicit expressions for the wave functions for ℓ^+ and ℓ^- into the Lagrangian, eq. (4.29), with

$$\ell(x) = \frac{(\alpha_{em} m_\ell)^{3/2}}{\sqrt{\pi}} \exp[-\alpha_{em} m_\ell |\vec{x}| - iEt]\xi \,, \tag{4.31}$$

ξ being a normalised Dirac spinor (to unity) of a non-relativistic particle or antiparticle. Then we perform the integration over d^3x. The Legendre transformation of the Lagrangian into the Hamiltonian gives us a minus sign and the different options of contracting the external fermion states with the lepton fields results in a factor four. Thus, we obtain the respective term in the Hamilton operator of the system. The result is that the new interaction does not affect the ortho-state, but it increases the energy of the para-state. The hyperfine splitting thus becomes smaller by

$$\Delta E_{\text{hfs}} = -\frac{\alpha_{em}^3 m_\ell^3}{8\pi} \frac{y^4}{64\pi^2 m_\chi^2} \frac{\mu^2 - 2\mu \log(\mu) - 1}{(\mu - 1)^3} \,. \tag{4.32}$$

For positronium, we therefore get

$$\Delta E_{\text{hfs}}^{e^+e^-} = -0.17\,\text{Hz} \times y^4 \left(\frac{100\,\text{GeV}}{m_\chi}\right)^2 \,, \tag{4.33}$$

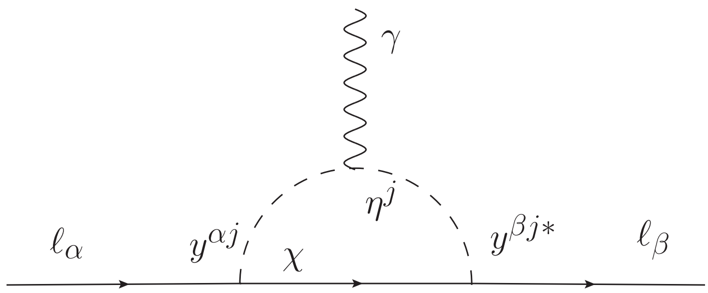

Figure 4.12: Feynman diagram at one-loop order describing the lepton flavour violating decays for $\alpha \neq \beta$ induced by the interaction with the DM particle χ and the mediators η^j.

comparing to the measurement of [398]

$$E_{\text{hfs}}^{e^+e^-} = [203.3942 \pm 0.0016(\text{stat.}) \pm 0.0013(\text{syst.})] \times 10^9\,\text{Hz}\,. \tag{4.34}$$

For the assumed values of $y \approx 1$ and $m_\chi \approx 100$ GeV we get a correction of $\mathcal{O}(10^{-12})$, far beyond the precision of the measurement and also beyond that of the SM prediction [399] of $203.39169(16) \times 10^9$ Hz. The low sensitivity is caused by the size of the positronium system, which is relatively large, while the contact interaction needs small distances to be effective. We obtain similar results for the mixed systems $e^\pm\mu^\mp$.

True muonium, the $\mu^+\mu^-$ bound state, however, seems to be a more promising probe for contact interactions (in our case described by eq. (4.29)) and of new physics in the lepton sector, in general. Although there are no measurements yet, precision experiments seem feasible in the future [400]. The modification from our simplified model results in

$$\Delta E_{\text{hfs}}^{\mu^+\mu^-} = -1.47\,\text{MHz} \times y^4 \left(\frac{100\,\text{GeV}}{m_\chi}\right)^2 , \tag{4.35}$$

which compares to the SM prediction of $E_{\text{hfs}}^{\mu^+\mu^-} \approx 4.23 \times 10^7$ MHz [401], again a small correction of $\mathcal{O}(10^{-7})$. In our model, for a Majorana DM particle with the relic density given in eq. (4.24), and assuming $m_\chi = 130$ GeV and $\mu = 1.1$, the accuracy of $E_{\text{hfs}}^{\mu^+\mu^-}$ would need to be at 0.2 MHz, to exclude thermal relic DM.

4.8 Lepton Flavour Violation

So far we have taken the coupling of the mediator η to be flavour conserving, but in general, the model could include any number of mediators coupling to all three left- and right-handed leptons. The most general Lagrangian, with a Dirac or Majorana fermion χ, can be written as (see eq (4.5)):

$$\mathcal{L} \supset \sum_{\alpha,j} \left(-y_R^{\alpha j} \bar{\chi} P_R \ell^\alpha \eta^j - y_L^{\alpha j} \bar{\chi} P_L \ell^\alpha \eta^j \right) - ie \sum_j \eta^j A^\mu \partial_\mu \eta^{j*} + \text{h.c.}\,. \tag{4.36}$$

The Yukawa couplings $y_{L,R}^{\alpha j}$ become here matrices and η^j are the mass eigenstates of the mediators. The interactions in this generalised model lead to flavour violating decays of the form $\ell_\alpha \to \ell_\beta \gamma$, depicted in Figure 4.12, concretely we obtain the decays $\mu \to e\gamma$, $\tau \to e\gamma$ and $\tau \to \mu\gamma$. We can calculate the decay rate to be

$$\Gamma_{\ell_\alpha \to \ell_\beta \gamma} = \frac{\alpha_{em} m_{\ell_\alpha}^3}{1024 \pi^4 m_\chi^2} \left(|c_L|^2 + |c_R|^2 \right), \tag{4.37}$$

where $c_{L,R}$ are the Wilson coefficients of an effective Lagrangian

$$\mathcal{L}^{\text{eff}}_{\ell_\alpha \to \ell_\beta \gamma} = \frac{e}{32\pi^2 m_\chi} \left[c_L \bar{\ell}_\beta \sigma^{\mu\nu} P_L \ell_\alpha + c_R \bar{\ell}_\beta \sigma^{\mu\nu} P_R \ell_\alpha \right] F_{\mu\nu} \tag{4.38}$$

with

$$c_L = \sum_j y_L^{\alpha j} y_R^{\beta j*} J(\mu_j) + \frac{m_{\ell_\alpha}}{m_\chi} \sum_j y_R^{\alpha j} y_R^{\beta j*} I(\mu_j)\,, \tag{4.39}$$

$$c_R = \sum_j y_R^{\alpha j} y_L^{\beta j*} J(\mu_j) + \frac{m_{\ell_\alpha}}{m_\chi} \sum_j y_L^{\alpha j} y_L^{\beta j*} I(\mu_j)\,. \tag{4.40}$$

$J(\mu)$ and $I(\mu)$ are loop functions:

$$J(\mu) = \frac{\mu^2 - 2\mu \log(\mu) - 1}{2(\mu - 1)^2}\,, \tag{4.41}$$

$$I(\mu) = \frac{\mu^3 - 6\mu^2 + 3\mu + 6\mu \log(\mu) + 2}{12(\mu - 1)^4}\,. \tag{4.42}$$

The mass ratios $\mu_j = m_{\eta_j}^2 / m_\chi^2$ are – as before – the ratios of mediator over DM mass.

To compare to experimental limits we will take the couplings to the left-handed leptons to vanish and assume the mediators to be degenerate in the following.[9] The branching ratios $\text{BR}_{\ell_\alpha \to \ell_\beta \gamma} \simeq \Gamma_{\ell_\alpha \to \ell_\beta \gamma} / \Gamma_{\text{SM}}$, normalised to the SM decay width Γ_{SM} of the decaying lepton, become

$$\text{BR}_{\mu \to e\gamma} \approx 0.032 \left(\frac{100\,\text{GeV}}{m_\chi} \right)^4 \left[\sum_j y_R^{\mu j} y_R^{ej*} I(\mu_j) \right]^2, \tag{4.43}$$

[9]In supersymmetry, a scenario with three mediators can be realized by taking all left-handed sleptons to be too heavy to be phenomenologically relevant.

$$\mathrm{BR}_{\tau\to\mu\gamma} \approx 0.0057 \left(\frac{100\,\mathrm{GeV}}{m_\chi}\right)^4 \left[\sum_j y_R^{\tau j} y_R^{\mu j*} I(\mu_j)\right]^2 , \tag{4.44}$$

$$\mathrm{BR}_{\tau\to e\gamma} \approx 0.0057 \left(\frac{100\,\mathrm{GeV}}{m_\chi}\right)^4 \left[\sum_j y_R^{\tau j} y_R^{ej*} I(\mu_j)\right]^2 . \tag{4.45}$$

The current experimental constraints for the flavour violating decays are

$$\mathrm{BR}_{\mu\to e\gamma} < 5.7 \times 10^{-13} \qquad (\text{Ref. [402]})\,, \tag{4.46}$$

$$\mathrm{BR}_{\tau\to\mu\gamma} < 4.4 \times 10^{-8} \qquad (\text{Ref. [403]})\,, \tag{4.47}$$

$$\mathrm{BR}_{\tau\to e\gamma} < 3.3 \times 10^{-8} \qquad (\text{Ref. [403]})\,. \tag{4.48}$$

When we assume a DM mass of $m_\chi = 100$ GeV and degenerate mediator masses with the ratios $\mu_j = 1.1$ we can set limits on the products of the couplings y_R:

Process	Coupling	Limit
$\mu \to e\gamma$	$\left[\sum_j (y_R^{\mu j} y_R^{ej*})^2\right]^{1/2}$	$< 1.0 \times 10^{-4}$
$\tau \to \mu\gamma$	$\left[\sum_j (y_R^{\tau j} y_R^{\mu j*})^2\right]^{1/2}$	$< 7.0\ 10^{-2}$
$\tau \to e\gamma$	$\left[\sum_j (y_R^{\tau j} y_R^{ej*})^2\right]^{1/2}$	$< 6.1\ 10^{-2}$

Since the relic density of our DM particle, given in eq. (4.24), requires a Yukawa coupling of about $0.1 - 1$, to avoid an overproduction of DM, the above constraints imply, that the flavour off-diagonal couplings need to be subdominant compared to the diagonal couplings. Therefore, they could be neglected in the calculation of *e.g.* the direct detection signals.

The decay $\mu \to 3e$ that is also induced by the flavour off-diagonal couplings, constrains a different combination of Yukawa couplings. It contains diagrams like in Figure 4.12 and also box-diagrams as in Figure 4.11. To estimate the limits set by this decay, we follow the calculation in Ref. [404] to express the branching fraction $\mathrm{BR}(\mu \to 3e)$ in terms of the Wilson coefficients of the effective operators introduced in eqs. (4.29) and (4.38). The experimental limits are taken from Refs. [397,405]. When we assume the flavour-diagonal Yukawa couplings to be of $\mathcal{O}(1)$, the limits on the flavour off-diagonal couplings result to be about a factor of 1/8 weaker than the limit from the decay $\mu \to e\gamma$. Planned searches will, however, improve limits on the branching fraction $\mathrm{BR}(\mu \to 3e)$ by up to four orders of magnitude, see Refs. [406, 407].

4.9 Conclusions

In this chapter we have studied a simplified leptophilic DM model, where a charged mediator η connects the SM leptons with the potential DM particle χ. DM annihilation can therefore be accompanied by the emission of a photon via a process called virtual internal bremsstrahlung (VIB). Models featuring this process are particularly interesting, since they can generate spectral peaks in the gamma ray spectrum that are easily distinguishable from astrophysical backgrounds and therefore facilitate an indirect detection of DM. Leptophilic DM models can be realised in supersymmetry or in radiative neutrino mass models and their parameter space is mostly relatively unconstrained.

In our work we established a connection between the emission of a photon by internal bremsstrahlung and the generation of loop-induced electromagnetic form factors. By connecting the lepton lines in the Feynman diagrams generating the internal bremsstrahlung process (Figure 4.1), we immediately obtain electromagnetic vertex corrections coupling the DM particle to the photon (Figure 4.4). For a Majorana DM particle, these diagrams create an anapole moment, while for a Dirac DM particle both, anapole and magnetic dipole moments are generated, but the dipole moment is larger and thus dominant in DM scattering processes. The anapole and dipole moments induce interactions of the DM with atomic nuclei and we can thus set constraints on the model from direct detection data. For Dirac DM we set constraints on the annihilation cross section for $\bar{\chi}\chi \to \ell^+\ell^-$, while for Majorana DM the anapole moment allows us to directly constrain the internal bremsstrahlung cross section of the process $\chi\chi \to \ell^+\ell^-\gamma$. The analysis was carried out using DM–nucleus scattering data from the LUX and XENON100 direct detection experiments and the limits turned out to be competitive with indirect searches, see Figure 4.9. The limits also grow stronger the closer the mass of the mediator and DM particle become ($\mu \to 1$), which is also the parameter space where the internal bremsstrahlung process generates a peak in the gamma ray spectrum.

The most important results of this chapter can be seen in Figure 4.9. First, we looked at a model with flavour specific couplings to the SM leptons for a Majorana DM candidate in Figure 4.9a. Direct detection limits on the DM annihilation cross section are induced by the anapole form factor, where the strongest limits are set when DM couples to the electron, closely followed by the muon, while the limits from DM coupling to the tau-lepton are about two orders of magnitude weaker. The limits were shown for a mass degeneracy parameter $\mu = m_\eta^2/m_\chi^2$ between 1.1 and 1.01. This plot highlights the most important results of this work. In Figure 4.9b we assumed three degenerate mediators to couple to the three charged SM leptons and the Majorana DM particle χ with a universal coupling constant y. We compared the limits induced by the anapole moment in direct detection experiments – in this case LUX – to gamma-ray searches, collider searches and limits from the lepton magnetic dipole moments. Direct detection limits turned out to be competitive with gamma-ray line searches and better than continuum gamma-ray constraints from dwarf galaxies. Limits from the magnetic moments of the leptons are strong at small DM masses, but otherwise weaker than direct limits and line searches. Collider searches for mono-photons by LEP are calculated for $m_\chi \approx m_\eta$ and turn out to be weaker than direct searches for DM masses $m_\chi \gtrsim 10$ GeV. For small mass splitting of DM and mediator $\mu \lesssim 1.1$, direct detection limits constrain the internal bremsstrahlung cross section $\langle\sigma v_{\rm rel}\rangle_{\chi\chi\to\ell^+\ell^-\gamma}$ to be below few $\times 10^{-28}$ cm^3/s for a DM mass $m_\chi \approx 20\,\mathrm{GeV}$. When the mass splitting – and thus μ – becomes larger, direct detection limits become weaker, but limits from direct collider searches for the mediator η favour a greater splitting, since the leptons from the decay of the mediator are not as soft and thus easier to detect. For $m_\eta/m_\chi \gg 1$ they disfavour $m_\eta \lesssim \mathrm{fex} \times 100\,\mathrm{GeV}$ [101,353].

For the case of a Dirac DM particle we looked at three different scenarios in Figure 4.9d, where DM and mediator couple to the electron, muon or tau-lepton, respectively. Direct detection limits for a coupling to the electron and muon are equal and a little stronger than for the tau-lepton. They are shown for a mass degeneracy between 1.1 and 1.01, as before. These limits are compared to indirect searches from Fermi-LAT and AMS. For larger DM masses $m_\chi \gtrsim 20$ GeV direct detection limits are dominant. Thermal relic production (where we assume $\mu \gtrsim 1.1$ to avoid coannihilations) is disfavoured for DM masses $m_\chi \gtrsim \mathcal{O}(10)$ GeV up to a few hundred GeV, but one should take a closer look since direct detection limits are strongest, just when coannihilations set in (namely when $\mu \to 1$). Line searches are not sensitive in this case, since for Dirac DM, no line-like signal is generated.

Updated searches should improve the direct detection limits by about two orders of magnitude, see Figure 4.9c. The upgraded experiments XENON1T and LUX-ZEPLIN should further exclude the thermal relic hypothesis. For the case of a signal detection, the spectrum of recoil events could distinguish anapole and dipole interaction and thus the Majorana from the Dirac DM scenario, with enough statistics at low energies (see Figure 4.7).

Low energy precision experiments also place important bounds on our simplified model. We analysed the contributions to the anomalous magnetic moments $(g-2)_\ell$ of the SM leptons and compared to measurements for the muon and electron. The deviation between SM prediction and the experimental value for the muon unfortunately has the opposite sign to the deviation induced by our simplified model. For both, muon and electron, the limits from the anomalous magnetic moments are weaker than direct detection limits for DM masses above $m_\chi \gtrsim 10\,\mathrm{GeV}$. If we include multiple mediators with flavour violating couplings, we obtain powerful bounds by the flavour violating decays $\mu \to e\gamma$, $\tau \to \mu\gamma$, $\tau \to e\gamma$ and $\mu \to 3e$ in Section 4.7. Finally, we looked at the hyperfine splitting in bound states of electrons and muons in Section 4.8. While for positronium (e^+e^-) the modifications are far beyond experimental precision, a measurement of true muonium $(\mu^+\mu^-)$ could place important bounds for light DM ($m_\chi \lesssim 10\,\mathrm{GeV}$). For heavier DM ($m_\chi \sim 100\,\mathrm{GeV}$) an experimental precision better than 10^{-7} seems challenging.

In summary, we showed that loop-induced interactions can place important bounds on leptophilic DM models. Resulting direct detection constraints are competitive or even stronger that indirect searches and precision experiments and place complementary limits. Particularly interesting is a scenario, where a peak is observed in the cosmic gamma ray spectrum with no other indirect signs for DM. Then, leptophilic DM models with internal bremsstrahlung provide a compelling explanation, and direct detection experiments can confirm this hypothesis via the induced electromagnetic moments. Direct detection limits also turn out to be strong precisely in the parameter region creating a line-like signal, namely when the mediator and DM mass are close to being degenerate.

Chapter 5

Summary and Conclusion

In this thesis, we have investigated several well-motivated extensions of the Standard Model (SM) that give rise to distinctive collider signatures, leave imprints in indirect and direct dark matter (DM) experiments, and can be constrained by high-precision measurements. We have placed particular focus on the interplay between gauge structure and particle content, the masses and decay patterns of dark sector particles and their experimental signatures, and the impact of loop-induced couplings on experimental observables. Across three complementary case studies, we demonstrated how detailed theoretical properties – such as anomaly cancellation, chiral structure, mass spectra, decay widths, and loop-induced effects – translate into concrete, experimentally testable predictions.

In our first project, presented in Chapter 2, we studied extensions of the SM by additional $U(1)$ gauge symmetries. Building on calculations in the literature that solve the divergences of the involved currents, we analysed the full anomalous $Z - Z' - \gamma$ vertex function and subsequently calculated the decay $Z \to Z'\gamma$ in the exemplary models of gauged baryon minus lepton number $U(1)_{B-L}$ and gauged baryon number $U(1)_B$. While the fermion content of $U(1)_{B-L}$ is anomaly free within the SM when augmented by three right-handed neutrinos, $U(1)_B$ is anomalous and requires the introduction of additional fermions for anomaly cancellation. This, in turn, permits non-trivial chiral structures within an anomaly-free set.
By performing a full calculation of the vertex function, we showed how anomaly cancellation and fermion chiral structure govern the decoupling behaviour of heavy fermions. While theories with a uniform chiral structure exhibit vanishing contributions from degenerate fermion sets, more intricate chiral assignments – such as in gauged baryon number – can lead to finite, non-decoupling effects. We presented the branching fractions for the decay $Z \to Z'\gamma$ in the $U(1)_{B-L}$ and $U(1)_B$ models, taking into account the finite fermion masses. These masses are determined by their Yukawa couplings to the corresponding scalar field and its vacuum expectation value (vev), which in turn links them to the mass of the Z' boson – they cannot be arbitrarily large.

We further derived constraints on the $U(1)_B$ parameter space from limits on the decay $Z \to Z'\gamma$, with subsequent $Z' \to q\bar{q}$, yielding a $(jj)\gamma$ final state, and compared them to existing collider and precision measurements. A comparison with an effective field theory description clarified the regime of validity and the limitations of approaches based on Wess-Zumino terms. Our results can be adapted to calculate the $Z \to Z'\gamma$ decay width for any other $U(1)$ gauge symmetry with fermions charged under the three symmetries, thereby deriving limits on the corresponding parameter space.
Summarising this project, we significantly improved the understanding of how chiral structure and anomaly cancellation conditions in SM extensions with additional $U(1)$ gauge symmetries impact observables such as the decay width $Z \to Z'\gamma$.

In Chapter 3, we explored the sensitivity of the Large Hadron Collider (LHC) to inelastic DM models, in which a DM particle is accompanied by a slightly heavier excited state. Owing to the suppression of diagonal couplings, direct detection experiments are insensitive to wide regions of parameter space, while DM production at colliders remains mostly unaffected. Constraints from monojet searches are therefore structurally analogous to those in the standard weakly interacting massive particle (WIMP) scenario. We found that collider signatures are largely independent of the mediator type at the level of kinematics, while production rates and decay widths determine the relative strength of the constraints. For monojet searches, the reach is dominated by the production cross section, yielding the strongest limits for vector mediated models. For all four mediator types, we excluded parts of the parameter space, in particular regions that reproduce the correct DM relic density within our simplified scenarios. The analysis could be significantly improved by combining multiple signal regions, thereby reducing systematic uncertainties.
Furthermore, in inelastic scenarios the decay of the heavier dark sector state can give rise to a measurable displacement, making displaced vertex searches a powerful probe of these models. Such analyses are particularly sensitive to long-lived excited states, which generally favour small mass splittings. In our study, the necessary requirements could only be met for pseudoscalar mediators. However, the cuts imposed on the invariant mass of the displaced vertex and its decay products forced us to consider a relatively large mass splitting between the two dark states. We showed that relaxing these cuts – a seemingly feasible modification – would substantially enhance the sensitivity of this analysis to inelastic DM scenarios. We also identified several additional searches that could be relevant for inelastic DM and leave their exploration to future work.
Overall, our study demonstrated the LHC's potential to constrain inelastic DM models, identifying in particular the parameters to which current searches are most sensitive, as well as modifications that could significantly enhance the reach of displaced vertex searches.

The final chapter, Chapter 4, investigated leptophilic DM models with a charged mediator and either a Majorana or Dirac DM candidate. In these models, DM annihilation can be accompanied by virtual internal bremsstrahlung, which in the Majorana case can produce sharp spectral features in gamma rays. By establishing a direct connection be-

tween internal bremsstrahlung and loop-induced electromagnetic form factors, we showed that these models inevitably generate anapole and/or dipole moments that can be probed by direct detection experiments. Using data from LUX, we derived constraints that are competitive with – and in some regions stronger than – those from indirect detection and collider searches, especially when the DM and mediator masses are nearly degenerate, precisely the region that produces pronounced gamma-ray lines.
We further showed that loop effects induce lepton magnetic dipole moments, modify the hyperfine splitting in lepton-antilepton systems, and generate lepton flavour-violating decays. In addition, we computed collider limits from the LEP e^+e^- collider. These limits are generally subdominant to direct detection bounds. Future direct detection experiments have the potential to further test the thermal relic hypothesis and, in the event of a discovery, may allow to distinguish between Majorana and Dirac DM through their recoil spectra.
In summary, this analysis investigated the interplay of direct and indirect searches for DM and derived new limits on leptophilic DM from direct detection experiments, where loop-induced couplings to photons lead to constraints that are competitive with existing bounds.

Taken together, the results of this thesis highlight the importance of combining model consistency, collider searches, direct and indirect detection, and precision measurements when probing physics beyond the SM. They demonstrate that seemingly subtle theoretical features – such as anomaly structure, mass splittings, mass degeneracies, and loop-induced interactions – can have profound phenomenological consequences, and that exploiting these connections is essential for fully exploring the remaining viable parameter space of new physics models.

Appendix A

Addendum to Leptophilic Dark Matter

A.1 Virtual Internal Bremsstrahlung

In Section 4.2 we showed in Figure 4.1 the Feynman graphs contributing to the process of virtual internal bremsstrahlung (VIB), wherefrom we can calculate the differential (eq. (4.7)) and the full cross section (eq. (4.8)) for the annihilation of two Majorana DM particles into two leptons and a photon, $\chi\chi \to \ell^+\ell^-\gamma$. Here we want to specify the matrix elements that are defined by the different contributions of virtual internal bremsstrahlung. The individual graphs with their respective labelling of the momenta are shown in Figure A.1.

The internal momenta, denoted by q_1 to q_6 relate to the external momenta by:

$$q_1 = k_1 - p_2 + (k_1 - p_1 - p_2) = k_1 - k_2 - p_1 + p_3 \tag{A.1}$$

$$q_2 = k_2 - k_1 - p_1 + p_3 \tag{A.2}$$

$$q_3 = p_1 + p_3 = k_1 + k_2 - p_3 \tag{A.3}$$

$$q_4 = p_1 + p_2 = k_1 + k_2 - p_3 = q_3 \tag{A.4}$$

$$q_5 = p_2 + p_3 = k_1 + k_2 - p_1 \tag{A.5}$$

$$q_6 = p_2 + p_3 = k_1 + k_2 - p_1 = q_5 \tag{A.6}$$

The matrix elements corresponding to the numbered Feynman diagrams in Figure A.1 are given by:

$$i\mathcal{A}_1 = [\bar{u}(\vec{p}_1)(iyP_R)u(\vec{k}_1)]\,[\bar{v}(\vec{k}_2)(iyP_R)v(\vec{p}_3)] \cdot \frac{i}{(k_1 - p_1)^2 - m_\eta^2} \cdot \\ \cdot \frac{i}{(k_2 - p_3)^2 - m_\eta^2} \cdot (ieq_{1\mu})\varepsilon^{*\mu}(p_2, \lambda) \tag{A.7}$$

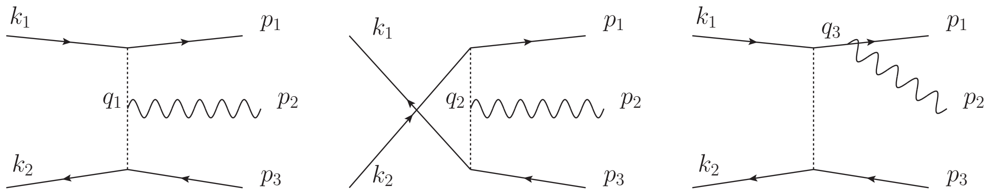

(a) Feynman graph no 1. **(b)** Feynman graph no 2. **(c)** Feynman graph no 3.

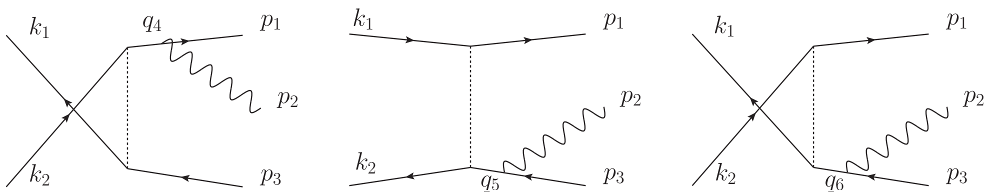

(d) Feynman graph no 4. **(e)** Feynman graph no 5. **(f)** Feynman graph no 6.

Figure A.1: Feynman graphs contributing to the process of virtual internal bremsstrahlung (VIB) including the labelling of the momenta.

$$
\begin{aligned}
i\mathcal{A}_2 &= [\bar{u}(\vec{p}_1)(iyP_R)u(\vec{k}_2)]\,[\bar{v}(\vec{k}_1)(iyP_R)v(\vec{p}_3)] \cdot \frac{i}{(k_2-p_1)^2-m_\eta^2}\cdot \\
&\qquad \cdot \frac{i}{(k_1-p_3)^2-m_\eta^2}\cdot(ieq_{2\mu})\varepsilon^{*\mu}(p_2,\lambda) && \text{(A.8)} \\
i\mathcal{A}_3 &= [\bar{v}(\vec{k}_2)(iyP_R)v(\vec{p}_3)]\,\frac{i}{(k_2-p_3)^2-m_\eta^2}[\bar{u}(\vec{p}_1)(ie\gamma^\mu)\frac{i\not{q}_3}{q_3^2}(iyP_R)u(\vec{k}_1)]\cdot \\
&\qquad \cdot\, \varepsilon^{*\mu}(p_2,\lambda) && \text{(A.9)} \\
i\mathcal{A}_4 &= [\bar{v}(\vec{k}_1)(iyP_R)v(\vec{p}_3)]\,\frac{i}{(k_1-p_3)^2-m_\eta^2}[\bar{u}(\vec{p}_1)(ie\gamma^\mu)\frac{i\not{q}_4}{q_4^2}(iyP_R)u(\vec{k}_2)]\cdot \\
&\qquad \cdot\, \varepsilon^{*\mu}(p_2,\lambda) && \text{(A.10)} \\
i\mathcal{A}_5 &= [\bar{u}(\vec{p}_1)(iyP_R)u(\vec{k}_1)]\,\frac{i}{(k_1-p_1)^2-m_\eta^2}[\bar{v}(\vec{k}_2)(iyP_R)\frac{i\not{q}_5}{q_5^2}(ie\gamma^\mu)v(\vec{p}_3)]\cdot \\
&\qquad \cdot\, \varepsilon^{*\mu}(p_2,\lambda) && \text{(A.11)} \\
i\mathcal{A}_6 &= [\bar{u}(\vec{p}_1)(iyP_R)u(\vec{k}_2)]\,\frac{i}{(k_2-p_1)^2-m_\eta^2}[\bar{v}(\vec{k}_1)(iyP_R)\frac{i\not{q}_6}{q_6^2}(ie\gamma^\mu)v(\vec{p}_3)]\cdot \\
&\qquad \cdot\, \varepsilon^{*\mu}(p_2,\lambda) && \text{(A.12)}
\end{aligned}
$$

The matrix elements and cross sections were calculated in Mathematica [174] using FeynCalc [408, 409]. For the case of Majorana DM, all of the diagrams in Figure A.1 have to be taken into account. We calculated the matrix element (eq. (4.6)) and the differential and full cross sections (eqs. (4.7) and (4.8)) for the process of the annihilation of Majorana DM $\chi\chi \to \ell^+\ell^-\gamma$, showing in Figure 4.2 the differential cross section with its characteristic cusp profile, that could be detected as a line-like feature in the gamma-ray spectrum of indirect detection data.

For the case of Dirac DM, the crossed diagrams, which are the Feynman graphs no. 2, 4, and 6, are absent. We do not obtain an analytic expression and show the numeric result in Figure 4.3.

Bibliography

[1] **UA1** Collaboration, G. Arnison et al., *Experimental Observation of Isolated Large Transverse Energy Electrons with Associated Missing Energy at* $\sqrt{s} = 540$ *GeV*, *Phys. Lett. B* **122** (1983) 103–116.

[2] **UA2** Collaboration, M. Banner et al., *Observation of Single Isolated Electrons of High Transverse Momentum in Events with Missing Transverse Energy at the CERN anti-p p Collider*, *Phys. Lett. B* **122** (1983) 476–485.

[3] **E598** Collaboration, J. J. Aubert et al., *Experimental Observation of a Heavy Particle J*, *Phys. Rev. Lett.* **33** (1974) 1404–1406.

[4] **SLAC-SP-017** Collaboration, J. E. Augustin et al., *Discovery of a Narrow Resonance in* e^+e^- *Annihilation*, *Phys. Rev. Lett.* **33** (1974) 1406–1408.

[5] **D0** Collaboration, S. Abachi et al., *Observation of the top quark*, *Phys. Rev. Lett.* **74** (1995) 2632–2637, [hep-ex/9503003].

[6] **CDF** Collaboration, F. Abe et al., *Observation of top quark production in* $\bar{p}p$ *collisions*, *Phys. Rev. Lett.* **74** (1995) 2626–2631, [hep-ex/9503002].

[7] **ATLAS** Collaboration, G. Aad et al., *Observation of a new particle in the search for the Standard Model Higgs boson with the ATLAS detector at the LHC*, *Phys. Lett. B* **716** (2012) 1–29, [arXiv:1207.7214].

[8] **CMS** Collaboration, S. Chatrchyan et al., *Observation of a New Boson at a Mass of 125 GeV with the CMS Experiment at the LHC*, *Phys. Lett. B* **716** (2012) 30–61, [arXiv:1207.7235].

[9] **Super-Kamiokande** Collaboration, Y. Fukuda et al., *Evidence for oscillation of atmospheric neutrinos*, *Phys. Rev. Lett.* **81** (1998) 1562–1567, [hep-ex/9807003].

[10] **SNO** Collaboration, Q. R. Ahmad et al., *Measurement of the rate of* $\nu_e + d \to p + p + e^-$ *interactions produced by* ^8B *solar neutrinos at the Sudbury Neutrino Observatory*, *Phys. Rev. Lett.* **87** (2001) 071301, [nucl-ex/0106015].

[11] **Particle Data Group** Collaboration, S. Navas et al., *Review of particle physics*, *Phys. Rev. D* **110** (2024), no. 3 030001.

[12] B. Pontecorvo, *Inverse Beta Processes and Nonconservation of Lepton Charge*, *Sov. Phys. JETP* **7** (1958) 172–173.

[13] Z. Maki, M. Nakagawa, and S. Sakata, *Remarks on the unified model of elementary particles*, *Prog. Theor. Phys.* **28** (1962) 870–880.

[14] **KATRIN** Collaboration, M. Aker et al., *Direct neutrino-mass measurement based on 259 days of KATRIN data*, *Science* **388** (2025), no. 6743 adq9592, [arXiv:2406.13516].

[15] **LSND** Collaboration, A. Aguilar et al., *Evidence for neutrino oscillations from the observation of $\bar{\nu}_e$ appearance in a $\bar{\nu}_\mu$ beam*, *Phys. Rev. D* **64** (2001) 112007, [hep-ex/0104049].

[16] **MiniBooNE** Collaboration, A. A. Aguilar-Arevalo et al., *Updated MiniBooNE neutrino oscillation results with increased data and new background studies*, *Phys. Rev. D* **103** (2021), no. 5 052002, [arXiv:2006.16883].

[17] **GALLEX** Collaboration, W. Hampel et al., *Final results of the Cr-51 neutrino source experiments in GALLEX*, *Phys. Lett. B* **420** (1998) 114–126.

[18] F. Kaether, W. Hampel, G. Heusser, J. Kiko, and T. Kirsten, *Reanalysis of the GALLEX solar neutrino flux and source experiments*, *Phys. Lett. B* **685** (2010) 47–54, [arXiv:1001.2731].

[19] **SAGE** Collaboration, J. N. Abdurashitov et al., *Measurement of the solar neutrino capture rate with gallium metal. III: Results for the 2002–2007 data-taking period*, *Phys. Rev. C* **80** (2009) 015807, [arXiv:0901.2200].

[20] V. V. Barinov et al., *Results from the Baksan Experiment on Sterile Transitions (BEST)*, *Phys. Rev. Lett.* **128** (2022), no. 23 232501, [arXiv:2109.11482].

[21] **CDF** Collaboration, T. Aaltonen et al., *High-precision measurement of the W boson mass with the CDF II detector*, *Science* **376** (2022), no. 6589 170–176.

[22] S. Iguro, T. Kitahara, and R. Watanabe, *Global fit to $b \to c\tau\nu$ anomalies as of Spring 2024*, *Phys. Rev. D* **110** (2024), no. 7 075005, [arXiv:2405.06062].

[23] **LHCb** Collaboration, R. Aaij et al., *Measurement of Form-Factor-Independent Observables in the Decay $B^0 \to K^{*0}\mu^+\mu^-$*, *Phys. Rev. Lett.* **111** (2013) 191801, [arXiv:1308.1707].

[24] **Belle** Collaboration, S. Wehle et al., *Lepton-Flavor-Dependent Angular Analysis of $B \to K^*\ell^+\ell^-$*, *Phys. Rev. Lett.* **118** (2017), no. 11 111801, [arXiv:1612.05014].

[25] **ATLAS** Collaboration, M. Aaboud et al., *Angular analysis of $B_d^0 \to K^*\mu^+\mu^-$ decays in pp collisions at $\sqrt{s} = 8$ TeV with the ATLAS detector*, *JHEP* **10** (2018) 047, [arXiv:1805.04000].

[26] **CMS** Collaboration, A. M. Sirunyan et al., *Measurement of angular parameters from the decay $\mathrm{B}^0 \to \mathrm{K}^{*0}\mu^+\mu^-$ in proton-proton collisions at $\sqrt{s} = 8$ TeV*, *Phys. Lett. B* **781** (2018) 517–541, [arXiv:1710.02846].

[27] **Muon g-2** Collaboration, D. P. Aguillard et al., *Measurement of the Positive Muon Anomalous Magnetic Moment to 127 ppb*, *Phys. Rev. Lett.* **135** (2025), no. 10 101802, [arXiv:2506.03069].

[28] R. Aliberti et al., *The anomalous magnetic moment of the muon in the Standard Model: an update*, *Phys. Rept.* **1143** (2025) 1–158, [arXiv:2505.21476].

[29] R. Pohl et al., *The size of the proton*, *Nature* **466** (2010) 213–216.

[30] A. Antognini et al., *Proton Structure from the Measurement of $2S - 2P$ Transition Frequencies of Muonic Hydrogen*, *Science* **339** (2013) 417–420.

[31] N. Bezginov, T. Valdez, M. Horbatsch, A. Marsman, A. C. Vutha, and E. A. Hessels, *A measurement of the atomic hydrogen Lamb shift and the proton charge radius*, *Science* **365** (2019), no. 6457 1007–1012.

[32] W. Xiong et al., *A small proton charge radius from an electron–proton scattering experiment*, *Nature* **575** (2019), no. 7781 147–150.

[33] M. D. Schwartz, *Quantum Field Theory and the Standard Model.* Cambridge University Press, 3, 2014.

[34] W. E. Burcham and M. Jobes, *Nuclear and particle physics.* 1995.

[35] M. E. Peskin and D. V. Schroeder, *An Introduction to quantum field theory.* Addison-Wesley, Reading, USA, 1995.

[36] C.-N. Yang and R. L. Mills, *Conservation of Isotopic Spin and Isotopic Gauge Invariance*, *Phys. Rev.* **96** (1954) 191–195.

[37] M. Gell-Mann, *A Schematic Model of Baryons and Mesons*, *Phys. Lett.* **8** (1964) 214–215.

[38] G. Zweig, *An SU(3) model for strong interaction symmetry and its breaking. Version 2*, pp. 22–101. 2, 1964.

[39] O. W. Greenberg, *Spin and Unitary Spin Independence in a Paraquark Model of Baryons and Mesons*, *Phys. Rev. Lett.* **13** (1964) 598–602.

[40] H. Fritzsch, M. Gell-Mann, and H. Leutwyler, *Advantages of the Color Octet Gluon Picture*, *Phys. Lett. B* **47** (1973) 365–368.

[41] D. J. Gross and F. Wilczek, *Ultraviolet Behavior of Nonabelian Gauge Theories*, *Phys. Rev. Lett.* **30** (1973) 1343–1346.

[42] H. D. Politzer, *Reliable Perturbative Results for Strong Interactions?*, *Phys. Rev. Lett.* **30** (1973) 1346–1349.

[43] S. L. Glashow, *Partial Symmetries of Weak Interactions*, *Nucl. Phys.* **22** (1961) 579–588.

[44] S. Weinberg, *A Model of Leptons*, *Phys. Rev. Lett.* **19** (1967) 1264–1266.

[45] A. Salam, *Weak and Electromagnetic Interactions*, *Conf. Proc. C* **680519** (1968) 367–377.

[46] P. W. Higgs, *Broken symmetries, massless particles and gauge fields*, *Phys. Lett.* **12** (1964) 132–133.

[47] P. W. Higgs, *Broken Symmetries and the Masses of Gauge Bosons*, *Phys. Rev. Lett.* **13** (1964) 508–509.

[48] N. Cabibbo, *Unitary Symmetry and Leptonic Decays*, *Phys. Rev. Lett.* **10** (1963) 531–533.

[49] M. Kobayashi and T. Maskawa, *CP Violation in the Renormalizable Theory of Weak Interaction*, *Prog. Theor. Phys.* **49** (1973) 652–657.

[50] P. Minkowski, *$\mu \to e\gamma$ at a Rate of One Out of 10^9 Muon Decays?*, *Phys. Lett. B* **67** (1977) 421–428.

[51] M. Gell-Mann, P. Ramond, and R. Slansky, *Complex Spinors and Unified Theories*, *Conf. Proc. C* **790927** (1979) 315–321, [`arXiv:1306.4669`].

[52] R. N. Mohapatra and G. Senjanovic, *Neutrino Mass and Spontaneous Parity Nonconservation*, *Phys. Rev. Lett.* **44** (1980) 912.

[53] F. Zwicky, *On the Masses of Nebulae and of Clusters of Nebulae*, *Astrophys. J.* **86** (1937) 217–246.

[54] V. C. Rubin and W. K. Ford, Jr., *Rotation of the Andromeda Nebula from a Spectroscopic Survey of Emission Regions*, *Astrophys. J.* **159** (1970) 379–403.

[55] V. C. Rubin, W. K. Ford, Jr., and N. Thonnard, *Extended rotation curves of high-luminosity spiral galaxies. IV. Systematic dynamical properties, Sa through Sc*, *Astrophys. J. Lett.* **225** (1978) L107–L111.

[56] M. S. Roberts, *A high-resolution 21-cm hydrogen-line survey of the andromeda nebula*, *The Astrophysical Journal* **144** (1966) 639–656.

[57] G. Bertone and D. Hooper, *History of dark matter*, *Rev. Mod. Phys.* **90** (2018), no. 4 045002, [arXiv:1605.04909].

[58] A. A. Penzias and R. W. Wilson, *A Measurement of excess antenna temperature at 4080-Mc/s*, *Astrophys. J.* **142** (1965) 419–421.

[59] S. S. Gershtein and Y. B. Zeldovich, *Rest Mass of Muonic Neutrino and Cosmology*, *JETP Lett.* **4** (1966) 120–122.

[60] D. Clowe, A. Gonzalez, and M. Markevitch, *Weak lensing mass reconstruction of the interacting cluster 1E0657-558: Direct evidence for the existence of dark matter*, *Astrophys. J.* **604** (2004) 596–603, [astro-ph/0312273].

[61] D. Clowe, M. Bradac, A. H. Gonzalez, M. Markevitch, S. W. Randall, C. Jones, and D. Zaritsky, *A direct empirical proof of the existence of dark matter*, *Astrophys. J. Lett.* **648** (2006) L109–L113, [astro-ph/0608407].

[62] **SDSS** Collaboration, D. J. Eisenstein et al., *Detection of the Baryon Acoustic Peak in the Large-Scale Correlation Function of SDSS Luminous Red Galaxies*, *Astrophys. J.* **633** (2005) 560–574, [astro-ph/0501171].

[63] **2dFGRS** Collaboration, S. Cole et al., *The 2dF Galaxy Redshift Survey: Power-spectrum analysis of the final dataset and cosmological implications*, *Mon. Not. Roy. Astron. Soc.* **362** (2005) 505–534, [astro-ph/0501174].

[64] **COBE** Collaboration, G. F. Smoot et al., *Structure in the COBE differential microwave radiometer first year maps*, *Astrophys. J. Lett.* **396** (1992) L1–L5.

[65] A. Einstein, *The foundation of the general theory of relativity.*, *Annalen Phys.* **49** (1916), no. 7 769–822.

[66] E. Hubble, *A relation between distance and radial velocity among extra-galactic nebulae*, *Proc. Nat. Acad. Sci.* **15** (1929) 168–173.

[67] **Supernova Cosmology Project** Collaboration, S. Perlmutter et al., *Measurements of Ω and Λ from 42 High Redshift Supernovae*, *Astrophys. J.* **517** (1999) 565–586, [astro-ph/9812133].

[68] **Supernova Search Team** Collaboration, A. G. Riess et al., *Observational evidence from supernovae for an accelerating universe and a cosmological constant*, *Astron. J.* **116** (1998) 1009–1038, [astro-ph/9805201].

[69] **WMAP** Collaboration, D. N. Spergel et al., *First year Wilkinson Microwave Anisotropy Probe (WMAP) observations: Determination of cosmological parameters*, *Astrophys. J. Suppl.* **148** (2003) 175–194, [astro-ph/0302209].

[70] **Planck** Collaboration, N. Aghanim et al., *Planck 2018 results. VI. Cosmological parameters*, *Astron. Astrophys.* **641** (2020) A6, [arXiv:1807.06209]. [Erratum: Astron.Astrophys. 652, C4 (2021)].

[71] R. V. Wagoner, W. A. Fowler, and F. Hoyle, *On the Synthesis of elements at very high temperatures*, *Astrophys. J.* **148** (1967) 3–49.

[72] G. Jungman, M. Kamionkowski, and K. Griest, *Supersymmetric dark matter*, *Phys. Rept.* **267** (1996) 195–373, [hep-ph/9506380].

[73] G. Servant and T. M. P. Tait, *Is the lightest Kaluza-Klein particle a viable dark matter candidate?*, *Nucl. Phys. B* **650** (2003) 391–419, [hep-ph/0206071].

[74] T. Flacke, K. Kong, and S. C. Park, *A Review on Non-Minimal Universal Extra Dimensions*, *Mod. Phys. Lett. A* **30** (2015), no. 05 1530003, [arXiv:1408.4024].

[75] H.-C. Cheng and I. Low, *TeV symmetry and the little hierarchy problem*, *JHEP* **09** (2003) 051, [hep-ph/0308199].

[76] J. Hubisz and P. Meade, *Phenomenology of the littlest Higgs with T-parity*, *Phys. Rev. D* **71** (2005) 035016, [hep-ph/0411264].

[77] N. Bozorgnia, J. Bramante, J. M. Cline, D. Curtin, D. McKeen, D. E. Morrissey, A. Ritz, S. Viel, A. C. Vincent, and Y. Zhang, *Dark matter candidates and searches*, *Can. J. Phys.* **103** (2025), no. 8 671–703, [arXiv:2410.23454].

[78] M. Cirelli, A. Strumia, and J. Zupan, *Dark Matter*, arXiv:2406.01705.

[79] J. Preskill, M. B. Wise, and F. Wilczek, *Cosmology of the Invisible Axion*, *Phys. Lett. B* **120** (1983) 127–132.

[80] L. F. Abbott and P. Sikivie, *A Cosmological Bound on the Invisible Axion*, *Phys. Lett. B* **120** (1983) 133–136.

[81] M. Dine and W. Fischler, *The Not So Harmless Axion*, *Phys. Lett. B* **120** (1983) 137–141.

[82] C. A. J. O'Hare, *Cosmology of axion dark matter*, *PoS* **COSMICWISPers** (2024) 040, [arXiv:2403.17697].

[83] L. Hui, J. P. Ostriker, S. Tremaine, and E. Witten, *Ultralight scalars as cosmological dark matter*, *Phys. Rev. D* **95** (2017), no. 4 043541, [arXiv:1610.08297].

[84] J. Jaeckel and A. Ringwald, *The Low-Energy Frontier of Particle Physics*, *Ann. Rev. Nucl. Part. Sci.* **60** (2010) 405–437, [arXiv:1002.0329].

[85] M. Pospelov, A. Ritz, and M. B. Voloshin, *Bosonic super-WIMPs as keV-scale dark matter*, *Phys. Rev. D* **78** (2008) 115012, [arXiv:0807.3279].

[86] J. Redondo and M. Postma, *Massive hidden photons as lukewarm dark matter*, *JCAP* **02** (2009) 005, [arXiv:0811.0326].

[87] S. Hawking, *Gravitationally collapsed objects of very low mass*, *Mon. Not. Roy. Astron. Soc.* **152** (1971) 75.

[88] Y. B. Zel'dovich and I. D. Novikov, *The Hypothesis of Cores Retarded during Expansion and the Hot Cosmological Model*, *Sov. Astron.* **10** (1967) 602.

[89] P. Ivanov, P. Naselsky, and I. Novikov, *Inflation and primordial black holes as dark matter*, *Phys. Rev. D* **50** (1994) 7173–7178.

[90] J. Yokoyama, *Formation of primordial black holes in the inflationary universe*, *Phys. Rept.* **307** (1998) 133–139.

[91] J. R. Espinosa, D. Racco, and A. Riotto, *Cosmological Signature of the Standard Model Higgs Vacuum Instability: Primordial Black Holes as Dark Matter*, *Phys. Rev. Lett.* **120** (2018), no. 12 121301, [arXiv:1710.11196].

[92] S. W. Hawking, I. G. Moss, and J. M. Stewart, *Bubble Collisions in the Very Early Universe*, *Phys. Rev. D* **26** (1982) 2681.

[93] H. Kodama, M. Sasaki, and K. Sato, *Abundance of Primordial Holes Produced by Cosmological First Order Phase Transition*, *Prog. Theor. Phys.* **68** (1982) 1979.

[94] A. Escrivà, F. Kuhnel, and Y. Tada, *Primordial Black Holes*, arXiv:2211.05767.

[95] A. M. Green and B. J. Kavanagh, *Primordial Black Holes as a dark matter candidate*, *J. Phys. G* **48** (2021), no. 4 043001, [arXiv:2007.10722].

[96] D. Tucker-Smith and N. Weiner, *Inelastic dark matter*, *Phys. Rev.* **D64** (2001) 043502, [hep-ph/0101138].

[97] A. Kamada, K. Kaneta, K. Yanagi, and H.-B. Yu, *Self-interacting dark matter and muon $g-2$ in a gauged $U(1)_{L_\mu - L_\tau}$ model*, *JHEP* **06** (2018) 117, [arXiv:1805.00651].

[98] Z.-W. Wang, Z.-L. Han, F. Huang, Y. Jin, and H. Li, *Prospects of Z' portal dark matter in U(1)Lμ-Lτ*, *Phys. Rev. D* **111** (2025), no. 9 095017, [arXiv:2501.08622].

[99] S. Baek and P. Ko, *Phenomenology of U(1)(L(mu)-L(tau)) charged dark matter at PAMELA and colliders*, *JCAP* **10** (2009) 011, [arXiv:0811.1646].

[100] Q.-H. Cao, E. Ma, and G. Shaughnessy, *Dark Matter: The Leptonic Connection*, *Phys.Lett.* **B673** (2009) 152–155, [arXiv:0901.1334].

[101] T. Bringmann, X. Huang, A. Ibarra, S. Vogl, and C. Weniger, *Fermi LAT Search for Internal Bremsstrahlung Signatures from Dark Matter Annihilation*, arXiv:1203.1312.

[102] **XENON** Collaboration, E. Aprile et al., *The XENONnT dark matter experiment*, *Eur. Phys. J. C* **84** (2024), no. 8 784, [arXiv:2402.10446].

[103] **XENON** Collaboration, E. Aprile et al., *WIMP Dark Matter Search Using a 3.1 Tonne-Year Exposure of the XENONnT Experiment*, *Phys. Rev. Lett.* **135** (2025), no. 22 221003, [arXiv:2502.18005].

[104] **XENON** Collaboration, E. Aprile et al., *First Search for Light Dark Matter in the Neutrino Fog with XENONnT*, *Phys. Rev. Lett.* **134** (2025), no. 11 111802, [arXiv:2409.17868].

[105] **LZ** Collaboration, J. Aalbers et al., *Dark Matter Search Results from 4.2 Tonne-Years of Exposure of the LUX-ZEPLIN (LZ) Experiment*, *Phys. Rev. Lett.* **135** (2025), no. 1 011802, [arXiv:2410.17036].

[106] **LZ** Collaboration, D. S. Akerib et al., *Searches for Light Dark Matter and Evidence of Coherent Elastic Neutrino-Nucleus Scattering of Solar Neutrinos with the LUX-ZEPLIN (LZ) Experiment*, arXiv:2512.08065.

[107] **PandaX** Collaboration, Z. Bo et al., *Dark Matter Search Results from 1.54 Tonne·Year Exposure of PandaX-4T*, *Phys. Rev. Lett.* **134** (2025), no. 1 011805, [arXiv:2408.00664].

[108] **PandaX** Collaboration, M. Zhang et al., *Search for Light Dark Matter with 259 Days of Data in PandaX-4T*, *Phys. Rev. Lett.* **135** (2025), no. 21 211001, [arXiv:2507.11930].

[109] **Fermi-LAT, HAWC, H.E.S.S., MAGIC, VERITAS** Collaboration, S. Abdollahi et al., *Combined dark matter search towards dwarf spheroidal galaxies with Fermi-LAT, HAWC, H.E.S.S., MAGIC, and VERITAS*, arXiv:2508.20229.

[110] **Fermi-LAT** Collaboration, M. N. Mazziotta, M. Giliberti, F. Loparco, and D. Serini, *Search for Dark Matter Lines in the gamma-ray energy spectra with the Fermi-LAT*, *PoS* **ICRC2023** (2023) 1387.

[111] **H.E.S.S.** Collaboration, M. Vecchi, J. Aschersleben, D. Horns, and E. Moulin, *Search for dark matter around intermediate mass black holes with the H.E.S.S. experiment*, *PoS* **ICRC2025** (2025) 534, [arXiv:2510.03023].

[112] **AMS** Collaboration, M. Aguilar et al., *The Alpha Magnetic Spectrometer (AMS) on the international space station: Part II — Results from the first seven years*, *Phys. Rept.* **894** (2021) 1–116.

[113] **IceCube** Collaboration, R. Abbasi et al., *Search for GeV-scale Dark Matter from the Galactic Center with IceCube-DeepCore*, arXiv:2511.00918.

[114] **IceCube** Collaboration, R. Abbasi et al., *Limits on WIMP-Scattering Cross Sections using Solar Neutrinos with Ten Years of IceCube Data*, *PoS* **ICRC2025** (2025) 502, [arXiv:2507.08519].

[115] **IceCube** Collaboration, R. Abbasi et al., *Search for dark matter from the center of the Earth with 10 years of IceCube data*, *Eur. Phys. J. C* **85** (2025), no. 5 490, [arXiv:2412.12972].

[116] **ATLAS** Collaboration, G. Aad et al., *Search for events with one displaced vertex from long-lived neutral particles decaying into hadronic jets in the ATLAS muon spectrometer in pp collisions at s=13 TeV*, *Phys. Rev. D* **112** (2025), no. 9 092001, [arXiv:2503.20445].

[117] **ATLAS** Collaboration, N. Fomin, *ATLAS Latest Dark Matter Searches*, *PoS* **DIS2024** (2025) 142.

[118] **CMS** Collaboration, S. S. Chauhan, *Searches for Dark Matter with CMS in Mono-X Signatures*, *PoS* **EPS-HEP2025** (2026) 039.

[119] **CMS** Collaboration, A. Hayrapetyan et al., *Search for dark matter produced in association with a Higgs boson decaying to bottom quarks in proton-proton collisions at $\sqrt{s}$ = 13 TeV*, arXiv:2601.11330.

[120] S. L. Adler, *Axial vector vertex in spinor electrodynamics*, *Phys. Rev.* **177** (1969) 2426–2438.

[121] J. S. Bell and R. Jackiw, *A PCAC puzzle: $\pi^0 \to \gamma\gamma$ in the σ model*, *Nuovo Cim.* **A60** (1969) 47–61.

[122] L. Rosenberg, *Electromagnetic interactions of neutrinos*, *Phys. Rev.* **129** (1963) 2786–2788.

[123] **DAMA** Collaboration, R. Bernabei et al., *Search for WIMP annual modulation signature: Results from DAMA / NaI-3 and DAMA / NaI-4 and the global combined analysis*, *Phys. Lett. B* **480** (2000) 23–31.

[124] **CDMS** Collaboration, R. Abusaidi et al., *Exclusion limits on the WIMP nucleon cross-section from the cryogenic dark matter search*, *Phys. Rev. Lett.* **84** (2000) 5699–5703, [astro-ph/0002471].

[125] S. Chang, G. D. Kribs, D. Tucker-Smith, and N. Weiner, *Inelastic Dark Matter in Light of DAMA/LIBRA*, *Phys.Rev.* **D79** (2009) 043513, [arXiv:0807.2250].

[126] J. March-Russell, C. McCabe, and M. McCullough, *Inelastic Dark Matter, Non-Standard Halos and the DAMA/LIBRA Results*, *JHEP* **05** (2009) 071, [arXiv:0812.1931].

[127] Y. Bai and T. M. Tait, *Inelastic Dark Matter at the LHC*, *Phys.Lett.* **B710** (2012) 335–338, [arXiv:1109.4144].

[128] **ATLAS** Collaboration, G. Aad et al., *Search for new phenomena in events with an energetic jet and missing transverse momentum in pp collisions at $\sqrt{s} = 13$ TeV with the ATLAS detector*, *Phys. Rev. D* **103** (2021) 112006, [arXiv:2102.10874].

[129] **ATLAS** Collaboration, M. Aaboud et al., *Search for long-lived, massive particles in events with displaced vertices and missing transverse momentum in $\sqrt{s}$ = 13 TeV pp collisions with the ATLAS detector*, *Phys. Rev.* **D97** (2018), no. 5 052012, [arXiv:1710.04901]. auxiliary material available at https://atlas.web.cern.ch/Atlas/GROUPS/PHYSICS/PAPERS/SUSY-2016-08/.

[130] The Fermi-LAT collaboration, *Search for Gamma-ray Spectral Lines with the Fermi Large Area Telescope and Dark Matter Implications*, arXiv:1305.5597.

[131] **LUX Collaboration** Collaboration, D. Akerib et al., *First results from the LUX dark matter experiment at the Sanford Underground Research Facility*, arXiv:1310.8214.

[132] L. Michaels and F. Yu, *Probing new $U(1)$ gauge symmetries via exotic $Z \to Z'\gamma$ decays*, *JHEP* **03** (2021) 120, [arXiv:2010.00021].

[133] P. Langacker, *The Physics of Heavy Z' Gauge Bosons*, *Rev. Mod. Phys.* **81** (2009) 1199–1228, [arXiv:0801.1345].

[134] A. Davidson, *$B - L$ as the fourth color within an $\mathrm{SU}(2)_L \times \mathrm{U}(1)_R \times \mathrm{U}(1)$ model*, *Phys. Rev. D* **20** (1979) 776.

[135] M. Carena, A. Daleo, B. A. Dobrescu, and T. M. Tait, *Z' gauge bosons at the Tevatron*, *Phys. Rev. D* **70** (2004) 093009, [hep-ph/0408098].

[136] P. Anastasopoulos, M. Bianchi, E. Dudas, and E. Kiritsis, *Anomalies, anomalous U(1)'s and generalized Chern-Simons terms*, *JHEP* **11** (2006) 057, [hep-th/0605225].

[137] P. Fileviez Perez and M. B. Wise, *Baryon and lepton number as local gauge symmetries*, *Phys. Rev. D* **82** (2010) 011901, [arXiv:1002.1754]. [Erratum: Phys.Rev.D 82, 079901 (2010)].

[138] P. Fileviez Perez and M. B. Wise, *Breaking Local Baryon and Lepton Number at the TeV Scale*, *JHEP* **08** (2011) 068, [arXiv:1106.0343].

[139] B. A. Dobrescu and F. Yu, *Coupling-Mass Mapping of Dijet Peak Searches*, *Phys. Rev. D* **88** (2013), no. 3 035021, [arXiv:1306.2629]. [Erratum: Phys.Rev.D 90, 079901 (2014)].

[140] Y. Cui and F. D'Eramo, *Surprises from complete vector portal theories: New insights into the dark sector and its interplay with Higgs physics*, *Phys. Rev. D* **96** (2017), no. 9 095006, [`arXiv:1705.03897`].

[141] J. A. Dror, R. Lasenby, and M. Pospelov, *New constraints on light vectors coupled to anomalous currents*, *Phys. Rev. Lett.* **119** (2017), no. 14 141803, [`arXiv:1705.06726`].

[142] G. Arcadi, P. Ghosh, Y. Mambrini, M. Pierre, and F. S. Queiroz, *Z' portal to Chern-Simons Dark Matter*, *JCAP* **11** (2017) 020, [`arXiv:1706.04198`].

[143] J. A. Dror, R. Lasenby, and M. Pospelov, *Dark forces coupled to nonconserved currents*, *Phys. Rev.* **D96** (2017), no. 7 075036, [`arXiv:1707.01503`].

[144] A. Ismail, A. Katz, and D. Racco, *On dark matter interactions with the Standard Model through an anomalous Z'*, *JHEP* **10** (2017) 165, [`arXiv:1707.00709`].

[145] A. Ismail and A. Katz, *Anomalous Z' and diboson resonances at the LHC*, *JHEP* **04** (2018) 122, [`arXiv:1712.01840`].

[146] J. A. Dror, R. Lasenby, and M. Pospelov, *Light vectors coupled to bosonic currents*, *Phys. Rev. D* **99** (2019), no. 5 055016, [`arXiv:1811.00595`].

[147] B. Dutta, S. Ghosh, and J. Kumar, *A sub-GeV dark matter model*, *Phys. Rev. D* **100** (2019) 075028, [`arXiv:1905.02692`].

[148] B. Dutta, S. Ghosh, and J. Kumar, *Opportunities for probing $U(1)_{T3R}$ with light mediators*, *Phys. Rev. D* **102** (2020), no. 7 075041, [`arXiv:2007.16191`].

[149] J. Ellis, M. Fairbairn, and P. Tunney, *Anomaly-Free Dark Matter Models are not so Simple*, *JHEP* **08** (2017) 053, [`arXiv:1704.03850`].

[150] J. Preskill, *Gauge anomalies in an effective field theory*, *Annals Phys.* **210** (1991) 323–379.

[151] **L3** Collaboration, P. Achard et al., *Search for heavy neutral and charged leptons in e^+e^- annihilation at LEP*, *Phys. Lett.* **B517** (2001) 75–85, [`hep-ex/0107015`].

[152] **ALEPH** Collaboration, A. Heister et al., *Search for charginos nearly mass degenerate with the lightest neutralino in e+ e- collisions at center-of-mass energies up to 209-GeV*, *Phys. Lett.* **B533** (2002) 223–236, [`hep-ex/0203020`].

[153] P. Batra, B. A. Dobrescu, and D. Spivak, *Anomaly-free sets of fermions*, *J. Math. Phys.* **47** (2006) 082301, [`hep-ph/0510181`].

[154] B. Allanach, J. Davighi, and S. Melville, *An Anomaly-free Atlas: charting the space of flavour-dependent gauged $U(1)$ extensions of the Standard Model*, *JHEP* **02** (2019) 082, [`arXiv:1812.04602`]. [Erratum: JHEP 08, 064 (2019)].

[155] D. B. Costa, B. A. Dobrescu, and P. J. Fox, *General Solution to the U(1) Anomaly Equations*, *Phys. Rev. Lett.* **123** (2019), no. 15 151601, [arXiv:1905.13729].

[156] D. B. Costa, B. A. Dobrescu, and P. J. Fox, *Chiral Abelian gauge theories with few fermions*, *Phys. Rev. D* **101** (2020) 095032, [arXiv:2001.11991].

[157] J. Wess and B. Zumino, *Consequences of anomalous Ward identities*, *Phys. Lett. B* **37** (1971) 95–97.

[158] C. G. Bollini and J. J. Giambiagi, *Dimensional Renormalization: The Number of Dimensions as a Regularizing Parameter*, *Nuovo Cim. B* **12** (1972) 20–26.

[159] G. 't Hooft and M. Veltman, *Regularization and Renormalization of Gauge Fields*, *Nucl. Phys. B* **44** (1972) 189–213.

[160] S. L. Adler and W. A. Bardeen, *Absence of higher order corrections in the anomalous axial vector divergence equation*, *Phys. Rev.* **182** (1969) 1517–1536.

[161] K. Fujikawa, *Path Integral Measure for Gauge Invariant Fermion Theories*, *Phys. Rev. Lett.* **42** (1979) 1195–1198.

[162] W. Pauli and F. Villars, *On the Invariant regularization in relativistic quantum theory*, *Rev. Mod. Phys.* **21** (1949) 434–444.

[163] A. Bilal, *Lectures on Anomalies*, arXiv:0802.0634.

[164] S. Weinberg, *The quantum theory of fields. Vol. 2: Modern applications.* Cambridge University Press, 2013.

[165] D. J. Gross and R. Jackiw, *Effect of anomalies on quasirenormalizable theories*, *Phys. Rev. D* **6** (1972) 477–493.

[166] S. Glashow, J. Iliopoulos, and L. Maiani, *Weak Interactions with Lepton-Hadron Symmetry*, *Phys. Rev. D* **2** (1970) 1285–1292.

[167] M. Duerr, P. Fileviez Perez, and M. B. Wise, *Gauge Theory for Baryon and Lepton Numbers with Leptoquarks*, *Phys. Rev. Lett.* **110** (2013) 231801, [arXiv:1304.0576].

[168] M. Duerr and P. Fileviez Perez, *Baryonic Dark Matter*, *Phys. Lett. B* **732** (2014) 101–104, [arXiv:1309.3970].

[169] B. A. Dobrescu and C. Frugiuele, *Hidden GeV-scale interactions of quarks*, *Phys. Rev. Lett.* **113** (2014) 061801, [arXiv:1404.3947].

[170] **ATLAS, CMS** Collaboration, G. Aad et al., *Measurements of the Higgs boson production and decay rates and constraints on its couplings from a combined ATLAS and CMS analysis of the LHC pp collision data at $\sqrt{s} = 7$ and 8 TeV*, *JHEP* **08** (2016) 045, [arXiv:1606.02266].

[171] T. Appelquist and M. S. Chanowitz, *Unitarity Bound on the Scale of Fermion Mass Generation*, *Phys. Rev. Lett.* **59** (1987) 2405. [Erratum: Phys. Rev. Lett.60,1589(1988)].

[172] A. Dedes and K. Suxho, *Heavy Fermion Non-Decoupling Effects in Triple Gauge Boson Vertices*, *Phys. Rev.* **D85** (2012) 095024, [arXiv:1202.4940].

[173] S. Treiman, E. Witten, R. Jackiw, and B. Zumino, *CURRENT ALGEBRA AND ANOMALIES*. Princeton University Press, 7, 2014.

[174] W. R. Inc., "Mathematica, Version 12.1." Champaign, IL, 2020.

[175] H. H. Patel, *Package-X: A Mathematica package for the analytic calculation of one-loop integrals*, *Comput. Phys. Commun.* **197** (2015) 276–290, [arXiv:1503.01469].

[176] H. H. Patel, *Package-X 2.0: A Mathematica package for the analytic calculation of one-loop integrals*, *Comput. Phys. Commun.* **218** (2017) 66–70, [arXiv:1612.00009].

[177] G. Passarino and M. J. G. Veltman, *One Loop Corrections for e+ e- Annihilation Into mu+ mu- in the Weinberg Model*, *Nucl. Phys.* **B160** (1979) 151–207.

[178] E. D'Hoker and E. Farhi, *Decoupling a Fermion in the Standard Electroweak Theory*, *Nucl. Phys. B* **248** (1984) 77.

[179] E. D'Hoker and E. Farhi, *Decoupling a Fermion Whose Mass Is Generated by a Yukawa Coupling: The General Case*, *Nucl. Phys. B* **248** (1984) 59–76.

[180] L. D. Landau, *On the angular momentum of a system of two photons*, *Dokl. Akad. Nauk SSSR* **60** (1948), no. 2 207–209.

[181] C.-N. Yang, *Selection Rules for the Dematerialization of a Particle Into Two Photons*, *Phys. Rev.* **77** (1950) 242–245.

[182] **L3** Collaboration, O. Adriani et al., *Isolated hard photon emission in hadronic Z0 decays*, *Phys. Lett. B* **292** (1992) 472–484.

[183] **L3** Collaboration, B. Adeva et al., *Search for narrow high mass resonances in radiative decays of the Z0*, *Phys. Lett. B* **262** (1991) 155–162.

[184] S. Tulin, *New weakly-coupled forces hidden in low-energy QCD*, *Phys. Rev. D* **89** (2014), no. 11 114008, [arXiv:1404.4370].

[185] D. Egana-Ugrinovic, M. Low, and J. T. Ruderman, *Charged Fermions Below 100 GeV*, *JHEP* **05** (2018) 012, [arXiv:1801.05432].

[186] **OPAL** Collaboration, P. Acton et al., *A Measurement of photon radiation in lepton pair events from Z0 decays*, *Phys. Lett. B* **273** (1991) 338–354.

[187] A. Djouadi, *The Anatomy of electro-weak symmetry breaking. I: The Higgs boson in the standard model*, *Phys. Rept.* **457** (2008) 1–216, [hep-ph/0503172].

[188] **ATLAS** Collaboration, M. Aaboud et al., *Measurements of Higgs boson properties in the diphoton decay channel with 36 fb^{-1} of pp collision data at $\sqrt{s} = 13$ TeV with the ATLAS detector*, *Phys. Rev.* **D98** (2018) 052005, [arXiv:1802.04146].

[189] P. Schwaller and J. Zurita, *Compressed electroweakino spectra at the LHC*, *JHEP* **03** (2014) 060, [arXiv:1312.7350].

[190] **ATLAS** Collaboration, G. Aad et al., *Search for electroweak production of charginos and sleptons decaying into final states with two leptons and missing transverse momentum in $\sqrt{s} = 13$ TeV pp collisions using the ATLAS detector*, *Eur. Phys. J. C* **80** (2020), no. 2 123, [arXiv:1908.08215].

[191] **ATLAS** Collaboration, G. Aad et al., *Searches for electroweak production of supersymmetric particles with compressed mass spectra in $\sqrt{s} = 13$ TeV pp collisions with the ATLAS detector*, *Phys. Rev. D* **101** (2020), no. 5 052005, [arXiv:1911.12606].

[192] A. Blondel et al., *Standard model theory for the FCC-ee Tera-Z stage*, in *Mini Workshop on Precision EW and QCD Calculations for the FCC Studies : Methods and Techniques*, vol. 3/2019 of *CERN Yellow Reports: Monographs*, (Geneva), CERN, 9, 2018. arXiv:1809.01830.

[193] **ALEPH, DELPHI, L3, OPAL, SLD, LEP Electroweak Working Group, SLD Electroweak Group, SLD Heavy Flavour Group** Collaboration, S. Schael et al., *Precision electroweak measurements on the Z resonance*, *Phys. Rept.* **427** (2006) 257–454, [hep-ex/0509008].

[194] **CMS** Collaboration, A. M. Sirunyan et al., *Search for Low-Mass Quark-Antiquark Resonances Produced in Association with a Photon at $\sqrt{s}$ =13 TeV*, *Phys. Rev. Lett.* **123** (2019), no. 23 231803, [arXiv:1905.10331].

[195] **CMS** Collaboration, A. M. Sirunyan et al., *Search for low mass vector resonances decaying into quark-antiquark pairs in proton-proton collisions at $\sqrt{s} = 13$ TeV*, *Phys. Rev. D* **100** (2019), no. 11 112007, [arXiv:1909.04114].

[196] **ARGUS** Collaboration, H. Albrecht et al., *An Upper Limit for Two Jet Production in Direct Υ (1s) Decays*, *Z. Phys. C* **31** (1986) 181.

[197] A. Aranda and C. D. Carone, *Limits on a light leptophobic gauge boson*, *Phys. Lett. B* **443** (1998) 352–358, [hep-ph/9809522].

[198] C. D. Carone and H. Murayama, *Possible light U(1) gauge boson coupled to baryon number*, *Phys. Rev. Lett.* **74** (1995) 3122–3125, [hep-ph/9411256].

[199] D. C. Bailey and S. Davidson, *Is there a vector boson coupling to baryon number?*, *Phys. Lett. B* **348** (1995) 185–189, [hep-ph/9411355].

[200] C. D. Carone and H. Murayama, *Realistic models with a light U(1) gauge boson coupled to baryon number*, *Phys. Rev. D* **52** (1995) 484–493, [hep-ph/9501220].

[201] P. Ilten, Y. Soreq, M. Williams, and W. Xue, *Serendipity in dark photon searches*, *JHEP* **06** (2018) 004, [arXiv:1801.04847].

[202] P. Cushman et al., *Working Group Report: WIMP Dark Matter Direct Detection*, in *Proceedings, 2013 Community Summer Study on the Future of U.S. Particle Physics: Snowmass on the Mississippi (CSS2013): Minneapolis, MN, USA, July 29-August 6, 2013*, 2013. arXiv:1310.8327.

[203] **LUX** Collaboration, D. S. Akerib et al., *Results from a search for dark matter in the complete LUX exposure*, *Phys. Rev. Lett.* **118** (2017), no. 2 021303, [arXiv:1608.07648].

[204] **PandaX-II** Collaboration, X. Cui et al., *Dark Matter Results From 54-Ton-Day Exposure of PandaX-II Experiment*, *Phys. Rev. Lett.* **119** (2017), no. 18 181302, [arXiv:1708.06917].

[205] **XENON** Collaboration, E. Aprile et al., *Dark Matter Search Results from a One Ton-Year Exposure of XENON1T*, *Phys. Rev. Lett.* **121** (2018), no. 11 111302, [arXiv:1805.12562].

[206] J. Billard et al., *Direct Detection of Dark Matter – APPEC Committee Report*, arXiv:2104.07634.

[207] **AMS** Collaboration, M. Aguilar et al., *The Alpha Magnetic Spectrometer (AMS) on the international space station: Part II — Results from the first seven years*, *Phys. Rept.* **894** (2021) 1–116.

[208] **Fermi-LAT, DES** Collaboration, A. Albert et al., *Searching for Dark Matter Annihilation in Recently Discovered Milky Way Satellites with Fermi-LAT*, *Astrophys. J.* **834** (2017), no. 2 110, [arXiv:1611.03184].

[209] **Fermi-LAT** Collaboration, M. Ackermann et al., *Searching for Dark Matter Annihilation from Milky Way Dwarf Spheroidal Galaxies with Six Years of Fermi Large Area Telescope Data*, *Phys. Rev. Lett.* **115** (2015), no. 23 231301, [arXiv:1503.02641].

[210] **Fermi-LAT** Collaboration, M. Ackermann et al., *Limits on Dark Matter Annihilation Signals from the Fermi LAT 4-year Measurement of the Isotropic Gamma-Ray Background*, *JCAP* **09** (2015) 008, [arXiv:1501.05464].

[211] **DAMA, LIBRA** Collaboration, R. Bernabei et al., *New results from DAMA/LIBRA*, *Eur. Phys. J. C* **67** (2010) 39–49, [arXiv:1002.1028].

[212] R. Bernabei et al., *First model independent results from DAMA/LIBRA-phase2*, `arXiv:1805.10486`.

[213] **CDMS** Collaboration, R. Agnese et al., *Silicon Detector Dark Matter Results from the Final Exposure of CDMS II*, *Phys. Rev. Lett.* **111** (2013), no. 25 251301, [`arXiv:1304.4279`].

[214] F. Pröbst et al., *Results of CRESST Phase I*, *Nucl. Phys. B Proc. Suppl.* **110** (2002) 67–69.

[215] **XENON** Collaboration, J. Angle et al., *First Results from the XENON10 Dark Matter Experiment at the Gran Sasso National Laboratory*, *Phys. Rev. Lett.* **100** (2008) 021303, [`arXiv:0706.0039`].

[216] S. Chang, G. D. Kribs, D. Tucker-Smith, and N. Weiner, *Inelastic dark matter in light of dama/libra*, *Physical Review D* **79** (Feb., 2009).

[217] Y. Cui, D. E. Morrissey, D. Poland, and L. Randall, *Candidates for Inelastic Dark Matter*, *JHEP* **05** (2009) 076, [`arXiv:0901.0557`].

[218] D. S. Alves, S. R. Behbahani, P. Schuster, and J. G. Wacker, *Composite Inelastic Dark Matter*, *Phys.Lett.* **B692** (2010) 323–326, [`arXiv:0903.3945`]. 5 pages (two-column), 1 figure, revised version, references added.

[219] H. An, S.-L. Chen, R. N. Mohapatra, S. Nussinov, and Y. Zhang, *Energy Dependence of Direct Detection Cross Section for Asymmetric Mirror Dark Matter*, *Phys. Rev. D* **82** (2010) 023533, [`arXiv:1004.3296`].

[220] J. Bagnasco, M. Dine, and S. D. Thomas, *Detecting technibaryon dark matter*, *Phys. Lett. B* **320** (1994) 99–104, [`hep-ph/9310290`].

[221] S. Chang, N. Weiner, and I. Yavin, *Magnetic Inelastic Dark Matter*, *Phys.Rev.* **D82** (2010) 125011, [`arXiv:1007.4200`].

[222] D. P. Finkbeiner, T. Lin, and N. Weiner, *Inelastic Dark Matter and DAMA/LIBRA: An Experimentum Crucis*, *Phys.Rev.* **D80** (2009) 115008, [`arXiv:0906.0002`].

[223] K. Schmidt-Hoberg and M. W. Winkler, *Improved Constraints on Inelastic Dark Matter*, *JCAP* **0909** (2009) 010, [`arXiv:0907.3940`].

[224] J. Kopp, T. Schwetz, and J. Zupan, *Global interpretation of direct Dark Matter searches after CDMS-II results*, *JCAP* **1002** (2010) 014, [`arXiv:0912.4264`].

[225] D. S. Alves, M. Lisanti, and J. G. Wacker, *Poker face of inelastic dark matter: Prospects at upcoming direct detection experiments*, *Phys.Rev.* **D82** (2010) 031901, [`arXiv:1005.5421`].

[226] S. Miao, C.-L. Shan, and Y.-F. Zhou, *Model-Independent Identification of Inelastic WIMPs from Direct Dark Matter Detection Experiments*, `arXiv:1303.1345`.

[227] N. Bozorgnia, J. Herrero-Garcia, T. Schwetz, and J. Zupan, *Halo-independent methods for inelastic dark matter scattering*, `arXiv:1305.3575`.

[228] S. Scopel and K. Yoon, *A systematic halo-independent analysis of direct detection data within the framework of Inelastic Dark Matter*, `arXiv:1405.0364`.

[229] G. Barello, S. Chang, and C. A. Newby, *A Model Independent Approach to Inelastic Dark Matter Scattering*, `arXiv:1409.0536`.

[230] J. Bramante, P. J. Fox, G. D. Kribs, and A. Martin, *The Inelastic Frontier: Discovering Dark Matter at High Recoil Energy*, *Submitted to: Phys. Rev. D* (2016) [`arXiv:1608.02662`].

[231] J. Eby, P. J. Fox, R. Harnik, and G. D. Kribs, *Luminous Signals of Inelastic Dark Matter in Large Detectors*, `arXiv:1904.09994`.

[232] R. F. Lang and W. Seidel, *Search for Dark Matter with CRESST*, *New J.Phys.* **11** (2009) 105017, [`arXiv:0906.3290`].

[233] **ZEPLIN-III Collaboration** Collaboration, D. Akimov et al., *Limits on inelastic dark matter from ZEPLIN-III*, *Phys.Lett.* **B692** (2010) 180–183, [`arXiv:1003.5626`].

[234] **CDMS-II, CDMS** Collaboration, Z. Ahmed et al., *Search for inelastic dark matter with the CDMS II experiment*, *Phys. Rev.* **D83** (2011) 112002, [`arXiv:1012.5078`].

[235] G. Angloher, M. Bauer, I. Bavykina, A. Bento, C. Bucci, et al., *Results from 730 kg days of the CRESST-II Dark Matter Search*, *Eur.Phys.J.* **C72** (2012) 1971, [`arXiv:1109.0702`].

[236] **XMASS-I Collaboration** Collaboration, H. Uchida et al., *Search for inelastic WIMP nucleus scattering on ^{129}Xe in data from the XMASS-I experiment*, `arXiv:1401.4737`.

[237] E. Aprile et al., *Search for WIMP Inelastic Scattering off Xenon Nuclei with XENON100*, `arXiv:1705.05830`.

[238] **COSINE-100** Collaboration, C. Ha et al., *The First Direct Search for Inelastic Boosted Dark Matter with COSINE-100*, `arXiv:1811.09344`.

[239] S. Patra and S. Rao, *A simple model for magnetic inelastic dark matter (MiDM)*, `arXiv:1112.3454`.

[240] A. Menon, R. Morris, A. Pierce, and N. Weiner, *Capture and Indirect Detection of Inelastic Dark Matter*, *Phys.Rev.* **D82** (2010) 015011, [`arXiv:0905.1847`].

[241] S. Nussinov, L.-T. Wang, and I. Yavin, *Capture of Inelastic Dark Matter in the Sun*, *JCAP* **0908** (2009) 037, [arXiv:0905.1333].

[242] M. McCullough and M. Fairbairn, *Capture of Inelastic Dark Matter in White Dwarves*, *Phys.Rev.* **D81** (2010) 083520, [arXiv:1001.2737].

[243] D. Hooper, D. Spolyar, A. Vallinotto, and N. Y. Gnedin, *Inelastic Dark Matter As An Efficient Fuel For Compact Stars*, *Phys.Rev.* **D81** (2010) 103531, [arXiv:1002.0005].

[244] J. Shu, P.-f. Yin, and S.-h. Zhu, *Neutrino Constraints on Inelastic Dark Matter after CDMS II*, *Phys.Rev.* **D81** (2010) 123519, [arXiv:1001.1076].

[245] M. Blennow, S. Clementz, and J. Herrero-Garcia, *Pinning down inelastic dark matter in the Sun and in direct detection*, arXiv:1512.03317.

[246] M. Blennow, S. Clementz, and J. Herrero-Garcia, *The distribution of inelastic dark matter in the Sun*, arXiv:1802.06880.

[247] N. F. Bell, G. Busoni, and S. Robles, *Heating up Neutron Stars with Inelastic Dark Matter*, *JCAP* **1809** (2018) 018, [arXiv:1807.02840].

[248] E. Izaguirre, G. Krnjaic, and B. Shuve, *Discovering Inelastic Thermal-Relic Dark Matter at Colliders*, arXiv:1508.03050.

[249] A. Berlin and F. Kling, *Inelastic Dark Matter at the LHC Lifetime Frontier: ATLAS, CMS, LHCb, CODEX-b, FASER, and MATHUSLA*, *Phys. Rev.* **D99** (2019), no. 1 015021, [arXiv:1810.01879].

[250] P. J. Fox, R. Harnik, J. Kopp, and Y. Tsai, *Missing Energy Signatures of Dark Matter at the LHC*, *Phys.Rev.* **D85** (2012) 056011, [arXiv:1109.4398].

[251] **CMS** Collaboration, A. M. Sirunyan et al., *Search for new physics in final states with an energetic jet or a hadronically decaying W or Z boson and transverse momentum imbalance at $\sqrt{s} = 13$ TeV*, *Phys. Rev. D* **97** (2018), no. 9 092005, [arXiv:1712.02345].

[252] **CMS** Collaboration, A. M. Sirunyan et al., *Search for long-lived particles using displaced jets in proton-proton collisions at $\sqrt{s} = 13$ TeV*, arXiv:2012.01581.

[253] **Particle Data Group** Collaboration, P. Zyla et al., *Review of Particle Physics*, *PTEP* **2020** (2020), no. 8 083C01.

[254] J. Alwall, M. Herquet, F. Maltoni, O. Mattelaer, and T. Stelzer, *MadGraph 5 : Going Beyond*, *JHEP* **06** (2011) 128, [arXiv:1106.0522].

[255] J. Alwall, R. Frederix, S. Frixione, V. Hirschi, F. Maltoni, O. Mattelaer, H. S. Shao, T. Stelzer, P. Torrielli, and M. Zaro, *The automated computation of tree-level and next-to-leading order differential cross sections, and their matching to parton shower simulations*, *JHEP* **07** (2014) 079, [`arXiv:1405.0301`].

[256] A. Alloul, N. D. Christensen, C. Degrande, C. Duhr, and B. Fuks, *FeynRules 2.0 - A complete toolbox for tree-level phenomenology*, *Comput. Phys. Commun.* **185** (2014) 2250–2300, [`arXiv:1310.1921`].

[257] T. Sjostrand, S. Mrenna, and P. Z. Skands, *PYTHIA 6.4 Physics and Manual*, *JHEP* **05** (2006) 026, [`hep-ph/0603175`].

[258] **DELPHES 3** Collaboration, J. de Favereau, C. Delaere, P. Demin, A. Giammanco, V. Lemaître, A. Mertens, and M. Selvaggi, *DELPHES 3, A modular framework for fast simulation of a generic collider experiment*, *JHEP* **02** (2014) 057, [`arXiv:1307.6346`].

[259] M. Baak, G. Besjes, D. Côte, A. Koutsman, J. Lorenz, and D. Short, *HistFitter software framework for statistical data analysis*, *Eur. Phys. J. C* **75** (2015) 153, [`arXiv:1410.1280`].

[260] J. R. Shewchuk, *Triangle: Engineering a 2D Quality Mesh Generator and Delaunay Triangulator*, in *Applied Computational Geometry: Towards Geometric Engineering* (M. C. Lin and D. Manocha, eds.), vol. 1148 of *Lecture Notes in Computer Science*, pp. 203–222. Springer-Verlag, May, 1996. From the First ACM Workshop on Applied Computational Geometry.

[261] J. Alwall, M. Herquet, F. Maltoni, O. Mattelaer, and T. Stelzer, *MadGraph 5 : Going Beyond*, *JHEP* **06** (2011) 128, [`arXiv:1106.0522`].

[262] T. Sjostrand, S. Mrenna, and P. Z. Skands, *PYTHIA 6.4 Physics and Manual*, *JHEP* **05** (2006) 026, [`hep-ph/0603175`].

[263] **DELPHES 3** Collaboration, J. de Favereau, C. Delaere, P. Demin, A. Giammanco, V. LemaÃ®tre, A. Mertens, and M. Selvaggi, *DELPHES 3, A modular framework for fast simulation of a generic collider experiment*, *JHEP* **02** (2014) 057, [`arXiv:1307.6346`].

[264] G. Bélanger, A. Mjallal, and A. Pukhov, *Recasting direct detection limits within micrOMEGAs and implication for non-standard Dark Matter scenarios*, *Eur. Phys. J. C* **81** (2021), no. 3 239, [`arXiv:2003.08621`].

[265] A. Belyaev, N. D. Christensen, and A. Pukhov, *CalcHEP 3.4 for collider physics within and beyond the Standard Model*, *Comput. Phys. Commun.* **184** (2013) 1729–1769, [`arXiv:1207.6082`].

[266] G. Bélanger, F. Boudjema, A. Goudelis, A. Pukhov, and B. Zaldivar, *micrOMEGAs5.0 : Freeze-in*, *Comput. Phys. Commun.* **231** (2018) 173–186, [arXiv:1801.03509].

[267] J. Kumar and D. Marfatia, *Matrix element analyses of dark matter scattering and annihilation*, *Phys. Rev. D* **88** (2013), no. 1 014035, [arXiv:1305.1611].

[268] **CMS** Collaboration, A. M. Sirunyan et al., *Search for narrow and broad dijet resonances in proton-proton collisions at $\sqrt{s} = 13$ TeV and constraints on dark matter mediators and other new particles*, *JHEP* **08** (2018) 130, [arXiv:1806.00843].

[269] **ATLAS** Collaboration, M. Aaboud et al., *Search for low-mass resonances decaying into two jets and produced in association with a photon using pp collisions at $\sqrt{s} = 13$ TeV with the ATLAS detector*, *Phys. Lett. B* **795** (2019) 56–75, [arXiv:1901.10917].

[270] **ATLAS** Collaboration, G. Aad et al., *Search for massive, long-lived particles using multitrack displaced vertices or displaced lepton pairs in pp collisions at $\sqrt{s}$ = 8 TeV with the ATLAS detector*, *Phys. Rev. D* **92** (2015), no. 7 072004, [arXiv:1504.05162].

[271] T. Sjöstrand, S. Ask, J. R. Christiansen, R. Corke, N. Desai, P. Ilten, S. Mrenna, S. Prestel, C. O. Rasmussen, and P. Z. Skands, *An introduction to PYTHIA 8.2*, *Comput. Phys. Commun.* **191** (2015) 159–177, [arXiv:1410.3012].

[272] E. Bernreuther, J. C. Mejia, F. Kahlhoefer, M. Krämer, and P. Tunney, *On the challenges of searching for GeV-scale long-lived particles at the LHC*, arXiv:2011.06604.

[273] G. Cottin, J. C. Helo, and M. Hirsch, *Searches for light sterile neutrinos with multitrack displaced vertices*, *Phys. Rev. D* **97** (2018), no. 5 055025, [arXiv:1801.02734].

[274] **ATLAS** Collaboration, T. A. collaboration, *Search for long-lived neutral particles decaying into displaced lepton jets in proton–proton collisions at $\sqrt{s}$ = 13 TeV with the ATLAS detector*, .

[275] **ATLAS** Collaboration, D. Salvatore, *Search for long-lived neutral particles decaying into Lepton-Jets with the ATLAS detector in proton-proton collision data at 13 TeV*, arXiv:1708.07625.

[276] **ATLAS** Collaboration, G. Aad et al., *Search for light long-lived neutral particles produced in pp collisions at $\sqrt{s}$ = 13 TeV and decaying into collimated leptons or light hadrons with the ATLAS detector*, arXiv:1909.01246.

[277] **CMS** Collaboration, A. Tumasyan et al., *Search for strongly interacting massive particles generating trackless jets in proton-proton collisions at $\sqrt{s} = 13$ TeV*, `arXiv:2105.09178`.

[278] **CMS** Collaboration, A. M. Sirunyan et al., *Search for long-lived particles decaying to jets with displaced vertices in proton-proton collisions at $\sqrt{s} = 13$ TeV*, *Phys. Rev. D* **104** (2021), no. 5 052011, [`arXiv:2104.13474`].

[279] **CMS** Collaboration, A. M. Sirunyan et al., *Search for long-lived particles using nonprompt jets and missing transverse momentum with proton-proton collisions at $\sqrt{s} = 13$ TeV*, *Phys. Lett. B* **797** (2019) 134876, [`arXiv:1906.06441`].

[280] **CMS** Collaboration, A. M. Sirunyan et al., *A deep neural network to search for new long-lived particles decaying to jets*, *Mach. Learn. Sci. Tech.* **1** (2020) 035012, [`arXiv:1912.12238`].

[281] **CMS** Collaboration, A. M. Sirunyan et al., *Search for long-lived particles using displaced jets in proton-proton collisions at $\sqrt{s} = 13$ TeV*, *Phys. Rev. D* **104** (2021), no. 1 012015, [`arXiv:2012.01581`].

[282] **ATLAS** Collaboration, G. Aad et al., *Search for events with a pair of displaced vertices from long-lived neutral particles decaying into hadronic jets in the ATLAS muon spectrometer in pp collisions at $\sqrt{s}$=13 TeV*, *Phys. Rev. D* **106** (2022), no. 3 032005, [`arXiv:2203.00587`].

[283] **ATLAS** Collaboration, G. Aad et al., *Search for long-lived neutral particles produced in pp collisions at $\sqrt{s} = 13$ TeV decaying into displaced hadronic jets in the ATLAS inner detector and muon spectrometer*, *Phys. Rev. D* **101** (2020), no. 5 052013, [`arXiv:1911.12575`].

[284] **ATLAS** Collaboration, G. Aad et al., *Search for neutral long-lived particles in pp collisions at $\sqrt{s} = 13$ TeV that decay into displaced hadronic jets in the ATLAS calorimeter*, *JHEP* **06** (2022) 005, [`arXiv:2203.01009`].

[285] **ATLAS** Collaboration, G. Aad et al., *The ATLAS Experiment at the CERN Large Hadron Collider*, *JINST* **3** (2008) S08003.

[286] **ATLAS** Collaboration, G. Aad et al., *Search for neutral long-lived particles that decay into displaced jets in the ATLAS calorimeter in association with leptons or jets using pp collisions at $\sqrt{s} = 13$ TeV*, *JHEP* **11** (2024) 036, [`arXiv:2407.09183`].

[287] **CMS** Collaboration, A. Hayrapetyan et al., *Search for Long-Lived Heavy Neutral Leptons with Lepton Flavour Conserving or Violating Decays to a Jet and a Charged Lepton*, *JHEP* **03** (2024) 105, [`arXiv:2312.07484`].

[288] **ATLAS** Collaboration, G. Aad et al., *Search for light long-lived neutral particles that decay to collimated pairs of leptons or light hadrons in pp collisions at $\sqrt{s}$ = 13 TeV with the ATLAS detector*, *JHEP* **06** (2023) 153, [arXiv:2206.12181].

[289] **CMS** Collaboration, A. Hayrapetyan et al., *Search for Inelastic Dark Matter in Events with Two Displaced Muons and Missing Transverse Momentum in Proton-Proton Collisions at s=13 TeV*, *Phys. Rev. Lett.* **132** (2024), no. 4 041802, [arXiv:2305.11649].

[290] **CMS** Collaboration, A. Hayrapetyan et al., *Dark sector searches with the CMS experiment*, *Phys. Rept.* **1115** (2025) 448–569, [arXiv:2405.13778].

[291] **CMS** Collaboration, A. Tumasyan et al., *Search for Long-Lived Particles Decaying in the CMS End Cap Muon Detectors in Proton-Proton Collisions at $\sqrt{s}$ =13 TeV*, *Phys. Rev. Lett.* **127** (2021), no. 26 261804, [arXiv:2107.04838].

[292] **CMS** Collaboration, A. Hayrapetyan et al., *Search for long-lived particles using displaced vertices and missing transverse momentum in proton-proton collisions at s=13 TeV*, *Phys. Rev. D* **109** (2024), no. 11 112005, [arXiv:2402.15804].

[293] **ATLAS** Collaboration, G. Aad et al., *Search for new resonances in mass distributions of jet pairs using 139 fb^{-1} of pp collisions at $\sqrt{s} = 13$ TeV with the ATLAS detector*, *JHEP* **03** (2020) 145, [arXiv:1910.08447].

[294] **CMS** Collaboration, A. M. Sirunyan et al., *Search for high mass dijet resonances with a new background prediction method in proton-proton collisions at $\sqrt{s}$ = 13 TeV*, *JHEP* **05** (2020) 033, [arXiv:1911.03947].

[295] M. Chala, F. Kahlhoefer, M. McCullough, G. Nardini, and K. Schmidt-Hoberg, *Constraining Dark Sectors with Monojets and Dijets*, *JHEP* **07** (2015) 089, [arXiv:1503.05916].

[296] F. Kahlhoefer, K. Schmidt-Hoberg, T. Schwetz, and S. Vogl, *Implications of unitarity and gauge invariance for simplified dark matter models*, *JHEP* **02** (2016) 016, [arXiv:1510.02110].

[297] J. Kopp, L. Michaels, and J. Smirnov, *Loopy Constraints on Leptophilic Dark Matter and Internal Bremsstrahlung*, *JCAP* **04** (2014) 022, [arXiv:1401.6457].

[298] F. Aharonian, D. Khangulyan, and D. Malyshev, *Cold ultrarelativistic pulsar winds as potential sources of galactic gamma-ray lines above 100 GeV*, arXiv:1207.0458.

[299] **PAMELA Collaboration** Collaboration, O. Adriani et al., *An anomalous positron abundance in cosmic rays with energies 1.5-100 GeV*, *Nature* **458** (2009) 607–609, [arXiv:0810.4995].

[300] **PAMELA Collaboration** Collaboration, O. Adriani et al., *The cosmic-ray positron energy spectrum measured by PAMELA*, `arXiv:1308.0133`.

[301] **LAT Collaboration** Collaboration, M. Ackermann et al., *Fermi LAT Search for Dark Matter in Gamma-ray Lines and the Inclusive Photon Spectrum*, `arXiv:1205.2739`.

[302] **AMS Collaboration** Collaboration, M. Aguilar et al., *First Result from the Alpha Magnetic Spectrometer on the International Space Station: Precision Measurement of the Positron Fraction in Primary Cosmic Rays of 0.5-350 GeV*, *Phys.Rev.Lett.* **110** (2013), no. 14 141102.

[303] **PAMELA Collaboration** Collaboration, O. Adriani et al., *PAMELA results on the cosmic-ray antiproton flux from 60 MeV to 180 GeV in kinetic energy*, *Phys.Rev.Lett.* **105** (2010) 121101, [`arXiv:1007.0821`].

[304] **ARGO-YBJ Collaboration** Collaboration, B. Bartoli et al., *Measurement of the cosmic ray antiproton/proton flux ratio at TeV energies with the ARGO-YBJ detector*, *Phys.Rev.* **D85** (2012) 022002, [`arXiv:1201.3848`].

[305] M. Cirelli, M. Kadastik, M. Raidal, and A. Strumia, *Model-independent implications of the e+-, anti-proton cosmic ray spectra on properties of Dark Matter*, *Nucl.Phys.* **B813** (2009) 1–21, [`arXiv:0809.2409`].

[306] F. Donato, D. Maurin, P. Brun, T. Delahaye, and P. Salati, *Constraints on WIMP Dark Matter from the High Energy PAMELA $\bar{p}/p$ data*, *Phys.Rev.Lett.* **102** (2009) 071301, [`arXiv:0810.5292`].

[307] E. Nardi, F. Sannino, and A. Strumia, *Decaying Dark Matter can explain the e+- excesses*, *JCAP* **0901** (2009) 043, [`arXiv:0811.4153`].

[308] G. Bertone, M. Cirelli, A. Strumia, and M. Taoso, *Gamma-ray and radio tests of the e+e- excess from DM annihilations*, *JCAP* **0903** (2009) 009, [`arXiv:0811.3744`].

[309] P. J. Fox and E. Poppitz, *Leptophilic Dark Matter*, *Phys.Rev.* **D79** (2009) 083528, [`arXiv:0811.0399`].

[310] C. Evoli, I. Cholis, D. Grasso, L. Maccione, and P. Ullio, *Antiprotons from dark matter annihilation in the Galaxy: astrophysical uncertainties*, `arXiv:1108.0664`.

[311] J. Kopp, *Constraints on dark matter annihilation from AMS-02 results*, `arXiv:1304.1184`.

[312] I. Cholis and D. Hooper, *Dark Matter and Pulsar Origins of the Rising Cosmic Ray Positron Fraction in Light of New Data From AMS*, `arXiv:1304.1840`.

[313] L. Bergstrom, T. Bringmann, I. Cholis, D. Hooper, and C. Weniger, *New limits on dark matter annihilation from AMS cosmic ray positron data*, *Phys.Rev.Lett.* **111** (2013) 171101, [arXiv:1306.3983].

[314] A. Ibarra, A. S. Lamperstorfer, and J. Silk, *Dark matter annihilations and decays after the AMS-02 positron measurements*, arXiv:1309.2570.

[315] D. Hooper and L. Goodenough, *Dark Matter Annihilation in The Galactic Center As Seen by the Fermi Gamma Ray Space Telescope*, *Phys.Lett.* **B697** (2011) 412–428, [arXiv:1010.2752].

[316] D. Hooper and T. Linden, *On The Origin Of The Gamma Rays From The Galactic Center*, *Phys.Rev.* **D84** (2011) 123005, [arXiv:1110.0006].

[317] D. Hooper, *The Empirical Case For 10 GeV Dark Matter*, arXiv:1201.1303.

[318] M. Su, T. R. Slatyer, and D. P. Finkbeiner, *Giant Gamma-ray Bubbles from Fermi-LAT: AGN Activity or Bipolar Galactic Wind?*, *Astrophys.J.* **724** (2010) 1044–1082, [arXiv:1005.5480].

[319] D. Hooper and T. R. Slatyer, *Two Emission Mechanisms in the Fermi Bubbles: A Possible Signal of Annihilating Dark Matter*, arXiv:1302.6589.

[320] W.-C. Huang, A. Urbano, and W. Xue, *Fermi Bubbles under Dark Matter Scrutiny. Part I: Astrophysical Analysis*, arXiv:1307.6862.

[321] W.-C. Huang, A. Urbano, and W. Xue, *Fermi Bubbles under Dark Matter Scrutiny Part II: Particle Physics Analysis*, arXiv:1310.7609.

[322] T. Linden, D. Hooper, and F. Yusef-Zadeh, *Dark Matter and Synchrotron Emission from Galactic Center Radio Filaments*, *Astrophys.J.* **741** (2011) 95, [arXiv:1106.5493].

[323] J. Hisano, K. Ishiwata, and N. Nagata, *Direct Detection of Dark Matter Degenerate with Colored Particles in Mass*, *Phys.Lett.* **B706** (2011) 208–212, [arXiv:1110.3719].

[324] M. Garny, A. Ibarra, M. Pato, and S. Vogl, *Closing in on mass-degenerate dark matter scenarios with antiprotons and direct detection*, arXiv:1207.1431.

[325] M. Garny, A. Ibarra, M. Pato, and S. Vogl, *Internal bremsstrahlung signatures in light of direct dark matter searches*, arXiv:1306.6342.

[326] A. Geringer-Sameth and S. M. Koushiappas, *Exclusion of canonical WIMPs by the joint analysis of Milky Way dwarfs with Fermi*, *Phys.Rev.Lett.* **107** (2011) 241303, [arXiv:1108.2914].

[327] **Fermi-LAT Collaboration** Collaboration, M. Ackermann et al., *Dark Matter Constraints from Observations of 25 Milky Way Satellite Galaxies with the Fermi Large Area Telescope*, `arXiv:1310.0828`.

[328] J. Goodman, M. Ibe, A. Rajaraman, W. Shepherd, T. M. Tait, et al., *Constraints on Light Majorana dark Matter from Colliders*, *Phys.Lett.* **B695** (2011) 185–188, [`arXiv:1005.1286`].

[329] Y. Bai, P. J. Fox, and R. Harnik, *The Tevatron at the Frontier of Dark Matter Direct Detection*, *JHEP* **1012** (2010) 048, [`arXiv:1005.3797`].

[330] T. Lin, E. W. Kolb, and L.-T. Wang, *Probing dark matter couplings to top and bottom at the LHC*, `arXiv:1303.6638`.

[331] The CMS collaboration, *Search for new physics in monojet events in pp collisions at sqrt(s)= 8 TeV*, . CMS-PAS-EXO-12-048.

[332] The ATLAS collaboration, *Search for New Phenomena in Monojet plus Missing Transverse Momentum Final States using 10fb-1 of pp Collisions at sqrts=8 TeV with the ATLAS detector at the LHC*, . ATLAS-CONF-2012-147, ATLAS-COM-CONF-2012-190.

[333] **ATLAS Collaboration** Collaboration, G. Aad et al., *Search for dark matter in events with a hadronically decaying W or Z boson and missing transverse momentum in pp collisions at* $\sqrt{s}$*=8 TeV with the ATLAS detector*, `arXiv:1309.4017`.

[334] **ATLAS** Collaboration, J. Boyd, *Overview of SUSY results from the ATLAS experiment*, 2013. talk given at the SUSY 2013 conference, slides available from http://susy2013.ictp.it.

[335] **CMS** Collaboration, J. D. Richman, *Searches for Supersymmetry in the CMS Experiment*, 2013. talk given at the SUSY 2013 conference, slides available from http://susy2013.ictp.it.

[336] J. Kopp, V. Niro, T. Schwetz, and J. Zupan, *DAMA/LIBRA and leptonically interacting Dark Matter*, *Phys. Rev.* **D80** (2009) 083502, [`arXiv:0907.3159`].

[337] R. Essig, J. Mardon, and T. Volansky, *Direct Detection of Sub-GeV Dark Matter*, *Phys.Rev.* **D85** (2012) 076007, [`arXiv:1108.5383`].

[338] R. Essig, A. Manalaysay, J. Mardon, P. Sorensen, and T. Volansky, *First Direct Detection Limits on sub-GeV Dark Matter from XENON10*, `arXiv:1206.2644`.

[339] D. Schmidt, T. Schwetz, and T. Toma, *Direct Detection of Leptophilic Dark Matter in a Model with Radiative Neutrino Masses*, *Phys.Rev.* **D85** (2012) 073009, [`arXiv:1201.0906`].

[340] E. Radescu, *Comments on the Electromagnetic Properties of Majorana Fermions*, *Phys.Rev.* **D32** (1985) 1266.

[341] B. Kayser and A. S. Goldhaber, *CPT and CP Properties of Majorana Particles, and the Consequences*, *Phys.Rev.* **D28** (1983) 2341.

[342] C. M. Ho and R. J. Scherrer, *Anapole Dark Matter*, `arXiv:1211.0503`.

[343] M. I. Gresham and K. M. Zurek, *Light Dark Matter Anomalies After LUX*, `arXiv:1311.2082`.

[344] Y. Gao, C. M. Ho, and R. J. Scherrer, *Anapole Dark Matter at the LHC*, `arXiv:1311.5630`.

[345] E. Del Nobile, G. B. Gelmini, P. Gondolo, and J.-H. Huh, *Direct detection of Light Anapole and Magnetic Dipole DM*, `arXiv:1401.4508`.

[346] J. H. Heo, *Minimal Dirac Fermionic Dark Matter with Nonzero Magnetic Dipole Moment*, *Phys.Lett.* **B693** (2010) 255–258, [`arXiv:0901.3815`].

[347] E. Masso, S. Mohanty, and S. Rao, *Dipolar Dark Matter*, *Phys. Rev.* **D80** (2009) 036009, [`arXiv:0906.1979`].

[348] E. Del Nobile, C. Kouvaris, P. Panci, F. Sannino, and J. Virkajarvi, *Light Magnetic Dark Matter in Direct Detection Searches*, `arXiv:1203.6652`.

[349] N. Weiner and I. Yavin, *UV Completions of Magnetic Inelastic Dark Matter and RayDM for the Fermi Line(s)*, `arXiv:1209.1093`.

[350] V. Barger, W.-Y. Keung, D. Marfatia, and P.-Y. Tseng, *Dipole Moment Dark Matter at the LHC*, `arXiv:1206.0640`.

[351] H. K. Dreiner, H. E. Haber, and S. P. Martin, *Two-component spinor techniques and Feynman rules for quantum field theory and supersymmetry*, *Phys. Rept.* **494** (2010) 1–196, [`arXiv:0812.1594`].

[352] P. B. Pal, *Dirac, majorana, and weyl fermions*, *American Journal of Physics* **79** (Apr., 2011) 485–498.

[353] J. Liu, B. Shuve, N. Weiner, and I. Yavin, *Looking for new charged states at the LHC: Signatures of Magnetic and Rayleigh Dark Matter*, `arXiv:1303.4404`.

[354] **Fermi-LAT** Collaboration, E. Bloom, E. Charles, E. Izaguirre, A. Snyder, A. Albert, B. Winer, Z. Yang, and R. Essig, *Search of the Earth Limb Fermi Data and Non-Galactic Center Region Fermi Data for Signs of Narrow Lines*, `arXiv:1303.2733`.

[355] **Fermi-LAT** Collaboration, M. Ackermann et al., *Updated search for spectral lines from Galactic dark matter interactions with pass 8 data from the Fermi Large Area Telescope*, *Phys. Rev. D* **91** (2015), no. 12 122002, [arXiv:1506.00013].

[356] B. Anderson, S. Zimmer, J. Conrad, M. Gustafsson, M. Sánchez-Conde, and R. Caputo, *Search for Gamma-Ray Lines towards Galaxy Clusters with the Fermi-LAT*, *JCAP* **02** (2016) 026, [arXiv:1511.00014].

[357] **H.E.S.S.** Collaboration, H. Abdalla et al., *H.E.S.S. Limits on Linelike Dark Matter Signatures in the 100 GeV to 2 TeV Energy Range Close to the Galactic Center*, *Phys. Rev. Lett.* **117** (2016), no. 15 151302, [arXiv:1609.08091].

[358] L. Bergstrom, *Radiative Processes in Dark Matter Photino Annihilation*, *Phys.Lett.* **B225** (1989) 372.

[359] V. Barger, Y. Gao, W. Y. Keung, and D. Marfatia, *Generic dark matter signature for gamma-ray telescopes*, *Phys.Rev.* **D80** (2009) 063537, [arXiv:0906.3009].

[360] T. Toma, *Internal Bremsstrahlung Signature of Real Scalar Dark Matter and Consistency with Thermal Relic Density*, *Phys.Rev.Lett.* **111** (2013) 091301, [arXiv:1307.6181].

[361] F. Giacchino, L. Lopez-Honorez, and M. H. Tytgat, *Scalar Dark Matter Models with Significant Internal Bremsstrahlung*, *JCAP* **1310** (2013) 025, [arXiv:1307.6480].

[362] K. Fukushima and J. Kumar, *Dipole Moment Bounds on Dark Matter Annihilation*, arXiv:1307.7120.

[363] V. Barger, W.-Y. Keung, and D. Marfatia, *Bremsstrahlung in dark matter annihilation*, *Phys.Lett.* **B707** (2012) 385–388, [arXiv:1111.4523].

[364] M. T. Frandsen, F. Sannino, I. M. Shoemaker, and O. Svendsen, *LUX Constraints on Magnetic Dark Matter in the $S\bar{E}\chi y$ Model with(out) Naturality*, arXiv:1312.3326.

[365] M. T. Frandsen, U. Haisch, F. Kahlhoefer, P. Mertsch, and K. Schmidt-Hoberg, *Loop-induced dark matter direct detection signals from gamma-ray lines*, *JCAP* **1210** (2012) 033, [arXiv:1207.3971].

[366] K. Sigurdson, M. Doran, A. Kurylov, R. R. Caldwell, and M. Kamionkowski, *Dark-matter electric and magnetic dipole moments*, *Phys.Rev.* **D70** (2004) 083501, [astro-ph/0406355].

[367] V. Barger, W.-Y. Keung, and D. Marfatia, *Electromagnetic properties of dark matter: Dipole moments and charge form factor*, *Phys.Lett.* **B696** (2011) 74–78, [arXiv:1007.4345].

[368] A. Fitzpatrick and K. M. Zurek, *Dark Moments and the DAMA-CoGeNT Puzzle*, *Phys.Rev.* **D82** (2010) 075004, [arXiv:1007.5325].

[369] T. Banks, J.-F. Fortin, and S. Thomas, *Direct Detection of Dark Matter Electromagnetic Dipole Moments*, arXiv:1007.5515.

[370] N. Weiner and I. Yavin, *How Dark Are Majorana WIMPs? Signals from MiDM and Rayleigh Dark Matter*, arXiv:1206.2910.

[371] E. Del Nobile, G. Gelmini, P. Gondolo, and J.-H. Huh, *Generalized Halo Independent Comparison of Direct Dark Matter Detection Data*, arXiv:1306.5273.

[372] **XENON100 Collaboration** Collaboration, E. Aprile et al., *Dark Matter Results from 225 Live Days of XENON100 Data*, arXiv:1207.5988.

[373] J. Kopp, T. Schwetz, and J. Zupan, *Light Dark Matter in the light of CRESST-II*, *JCAP* **1203** (2012) 001, [arXiv:1110.2721].

[374] M. Pospelov and T. ter Veldhuis, *Direct and indirect limits on the electromagnetic form-factors of WIMPs*, *Phys.Lett.* **B480** (2000) 181–186, [hep-ph/0003010].

[375] **XENON100 Collaboration** Collaboration, E. Aprile et al., *Dark Matter Results from 100 Live Days of XENON100 Data*, *Phys.Rev.Lett.* (2011) [arXiv:1104.2549].

[376] C. McCabe, *The Astrophysical Uncertainties Of Dark Matter Direct Detection Experiments*, *Phys.Rev.* **D82** (2010) 023530, [arXiv:1005.0579].

[377] M. Farina, D. Pappadopulo, A. Strumia, and T. Volansky, *Can CoGeNT and DAMA Modulations Be Due to Dark Matter?*, *JCAP* **1111** (2011) 010, [arXiv:1107.0715].

[378] A. M. Green, *Astrophysical uncertainties on direct detection experiments*, *Mod.Phys.Lett.* **A27** (2012) 1230004, [arXiv:1112.0524].

[379] M. Fairbairn, T. Douce, and J. Swift, *Quantifying Astrophysical Uncertainties on Dark Matter Direct Detection Results*, arXiv:1206.2693.

[380] S. Yellin, *Finding an upper limit in the presence of unknown background*, *Phys. Rev.* **D66** (2002) 032005, [physics/0203002].

[381] **WMAP** Collaboration, G. Hinshaw et al., *Nine-Year Wilkinson Microwave Anisotropy Probe (WMAP) Observations: Cosmological Parameter Results*, *Astrophys.J.Suppl.* **208** (2013) 19, [arXiv:1212.5226].

[382] **Planck Collaboration** Collaboration, P. Ade et al., *Planck 2013 results. XVI. Cosmological parameters*, arXiv:1303.5076.

[383] **XENON1T collaboration** Collaboration, E. Aprile, *The XENON1T Dark Matter Search Experiment*, `arXiv:1206.6288`.

[384] D. Malling, D. Akerib, H. Araujo, X. Bai, S. Bedikian, et al., *After LUX: The LZ Program*, `arXiv:1110.0103`. see also http://www.hep.ucl.ac.uk/darkMatter/LZ.shtml.

[385] Q.-H. Cao, C.-R. Chen, C. S. Li, and H. Zhang, *Effective Dark Matter Model: Relic density, CDMS II, Fermi LAT and LHC*, *JHEP* **1108** (2011) 018, [`arXiv:0912.4511`].

[386] M. Beltran, D. Hooper, E. W. Kolb, Z. A. Krusberg, and T. M. Tait, *Maverick dark matter at colliders*, *JHEP* **1009** (2010) 037, [`arXiv:1002.4137`].

[387] J. Goodman, M. Ibe, A. Rajaraman, W. Shepherd, T. M. Tait, et al., *Constraints on Dark Matter from Colliders*, *Phys.Rev.* **D82** (2010) 116010, [`arXiv:1008.1783`].

[388] J. Goodman and W. Shepherd, *LHC Bounds on UV-Complete Models of Dark Matter*, `arXiv:1111.2359`.

[389] P. J. Fox, R. Harnik, J. Kopp, and Y. Tsai, *LEP Shines Light on Dark Matter*, *Phys.Rev.* **D84** (2011) 014028, [`arXiv:1103.0240`].

[390] H. Dreiner, M. Huck, M. Kramer, D. Schmeier, and J. Tattersall, *Illuminating Dark Matter at the ILC*, `arXiv:1211.2254`.

[391] J. Alwall, P. Demin, S. de Visscher, R. Frederix, M. Herquet, et al., *MadGraph/MadEvent v4: The New Web Generation*, *JHEP* **0709** (2007) 028, [`arXiv:0706.2334`].

[392] **DELPHI Collaboration** Collaboration, J. Abdallah et al., *Photon events with missing energy in e+ e- collisions at s**(1/2) = 130-GeV to 209-GeV*, *Eur.Phys.J.* **C38** (2005) 395–411, [`hep-ex/0406019`].

[393] **DELPHI Collaboration** Collaboration, J. Abdallah et al., *Search for one large extra dimension with the DELPHI detector at LEP*, *Eur.Phys.J.* **C60** (2009) 17–23, [`0901.4486`].

[394] **ILD Concept Group - Linear Collider Collaboration** Collaboration, T. Abe et al., *The International Large Detector: Letter of Intent*, `arXiv:1006.3396`.

[395] C. Bartels, *WIMP search and a Cherenkov detector prototype for ILC polarimetry*, .

[396] T. Aoyama, M. Hayakawa, T. Kinoshita, and M. Nio, *Tenth-Order QED Contribution to the Electron g-2 and an Improved Value of the Fine Structure Constant*, *Phys.Rev.Lett.* **109** (2012) 111807, [`arXiv:1205.5368`].

[397] **Particle Data Group** Collaboration, J. Beringer et al., *Review of Particle Physics (RPP)*, *Phys.Rev.* **D86** (2012) 010001.

[398] A. Ishida, T. Namba, S. Asai, T. Kobayashi, H. Saito, et al., *New Precision Measurement of Hyperfine Splitting of Positronium*, `arXiv:1310.6923`.

[399] K. Melnikov and A. Yelkhovsky, *$O(\alpha^3 ln\alpha)$ corrections to muonium and positronium hyperfine splitting*, *Phys. Rev. Lett.* **86** (2001) 1498–1501, [`hep-ph/0010131`].

[400] S. J. Brodsky and R. F. Lebed, *Production of the Smallest QED Atom: True Muonium (mu+ mu-)*, *Phys.Rev.Lett.* **102** (2009) 213401, [`arXiv:0904.2225`].

[401] U. Jentschura, G. Soff, V. Ivanov, and S. G. Karshenboim, *Decay rates and hyperfine structure of the bound mu+ mu- system*, `hep-ph/9706401`.

[402] **MEG Collaboration** Collaboration, J. Adam et al., *New constraint on the existence of the $\mu^+ \to e^+ gamma$ decay*, `arXiv:1303.0754`.

[403] **BaBar Collaboration** Collaboration, B. Aubert et al., *Searches for Lepton Flavor Violation in the Decays $\tau^\pm \to e^\pm\gamma$ and $\tau^\pm \to \mu^\pm\gamma$*, *Phys.Rev.Lett.* **104** (2010) 021802, [`arXiv:0908.2381`].

[404] Y. Kuno and Y. Okada, *Muon decay and physics beyond the standard model*, *Rev.Mod.Phys.* **73** (2001) 151–202, [`hep-ph/9909265`].

[405] **SINDRUM Collaboration** Collaboration, U. Bellgardt et al., *Search for the Decay $\mu^+ \to e^+e^+e^-$*, *Nucl.Phys.* **B299** (1988) 1.

[406] A. Blondel, A. Bravar, M. Pohl, S. Bachmann, N. Berger, et al., *Research Proposal for an Experiment to Search for the Decay $\mu \to eee$*, `arXiv:1301.6113`.

[407] **Mu3e** Collaboration, C. Martín Pérez, *Search for the lepton flavor violating decay $\mu\ ^+ \to e\ ^+\ e\ ^-\ e\ ^+$ with the Mu3e experiment at PSI*, *JINST* **18** (2023), no. 08 C08004.

[408] V. Shtabovenko, R. Mertig, and F. Orellana, *New Developments in FeynCalc 9.0*, *Comput. Phys. Commun.* **207** (2016) 432–444, [`arXiv:1601.01167`].

[409] R. Mertig, M. Bohm, and A. Denner, *FEYN CALC: Computer algebraic calculation of Feynman amplitudes*, *Comput. Phys. Commun.* **64** (1991) 345–359.

[410] D. Binosi and L. Theußl, *JaxoDraw: A Graphical user interface for drawing Feynman diagrams*, *Comput. Phys. Commun.* **161** (2004) 76–86, [`hep-ph/0309015`].

[411] J. D. Hunter, *Matplotlib: A 2d graphics environment*, *Computing in Science & Engineering* **9** (2007), no. 3 90–95.

Acknowledgements

All names and personal references were removed in the electronic publication of this dissertation.

First and foremost, I would like to thank my supervisor for his guidance throughout this work and for his patience along the way. This thesis would not have been possible without his continuous support, valuable insights, and tireless encouragement.

I am very grateful to my collaborator and, in some ways, a second advisor, for always taking the time to answer my many questions and for his invaluable support throughout our project and during the writing of this thesis. I would also like to thank my other collaborator and close friend for her constant support and guidance throughout my PhD, and especially during our project. Even in challenging times, she always made time to help and offer advice. Her example and encouragement were instrumental in helping me persevere, and it was a special honour to work with her. My thanks also go to my other collaborator for his contributions to our joint project with my supervisor, and to both of them for bringing it to such a successful publication. I am also grateful to my friend and former colleague for his help with the manuscript and with programming questions throughout this thesis.

I would like to thank all my colleagues who shared part of this journey with me in Mainz and Heidelberg, and who contributed to making this time truly enjoyable. Their support, stimulating discussions, and companionship made this period very rewarding. I will always value our coffee breaks, conversations, and the sense of community we shared. I would also like to thank the administrative staff for their constant help and kindness with all administrative matters, and for making this work possible in the first place.

I am especially grateful to two of my colleagues, who became invaluable friends. Their kindness, the fact that they always made time to listen and talk things through whenever needed, and their steady encouragement – especially during difficult times – meant more to me than I can fully express. They helped me regain motivation and clarity when I needed it most, and their support made a lasting difference throughout this work. More generally, I am deeply thankful to all my friends for their encouragement, for always being there for me, for never losing faith in me, and for providing moments of relief from the stress.

Last but not least, I would like to thank my family for their support, patience, and encouragement. Their love has sustained me throughout this time, and their presence helped me stay grounded and keep perspective on what is important in life.

Colophon

This thesis was typeset with LaTeX2e using the document class `scrbook` of KOMA-Script from Markus Kohm published on `http://www.komascript.de/` under the LaTeX Project Public License, version 1.3c and BibTeX with the bibliography style file from the *Journal of High Energy Physics* published on `https://jhep.sissa.it/jhep/` under the LaTeX Project Public License, version 1.3c. Feynman graphs were drawn with JaxoDraw [410] (Figures 1.1, 2.1, 2.2, 2.3, 3.2, 3.11, 3.15, 4.1, 4.4, 4.10, 4.11, 4.12, and A.1) which is distributed under the Gnu general public licence, numerical calculations and plots thereof were performed in Mathematica [174] (Figures 2.4, 2.5, 2.6, 2.7, 2.8, 2.9, 3.3, 3.13, 4.2, and 4.3, 4.5, 4.6, 4.7, 4.8, 4.9). Other plots were generated using Matplotlib [411] in python (Figures 3.4, 3.5, 3.6, 3.9, 3.10, 3.16, and 3.17). The curriculum vitae uses the LaTeX document class Moderncv from Xavier Danaux published on `https://github.com/xdanaux/moderncv` under the LaTeX Project Public License, version 1.3c.

Utilisation of KI-tools

The following KI-tools were used in this thesis:

KI tool	used for	why	where
ChatGPT	text smoothing	better readability	Abstract, Introduction, Summary and Conclusions
ChatGPT	writing code for data processing in python	visualisation of data	Figures 3.4, 3.5, 3.6, 3.9, 3.10, 3.16, and 3.17

Table A.1